University of Oklahoma

Graduate College

Hot Electrons and Radial Transport in Saturn's Inner Magnetosphere: Modeling the Effects on Ion Chemistry

A Dissertation

Submitted to the Graduate Faculty

in partial fulfillment of the requirements for the

Degree of

Doctor of Philosophy

By

Bobby L. Fleshman
Norman, Oklahoma
2012

Downloaded from SHAREOK. Persistent Handle URL: https://hdl.handle.net/11244/8104

Hot Electrons and Radial Transport in Saturn's Inner Magetosphere: Modeling the Effects on Ion Chemistry

A Dissertation Approved for the
Homer L. Dodge Department of Physics and Astronomy

By

Dr. Edward Baron (Chair)

Dr. Fran Bagenal

Dr. Peter Delamere

Dr. John Cowan

Dr. David Branch

Dr. Ron Kantowski

Dr. Charles Rice

© Copyright Bobby L. Fleshman 2012
All Rights Reserved.

For Paul.

Acknowledgements

I have inevitably forgotten to include as many as I haven't. For that, I genuinely apologize. And do take it up with me over our next pint...

Margaret Mullican, thank you for the introduction to Physics. Thank you Rodney Fish and Randy Penner—two of the brightest and hardest-working people I have had the pleasure to know.

Thank you Saeed Shadfar for being such a good friend, and for demanding the most of me at the outset. Thank you Bob Trail and Klaus Rossberg for suggesting I take this journey—and for loving what you do.

Thank you Brad, Ron, Kim, David, and John. You are some of the finest researchers and instructors one could hope to know. Chuck, thank you for taking this appointment on with such short notice. Ralph, thank you for sitting on the committee before taking the position at Duquesne. Eddie, thank you for embracing this collaboration, and laboring through the obligatory ski days.

A NASA fellowship (NESSF) has funded my research for these last three years. For that I am obviously grateful. Thank you Sonya, Debbie, Danette, Dede, and Sharon for making the red tape as smooth as possible.

Fran, thank you for inspiring me personally and professionally. Thank you for taking the chance. Peter, you have influenced me as scientist immeasurably.

To say one doesn't choose their family sells my own short. Thank you mom, dad, Karen, and Steve for backing me in everything I do. Thank you Kevin, Val, Cindi, and Mike. Thanks to everyone for supporting Al and me throughout, despite our

all-too-often conspicuous absence.

Thank you to so many other friends from whom I've drawn inspiration: Larry (also for this thesis template), Jack, Laura, Stacy, Junior, Gordon, Levi, Stephane, Shayne,...Brent. To my friends in Colorado: Tim, Licia, Mariel, Rob, and Crusher. I could not have imagined a better work environment; nor could I have hand-picked so many amazing friends.

To Chance, my loyal sidekick from even before I left construction.

To Al, all I can say is, "Never a dull moment!" What a journey it has been. And will be.

Contents

Acknowledgements **iv**

Abstract **xviii**

1 Introduction **1**
1.1 Physical chemistry model (Chapter 2) . . . 5
1.2 Plume–plasma interaction (Chapter 3) . . . 7
1.3 Neutral cloud model (Chapter 4) . . . 9
1.4 Radial ion chemistry model (Chapter 5) . . . 10

2 One-box chemistry model **13**
2.1 Introduction . . . 14
2.2 Observations . . . 18
2.2.1 Parameters . . . 18
2.2.2 Constraints (n_e, T_e, W^+/H^+) . . . 22
2.3 Model . . . 24
2.4 Baseline solution . . . 27
2.4.1 Procedure . . . 27
2.4.2 Results . . . 28
2.4.3 Sensitivity . . . 39
2.5 Grid search . . . 41
2.5.1 Results . . . 41
2.6 Hot electron (f_{eh}) modulation . . . 53
2.7 Conclusions . . . 56

3 Modeling the plume–plasma interaction **59**
3.1 Introduction . . . 59
3.2 Model . . . 61
3.3 Results . . . 65
3.4 Discussion and conclusions . . . 70

4 The roles of charge exchange and dissociation in spreading Saturn's neutral clouds **72**
4.1 Introduction . . . 73
4.2 Model . . . 76
4.2.1 Neutral torus model . . . 76
4.2.2 Neutral cloud model . . . 82
4.3 Results . . . 92
4.3.1 Charge exchange . . . 92
4.3.2 Dissociation . . . 99
4.3.3 Fates of neutral atoms and molecules . . . 100
4.4 Discussion . . . 107
4.5 Conclusions . . . 111

5 Characterizing ion conditions between 4 and 10 R_S **115**
5.1 Introduction . . . 116
5.2 Model . . . 118
5.2.1 Prescribed quantities . . . 118
5.2.2 Parameters . . . 121
5.2.3 Constraints . . . 123
5.2.4 Method . . . 124
5.3 Results . . . 131
5.3.1 Nominal case . . . 131
5.3.2 Sensitivity study . . . 148
5.4 Discussion . . . 162
5.5 Conclusions and Future . . . 164

6 Future work **166**

REFERENCES **167**

A One-box model: calculations and tables **178**
A.1 Equations . . . 178
A.1.1 Ion Rate Equations . . . 179
A.1.2 Electron Rate Equation . . . 183
A.1.3 Neutral Rate Equations . . . 184

B Charge exchange collision probability **201**

C Radial model sensitivity plots **203**

List of tables

2.1 Model constraints (see Section 2.2.2 for references) and output for the best fit baseline solution. The fit is defined as the combination of parameters $T_{\rm eh}$, $f_{\rm eh}$, $f_{\rm H^+}$, $\tau_{\rm trans}$, and $N_{\rm src}$ that gives the smallest total fractional difference between the data and the model output. Notice that the model output for the constraints (in bold) agrees with the data to at least two significant figures. No reaction leads to H_3O in our set of reactions (Appendix A). 18

2.2 Baseline lifetimes for each species by mechanism in descending order of frequency (Rate $= 1/\tau$). Electron-impact ionization and photoionization include processes that are both ionizing and dissociative. A listing of lifetimes by reaction can be found in Appendix A. 29

2.3 List of the most important reactions for the baseline case. The left column gives the relevant impact, dissociative, and photolytic reactions, and the right column gives all relevant charge exchanges and recombinations. The full set of reactions are given in Appendix A, but steady-state densities and temperatures are all within 3% of the properly calculated values when only the above reactions are turned on. 38

3.1 Pickup rates from charge exchange ($\dot{M}_{\rm exch}$) and impact/photoionization ($\dot{M}_{\rm ioz}$) for the eight cases discussed in the text. Only $\dot{M}_{\rm ioz}$ increases the plasma density ($n_{\rm e}$). The cases labeled with 'a' correspond to a neutral source rate of 200 kg s^{-1}; those labeled with 'b' correspond to a neutral source rate of 1600 kg s^{-1}. Case (1a), in bold, is the nominal case from which Figure 3.1 and Figure 3.2 have been generated. 68

5.1 Parameters describing the radial profiles for radial transport and hot electron density (Equation 5.6 and Equation 5.8). Nominal values are given in each case. In square brackets are the ranges for which each parameter has been set in producing Figure 5.2 and Figure 5.3. 123

A.1 Particle flow for the baseline solution. Listed are fast neutrals and transported ions in both particle flux and mass flux for a torus volume of $2\pi(4R_{\rm S})(2R_{\rm S})^2$. The source is $N_{\rm H_2O} = 2.0\times10^{-4}\,{\rm cm^{-3}\,s^{-1}} = 130\,{\rm kg\,s^{-1}}$. Percentages are given in parentheses, and the bold-facings are sub-totals. 186

A.2 Energy flow for the baseline solution. Charge-exchange and impact ionization as well as hot-electron coupling serve as energy input. (Internal electron–ion coupling is *not* part of the energy input.) Energy leaves the box via radial transport, hot neutrals, and radiation by electron impact excitation. Power is calculated for a torus volume of $2\pi(4R_{\rm S})(2R_{\rm S})^2$. Percentages are given in parentheses, and the bold-facings are sub-totals. 187

A.3 Electron impact ionization reactions. Values presented are for the baseline solution. The I's are the rate coefficients [$I_\alpha \equiv I_\alpha(T_\mathrm{e})$; $I_\alpha^\mathrm{h} \equiv I_\alpha(T_\mathrm{eh})$], and the third column gives the number of each reaction occurring per cubic centimeter per second. The bold facing guides the eye to the most important reactions. 188
A.4 Electron impact ionization–dissociation reactions. Values presented are for the baseline solution. The I's are the rate coefficients [$I_\alpha^\mathrm{diss} \equiv I_\alpha^\mathrm{diss}(T_\mathrm{e})$; $I_\alpha^\mathrm{diss,h} \equiv I_\alpha^\mathrm{diss}(T_\mathrm{eh})$], and the third column gives the number of each reaction occurring per cubic centimeter per second. The bold facing guides the eye to the most important reactions. 189
A.5 Electron recombination reactions. Values presented are for the baseline solution. The R's are the rate coefficients [$R_\alpha \equiv R_\alpha(T_\mathrm{e})$; $R_\alpha^\mathrm{h} \equiv R_\alpha(T_\mathrm{eh})$], and the third column gives the number of each reaction occurring per cubic centimeter per second. Notice that molecular recombinations (Table A.6) are far more likely than the atomic recombinations listed here. . . . 190
A.6 Dissociative electronic recombination reactions. Values presented are for the baseline solution. The R's are the rate coefficients [$R_\alpha^\mathrm{diss} \equiv R_\alpha^\mathrm{diss}(T_\mathrm{e})$; $R_\alpha^\mathrm{diss,h} \equiv R_\alpha^\mathrm{diss}(T_\mathrm{eh})$], and the third column gives the number of each reaction occurring per cubic centimeter per second. The bold facing guides the eye to the most important reactions. 191
A.7 Photolytic reactions. The κ's are the rate coefficients at 9.5 AU, and the third column gives the number of each reaction occurring per cubic centimeter per second for the baseline solution. The bold facing guides the eye to the most important reactions. 192
A.8 Charge exchange reactions. The k's are the reaction rates, and the third column gives the number of each reaction occurring per cubic centimeter per second for the baseline solution. The bold facing guides the eye to the most important reactions. [a]The resonant exchange reaction rate for H_2O is calculated as a function of ion temperature by convolution of the cross sections from *Lishawa et al.* (1990); the k presented here is for the baseline solution (all other k's are constants). 193
A.9 Impact dissociation reactions. Values presented are for the baseline solution. The D's are the rate coefficients [$D_\alpha \equiv D_\alpha(T_\mathrm{e})$; $D_\alpha^\mathrm{h} \equiv D_\alpha(T_\mathrm{eh})$], and the third column gives the number of each reaction occurring per cubic centimeter per second. The bold facing guides the eye to the most important reactions. 194
A.10 Baseline lifetimes for neutral species by reaction in descending order of importance (Rate $= 1/\tau$). Dominant loss mechanisms are typeset in bold (the cut-off is arbitrarily chosen at 500 days). 195
A.11 Baseline lifetimes for charged species by reaction in descending order of importance (Rate $= 1/\tau$). The bolding indicates the cut-off for those reactions occuring within the radial transport timescale ($\tau_\mathrm{trans}^\mathrm{baseline} = 26$ days). 196

List of figures

1.1 Image of Saturn eclipsing the sun, taken from Cassini in 2006 (NASA). In addition to Saturn's main rings, the neutral torus embedding Enceladus's orbit (commonly referred to as the E ring) can also be made out from reflected sunlight. Above the main rings on the left, one can barely make at out the pale blue light reflected from the earth's atmosphere. 2

1.2 Enceladus with its tiger-striped south pole, along which a number of geysers eject water into orbit around Saturn (NASA). At 500 km, the diameter of Enceladus is about the width of the United Kingdom. . . . 3

1.3 Enceladus plumes from an early flyby in 2005 (*Dougherty et al.*, 2006b; *Hansen et al.*, 2006), from which estimates of the mass ejection rates were obtained (NASA). At this distance only the largescale structure can be made out, though the plumes are produced from many active fissures (see Figure 1.4). 4

1.4 A close-up of the Enceladus plumes from a later flyby in 2009. In this case, the individual plumes are resolvable (image courtesy ciclops.org). . 4

2.1 Particle flow for the baseline case. We have assumed a torus volume of $2\pi(4R_S)(2R_S)^2$ to calculate the volumetric mass flow. The percentages given here are for particle *number* (not mass). Individual species contributions to the particle outflow can be found in Appendix A. . . . 32

2.2 Energy flow for the baseline case. We have assumed a torus volume of $2\pi(4R_S)(2R_S)^2$ to calculate the volumetric energy flow. Individual species contributions to the energy outflow can be found in Appendix A. 32

2.3 Sensitivity plots of f_{diff} for every parameter combination. In each case, the remaining three parameters are fixed at their baseline values (Table 2.1) to ascertain trends due solely to variation of a single parameter at a time. The intersection of dashed lines indicates the baseline solution, and the gray shading inside of $f_{\text{diff}} = 1$ is intended to guide the eye. (Contours are plotted logarithmically.) 40

2.4 Sensitivity plots between hot electron temperature (T_{eh}) and hot electron fraction (f_{eh}) generated from the grid search. The over-plotted box represents the baseline solution, discussed in Section 2.4. The $f_{\text{diff}} = 0.05$ curve (Panel 1) has been over-plotted on Panels 5–13 in gray. The three parameters in Panels 5–7 (τ_{trans}, N_{src}, and f_{H^+}) have taken on values yielding best agreement between model output and $n_e = 60$ cm^{-3}, $T_e = 2$ eV, and $W^+/H^+ = 12$. Combinations of T_{eh} and f_{eh} within the gray contour are consistent with these constraints. All panels are discussed in Section 2.5.1. 43

2.5 Electron-impact reaction rates for the water group ($O + OH + H_2O$) and hydrogen. The bottom panel emphasizes that water-group reaction rates fall faster than hydrogen reaction rates as T_{eh} increases. 47

2.6 Sensitivity plots between radial transport timescale ($\tau_{\rm trans}$) and hot electron fraction ($f_{\rm eh}$) generated from the grid search. The over-plotted box represents the baseline solution, discussed in Section 2.4. The $f_{\rm diff} = 0.05$ curve (Panel 1) has been over-plotted on Panels 5–13 in gray. The three parameters in Panels 5–7 ($N_{\rm src}$, $\tau_{\rm trans}$, and $f_{\rm H^+}$) have taken on values yielding best agreement between model output and $n_{\rm e} = 60$ cm^{-3}, $T_{\rm e} = 2$ eV, and $\rm W^+/H^+ = 12$. Combinations of $\tau_{\rm trans}$ and $f_{\rm eh}$ within the gray contour are consistent with these constraints. All panels are discussed in Section 2.5.1. 48

2.7 Solutions for various proton dilution factors ($f_{\rm H^+} = 0.7, 0.85, 1.0$) found from the grid search in Section 2.5.1. The parameters in the left panel are normalized to the values listed in Table 2.1. In the right panel are the water-group abundance ratios. Proton production is strongly controlled by impact ionization of hydrogen by hot electrons, and so $f_{\rm H^+}$ is coupled to $T_{\rm eh}$ and $f_{\rm eh}$. This coupling diminishes the significance of $f_{\rm H^+}$ and effectively reduces the parameter space to four dimensions. 49

2.8 Solutions for primary constraint values representing a wide range of observations found from the grid search in Section 2.5.1. In each case, $n_{\rm e} = 60$ cm^{-3}, $T_{\rm e} = 2$ eV, and $\rm W^+/H^+ = 12$ unless otherwise specified. The parameter fits given in the left panel of each bar chart are normalized to the fit given in Table 2.1. The over-plotted ranges on the parameters are derived from the corresponding $f_{\rm diff} = 0.05$ sensitivity contours. No such ranges exist for the $T_{\rm e} = 1$ eV and $T_{\rm e} = 3$ eV solutions because the best fits have a fractional difference of 0.43 and 0.19, respectively. The corresponding model output for water-group composition is presented on the right. The choice of electron density ($n_{\rm e}$) has a weak effect, while the ratio $\rm W^+/H^+$ ratio alters composition markedly. 52

2.9 Composition variability due to hot electron modulation. The hot electron fraction, $f_{\rm eh}$, alone drives the variation since all other parameters are held at their baseline values. The quantities $\rm O^+/W^+$, $\rm OH^+/W^+$, $n_{\rm e}$, and $T_{\rm e}$ are in phase while $\rm W^+/H^+$, $\rm H_2O^+/W^+$, and $\rm H_3O^+/W^+$ are out of phase with $f_{\rm eh}$. The bottom panel shows how strongly and how linearly each quantity responds to perturbations in $f_{\rm eh}$; the solid lines represent quantities in phase with $f_{\rm eh}$, and the dashed lines represent quantities out of phase with $f_{\rm eh}$. 54

3.1 *Upper-left*: the x component of the assumed local plasma flow speed (Section 3.2) normalized to the ambient flow speed (80% of rigid corotation). *Upper-right*: water-group to proton abundance ratio. *Lower-left*: $\rm H_3O^+/W^+$ abundance ratio. *Lower-right*: $\rm H_3O^+$ temperature. The plane represented here is 7.5 $\rm R_E$ south of Enceladus. Model output along the dashed line is given in Figure 3.2. 66

3.2 *Top*: Abundances and electron density from the simulation along the dashed line in Figure 3.1. *Bottom*: Electron, proton and H_3O^+ temperatures along the same cut. The electron temperature is normalized to its ambient temperature (2 eV), and the ion temperatures are normalized to their ambient pickup energies—1.5 and 29 eV for H^+ and H_3O^+ respectively. 67

4.1 Sketch of gyrating ions in the neutral frame with guiding centers moving along a prescribed flow field, shown here near Enceladus for scale. Warm ions ($v_\perp > v_{\rm flow}$) move on trajectories that coil around themselves and do not reach zero relative velocity with respect to the neutrals at any point. Cool ions ($v_\perp < v_{\rm flow}$) essentially trace their guiding centers with 'snake-like' trajectories, and also do not obtain zero relative velocity. Fresh pickup ions ($v_\perp \approx v_{\rm flow}$) do, however, obtain near zero relative velocity at the cusps of their cycloidal trajectories. Neutrals produced by charge exchange (whose trajectories are indicated by the red lines) tend to be created with velocities at which the respective reaction rates peak (Figure 4.2). 86

4.2 (a.) Cross sections for the reactions listed in the legend. Data for Reaction 4.3a and Reaction 4.3b are from *Lishawa et al.* (1990), and data for reaction Reaction 4.3c is from *Li et al.* (1995). $\sigma_{\rm OH}^{\rm extrapolated}$, $\sigma_{\rm OH}^{\rm symmetric}$, and $\sigma_{\rm OH}^{\rm asymmetric}$ are hypothetical fits applying to the OH^*-producing reaction, and are explored in Figure 4.4. Ions oscillate between ≈ 0 and 36 km s^{-1}in the Enceladus torus. (b.) Collision frequency, $n\sigma(v)v$, for a given density of $n_{H_2O} = 10^3$ cm^{-3} plotted over the same energy range. The collision frequency increases with energy in the oxygen-forming reaction, while the water-forming reaction is independent of energy and the OH-forming reaction declines with energy. 88

4.3 Neutral clouds produced by the reactions shown in Figure 4.2. (a.) Oxygen is the most abundant because the cross section is 10× higher than than with O and OH. The lifetime of oxygen against photoionization is also much longer than the lifetime for either OH or H_2O against photodissociation. (b.) Same as above, but normalized to peak. Oxygen shows the most spreading because reactants are produced with higher velocities (Figure 4.2b), which expands the cloud. The same trend holds with H_2O and OH, where OH tends to be created with the lowest velocities (Figure 4.2, $\sigma_{\rm OH}^{\rm extrapolated}$). 89

4.4 Neutral OH clouds produced from three hypothetical charge exchange cross sections: $\sigma_{\rm OH}^{\rm extrapolated}$, $\sigma_{\rm OH}^{\rm symmetric}$, and $\sigma_{\rm OH}^{\rm asymmetric}$ (Figure 4.2). (a.) $\sigma_{\rm OH}^{\rm extrapolated}$ produces the highest density ($\sigma_{\rm OH}^{\rm asymmetric}$, the lowest) at Enceladus because of the creation of additional low-velocity particles. (b.) Same as above, but normalized to peak. The differences in density in the tail is not an indication of spreading, but rather further illustrates the deficiency in the peak density, going from $\sigma_{\rm OH}^{\rm extrapolated}$ to $\sigma_{\rm OH}^{\rm asymmetric}$. 90

4.5 (a) Comparison between charge exchanged neutrals produced near the Enceladus plume and those produced from the neutral torus as a whole—in this case for oxygen. (b.) Though shown here for oxygen, all charge exchange reactions near the plume result in a cloud with less spreading than their global counterpart due to the imposed slowing of the plasma (and hence, the release of slower neutral products) near the plume in response to mass-loading (Chapter 3). 98
4.6 OH clouds produced from charge exchange and high- and low-speed dissociation. Dissociation dominates neutral cloud production inside 9–15 R_S, at which point charge exchange becomes the dominant contributor. 100
4.7 Neutral cloud densities in the r–z plane. (a.) Hydrogen produced purely from H_2O dissociation. (b.) Oxygen produced purely from charge exchange (Reaction 4.3c). (c.) Hydroxyl produced from the combination of charge exchange and dissociation. Dissociation dominates inward of 9–15 R_S along the equator, while charge exchange (Reaction 4.3b) tenuously fills the magnetosphere elsewhere. (d.) Water produced entirely by charge exchange (Reaction 4.3a). (e.) Dense torus fed directly by the Enceladus plumes (Section 4.2.1). 101
4.8 The fates of neutrals in the model along with the results from other models. (a.) Dissociation produces low-velocity neutrals and OH is thus not likely to escape or to be absorbed. Conversely, dissociation also produces hydrogen which largely leaves the system. (b.) The results of J06 (*Johnson et al.*, 2006), J07 (*Jurac and Richardson*, 2007), and C10 (*Cassidy and Johnson*, 2010), along with our own weighted totals (excluding hydrogen; see Section 4.3.3). In the case of τ_{phot}, the lifetime of the cloud is determined by photoionization/dissociation only, whereas with τ_{all}, we limit the lifetimes by also including electron impact and charge exchange. These limiting cases bound the previous studies, except that C10 has more absorption attributed to neutral–neutral collisions. . 102
4.9 (a.) Neutrals absorbed by Saturn, plotted by species. Partitions with horizontal lines indicate percentages absorbed by Saturn's rings. (b.) Neutral flux on Saturn as a function of latitude. Neutrals produced by charge exchange (H_2O, OH, and O) peak in flux at low latitudes due to the nature of the ion distributions from which they orginate, which have initial velocity vectors predominantly in the ring plane. Conversely, hydrogen flux is constant across Saturn because it originates from dissociation, whose velocity distribution is prescribed as isotropic. Note that OH produced by dissociation is not energetic enough to reach Saturn. . 107

4.10 (a.) Total neutral clouds from our model, compared with *Cassidy and Johnson* (2010) (C10). All clouds include contributions from charge exchange (Reaction 4.3a, Reaction 4.3b, and Reaction 4.3c), while H_2O is largely comprised of water sourced directly from Enceladus, and OH includes contributions from dissociation. The cloud densities are limited by photodissociation for OH and H_2O and by photoionization for O. Including charge exchange as a loss for cloud neutrals would reduce the lifetime for O more than for either the OH or H_2O, and would lower the relative oxygen abundance accordingly. (b.) Equatorial column densities found by integrating the plotted equatorial densities. The H_2O column density is similar to C10, despite their having a very different radial distributions. (c.) Total neutral cloud content. Our total H_2O content is less than C10 found, while our H_2O column density is higher because our H_2O cloud is not subjected to neutral collisions and is thus more confined. 110

5.1 Neutral densities from *Cassidy and Johnson* (2010), extrapolated to higher latitudes using Equation 5.1 and Equation 5.2. H_2O peaks strongly at Enceladus's orbit (4 R_S), while the hydrogen cloud is the least confined to the equator. The oxygen and OH clouds represent intermediate cases, having been formed by the combination of dissociation and charge exchange. 119

5.2 Selected hot electron and transport profiles, here for the 1-D model. Plots on the left are for varying normalization (τ_0 and f_{eh0}). On the right are plots for varying slopes (α and β). The middle panels are the integral of $\tau(L)$ from $L = 4$. Dashed lines are the nominal profiles. . . . 132

5.3 Selected hot electron and transport profiles, here for the 2-D model. Plots on the left are for varying normalization (τ_0 and f_{eh0}). On the right are plots for varying slopes (α and β). The middle panels are the integral of $\tau(L)$ from $L = 4$. Dashed lines are the nominal profiles. . . . 133

5.4 Total mass and total mass source rate for the 1-D model. The upper-left panel is the mass per L shell, the integral of which is plotted in lower-left. On the right is the mass source rate given by Equation 5.22. 135

5.5 Total mass and total mass source rate for the 2-D model. The Upper-left panel is the mass per L shell, the integral of which is plotted in lower-left. On the right is the mass source rate given by Equation 5.22. 136

5.6 Equatorial ion and electron conditions for the 1-D nominal case. W08 are the fits from *Wilson et al.* (2008) given in Equation 5.12 and Equation 5.13. S06 are the fits from *Sittler et al.* (2006, 2007) given in Equation 5.9 and Equation 5.10. The electron densities and temperatures observations are from *Schippers et al.* (2008), where the temperatures given in Equation 5.11 and Equation 5.4. E_{pu} is the local pickup energy derived from the v_ϕ radial profile found in *Wilson et al.* (2008). 138

5.7 Equatorial ion and electron conditions for the 2-D nominal case. W08 are the fits from *Wilson et al.* (2008) given in Equation 5.12 and Equation 5.13. S06 are the fits from *Sittler et al.* (2006, 2007) given in Equation 5.9 and Equation 5.10. The electron densities and temperatures observations are from *Schippers et al.* (2008), where the temperatures given in Equation 5.11 and Equation 5.4. $E_{\rm pu}$ is the local pickup energy derived from the v_ϕ radial profile found in *Wilson et al.* (2008). 139
5.8 Nominal densities along the equator for the 1-D model. Proton and total water-group densities from observations are also plotted for reference (see Equation 5.12 and Equation 5.13). 140
5.9 Nominal densities along the equator for the 2-D model. Proton and total water-group densities from observations are also plotted for reference (see Equation 5.12 and Equation 5.13). 141
5.10 Nominal temperatures (independent of latitude) for the 1-D model. Proton and water-group ion data are given by Equation 5.9 and Equation 5.10, respectively (*Sittler et al.*, 2006, 2007). The shaded region is bounded from above by local pickup energies, and from below by the hypothetical temperature of fresh pickup ions transported adiabatically from at $L = 4$. 142
5.11 Nominal temperatures (independent of latitude) for the 2-D model. Proton and water-group ion data are given by Equation 5.9 and Equation 5.10, respectively (*Sittler et al.*, 2006, 2007). The shaded region is bounded from above by local pickup energies, and from below by the hypothetical temperature of fresh pickup ions transported adiabatically from at $L = 4$. 143
5.12 Nominal 2-D densities. Adjacent contours are separated by a factor of 0.41. 144
5.13 Nominal equatorial water-group composition from the 1-D model compared to data from *Sittler et al.* (2008). Although our results have not been constrained by these observations, the trends in the model bode well for a future comparison to CAPS data acquired throughout Cassini's Saturn campaign. 146
5.14 Nominal equatorial water-group composition from the 2-D model compared to data from *Sittler et al.* (2008). Although our results have not been constrained by these observations, the trends in the model bode well for a future comparison to CAPS data acquired throughout Cassini's Saturn campaign. 147
5.15 Loss rates for each species, derived from the 2-D model (similar in the 1-D model). Charge exchange dominates inside $L \approx 6$ for all species, beyond which transport dominates. Recombination plays an important role in removing H_3O^+ inside this critical point, but not for either OH^+ or H_2O^+. The short lifetimes for H^+ against charge exchange, make it difficult to match observed proton densities with the model (Figure 5.16–Figure 5.23). 148

5.16 Results from the 1-D model for a range of τ_0. All other parameters are set to the values given in Table 5.1. 149
5.17 Results from the 2-D model for a range of τ_0. All other parameters are set to the nominal values in Table 5.1. 150
5.18 Results from the 1-D model for a range of α. All other parameters are set to the nominal values in Table 5.1. 151
5.19 Results from the 2-D model for a range of α. All other parameters are set to the nominal values in Table 5.1. 152
5.20 Results from the 1-D model for a range of $f_{\rm eh0}$. All other parameters are set to the nominal values in Table 5.1. 153
5.21 Results from the 2-D model for a range of $f_{\rm eh0}$. All other parameters are set to the nominal values in Table 5.1. 154
5.22 Results from the 1-D model for a range of β. All other parameters are set to the nominal values in Table 5.1. 155
5.23 Results from the 2-D model for a range of β. All other parameters are set to the nominal values in Table 5.1. 156
5.24 1-D model sensitivity: τ_0 versus α. The statistic f is defined by Equation 5.14. 159
5.25 2-D model sensitivity: τ_0 versus α. The statistic f is defined by Equation 5.14. 160
5.26 1-D model sensitivity: τ_0 versus $f_{\rm eh0}$. The statistic f is defined by Equation 5.14. 161
5.27 2-D model sensitivity: τ_0 versus $f_{\rm eh0}$. The statistic f is defined by Equation 5.14. 162

A.1 Sensitivity plot of transport time versus neutral source rate. The intersection of dashed lines indicates the baseline solution. Panel 1 gives the total fractional difference ($f_{\rm diff}$) between model output and $n_{\rm e} = 60$ cm^{-3}, $T_{\rm e} = 1$ eV, and $W^+/H^+ = 12$. Panels 5−7 give the values of the 3 free parameters, and Panels 8−13 give the values for water-group composition, UV power, and mass-loading due to radially-diffused ions. Volumetric quantities (Panels 12 and 13) are calculated using a volume $= 2\pi(4R_{\rm S})(2R_{\rm S})^2$. The over-plotted gray region on Panels 5−13 delineates $f_{\rm diff} = 0.05$ (Panel 1). 197
A.2 Sensitivity plot of hot-electron fraction versus neutral source rate. See also caption, Figure A.1. 198
A.3 Sensitivity plot of hot-electron temperature versus neutral source rate. See also caption, Figure A.1. 199
A.4 Sensitivity plot of radial transport timescale versus hot-electron temperature. See also caption, Figure A.1. 200

C.1 1-D model sensitivity: τ_0 versus β. The statistic f is defined by Equation 5.14 on Page 124. 204
C.2 2-D model sensitivity: τ_0 versus β. The statistic f is defined by Equation 5.14 on Page 124. 204

C.3 1-D model sensitivity: α versus f_{eh0}. The statistic f is defined by Equation 5.14 on Page 124. 205
C.4 2-D model sensitivity: α versus f_{eh0}. The statistic f is defined by Equation 5.14 on Page 124. 205
C.5 1-D model sensitivity: α versus β. The statistic f is defined by Equation 5.14 on Page 124. 206
C.6 2-D model sensitivity: α versus β. The statistic f is defined by Equation 5.14 on Page 124. 206
C.7 1-D model sensitivity: f_{eh0} versus β. The statistic f is defined by Equation 5.14 on Page 124. 207
C.8 2-D model sensitivity: f_{eh0} versus β. The statistic f is defined by Equation 5.14 on Page 124. 207

Abstract

The E-ring of Saturn, located just beyond the main rings at four Saturn radii, was known to be made mostly of water and its by-products before the Cassini spacecraft arrived at Saturn in 2005. Since then, Cassini has observed water geysers on the tiny moon of Enceladus ejecting $\approx$ 100 kg of water per second into orbit around Saturn, which most agree is the chief contributor to neutrals in the E-ring. Following several key reactions, many of these neutrals go on to populate large, tenuous structures, known as neutral clouds, extending 10s of Saturn radii.

The other side of the story are the ions, which are largely created by the ionization of same neutrals sourced from Enceladus. A key distinction between the neutrals and ions is that ions are carried along by Saturn's magnetic field, and revolve around Saturn at the rotation rate of the planet, while neutrals generally have much slower Keplerian speeds.

It is the study of the chemical interaction of these separate, but related populations that is the subject of this thesis. We have developed a series of models to study how the coupling of these systems affect details of the other, such as composition.

The first step (Chapter 2) was the development of a water-group physical chemistry model, which includes suprathermal electrons and the effect of radial ion transport. With this "one-box" model, we are able to reproduce observed water and hydrogen ion densities in Enceladus's orbit, but only when the hot electron density is $\approx 0.5\%$ of the total plasma density. Radial transport is found to be slow, requiring 26 days to remove ions from the orbit of Enceladus.

Moving toward the development of a radial model of ion chemistry, in Chapter 4 we present a model of Saturn's neutral clouds, which are made of material outgassing from Enceladus. The effects of dissociation and charge exchange are considered, where the details of the latter prove to be of great consequence on neutral cloud morphology. The oxygen cloud is found to the most extended, followed by H_2O, and finally OH.

The above efforts are combined in Chapter 5, where a neutral cloud model is used to construct a radial model of ion chemistry. It is shown that neutral H_2O requires more spreading than yet modeled in order to recover observed water and hydrogen ion abundances near Enceladus. The relative abundance of water-group ion species presented will be useful for analyses of CAPS-IMS data, while loss rates derived from the model can be used to improve neutral cloud models. The case is made that ion chemistry models and neutral cloud models must be developed alongside one another in order to improve understanding of these interrelated populations at Saturn.

Chapter 1

Introduction

Like Jupiter, Earth, Uranus, and indeed the Sun itself, the magnetosphere of Saturn defines the volume within which Saturn's own internal magnetic field shields it from the solar wind and its high-energy charged particles. Our own moon orbits in and out of the Earth's magnetosphere once a month, while the magnetospheres of Jupiter and Saturn (and of course the Sun) are large enough that many of their satellites are protected throughout their orbits.

At least two of these moons—Io at Jupiter and Enceladus at Saturn—are volcanically active, which is not commonly observed in its own right, at least not on the timescale of a human lifetime. Io's volcanoes release dust and gas comprised mostly of sulfur dioxide, and Enceladus's plumes release water molecules and frozen water grains.

In the case of Io, ion temperatures and densities are high enough in its immediate surroundings to destroy much of the neutral gas initially released (*Dols et al.*, 2008). At Enceladus, many of the water neutrals escape unharmed, due to (1) the relative sparcity of ions and electrons to collide with, and (2) lower ion and electron temperatures.[a]

Despite potentially harsh local conditions (particularly with Io), a substantial amount of the neutral gas produced by both Io and Enceladus ($\approx 10^3$ and 10^2 kg s^{-1}, respectively) is released from their surfaces and goes on to ultimately supply the plasma disks and the neutral tori, which embed the moons' orbits.

In 1997, the Cassini–Huygens mission was launched to Saturn with several mis-

[a]Ion and electron temperatures are associated with the rotational speed of the magnetospheres at the orbits of the respective moons (Appendix A).

sion objectives, including to study of the dynamics of Saturn's magnetosphere and the geologic history of its moons. After arriving in 2004, Cassini indirectly detected Enceladus's plumes by measuring magnetic field perturbations, which led to the scheduling of later flybys with the purpose of detecting the plumes visually, spectroscopically, and with ion mass spectrometry.

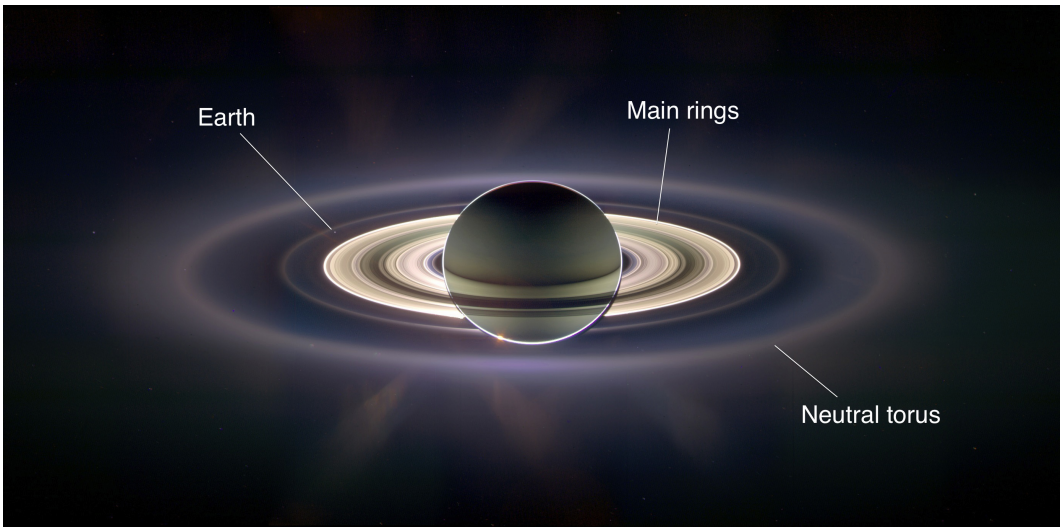


Figure 1.1 Image of Saturn eclipsing the sun, taken from Cassini in 2006 (NASA). In addition to Saturn's main rings, the neutral torus embedding Enceladus's orbit (commonly referred to as the E ring) can also be made out from reflected sunlight. Above the main rings on the left, one can barely make at out the pale blue light reflected from the earth's atmosphere.

Saturn has been in the public eye for nearly a decade now thanks to images taken from Cassini such as the one in Figure 1.1, where Saturn's rings, as well as the neutral torus fed by Enceladus, are impressively on display. This image is poignant and inspiring, as it provides a very distant perspective of the Earth just above the main rings on the left. Equally stunning views of Enceladus itself from early and subsequent flybys have also been imaged. For example, in Figure 1.2, one can make out surface features termed 'tiger stripes,' which have been shown to coincide with the plume lo-

cations themselves, along with relatively warm surface features observed in infrared wavelengths (*Spencer et al.*, 2006; *Porco et al.*, 2006). The large scale structure of Enceladus's plumes can be seen in Figure 1.3 at a distance of 1600 km, while a later flyby from less than 100 km in Figure 1.4 reveals finer structure.

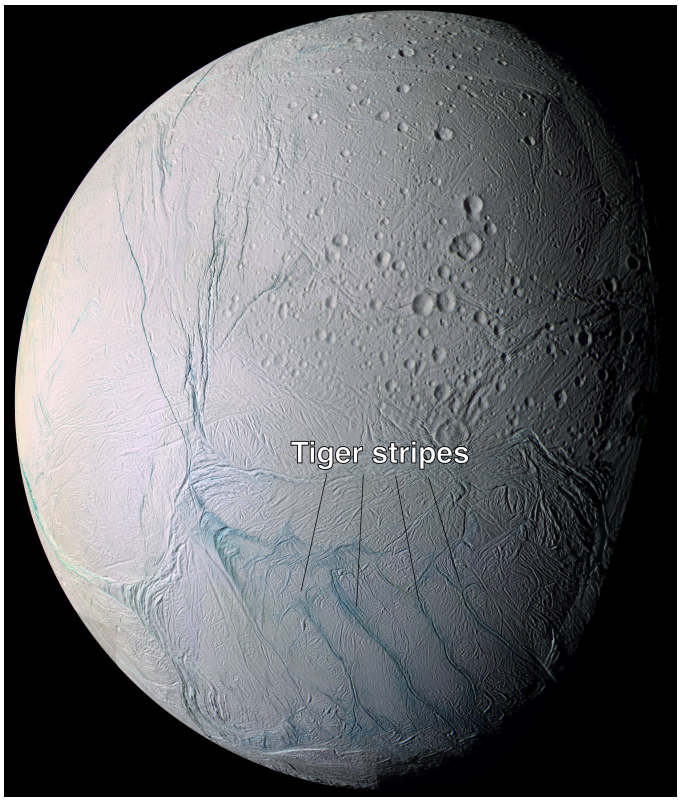


Figure 1.2 Enceladus with its tiger-striped south pole, along which a number of geysers eject water into orbit around Saturn (NASA). At 500 km, the diameter of Enceladus is about the width of the United Kingdom.

The present work is on the evolution of water-group[a] neutrals released by Enceladus. As mentioned, the gas escaping Enceladus has little trouble maintaining neutrality to form the neutral torus. Over time, however, the source of neutrals must be balanced by sinks. One possibility is that the neutrals are heated collisionally until their orbits

[a]The term water group refers to oxygen plus between zero and three hydrogen atoms: O, OH, H_2O, H_3O.

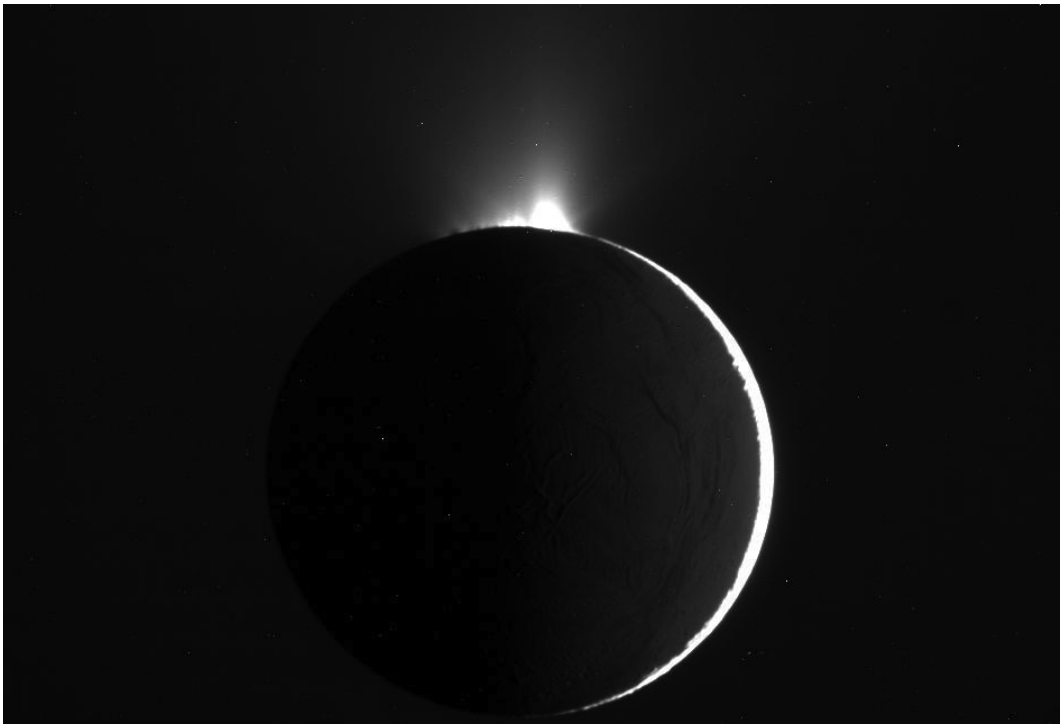


Figure 1.3 Enceladus plumes from an early flyby in 2005 (*Dougherty et al.*, 2006b; *Hansen et al.*, 2006), from which estimates of the mass ejection rates were obtained (NASA). At this distance only the largescale structure can be made out, though the plumes are produced from many active fissures (see Figure 1.4).

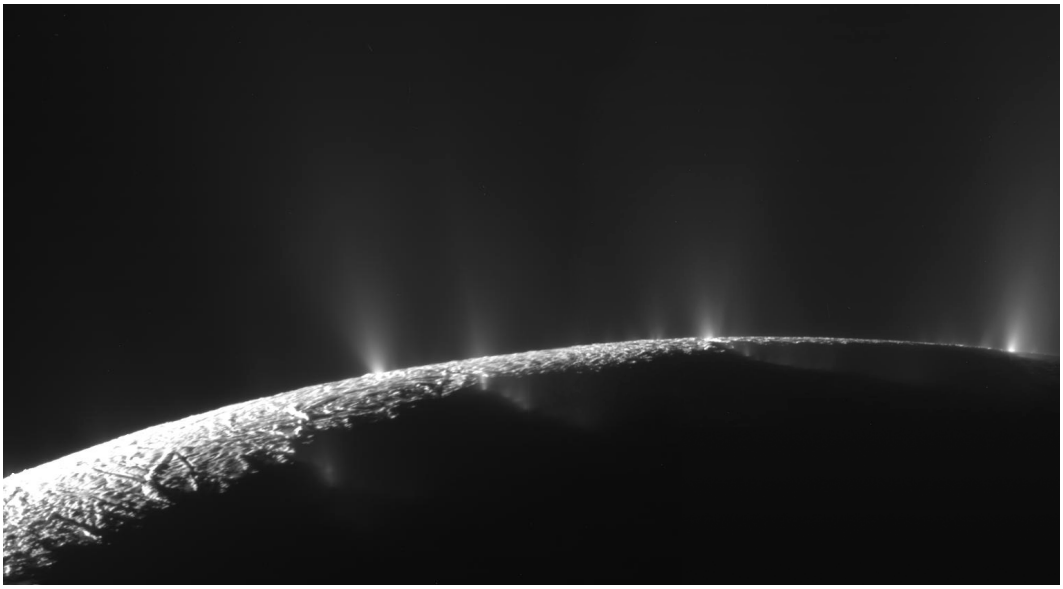


Figure 1.4 A close-up of the Enceladus plumes from a later flyby in 2009. In this case, the individual plumes are resolvable (image courtesy ciclops.org).

extend to 10s of Saturn radii (*Cassidy and Johnson*, 2010). They may also be absorbed onto Saturn's rings or into its upper atmosphere. A third outcome is that neutrals become ionized, either by colliding with hot electons (< 10 eV), or by exchanging an electron with positively-charged ions moving along with Saturn's magnetic field.

Of course, these newly-created ions must also be removed from the system eventually. The important processes are recombination and—once again—charge exchange, whereby the one ion is replaced with another. This may appear to be without consequence at first, but the key is that before the exchange, ions are attached to the magnetic field, and thus have higher velocities than do the neutrals. The end result is that the neutral product is often formed with speeds high enough to escape Saturn's gravity. A third possibility is that the ions are simply transported outward, and are lost down the tail of Saturn's magnetosphere, brought about by the convective process of magnetic flux tube interchange (see Chapter 23 in *Bagenal et al.* (2004)).

In the following sections, a brief discussion is provided on the neutrals and ions produced by Enceladus and how they are affected by hot electrons, charge exchange, and radial transport. It is through these key processes that several features at Saturn can be explained, including neutral cloud structure, relative abundances of ions, and mass/energy throughput in the inner magnetosphere.

1.1 Physical chemistry model (Chapter 2)

When studying the flow of mass and energy within magnetospheres, considerable attention is often paid to magnetohydrodynamics (MHD). Rightfully so, especially at dis-

tances where collisions between neutrals and ions become increasingly unlikely. MHD models can also be improved in principle by iterating with chemistry models to estimate loss rates and mass-loading rates.[a] Mass-loading refers to stresses on the magnetosphere caused by the formation of fresh ions, whether by ionization or electron transfer (charge exchange), where the latter has no effect on plasma density (see Chapter 3).

In order to capture information about more than one ion species and to study composition, however, a physical chemistry model is preferred. The trade-off is that—unlike with MHD—the electric and magnetic fields (as well as their response to mass-loading) and plasma flow speeds must be prescribed.

Mass-loading becomes more of an issue for chemical models in Chapter 3, wherein the focus is on the neutral-dense region near Enceladus. If, however, one is interested in the tenuous plasma–neutral torus encircling Saturn at the orbit of Enceladus, corrections to the field due to mass-loading can be ignored.

A second issue involves radial transport of ions, which occurs because of convective motions associated with magnetic flux tube interchange. A diffusion equation can be used to describe the evolution of mass and energy density as a function of time and distance from Saturn. Because the chemical timescales are long at Saturn compared to diffusion, we deal with diffusion by inserting a parameterized loss term into the chemical rate equations for each ion species.

Besides giving us the ability to accurately estimate ion densities and temperatures, the chemistry model also allows us to study the effects of high energy ($\approx$ 100 eV)

[a]Mass-loading results from the formation of fresh ions, which represent stresses on the magnetosphere, and thus must be accelarated from the slow-moving neutral frame. We study mass-loading from the point of view of chemistry in Chapter 3, but the reader is encouraged to see estimates made with MHD models, such as *Saur et al.* (2008).

electrons, known to exist not only in the Enceladus torus, but also at Jupiter in the Io torus (*Delamere et al.*, 2005). The importance of hot electrons at Enceladus cannot be overstated. Despite providing only a small amount of energy to the system directly, hot electrons provide for the ions initially, which are accelerated by the magnetosphere and heated by field-aligned currents connecting Saturn's ionosphere to the plasma disk. Effectively, warming in the torus is due to energy sourced ultimately from Saturn's rotation.

Hot electrons are also necessary for the ionization of hydrogen to form protons. Without hot electrons, the ratio of heavy (water) ions would outnumber protons by more than 100:1, whereas observations suggest a ratio of 10:1.

In Chapter 2, we study the effects of hot electrons and radial transport on ion conditions at Saturn with a "one-box" physical chemistry model following the methods of *Barbosa et al.* (1983) and *Delamere et al.* (2005). As stated, we ignore any perturbations to the fields and velocity which occur from mass-loading, reserving that discussion for Chapter 3.

1.2 Plume–plasma interaction (Chapter 3)

Enceladus sustains Saturn's neutral clouds and indirectly supplies many of the ions within inner magnetosphere. But how important is the local interaction? By this, we mean to pose the following questions:

1. What percentage of the neutrals produced at Enceladus directly feed the neutral torus as well as the widely-spread neutral clouds?

2. How does charge exchange at Enceladus affect incoming plasma?

3. What is the effect of hot electrons locally in terms of fresh ion pickup (mass-loading)?

The first question will be addressed in Section 1.3; the remaining two are in fact related and will be discussed here. Hot electrons are responsible for the creation of new ions, while charge exchange removes one ion in favor of another, leaving the overall plasma density unchanged. But from the perspective of the magnetic field, the two processes are indistinguishable: both result in fresh ions, and both types of ions must be accelerated up to the speed of the magnetosphere. This is what is meant by the term mass-loading, despite the fact that mass itself may or may not be affected. Estimates of mass-loading derived with MHD models constrained by field perturbations vary somewhat between 0.2 and a few kg s^{-1} near Enceladus, depending on which flyby the measurements were made (*Saur et al.*, 2008).

For charge exchange to occur, however, a population of ions must first exist. For this reason, hot electrons serve to provide many of the ions whose identities are subsequently altered by charge exchange, sometimes resonantly, as in the case of $H_2O + H_2O^+ \rightarrow H_2O^+ + H_2O$, and other times in non-resonant reactions such as $O^+ + H_2O \rightarrow O + H_2O^+$.

With the chemistry model, we can evolve a parcel of plasma along prescribed flow fields to calculate mass-loading, purely from the perspective of chemistry. The strength of the plume can also be varied to test the sensitivity of our results to changes in plume activity between flybys. Our results motivate the need for a source of hot electrons at

Enceladus to match mass-loading estimates derived from MHD models. Such electrons may be related to field-aligned currents connecting Enceladus to Saturn (*Pryor et al.*, 2011).

Additional information obtained from the chemistry model is on the relative ion abundances following passage through the water plumes. Charge exchange occurring in stagnated plasma flows produces a significant amount of H_3O^+ ions, an important conclusion we return to when discussing our 2-D model of Saturn's chemistry in Section 1.4.

1.3 Neutral cloud model (Chapter 4)

The end goal of this work is to provide an estimate of ion temperatures and relative abundances throughout Saturn's inner magnetosphere (4 R_S to 10 R_S), along with an understanding of the system's sensitivity to transport timescales and hot electron density.

When moving from a one-box chemistry model to one with spatial information, it is best to treat the neutrals separately with a neutral cloud model. A neutral cloud model is a Monte Carlo simulation, wherein neutrals are allowed to orbit Saturn and collision probabilites are estimated throughout the system after every timestep. As such, we constructed a model with which to calculate neutral densities associated with the Enceladus torus as well as Saturn's neutral clouds. Along the way, we became side-tracked by the detailed roles of charge exchange and molecular dissociation in the formation of Saturn's neutral cloud.

Previous work on neutral clouds at Saturn includes that of *Johnson et al.* (2006),

who were the first to show that Saturn's neutral OH cloud can be explained as having been formed by fast moving neutrals produced via charge exchange in the Enceladus torus. Soon after, *Farmer* (2009) and *Cassidy and Johnson* (2010) used separate techniques to show the importance of neutral–neutral collisions in spreading the neutral clouds beyond that expected from charge exchange alone. Dissociation has been included in these and other previous studies (i.e., *Jurac and Richardson* (2005)), but only by assigning a single speed for the dissociated OH product.

The model of *Cassidy and Johnson* (2010) is a valuble one in terms of capturing much of the physics necessary to explain neutral cloud morphology at Saturn, and indeed we employ their results when developing our radial model in Chapter 5. As with *Jurac and Richardson* (2005), one deficiency of that model, however, is that charge exchange is treated with a single cross section, and dissociation is prescribed with a single speed. A second limitation is that only resonant charge exchange is considered, so that charge exchange does not alter relative ion abundances in those models.

In Chapter 4, we take a second look at charge exchange with respect to Saturn's neutral cloud, not only by employing energy-dependent cross sections unique to individual reactions, but also by allowing non-resonant charge exchange, which affects ion relative abundances. We also explore the effects of dissociation, where the products are formed with a range of velocities. Our findings are currently being used to improve the neutral cloud model of *Cassidy and Johnson* (2010).

1.4 Radial ion chemistry model (Chapter 5)

In Chapter 5, we use the latest neutral densities from *Cassidy and Johnson* (2010) to model radial ion abundances and temperatures. In our case, we seek the response of Saturn's ion chemistry to radial transport and hot electron density. In Chapter 2, we performed a similar study, but with a one-box model, with no spatial information. In Chapter 5, we extend that model to study radial variations with a 1-D model; we also present a 2-D model, where low-latitude ($\leq 30°$) dependence is also considered.

As with the one-box model, we once again prescribe a transport timescale in each radial bin, leaving the robust application of the diffusion equation for a future study. We also impose the density of hot electrons in every bin, the value we find agreeing well with the one-box model in Chapter 2.

The obvious complication in going from the one-box model to the radial one is radial transport, through which one radial bin communicates with the next. The timescale for transporting energy and mass from one radial bin to the next is prescribed, but care is required in associating both density and temperature betweens cells with variable volume. In particular, if the transport process is adiabatic, temperature must decrease as ions diffuse outward into larger volumes. With the 2-D model, a second issue arises in that the various ion species uniquely align themselves along the magnetic field, so that the chemistry must be updated in each latitudinal bin. The ions must then be redistributed in latitude to maintain charge neutrality everywhere. While increasing computational workload, these issues present no difficulty in principle.

With both models we study the effects of ion radial transport and hot electron

density on ion temperature and composition. By calculating the total mass of each ion per unit distance, a window is also opened into which regions of the magnetosphere serve as the origin for each ion species.

One can also derive the rate at which mass exits the system at any distance, $\dot{M}(r)$. Beyond 10 R_S, chemistry becomes unimportant because (1) the densities of all species decrease away from the orbit of Enceladus, making reactions increasingly unlikely for a given time period, and (2) the system becomes centrifugally unstable, and transport becomes more rapid with distance, ensuring that ions leave the system before having the opportunity to say, recombine. In other words, sources and sinks become unimportant beyond 10 R_S, so that the mass source rate at 10 R_S found with the model is a good estimate for $\dot{M}$ down the magnetotail, and can be compared directly with the momentum lost by the solar wind to Saturn's magnetosphere, effectively bridging chemical and magnetospheric models from a global point of view. Our early estimates agree well with *Delamere and Bagenal* (2012).

Note to reader: Chapters 2–4 of this dissertation are drawn heavily from the following peer-reviewed articles, and serve as the foundation for Chapter 5:[a]

- Chapter 2: Fleshman, B. L., P. A. Delamere, and F. Bagenal (2010), *A sensitivity study of the Enceladus torus*, Journal of Geophysical Research (Planets) (*Fleshman et al.*, 2010b)

- Chapter 3: Fleshman, B. L., P. A. Delamere, and F. Bagenal (2010), *Modeling the Enceladus plume–plasma interaction*, Geophysical Research Letters (*Fleshman*

[a]Not yet submitted for publication at the time of this dissertation.

et al., 2010a)

- Chapter 4: Fleshman, B. L., P. A. Delamere, F. Bagenal, and T. Cassidy (2012), *The roles of charge exchange and dissociation in spreading Saturn's neutral clouds*, Journal of Geophysical Research (Planets) (*Fleshman et al.*, 2012)

Chapter 2

One-box chemistry model

Abstract

We have developed a homogeneous model of physical chemistry to investigate the neutral-dominated, water-based Enceladus torus. Electrons are treated as the summation of two isotropic Maxwellian distributions—a thermal component and a hot component. The effects of electron impact, electron recombination, charge exchange, and photo-chemistry are included. The mass source is neutral H_2O, and a rigidly-corotating magnetosphere introduces energy via pickup of freshly-ionized neutrals. A small fraction of energy is also input by Coulomb collisions with a small population ($< 1\%$) of suprathermal electrons. Mass and energy are lost to ion radial transport, escaping fast neutrals produced by charge exchange and recombination, and a small amount of radiative cooling. We explore a constrained parameter space spanned by water source rate, radial transport, hot electron temperature, and hot electron density. The key findings are: (1) radial transport must take longer than 12 days; (2) water is input at a rate of 100–180 kg s^{-1}; (3) hot electrons have energies between 100 and 250 eV; (4) neutrals dominate ions by a ratio of 40:1 and continue to dominate even when thermal electrons have temperatures as high as ≈ 5 eV; (5) hot electrons do not exceed 1% of the total electron population within the torus; (6) if hot electrons alone drive the observed longitudinal variation in thermal electron density, then they also drive a significant variation in ion composition.

2.1 Introduction

Absorption of UV starlight during occultation of Saturn's moon Enceladus showed that it continuously ejects neutral H_2O at a rate of ≈ 150–$300\,\mathrm{kg\,s^{-1}}$ from water-ice geysers located at its southern pole (*Hansen et al.*, 2006). Models suggest that the water and its chemical by-products form an extended neutral-dominated torus centered on the orbit of Enceladus (*Jurac and Richardson*, 2005). Similarly, Jupiter's volcanic moon Io emits a mixture of SO_2 and S_2 at a rate of $\approx 1\,\mathrm{ton\,s^{-1}}$, and chemical by-products produce a plasma torus centered on the orbit of Io (see review by *Thomas et al.* (2004)). The Hubble Space Telescope (HST) observations by *Shemansky et al.* (1993b) revealed that the neutral-to-ion ratio in the Enceladus torus (≈ 10) is three orders of magnitude greater than in the Io torus ($\approx 10^{-2}$). Compositional differences and the degree of ionization within these two systems can be attributed to their chemistry (Io's based on sulfur dioxide and Enceladus's based on water) as well as the fact that fresh ions are picked with five times more energy in the Io torus than in the Enceladus torus (*Delamere et al.*, 2007).

An important lesson learned from studying the physical chemistry of the Io torus is that a small fraction of hot electrons ($< 1\%$) play a critical role in determining composition. To model the Cassini UltraViolet Imaging Spectrograph (UVIS) data obtained during Cassini's E2 flyby of Jupiter (October 2000 to March 2001), *Steffl et al.* (2004a,b, 2006, 2008) adapted the *Delamere and Bagenal* (2003) Io torus model. *Steffl et al.* used their models to study radial, temporal, and azimuthal variation in mixing ratios (ion-to-electron density ratios), thermal electron density, and thermal

electron temperature. *Steffl et al.* (2008) concluded that hot electrons are necessary for the Io torus energy budget and that two modulations of the hot electron population are required to reproduce both the temporal and spatial variations in composition observed in the data, one modulating in Jupiter's System III longitude, the other in System IV. We anticipate that hot electrons are similarly important in Saturn's Enceladus torus.

Delamere et al. (2007) developed a simplified oxygen-based model to compare the Enceladus and Io tori. They found that collisional heating by a population of hot electrons is much less important at Enceladus, contributing only 0.5% of the energy to the torus, compared to 60% at Io. They also cited two major reasons for the discrepancy in the neutral-to-ion ratio between the two systems. First, newly created ions are picked up in the Io torus by Jupiter's magnetosphere at roughly five times the energies as are those in the Enceladus torus by Saturn's magnetosphere. The higher-energy pickup ions in the Io torus warm the thermal electrons, which then reduces the neutral-to-ion ratio via impact ionization. Second, because of the high abundance of molecular ions compared with atomic oxygen ions in the Enceladus torus (e.g., *Sittler et al.* (2005)), *Delamere et al.* (2007) expected that molecular dissociative recombination (not included in their model) will therefore drive the ratio even higher in the Enceladus torus. From the conclusion of *Delamere et al.* (2007): "The addition of the full water-group molecular chemistry will introduce an additional plasma sink through dissociative recombination of the molecular ions. Therefore, our simplified O-based chemistry likely represents a lower limit for the neutral/ion ratio." To investigate the consequences of a water-based Enceladus torus dominated by molecular chemistry, we have improved on the Delamere model by including a comprehensive set of water-

based reactions and species to more accurately estimate steady-state densities and temperatures of ions and electrons. We have also added neutral and ionized molecules. Molecules are more abundant in the Enceladus torus where low plasma density allows H_2O to escape from Enceladus largely intact, whereas the more energetic local plasma interaction at Io results in dissociation of SO_2 (*Dols et al.*, 2008). Moreover, thermal electrons ($\approx 2\,\mathrm{eV}$) throughout the Enceladus torus dissociate H_2O approximately ten times less easily than thermal electrons ($\approx 5\,\mathrm{eV}$) in the Io torus dissociate SO_2 (*V. Dols, personal comm.*).

Previous models of molecular chemistry in Saturn's magnetosphere were driven by Pioneer 11 and Voyager 1 and 2 observations (*Frank et al.*, 1980; *Trainor et al.*, 1980; *Wolfe et al.*, 1980; *Bridge et al.*, 1981, 1982; *Sittler et al.*, 1983). *Richardson et al.* (1986) showed the importance of recombination under conditions of slow radial transport. Using essentially the same chemical reactions as *Richardson et al.* (1986), *Richardson et al.* (1998) determined ion and neutral lifetimes within Saturn's inner magnetosphere ($\lesssim 12 R_S$; $R_S \equiv$ Saturn radius $= 6.0 \times 10^9\,\mathrm{cm}$), constrained by HST observations of the extended OH cloud (see their Figure 2, and references therein). They solved the rate equations for number densities while also solving the radial diffusion equation, but energy conservation was not considered. *Jurac et al.* (2002) and *Jurac and Richardson* (2005) further improved on these models by considering neutral cloud expansion, and solved for plasma and neutral distributions self-consistently in order to study the source of water within Saturn's inner magnetosphere.

Our model is focused on the molecular chemistry. We start with a uniform box and characterize transport by just a timescale. However, we do consider energy balance.

More importantly, unlike the above models, we retain H_3O^+ in our model, which proves to be a significant component.

The purpose of this paper is to summarize the sensitivity of the chemistry of Enceladus's torus to several parameters. The parameters we investigated are hot electron temperature, hot electron density, H_2O source rate, and the rate of ion transport. A fifth parameter relates to proton densities. Being lighter, protons are less bound to the equator (*Bagenal et al.*, 1980; *Sittler et al.*, 2008; *Persoon et al.*, 2009). This means protons spend only a fraction of the time interacting with the heavy ions and molecules. This effect is simulated with a 'proton dilution' factor (Section 2.3). We search for values of these parameters leading to thermal electron temperature, thermal electron density, and water-group ($W^+ \equiv O^+ + OH^+ + H_2O^+ + H_3O^+$) ion-to-proton ratio consistent with available Cassini data (Section 2.2.2).

The observations used to constrain our model and to define the parameter space are given in Section 2.2. The model is described in Section 2.3. The best fit (baseline solution) and the procedure used to find it are discussed in Section 2.4. Model sensitivity to each of the parameters is discussed in Section 2.5. Finally, the importance of hot electrons with regard to water-group ion composition is demonstrated in Section 2.6.

2.2 Observations

2.2.1 Parameters

Here we present the observations used to bound the parameter search (Section 2.3). The baseline parameter values (listed in Table 2.1) are mentioned throughout this section and are discussed at length in Section 2.4.

Data (Constraints)		Baseline Fit	
n_e/cm^{-3}	: 60	T_{eh}/eV	: 160
T_e/eV	: 2.0	f_{eh}	: 0.46 %
W^+/H^+	: 12	f_{H^+}	: 1.0
		$\tau_{trans}/days$	: 26
		$N_{src}/cm^{-3}\,s^{-1}$	: 2.0E-4
Neutral Densities (cm^{-3})		Mixing Ratios	
n_H	: 720	O^+/W^+	: 0.15
n_{H_2}	: $\ll 1$	OH^+/W^+	: 0.30
n_O	: 700	H_2O^+/W^+	: 0.37
n_{OH}	: 770	H_3O^+/W^+	: 0.18
n_{H_2O}	: 190	O^+/H^+	: 1.8
n_{H_3O}	: −	$\mathbf{W^+/H^+}$	: **12**
Ion/Electron Densities (cm^{-3})		Ion/Electron Temperatures (eV)	
$\mathbf{n_e}$	: **60**	$\mathbf{T_e}$	: **2.0**
n_{eh}	: 0.28	T_{eh}	: 160
n_{H^+}	: 4.6	T_{H^+}	: 4.0
$n_{H_2^+}$	: $\ll 1$	$T_{H_2^+}$	: 6.5
n_{O^+}	: 8.4	T_{O^+}	: 38
$n_{O^{++}}$	: 0.078	$T_{O^{++}}$	: 35
n_{OH^+}	: 17	T_{OH^+}	: 39
$n_{H_2O^+}$	: 20	$T_{H_2O^+}$	: 42
$n_{H_3O^+}$	: 9.8	$T_{H_3O^+}$	: 42

Table 2.1 Model constraints (see Section 2.2.2 for references) and output for the best fit baseline solution. The fit is defined as the combination of parameters T_{eh}, f_{eh}, f_{H^+}, τ_{trans}, and N_{src} that gives the smallest total fractional difference between the data and the model output. Notice that the model output for the constraints (in bold) agrees with the data to at least two significant figures. No reaction leads to H_3O in our set of reactions (Appendix A).

Neutral source ($N_{\rm src}$) The baseline water source rate from the model is $N_{\rm scr} = 2.0 \times 10^{-4}$ molecules cm^{-3} s^{-1}. A torus centered on Enceladus with cross section $(2R_{\rm S})^2$ has a volume of $\approx 2\pi(4R_{\rm S})(2R_{\rm S})^2 = 2.2 \times 10^{31}$ cm^3, giving a volumetric source rate of 4.4×10^{27} H_2O molecules s^{-1}, or 130 kg s^{-1}. If one chooses a smaller or larger torus volume, the net neutral source rate is adjusted accordingly. The best estimates of the Enceladus source come from Cassini observations. *Hansen et al.* (2006) estimated $150 \lesssim N_{\rm src}/({\rm kg\ s^{-1}}) \lesssim 350$ from two stellar occultation observations of the Enceladus plume with Cassini UVIS. *Tokar et al.* (2006) inferred a source rate of 100 kg s^{-1} from the CAssini Plasma Spectrometer (CAPS) data acquired during the E2 Cassini flyby of Enceladus on 14 July 2005.

Earlier source estimates come from models of the neutral clouds. *Jurac et al.* (2002) included the effects of collisional heating and developed a model to simulate the morphology of the extended OH cloud. They used neutral lifetimes derived from a two-dimensional model by *Richardson et al.* (1998) to determine the neutral H_2O source responsible for the OH radial profile constrained by 1996 HST faint-object spectrograph observations. They found a total water source required to maintain the OH cloud of $N_{\rm src} = 112$ kg s^{-1}, 93 kg s^{-1} coming from the orbit of Enceladus.

In a later paper, *Jurac and Richardson* (2005) improved their model, treating plasma and neutrals self-consistently by tracking neutrals with a Monte Carlo algorithm and transporting plasma with a diffusion equation. They found a total water source rate of ≈ 300 kg s^{-1}. A similar result was found by *Burger et al.* (2007) with a three-dimensional Monte Carlo simulation of neutrals constructed to simultaneously model the Ion and Neutral Mass Spectrometer (INMS) and UVIS observations made

during the E2 Cassini flyby of Enceladus.

Radial transport timescale ($\tau_{\rm trans}$) The baseline radial transport timescale from the model is $\tau_{\rm trans}^{\rm baseline} = 26$ days. *Richardson et al.* (1998) estimated $\tau_{\rm trans} \approx 23$ days from Voyager-era data and HST OH observations. Using the radial velocities of *Sittler et al.* (2006) (their Figure 9), one finds a transport timescale at Enceladus of $\approx 2R_{\rm S}/v_{\rm R}(r = 4R_{\rm S}) \approx 12$ days. This more rapid transport might suggest that the magnetosphere was compressed on Saturn Orbital Insertion (SOI), which would increase the angular speed to beyond corotation as momentum is conserved, ultimately resulting in enhanced radial outflow velocities (reduced transport times). Thus, the *Sittler et al.* (2006) radial velocities based on SOI data may not represent the entire magnetosphere, and not for all epochs. Radial convection may also be superimposed on the diffusive motions throughout Saturn's inner magnetosphere due to flux tube interchange instabilities (*Rymer et al.*, 2008). A major goal of this study is to explore the consequences of such a wide range of timescales for radial transport.

Hot electron temperature and fraction ($T_{\rm eh}$, $f_{\rm eh}$) Our model gives a baseline hot electron temperature of $T_{\rm eh}^{\rm baseline} = 160$ eV. The Cassini Radio and Plasma Wave Science (RPWS) measurements by *Moncuquet et al.* (2005) indicated a hot electron component within 3–5$R_{\rm S}$ with $40 \lesssim T_{\rm eh}/({\rm eV}) \lesssim 90$. From Cassini CAPS ELectron Spectrometer (ELS) observations acquired during the SOI period, *Young et al.* (2005) found that $T_{\rm eh}$ ranged from $\approx$ 500–1000 eV inbound and $\approx$ 800–3000 eV outbound (SOI), indicating a strong longitudinal and/or temporal dependence. *Lewis et al.* (2008) performed moment calculations on CAPS–ELS data with two different methods and

found $300 \lesssim T_{\rm eh}/({\rm eV}) \lesssim 2000$ eV and $1500 \lesssim T_{\rm eh}/({\rm eV}) \lesssim 4000$. *Schippers et al.* (2008) combined CAPS–ELS and Cassini Magnetospheric IMaging Instruement (MIMI) data and found significant scatter in $T_{\rm eh}$ and calculated $200 \lesssim T_{\rm eh}/({\rm eV}) \lesssim 2000$ at the closest approach of $5.4 R_{\rm S}$.

Our baseline value for the fraction of the electron density in the hot component is found to be $f_{\rm eh}^{\rm baseline} = 0.46\%$. *Young et al.* (2005) found that $f_{\rm eh}$ ranged between 0.01% and 5% within 3–$5 R_{\rm S}$. As with $T_{\rm eh}$, $f_{\rm eh}$ varied significantly between the inbound and the outbound data. *Lewis et al.* (2008) found $f_{\rm eh}$ from their 3-D moment calculation to be $\lesssim 1\%$. *Schippers et al.* (2008) calculated $f_{\rm eh}$ as low as 0.1% (inbound) and as high as 0.3% (outbound).

At the time of *Sittler et al.* (2008), the authors felt that hot electron parameters measured by CAPS ELS were highly uncertain in the vicinity of Enceladus, due to penetrating radiation. Instead, they used the *Moncuquet et al.* (2005) RPWS observations, which found that $T_{\rm eh} \approx 50$ eV. For the hot electron density, they used $n_{\rm eh} \approx 0.1$ cm^{-3} from the *Sittler et al.* (1983) Voyager observations (which are not affected by penetrating radiation). *Sittler et al.* (2008) combined the *Moncuquet et al.* (2005) Cassini RPWS data for $T_{\rm eh}$ and the Voyager data for $n_{\rm eh}$ to compute the total (effective) electron temperatures $T_{\rm e}$. Since Voyager and Cassini SOI were so different in time, they used only the total electron temperatures for their reaction rates.

Proton dilution ($f_{\rm H^+}$) Previous work by *Sittler et al.* (2008) (their Figure 4) showed that $\approx 2/3$ of the proton population are distributed within a distance of $\approx 1 R_{\rm S}$ from the centrifugal equator at the orbit of Enceladus. Protons are pulled above the equator

by the ambipolar electric field and do not couple efficiently to the heavy water-group ions.

In Section 2.5.1, we show that the proton abundance is strongly coupled to the hot electron population via impact ionization. Our model is consistent with any value of the proton dilution parameter f_{H^+} between 0.7 and 1.0. Values of $f_{H^+} = 1$ or 0 represents the cases where no or all newly created protons are excluded from the model. Thus, to simplify the present analysis, $f_{H^+}^{\text{baseline}}$ has been set to unity.

2.2.2 Constraints (n_e, T_e, W^+/H^+)

Parameter combinations are evaluated by comparing the corresponding model output to the following observations. We have chosen $n_e = 60\,\text{cm}^{-3}$, $T_e = 2\,\text{eV}$, and $W^+/H^+ = 12$ as the initial model constraints (Section 2.4).

Total electron density (n_e) *Gurnett et al.* (2005) reported $20 \lesssim n_e/(\text{cm}^{-3}) \lesssim 100$ within 3–5R_S during the approach and first orbit around Saturn (SOI) from the Upper Hybrid resonance Frequency (UHF), acquired by the RPWS instrument. *Moncuquet et al.* (2005) considered RPWS Quasi-Thermal Noise (QTN) on SOI and found $40 \lesssim n_e/(\text{cm}^{-3}) \lesssim 70$ within 3–5R_S. *Persoon et al.* (2005) used the RPWS UHF to determine n_e from five later orbits. They discovered variability inside $\approx 5R_S$, with n_e ranging from 35–105 cm^{-3}. In a later paper, *Persoon et al.* (2009) developed a diffusive equilibrium model from RPWS and CAPS data acquired on 50 passes through Saturn's inner magnetosphere from 30 June 2004 to 30 September 2007, and calculated an electron density of over $50\,\text{cm}^{-3}$ near the orbit of Enceladus.

Lewis et al. (2008) derived $6 \lesssim n_e/(\mathrm{cm}^{-3}) \lesssim 20$ within 3–5R_S from the moment calculations with CAPS–ELS electron distribution data. Their analysis was based on SOI data when CAPS was not fully actuating (*Sittler et al.*, 2006, 2007). Also, Cassini is a three-axis stabilized spacecraft with a fixed field of view. Hence, sampling is limited, and moment calculations are not as straight forward as they are for spinning spacecraft, as discussed by *Lewis et al.* (2008). Additionally, Cassini was likely negatively charged on SOI (*Young et al.*, 2005), resulting in a lower-than-expected n_e from the moment calculations.

Schippers et al. (2008) performed a multi-instrument analysis of the electron populations for several orbits and found $n_e \approx 10$ cm^{-3} from their own CAPS–ELS analysis, but admitted that a negative spacecraft potential inside $9R_S$ likely resulted in an underestimate of the thermal electron density. Instead they used the RPWS UHF analysis by *Gurnett et al.* (2004) in this region, where $n_e \approx 50$ cm^{-3} near the orbit of Enceladus.

From consideration of the observations cited above, we take a value of $n_e = 60\,\mathrm{cm}^{-3}$ for the total electron density in our model.

Thermal electron temperature (T_e) *Moncuquet et al.* (2005) derived $1 \lesssim T_e/(\mathrm{eV}) \lesssim 4$ within 3–5R_S from RPWS data. The SOI CAPS analysis by *Young et al.* (2005) found that $2 \lesssim T_e/(\mathrm{eV}) \lesssim 20$. By comparison, the CAPS analysis by *Lewis et al.* (2008) found that T_e ranged from roughly 2 to 4 eV within 3–5R_S using one method, and between 1 and 4 eV using another. *Sittler et al.* (2006, 2007) found $T_e \approx 1.5$ eV between 3.5 and 4.5 R_S. *Schippers et al.* (2008) calculated $T_e \approx 2$ eV at closest approach (5.4R_S) from a multi-instrument analysis. This value of $T_e = 2$ eV is the one we use for the thermal

electron temperature in our model.

Ion composition (W^+/H^+) *Sittler et al.* (2008) calculated H^+ and W^+ densities from the CAPS SOI results of *Sittler et al.* (2006, 2007). Their Figures 5 and 6 show that W^+/H^+ ranged from $\approx$ 3–15 over the torus (3–5R_S). The CAPS SOI analysis of *Young et al.* (2005) found $6 \lesssim W^+/H^+ \lesssim 35$ within 3–5R_S. The *Young et al.* (2005) analysis was based on non-coincident CAPS IMS singles data, whereas the *Sittler et al.* (2008) results were based on coincident time-of-flight data. It is challenging to distinguish protons from water-group ions in the singles data, while protons are well-separated from the water-group ions in their respective time-of-flight channels. Observations based on IMS singles data are thus likely to overestimate the W^+/H^+ ratio.

Wilson et al. (2008) applied a forward modeling technique to CAPS data for dayside equatorial orbits between 5.5 and 11R_S to calculate ion densities and temperatures. Extrapolating their results down to 5R_S gives $W^+/H^+ \approx 15$. *Persoon et al.* (2009) used anisotropy measurements from CAPS and temperature measurements from RPWS and CAPS to estimate equilibrium distributions within Saturn's inner magnetosphere. Near the Enceladus torus, they found $W^+/H^+ \approx 10$. We choose a value of $W^+/H^+ = 12$ for the water-group to proton density ratio in our model.

2.3 Model

Here we present a model based on the Neutral Cloud Theory (NCT) model described in *Delamere and Bagenal* (2003), which was developed to address the variability of plasma conditions in the Io torus. The Delamere model was based on the earlier NCT models

of *Shemansky* (1988), *Barbosa* (1994), *Schreier et al.* (1998), and *Lichtenberg et al.* (2001). The tools developed by *Delamere and Bagenal* (2003) to study sensitivity of the plasma-dominated environment at Io are utilized here to study the neutral-dominated water-based Enceladus torus.

The model is 0-dimensional and homogeneous. In this paper, we calculate steady-state densities and temperatures of ions and neutrals originating from a pure H_2O source. When volumetric quantities are reported, we have adopted the volume used by *Delamere et al.* (2007) [$2\pi(4R_S)(2R_S)^2 \approx 2 \times 10^{31}\,\mathrm{cm}^3$], which roughly corresponds to a torus of minor radius $1R_S$ centered on Enceladus's orbit at $4R_S$. Because pickup temperatures vary with radial distance along Saturn's equatorial plane (Appendix A, Equation A.6 and Equation A.7), the scaling is only approximately valid for the span considered here of 3–5R_S.

The basic equations (*Barbosa et al.*, 1983) for number density and energy density for species α are

$$\frac{\partial n_\alpha}{\partial t} = \mathcal{S}_{\mathrm{m},\alpha} - \mathcal{L}_{\mathrm{m},\alpha} \tag{2.1}$$

and

$$\frac{\partial(\frac{3}{2} n_\alpha T_\alpha)}{\partial t} = \mathcal{S}_{\mathrm{E},\alpha} - \mathcal{L}_{\mathrm{E},\alpha.} \tag{2.2}$$

The $\mathcal{S}_\alpha$'s and $\mathcal{L}_\alpha$'s represent source rates and loss rates, respectively, for species α. Following the convention of *Delamere and Bagenal* (2003), the factor of 3/2 in Equation 2.2 will be dropped henceforth, so that we are actually solving for an 'effective' temperature rather than energy. The temperature is described as effective because for pickup ions, the temperatures perpendicular to the magnetic field are expected to be greater

than the parallel temperature (for observations and further discussion see *Richardson and Sittler* (1990); *Moncuquet et al.* (2005); *Sittler et al.* (2006, 2007); *Tokar et al.* (2008); *Persoon et al.* (2009)). A complete discussion of Equation 2.1 and Equation 2.2 for ions, electrons, and neutrals can be found in Appendix A.

The rate at which the H_2O particles are introduced into the model ($N_{\rm src}$) is a free parameter. Chemical pathways encompass a set of reactions involving H, H^+, H_2, H_2^+, O, O^+, O^{++}, OH, OH^+, H_2O, H_2O^+, and H_3O^+ (see Appendix A for a complete list of reactions). Consistent with *Richardson et al.* (1998), we assume that 50% of the hydrogen produced from impact dissociation of H_2O and OH has enough energy to escape the model. Neutrals are assumed to be cold, having only bulk motion. They are not collisionally-heated in the model, and here we assume that neutrals created from ion charge exchange have velocities greater than the escape speed from Saturn and are ejected from the model. Steady-state number and energy densities are found for each species by solving Equation 2.1 and Equation 2.2 iteratively using a modified Euler method with second-order accuracy.

At the heart of this work is a sensitivity investigation of model output within the parameter space spanned by:

- Neutral source rate ($N_{\rm src}/10^{-4}\,{\rm cm^{-3}\,s^{-1}}$): 0.2 $\rightarrow$ 3.0
- Hot electron temperature ($T_{\rm eh}$/eV): 20 $\rightarrow$ 400
- Hot electron fraction ($f_{\rm eh} \equiv n_{\rm eh}/n_{\rm e}$): 0.05 $\rightarrow$ 1.0%
- Radial transport timescale ($\tau_{\rm trans}$/days): 2 $\rightarrow$ 60
- Proton dilution factor ($f_{\rm H^+}$): 0.7 $\rightarrow$ 1.0.

These ranges reflect the broad set of observations given in Section 2.2.1. The proton dilution factor, f_{H^+}, removes protons from the model, and has been implemented by modifying the source term in Equation 2.1 for protons:

$$\frac{\partial n_{H^+}}{\partial t} = f_{H^+}\mathcal{S}_{m,H^+} - \mathcal{L}_{m,H^+}. \tag{2.3}$$

In reality, the heavy ion abundance peaks near the centrifugal equator, while the proton abundance peaks well away from the equator and out of our model domain (*Persoon et al.*, 2009). We apply the above equation to crudely address and investigate this phenomenon.

2.4 Baseline solution

2.4.1 Procedure

Initially we set $f_{H^+} = 1$ (see further discussion in Section 2.5.1) and explore the space spanned only by f_{eh}, T_{eh}, τ_{trans}, and N_{src}. The model was run with a random-walk Monte Carlo algorithm to find the combination of the above yielding the best agreement between model output and the constraints. The following have been chosen as the constraints on the model (Section 2.2.2): $n_e = 60\,cm^{-3}$, $T_e = 2\,eV$, $W^+/H^+ = 12$. In Section 2.5.1 we accommodate a wider range of observations and investigate how composition is affected by these choices of n_e, T_e, W^+/H^+.

We define best agreement as the smallest total fractional difference between the

model output and the constraints:

$$f_{\rm diff} = \sum_i \left| 1 - \frac{\rm Model_i}{\rm Constraint_i} \right|, \tag{2.4}$$

where $i = n_{\rm e}$, $T_{\rm e}$, W^+/H^+ in the present case. The baseline solution (parameter combination with the smallest $f_{\rm diff}$) was found by starting the random-walk algorithm from a point in parameter space near the global minimum in $f_{\rm diff}$. The procedure used to find the global minimum is discussed in Section 2.5. Model output was evaluated and a step was randomly taken in the direction of one of the four parameters. The step sizes were also random in length and constraint-dependent. For example, the step size for the hot electron fraction ranged from 0–0.001, while the step size for the transport time ranged from 0–86,400 seconds (1 day). Every value throughout the step intervals had equal weight. The model output was then evaluated ($f_{\rm diff}$ calculated), and the procedure was repeated until a minimum in $f_{\rm diff}$ was found. The random walk led to the baseline parameter combination, where $f_{\rm diff}^{\rm baseline} \approx 0$.

The solution and corresponding model output are given in Table 2.1. Lists of the values of lifetimes of each species controlled by the primary source/losses mechanisms are presented in Table 2.2, and lifetimes listed by each separate reaction can be found in Appendix A.

2.4.2 Results

Table 2.1 presents the model output for the densities and temperatures of all species. We find a torus composition that is dominated by neutral species with roughly equal

	Mechanism	Rate (s^{-1})	τ (days)		Mechanism	Rate (s^{-1})	τ (days)
H	Charge Exchange	7.3×10^{-8}	1.6×10^{2}	H^+	Charge Exchange	6.1×10^{-6}	1.9×10^{0}
	Impact Ionization	9.6×10^{-9}	1.2×10^{3}		Radial Transport	4.4×10^{-7}	2.6×10^{1}
	Photoionization	8.0×10^{-10}	1.5×10^{4}		Recombination	5.1×10^{-9}	2.3×10^{3}
H_2	Impact Dissociaton	7.6×10^{-7}	1.5×10^{1}	H_2^+	Charge Exchange	2.6×10^{-6}	4.4×10^{0}
	Charge Exchange	5.2×10^{-8}	2.2×10^{2}		Dissociative Recomb.	1.2×10^{-6}	9.6×10^{0}
	Photoionization	6.9×10^{-10}	1.7×10^{4}		Radial Transport	4.4×10^{-7}	2.6×10^{1}
	Photodissociation	4.9×10^{-10}	2.4×10^{4}				
O	Charge Exchange	6.6×10^{-8}	1.7×10^{2}	O^+	Charge Exchange	3.1×10^{-6}	3.7×10^{0}
	Impact Ionization	2.6×10^{-8}	4.5×10^{2}		Radial Transport	4.4×10^{-7}	2.6×10^{1}
	Photoionization	2.3×10^{-9}	5.0×10^{3}		Impact Ionization	7.5×10^{-9}	1.5×10^{3}
					Recombination	1.9×10^{-11}	6.1×10^{5}
				O^{++}	Radial Transport	4.4×10^{-7}	2.6×10^{1}
					Charge Exchange	3.7×10^{-7}	3.2×10^{1}
					Recombination	1.1×10^{-10}	1.0×10^{5}
OH	Photodissociation	5.5×10^{-8}	2.1×10^{2}	OH^+	Charge Exchange	1.1×10^{-6}	1.1×10^{1}
	Impact Ionization	3.5×10^{-8}	3.3×10^{2}		Dissociative Recomb.	5.8×10^{-7}	2.0×10^{1}
	Impact Dissociation	2.7×10^{-8}	4.3×10^{2}		Radial Transport	4.4×10^{-7}	2.6×10^{1}
	Charge Exchange	1.6×10^{-8}	7.4×10^{2}				
	Photoionization	3.7×10^{-9}	3.1×10^{3}				
H_2O	Impact Dissociation	4.9×10^{-7}	2.4×10^{1}	H_2O^+	Dissociative Recomb.	1.2×10^{-6}	9.9×10^{0}
	Charge Exchange	3.6×10^{-7}	3.2×10^{1}		Radial Transport	4.4×10^{-7}	2.6×10^{1}
	Photodissociation	1.3×10^{-7}	9.3×10^{1}		Charge Exchange	4.0×10^{-7}	2.9×10^{1}
	Impact Ionization	5.2×10^{-8}	2.2×10^{2}				
	Photoionization	4.5×10^{-9}	2.6×10^{3}				
				H_3O^+	Dissociative Recomb.	8.1×10^{-7}	1.4×10^{1}
					Radial Transport	4.4×10^{-7}	2.6×10^{1}

Table 2.2 Baseline lifetimes for each species by mechanism in descending order of frequency (Rate $= 1/\tau$). Electron-impact ionization and photoionization include processes that are both ionizing and dissociative. A listing of lifetimes by reaction can be found in Appendix A.

amounts of H, O and OH ($\approx$700 cm^{-3} each) with a lesser amount of water molecules (190 cm^{-3}) and trace amounts of H_2. The ion species are dominated by H_2O^+ and OH^+ ($\approx$20 cm^{-3}) followed by H_3O^+ and O^+ ($\approx$10 cm^{-3}), H^+ ($\approx$5 cm^{-3}) and trace amounts of O^{++} and H_2^+.

When we compare our baseline OH density (770 cm^{-3}) to Figure 3 of *Jurac et al.* (2002) we find very similar values. Their model was developed to simulate the morphology of Saturn's extended OH cloud, as measured by HST, October 2002. They found an OH density of $\gtrsim$750 cm^{-3} centered on the orbit of Enceladus (see also *Jurac and Richardson* (2005)). This is an independent test of our results since no radiative constraints were used to determine the baseline solution.

Our model shows that all ion species have temperatures close to their initial pickup temperature, consistent with negligible loss of energy via radiation and Coulomb collisions with electrons. The thermal coupling time between electrons and ions derived from the model is $\approx$60 days. Because ions are transported out of the box in 26 days, they do not efficiently transfer energy to the electrons. Oxygen ions are picked up by the corotating magnetosphere with a temperature of 38.4 eV (Appendix A, Equation A.7). OH, H_2O, and H_3O ions are picked up with 40.8, 43.2, and 45.6 eV, respectively. As shown in Table 2.1, very little of these heavy ions' thermal energy has been transferred to the thermal electrons. This result has also been established in Figure 2.2 by the small energy coupling (2.4%) between ions and electrons.

The water-group temperatures from our model ($\approx$38–42 eV) are warmer than the CAPS data suggest. *Sittler et al.* (2006, 2007) observed that $T_{\perp,W^+} \approx$35–40 eV near the Encaladus torus. With their anisotropy of $(T_\perp/T_\parallel)_{W^+} \approx 5$, the effective water-group

temperature is reduced to $T_{W^+} = (2T_\perp + T_\parallel)/3 \approx 27$ eV. The discrepancy between our model and the data may be explained by a sub-corotating plasma torus near Enceladus' L shell. An $\approx 20\%$ sub-corotation of the plasma flow, as measured by CAPS at $4R_S$ (R. Wilson, personal comm.), would reduce pickup energies and may account for the difference between our model temperatures and the *Sittler et al.* (2006, 2007) observations (40 eV and 27 eV, respectively).

In our model, we have assumed that the ion velocity distributions are isotropic and thus cannot comment on the parallel and perpendicular temperatures individually (Section 2.3). Because the data suggest that the water-group ion has an anisotropy of $T_\perp/T_\parallel \approx 5$ and the protons have an anisotropy of $T_\perp/T_\parallel \approx 2$ (*Richardson and Sittler*, 1990; *Moncuquet et al.*, 2005; *Sittler et al.*, 2006, 2007), we hope to include anisotropic ion velocity distributions in the future.

The flow of mass and energy is shown in Figure 2.1 and Figure 2.2 (contributions from individual species are listed in Appendix A). Mass is introduced into the model by way of H_2O only and leaves when ions are transported radially, charge exchange with neutrals, or recombine with electrons (for singly-ionized species). Recombination and charge exchange represent mass sinks because the ions become 'fast neutrals,' assumed to possess enough velocity to escape the torus. We find that 94% of the particles leave the torus as fast neutrals and 6% as ion transport.

Energy is introduced almost entirely by pickup ions, and a small amount (1.8%) comes from Coulomb collisions between the hot electrons and the thermal electrons/ion species. Pickup ions represent an energy source due to the velocity difference between neutrals and ions in the Enceladus torus; a freshly-ionized neutral is accelerated to

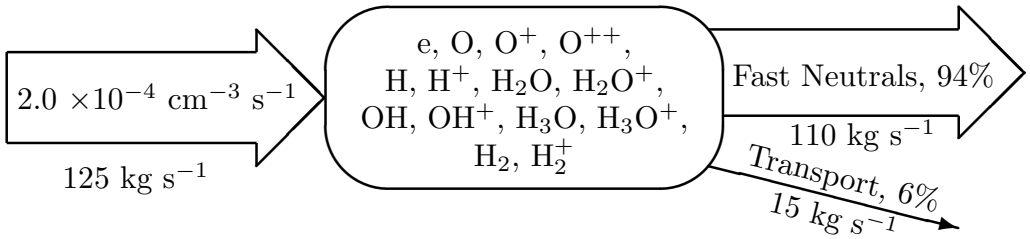


Figure 2.1 Particle flow for the baseline case. We have assumed a torus volume of $2\pi(4R_S)(2R_S)^2$ to calculate the volumetric mass flow. The percentages given here are for particle *number* (not mass). Individual species contributions to the particle outflow can be found in Appendix A.

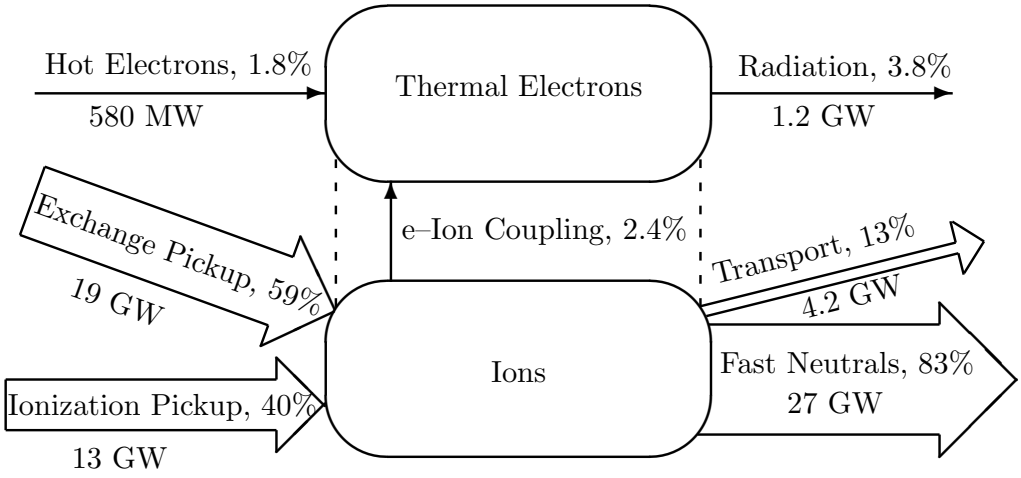


Figure 2.2 Energy flow for the baseline case. We have assumed a torus volume of $2\pi(4R_S)(2R_S)^2$ to calculate the volumetric energy flow. Individual species contributions to the energy outflow can be found in Appendix A.

magnetospheric corotation via current systems established between Saturn's ionosphere and the Enceladus torus. Fresh pickup ions may be produced either by electron impact or charge exchange between an ion and a neutral. Energy is carried away in the model by the fast neutrals, transported ions, and radiation induced by electron-impact excitation. Figure 2.2 indicates that most energy (83%) leaves the model with the fast neutrals.

Figure 2.1 and Figure 2.2 can be compared to the energy and particle flow diagrams found with the oxygen-based model of *Delamere et al.* (2007) (their Figure 1). On the partitioning of particle flow between radial transport and fast neutrals, their simplified model is remarkably similar to our solution, though their neutral source rate ($4 \times 10^{-4}\,\mathrm{cm^{-3}\,s^{-1}}$) is twice as strong.

The total energy flowing through our model is roughly 40% of that found by *Delamere et al.* (2007) ($9.4\,\mathrm{eV\,cm^{-3}\,s^{-1}}$ compared to $23\,\mathrm{eV\,cm^{-3}\,s^{-1}}$). They used a smaller hot electron fraction ($f_{\mathrm{eh}} = 0.3\%$) and a higher hot electron temperature ($T_{\mathrm{eh}} = 1000\,\mathrm{eV}$) than the values we used to produce Figure 2.1 and Figure 2.2. In addition, their transport time was considerably longer at 45 days.

Regarding energy output, we find that more energy is transported out of the torus by ions than by fast neutrals when compared to *Delamere et al.* (2007), though we agree on the radiated power partition of a few percent. Energy input is remarkably different because we have included molecular chemistry, while *Delamere et al.* (2007) included atomic oxygen only. Hot electron thermal coupling plays a bigger role as an energy source with 1.8% of the total energy input compared to 0.5% in *Delamere et al.* (2007). In our model, charge exchange only marginally exceeds the combination

of photoionization and impact ionization as a means of adding fresh pickup ions to the system, whereas in *Delamere et al.* (2007) charge exchange was found to dominate these mechanisms by a factor of 19. One reason for this major difference is the relative ease at which OH is ionized via electron impact with respect to O. This reaction can contribute greatly to the overall energy budget since OH is the dominant species (Table 2.1). Photoionization of OH and O occurs at roughly the same, much lower rate for the baseline case. If oxygen were the only species in the model, energy input would be a competition between the highly-likely resonant charge exchange between O and O^+ and the order-of-magnitude-less-likely photo- plus impact ionization of O. [a]

Dissociative recombination represents an important plasma sink to the Enceladus torus, and has a profound effect on the neutral-to-ion ratio in the torus. The *Delamere et al.* (2007) model found $n_{\rm neut}/n_{\rm ions} = 12$, but they argued that this ratio represents a lower limit since their model is oxygen-based and does not include dissociative-recombination reactions; the recombining ions' neutral products have escape velocities and leave the model, as do recombining atomic ion species. We find $n_{\rm neut}/n_{\rm ions} = 40$ with the full water-based molecular chemistry.

Sittler et al. (2008) showed that the combination of cold electrons ($\approx$ 1 eV) and the dominance of molecular ions over atomic oxygen ions near Enceladus (*Young et al.*, 2005) drives a rapid dissociative-recombination timescale. They also showed that this process increases the neutral-to-ion production ratio to $\approx$50 near Enceladus (their Figures 18 and 20).

To illustrate the importance of dissociative recombination in our model, we in-

[a]Reaction rates related the above discussion can be found in Appendix A.

creased T_e by increasing the pickup temperature in the Enceladus torus (Appendix A, Eq. 7). Indeed, if the parameters are fixed at the baseline values (Table 2.1), and T_e is increased to 6 eV (as in the ion-dominated Io torus), dissociative recombination continues to prevent ions from dominating neutrals (Section 2.4.2). At Saturn, impact ionization by thermal electrons cannot compete with dissociative recombination as an ion sink, even when $T_e = 6$ eV.

Derived quantities The field strength in the Enceladus torus is 325 nT (*Dougherty et al.*, 2006b), giving a plasma beta of

$$\beta = \frac{\sum_{j=\text{ions,e,eh}} n_j T_j}{B^2/8\pi} = 0.0091 \approx 1\%, \tag{2.5}$$

where the summation is taken over all charged species, including both the thermal- and hot electron populations (Table 2.1). This value is consistent with the *Sittler et al.* (2008) analysis, which found $\beta = 0.1$–5% between 3 and $5R_S$. The Alfvén speed is given by

$$v_A = B/\sqrt{4\pi\rho} = 230\,\text{km}\,\text{s}^{-1}, \tag{2.6}$$

where $\rho = \sum_{j=\text{ions}} n_j m_j$. If the plasma is at full corotation at the orbit of Enceladus,[a] then the Alfvén Mach number is

$$M_A = v_\phi/v_A = (4R_S)\Omega_S/v_A = 0.17. \tag{2.7}$$

[a] As has been assumed in the model for calculating E_{pu} (Appendix A, Eq. 7).

This can be compared to *Sittler et al.* (2008), who find $0.01 < M_A < 0.5$ between 3 and $5R_S$. *Sittler et al.* (2008) use ion–electron fluid parameters as boundary conditions to solve for ion field-line distributions throughout Saturn's inner-magnetosphere. The fluid parameters are derived from CAPS data acquired during the approach phase of the SOI period (*Sittler et al.*, 2006, 2007). In Chapter 5, we address radial mass transport and present a self-consistent map of the ion distribution throughout Saturn's inner magnetosphere.

Lifetimes

The lifetimes for each species are listed by mechanism in Table 2.2 and by reaction in Appendix A. The transport timescale (τ_{trans}) has not been well constrained by this study. In Section 2.5, we show that the model is consistent with a transport timescale of 12 days or longer. Because our study cannot place an upper limit on τ_{trans}, it is not possible to say which mechanisms occur more rapidly than radial transport and are therefore more important.

Our model does not account for collisional heating that would give neutrals enough speed to escape the torus. Thus, we have assumed that the timescales for such neutral escape are longer than the timescales for the included mechanisms. Based on the Enceladus torus study by *Farmer* (2009), we now examine this assumption with the conclusion that the effects of collisional heating should be included in future iterations of our model, especially in the case of OH.

Neutral H_2O has an effective cross-section to neutral–neutral collisions due to dipole–dipole interactions such that an H_2O molecule will be transported outside our

modeled torus ($> 5R_S$) after ≈ 40 days (Figure 2 in *Farmer* (2009)). Then, according to Table 2.2, only impact dissociation and charge exchange are important loss mechanisms for H_2O. A similar timescale (40 days) may also limit OH lifetimes because its induced dipole is comparable to that of H_2O. Under this assumption, collisional heating would be the *most* important loss mechanism for OH.

The *Farmer* (2009) result can also be used to estimate oxygen lifetimes against neutral–neutral collisions. Because the geometric cross section for H_2O is a factor of 10 smaller than the induced-dipole cross section ($\sigma_{H_2O} = 5\,\text{Å}^2 \rightarrow \sigma^{\text{ind}}_{H_2O} = 54\,\text{Å}^2$, *Farmer* (2009)), and because the collision frequency is proportional to σ, one might expect that O will take roughly 10 times *longer* to be scattered outside the torus. That is, only those mechanisms occurring on a timescale of $\lesssim 400$ days (charge exchange and impact ionization) would occur before neutral collisions remove oxygen from the torus.

Dominant chemistry

Reactions occurring more frequently than 10^{-6} cm^{-3} s^{-1} , shown in Table 2.3, are the ones of primary importance in the torus. Appendix A lists the full set of reactions and reaction rates for the baseline case. Indeed, if we run the model with every reaction in Appendix A turned on (and the parameters set at the baseline values) all densities and ion temperatures are within 3% of the results from the calculation using the reduced set in Table 2.3. The most dominant reaction is impact dissociation of H_2O by hot electrons ($H_2O + e_h \rightarrow OH + H + e$). Dissociation of H_2O by hot electrons occurs so frequently because of the relatively large reaction rate at $T^{\text{baseline}}_{\text{eh}} = 160$ eV (Appendix A) as well as the high baseline density of H_2O (Table 2.1). Several other charge-

Dominant Reactions			
$H + e_h$	$\rightarrow H^+ + 2e$	$H^+ + H$	$\rightarrow H + H^+$
$O + e_h$	$\rightarrow O^+ + 2e$	$H^+ + O$	$\rightarrow H + O^+$
$OH + e$	$\rightarrow OH^+ + 2e$	$H^+ + OH$	$\rightarrow H + OH^+$
$OH + e_h$	$\rightarrow OH^+ + 2e$	$H^+ + H_2O$	$\rightarrow H + H_2O^+$
$H_2O + e_h$	$\rightarrow H_2O^+ + 2e$	$O^+ + H$	$\rightarrow O + H^+$
$H_2O + e_h$	$\rightarrow OH^+ + H + 2e$	$O^+ + O$	$\rightarrow O + O^+$
$H_2O + e_h$	$\rightarrow H^+ + OH + 2e$	$O^+ + OH$	$\rightarrow O + OH^+$
$OH + e$	$\rightarrow O + H + e$	$O^+ + H_2O$	$\rightarrow O + H_2O^+$
$OH + e_h$	$\rightarrow O + H + e$	$OH^+ + OH$	$\rightarrow O + H_2O^+$
$H_2O + e$	$\rightarrow OH + H + e$	$OH^+ + H_2O$	$\rightarrow OH + H_2O^+$
$H_2O + e_h$	$\rightarrow OH + H + e$	$OH^+ + H_2O$	$\rightarrow O + H_3O^+$
$O + \gamma$	$\rightarrow O^+ + e$	$H_2O^+ + H_2O$	$\rightarrow OH + H_3O^+$
$OH + \gamma$	$\rightarrow OH^+ + e$	$H_2O^+ + H_2O$	$\rightarrow H_2O + H_2O^+$
$OH + \gamma$	$\rightarrow O + H$	$OH^+ + e$	$\rightarrow O + H$
$H_2O + \gamma$	$\rightarrow H + OH$	$H_2O^+ + e$	$\rightarrow OH + H$
$H_2O + \gamma$	$\rightarrow H_2 + O$	$H_3O^+ + e$	$\rightarrow OH + H_2$

Table 2.3 List of the most important reactions for the baseline case. The left column gives the relevant impact, dissociative, and photolytic reactions, and the right column gives all relevant charge exchanges and recombinations. The full set of reactions are given in Appendix A, but steady-state densities and temperatures are all within 3% of the properly calculated values when only the above reactions are turned on.

exchange, photolytic, and electron-impact reactions are competitive behind H_2O impact dissociation.

Impact ionization by hot electrons contributes roughly the same amount of energy (22% of total input) via magnetospheric pickup as does photoionization (16%). Impact ionization by thermal electrons is a minor source of energy to the torus ($\approx 1\%$). In fact, only one reaction in Table 2.3 involves thermal electron impact ionization ($OH + e \rightarrow OH^+ + 2e$). *Delamere et al.* (2007) found that charge exchange is far more important than photo- and impact ionization combined as a torus energy source. Here we find that charge exchange is only marginally more important ($\approx 60\%$) than the combination of these other ionization sources ($\approx 40\%$) for providing fresh pickup ions to the torus. This discrepancy (discussed in Section 2.4.2) is due largely to the fact

that the earlier model did not include molecular chemistry.

2.4.3 Sensitivity

Contour plots of the total fractional difference ($f_{\rm diff}$, Equation 2.4) between the model output and the constraints have been created for every parameter combination are shown in Figure 2.3. The intersection of the dashed lines indicates the baseline solution (Table 2.1). In each case, the remaining three parameters are fixed at the baseline values. The shading inside the $f_{\rm diff} = 1$ contour is intended to guide the eye for comparing one panel to another. Because the remaining two parameters are fixed in each panel, these plots show the sensitivity of $f_{\rm diff}$ to each parameter individually.

The source rate is inversely related to $\tau_{\rm trans}$ (Panel 1) and $f_{\rm eh}$ (Panel 2). The trend between $N_{\rm src}$ and $\tau_{\rm trans}$ can be understood as a balance between source and sink; plasma taking longer to transport out of the torus must be accompanied by a decrease in H_2O. Similarly, an increase in hot electrons results in higher ionization. Finally, a reduced neutral source rate is required to maintain $n_{\rm e}$ and W^+/H^+.

The total fractional difference, $f_{\rm diff}$, strongly depends on $f_{\rm eh}$, with a pronounced valley in all cases (Panels $2, 4, 5$). The hot electron population is critical for ionizing H efficiently to obtain $W^+/H^+ \approx 12$ (and hence, minimizing $f_{\rm diff}$). The hot electrons are equally necessary for attaining a higher overall ionized composition, thereby increasing $n_{\rm e}$, and for heating the thermal electrons ($T_{\rm e}$) via Coulomb coupling.

A similar dependence exists for $T_{\rm eh}$, except that the strong dependence is at low $T_{\rm eh}$ only (Panels $3, 5, 6$). Beyond the baseline temperature of 160 eV, $f_{\rm diff}$ is roughly independent of $T_{\rm eh}$. The other three parameters dominate variation in $f_{\rm diff}$ when the

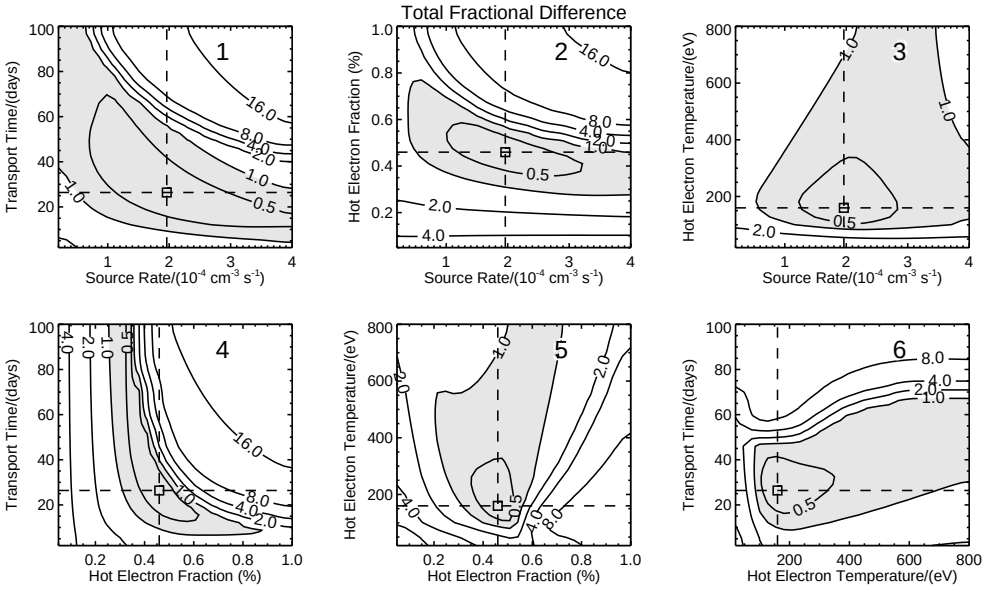


Figure 2.3 Sensitivity plots of $f_{\rm diff}$ for every parameter combination. In each case, the remaining three parameters are fixed at their baseline values (Table 2.1) to ascertain trends due solely to variation of a single parameter at a time. The intersection of dashed lines indicates the baseline solution, and the gray shading inside of $f_{\rm diff} = 1$ is intended to guide the eye. (Contours are plotted logarithmically.)

hot electron population is sufficiently energetic ($\gtrsim$ 160 eV).

Delamere et al. (2007) present sensitivity contour plots of the neutral-to-ion ratio and thermal electron temperature from their oxygen-based model (their Figure 2). We have generated similar contours (not shown) and find that the torus composition is neutral-dominated despite $T_{\rm e}$ approaching 6 eV, whereas *Delamere et al.* (2007) find that ions dominate when $T_{\rm e}$ is as low as 3 eV. The key difference between their model and ours is that we have included an exhaustive water-based set of reactions, and we have included the effects of dissociative recombination not present in the Delamere model.

Because we are varying only two parameters at a time in each panel of Figure 2.3,

we are not necessarily finding the smallest possible $f_{\rm diff}$ throughout, an issue we take up in the following section.

2.5 Grid search

In search of the best possible match to our three observable constraints, we have explored the full 5-dimensional parameter space ($f_{\rm eh}$, $T_{\rm eh}$, $f_{\rm H^+}$, $N_{\rm src}$, $\tau_{\rm trans}$) by solving Equation 2.1 and Equation 2.2 systematically for a variety of parameter combinations. We divided the domain for each parameter (Section 2.3) into 30 discrete, uniformly-spaced values, and created a table of model densities and temperatures corresponding to each combination. This 5-dimensional table is also useful for finding models agreeing with an assortment of observations (Section 2.5.1). The computationally-expensive procedure of creating the grid will only need repeating once additional or updated chemical reactions are introduced to the model. The downside of the grid search is limited resolution, and to double the resolution would require 2^5 times more computational time. Fortunately, the calculation can in principle be done in parallel, and wall-clock time can be reduced linearly with the number of computer processors.

2.5.1 Results

Using the constraints in Section 2.4 ($n_{\rm e} = 60$ cm^{-3}, $T_{\rm e} = 2$ eV, $\rm W^+/H^+ = 12$), we have used the grid described in the previous section to generate sensitivity contours for every parameter combination by searching for the smallest $f_{\rm diff}$ everywhere, from which the following parameter limits can be inferred:

$$1.5 \lesssim N_{\rm src}/(10^{-4}\ {\rm cm}^{-3}\ {\rm s}^{-1}) \lesssim 2.7$$

$$12 \text{ days} \lesssim \tau_{\text{trans}}$$

$$0.3 \lesssim f_{\text{eh}}(\%) \lesssim 0.9$$

$$100 \lesssim T_{\text{eh}}/\text{eV} \lesssim 250$$

$$f_{\text{H}^+} \leq 1.$$

We will also demonstrate that the solution space found by searching the grid is smoothly varying and well-behaved.

The sensitivity contours between the parameters f_{eh} and T_{eh} are shown in Figure 2.4. Panel 1 is the plot of the smallest possible f_{diff} for the parameter ranges given in Section 2.3. Recall that f_{diff} is the sum of fractional differences between model output and primary model constraints for n_{e}, T_{e}, and W^+/H^+ (Section 2.2). To illustrate the individual contributions to f_{diff}, we show T_{e}, n_{e}, and W^+/H^+ in Panels 2, 3, and 4 respectively; the dotted contours define the primary constraints against which f_{diff} is evaluated. The corresponding values of τ_{trans}, N_{src}, and f_{H^+} are plotted in Panels 5–7. The remaining plots in order are: water-group composition (Panels 8–11), total UV power (Panel 12), and mass radial transport rate (Panel 13).

The $f_{\text{diff}} = 0.05$ contour in Panel 1 has been shaded in gray and over-plotted in Panels 5–13 to indicate a parameter subspace consistent with the observations. This contour can be expanded or reduced to reflect observational uncertainty. The random-walk algorithm used in Section 2.4 to find the baseline solution was initialized with parameter values near this global minimum. The intersecting dashed lines indicate the baseline solution discussed in Section 2.4.[a] From Figure 2.4, we find that $0.3 \lesssim$

[a]Though the baseline solution is encompassed in the solution space, it is not unique. The solution space is bounded by a range of parameters for which a solution can be found that agrees with the data

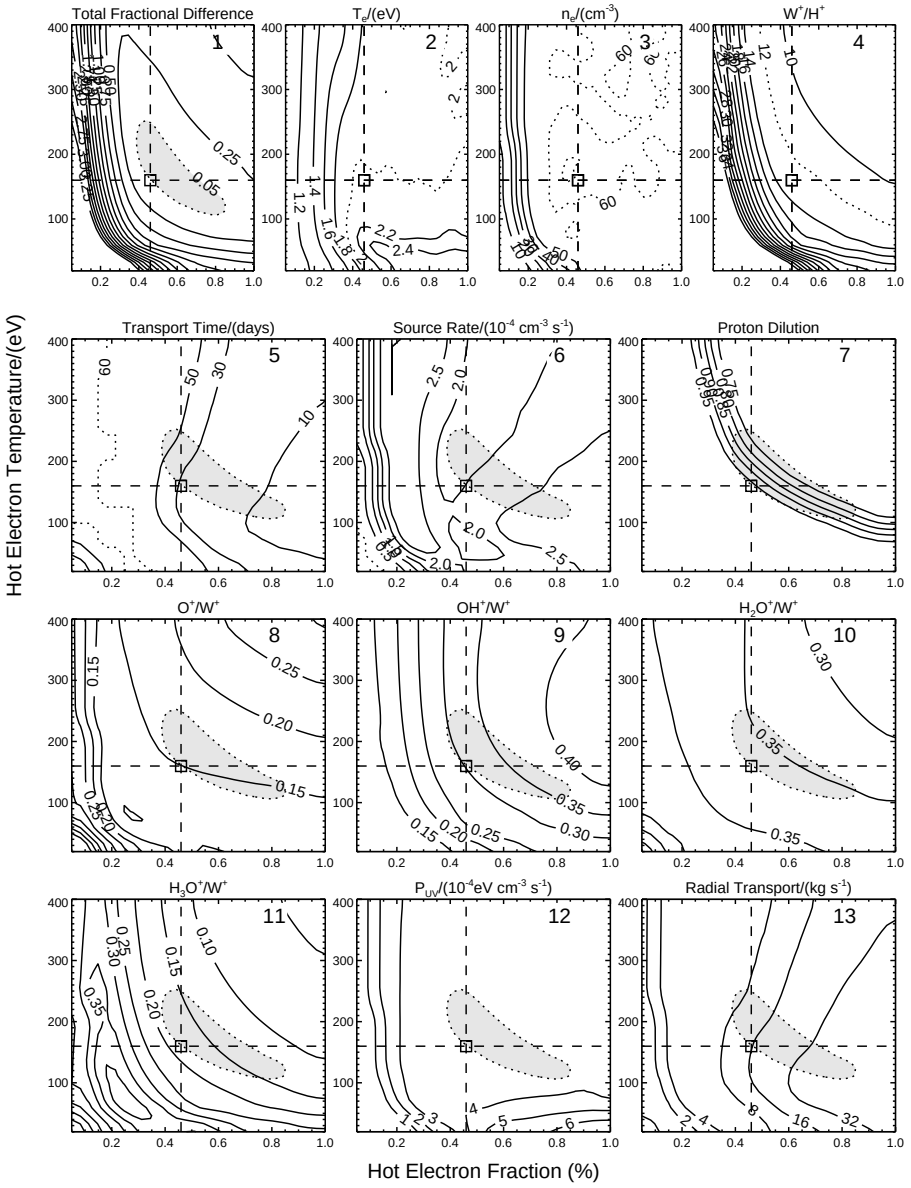


Figure 2.4 Sensitivity plots between hot electron temperature ($T_{\rm eh}$) and hot electron fraction ($f_{\rm eh}$) generated from the grid search. The over-plotted box represents the baseline solution, discussed in Section 2.4. The $f_{\rm diff} = 0.05$ curve (Panel 1) has been over-plotted on Panels 5–13 in gray. The three parameters in Panels 5–7 ($\tau_{\rm trans}$, $N_{\rm src}$, and $f_{\rm H^+}$) have taken on values yielding best agreement between model output and $n_{\rm e} = 60$ cm^{-3}, $T_{\rm e} = 2$ eV, and $\rm W^+/H^+ = 12$. Combinations of $T_{\rm eh}$ and $f_{\rm eh}$ within the gray contour are consistent with these constraints. All panels are discussed in Section 2.5.1.

$f_{\rm eh}(\%) \lesssim 0.9$ and $100 \lesssim T_{\rm eh}/({\rm eV}) \lesssim 250$.

Because parameter combinations are evaluated according to model output for $n_{\rm e}$, $T_{\rm e}$, and W^+/H^+ alone, one cannot rule out a priori that adjacent points in these contours sample wildly different values of $\tau_{\rm trans}$, $N_{\rm src}$, and f_{H^+}. That the contours for these constraints (Panels 5–7) and for the composition (Panels 8–13) are smoothly varying and well-behaved proves this not to be the case.

Because the different water-group ion species have similar masses, and because composition varies significantly with longitude in the Enceladus region (*Williams et al.*, 2008), the water-group density ratios (Panels 8–11) are difficult to distinguish in the CAPS observations. However, *Sittler et al.* (2008) have calculated with CAPS SOI data that $H_3O^+/W^+ \approx 0.45$, $H_2O^+/W^+ \approx 0.15$, and $OH^+/W^+ \approx O^+/W^+ \approx 0.2$ near the orbit of Enceladus. Preliminary CAPS results by *Williams et al.* (2008) also suggest that H_3O^+ is the dominant water-group species in the Enceladus torus.

INMS data acquired downstream of Enceladus suggest that the local chemistry, dominated by charge exchange, may represent a significant source of H_3O^+ not included in our model (*Cravens et al.*, 2009). In Chapter 3, we present a model of the chemical interaction between Enceladus's water-based plumes and the corotating plasma, whereby chemical pathways leading to H_3O^+ are identified.

The UV power due to impact excitation (Panel 12) was calculated from line emissions and scales to roughly 1 GW for the entire torus. This estimate likely represents a lower limit since emission from H_2O, for example, has not been included in the model

nearly as well.

(see Appendix A).[a] Most of the radiated power ($\approx 80\%$) comes from the 1304, 1356, and 6300 Å neutral oxygen emission lines. In future studies, P_{UV} would prove a powerful constraint for the model (*Esposito et al.*, 2005).

The mass transport rate ($\dot{M}$, Panel 13), is defined as:

$$\text{Radial Transport Rate} \equiv \frac{\text{Vol}}{\tau_{\mathrm{trans}}} \sum_{j=\mathrm{ion,e}} m_j n_j, \tag{2.8}$$

where a torus volume of $2\pi(4R_{\mathrm{S}})(2R_{\mathrm{S}})^2$ has been used, and m_j is the mass of ion species j. We find that ion transport may vary by a factor of six or more ($\approx$ 8–50 kg s^{-1}) and still be consistent with the solution space presented here. We note that the radial chemistry models in Chapter 4 and Chapter 5 agree well with this estimate on $\dot{M}$, although those models pertain to global production—not just in Enceladus's orbit.

The solution space can be further constrained when better data for the parameters themselves [N_{src}, f_{eh}, T_{eh}, $f_{\mathrm{H^+}}$, τ_{trans} (Section 2.2.1)] become available. Limits derived from such measurements could be used to define contour levels in Panels 5–7 that would limit the solution space in gray. The same can also be said for torus ultraviolet emission (P_{UV}).

The fractional difference contours in Panel 1 of Figure 2.4 are much broader than in Panel 5 of Figure 2.3. The difference of course being that τ_{trans}, N_{src}, and $f_{\mathrm{H^+}}$ are fixed in Figure 2.3 while in Figure 2.4 they are free. We offer the following interpretation to help the reader visualize how freeing the parameters (Panels 5–7) has expanded the solution space. For clarity—and because the proton abundance is strongly coupled to

[a]The radial chemistry model in Chapter 5, however, does include cooling from OH and H_2O excitation, where there we adopt the oxygen cooling term for each.

hot electrons (Section 2.5.1)—we restrict our discussion to transport time and neutral source rate. Attention is called to the upper-right quadrant of Panels 5, 6 and 7 in Figure 2.4—the region where the total fractional difference contours (Panel 1) have been broadened most when compared to Figure 2.3. The transport time increases slightly ($\tau_{\rm trans} \uparrow$) with increasing hot electron temperature ($T_{\rm eh} \uparrow$) and decreases sharply ($\tau_{\rm trans} \downarrow$) as the hot electron fraction increases ($f_{\rm eh} \uparrow$). The neutral source rate is remarkably constant at a value near the baseline value of 2.0×10^{-4} cm^{-3} s^{-1}, varying by only 30% throughout the entire upper-right quadrant.

The trends between $\tau_{\rm trans}$, $f_{\rm eh}$, and $T_{\rm eh}$ are in part driven by the thermal electron density. As the hot electrons increase in temperature beyond the baseline hot electron temperature, 160 eV ($T_{\rm eh} \uparrow$), the impact ionization rate of both hydrogen and water-group molecules decreases (Figure 2.5); to maintain the total ionization ($n_{\rm e}$), the ions must remain in the torus longer ($\tau_{\rm trans} \uparrow$). Similarly, as the hot electrons increase in *number* ($f_{\rm eh} \uparrow$), both protons and water-group ions build up and must be transported more *rapidly* ($\tau_{\rm trans} \downarrow$) to maintain $n_{\rm e}$.

In Figure 2.6, we also include the same set of sensitivity contours, only this time between $\tau_{\rm trans}$ and $f_{\rm eh}$. The solution space is bounded by $0.3 \lesssim f_{\rm eh}(\%) \lesssim 0.9$, but $\tau_{\rm trans}$ is only bounded from below at 12 days. There are three other sensitivity plots in Appendix A with which to constrain $\tau_{\rm trans}$, but $\tau_{\rm trans}$ is never constrained from above because recombination and charge-exchange dominate the chemistry when $\tau_{\rm trans} \gtrsim 26$ days. That is, varying $\tau_{\rm trans}$ in this regime has no effect on the model. The relevance of recombination near Enceladus's orbit has also been discussed by *Sittler et al.* (2008).

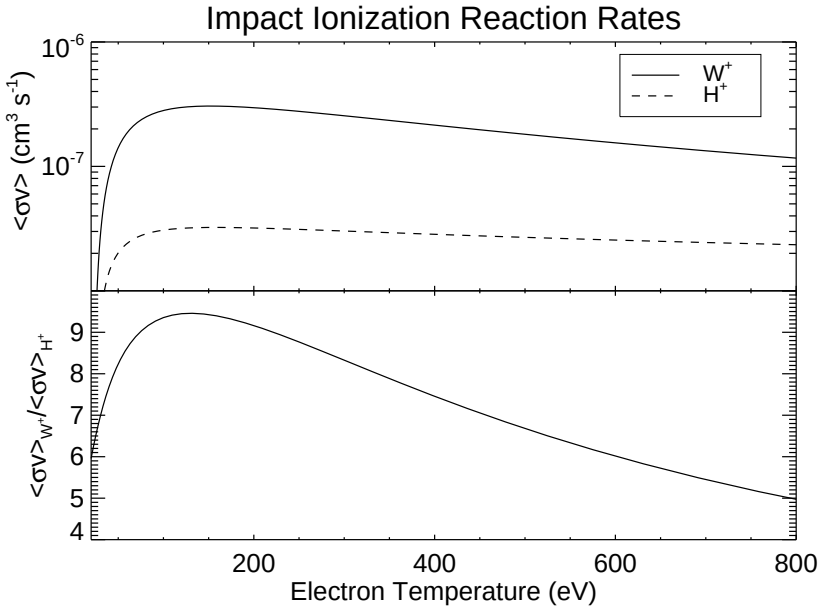


Figure 2.5 Electron-impact reaction rates for the water group ($O + OH + H_2O$) and hydrogen. The bottom panel emphasizes that water-group reaction rates fall faster than hydrogen reaction rates as $T_{\rm eh}$ increases.

Sensitivity plots similar to Figure 2.4 and Figure 2.6 for the eight remaining parameter combinations can be found in Appendix A. The $f_{\rm diff} = 0.05$ shaded contours in Appendix A have been used to find the limits on the neutral source rate ($N_{\rm src}$) and the proton dilution factor ($f_{\rm H^+}$) discussed above and in Section 2.7.

Proton dilution

The grid search has revealed that $f_{\rm H^+}$ is a weak parameter in the as illustrated in Figure 2.4 and Figure 2.6. Panel 7 in each figure shows that small changes in $T_{\rm eh}$ and $f_{\rm eh}$ can compensate for large changes in $f_{\rm H^+}$. In fact, the full domain of $f_{\rm H^+}$ (0.7–1.0) fits entirely into the shaded solution subspace. Table 2.3 (and the reaction rates in Appendix A) indicates that the dominant reaction for creating protons is impact

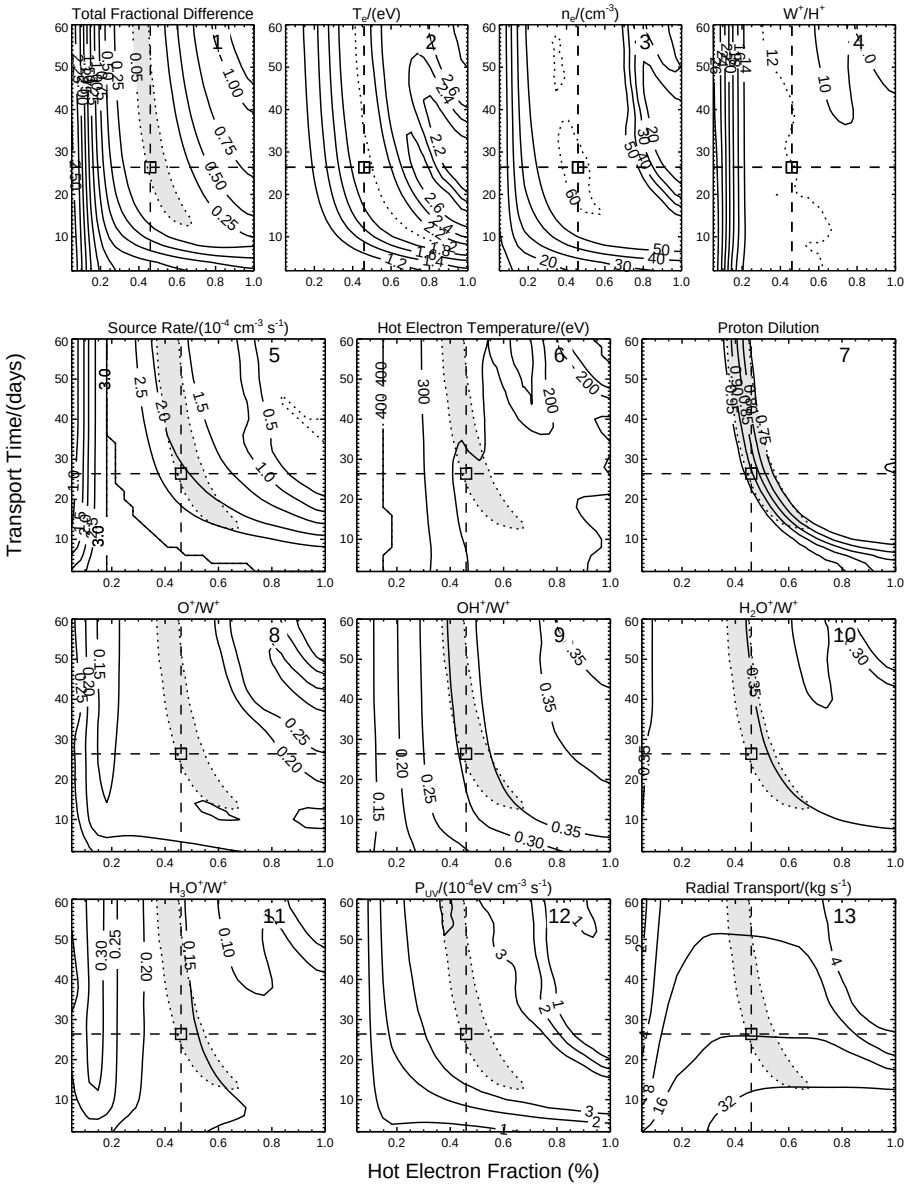


Figure 2.6 Sensitivity plots between radial transport timescale ($\tau_{\rm trans}$) and hot electron fraction ($f_{\rm eh}$) generated from the grid search. The over-plotted box represents the baseline solution, discussed in Section 2.4. The $f_{\rm diff} = 0.05$ curve (Panel 1) has been over-plotted on Panels 5–13 in gray. The three parameters in Panels 5–7 ($N_{\rm src}$, $\tau_{\rm trans}$, and $f_{\rm H^+}$) have taken on values yielding best agreement between model output and $n_{\rm e} = 60$ cm^{-3}, $T_{\rm e} = 2$ eV, and $W^+/H^+ = 12$. Combinations of $\tau_{\rm trans}$ and $f_{\rm eh}$ within the gray contour are consistent with these constraints. All panels are discussed in Section 2.5.1.

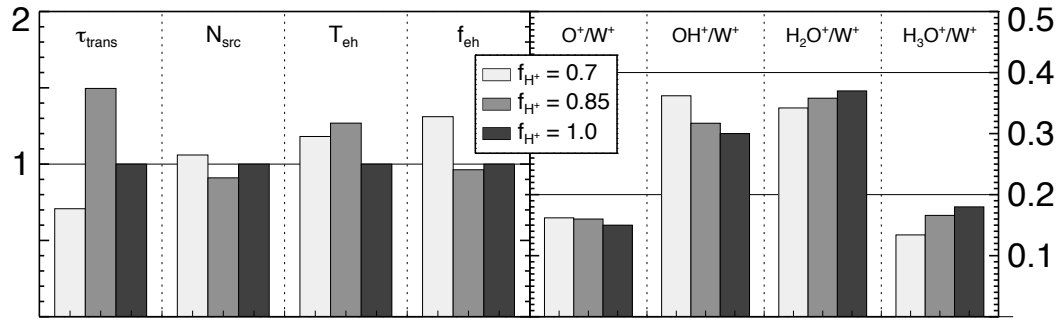


Figure 2.7 Solutions for various proton dilution factors ($f_{\mathrm{H^+}} = 0.7, 0.85, 1.0$) found from the grid search in Section 2.5.1. The parameters in the left panel are normalized to the values listed in Table 2.1. In the right panel are the water-group abundance ratios. Proton production is strongly controlled by impact ionization of hydrogen by hot electrons, and so $f_{\mathrm{H^+}}$ is coupled to T_{eh} and f_{eh}. This coupling diminishes the significance of $f_{\mathrm{H^+}}$ and effectively reduces the parameter space to four dimensions.

ionization of hydrogen by hot electrons:

$$\mathrm{H} + \mathrm{e_h} \rightarrow \mathrm{H^+} + 2\mathrm{e}. \tag{2.9}$$

This reaction strongly couples $f_{\mathrm{H^+}}$ to f_{eh}, effectively reducing the parameter space to four dimensions. The reaction $\mathrm{H_2O} + \mathrm{e_h} \rightarrow \mathrm{H^+} + \mathrm{OH} + 2\mathrm{e}$ is only about 1/3 as effective as hot electron impact ionization at producing fresh $\mathrm{H^+}$ (Appendix A), while $\mathrm{O^+} + \mathrm{H} \rightarrow \mathrm{O} + \mathrm{H^+}$ is independent of hot electrons altogether.

Figure 2.7 illustrates that both the fit and the composition depend weakly on the choice of $f_{\mathrm{H^+}}$. The grid was searched to find the best combination of T_{eh}, f_{eh}, N_{src}, and τ_{trans} for three different values of $f_{\mathrm{H^+}}$: 0.7, 0.85, 1.0. The combination yielding the best agreement is shown in the left panel—normalized to the baseline values in Table 2.1—and the model output for water-group composition is shown in the right panel.

Varying primary constraints (n_e, T_e, W^+/H^+)

The parameter space can be thought of as 8-dimensional if variation in the primary constraints (n_e, T_e, and W^+/H^+) is allowed. In this case we are interested in how composition is affected by allowing these primary constraints to take on values reflecting a range of observations (Section 2.2.2), an exercise that illustrates how the choice of constraints affects the baseline solution. As with the baseline solution, we set $f_{H^+} = 1$ in all cases since the results are only mildly sensitive to f_{H^+} (Section 2.5.1).

To this end, the grid was searched to find parameter combinations consistent with the following six constraint combinations:

$$n_e = 40\,\mathrm{cm}^{-3} \qquad T_e = \mathbf{2\,eV} \qquad W^+/H^+ = \mathbf{12}$$

$$n_e = 80\,\mathrm{cm}^{-3} \qquad T_e = \mathbf{2\,eV} \qquad W^+/H^+ = \mathbf{12}$$

$$n_e = \mathbf{60\,cm^{-3}} \qquad T_e = 1\,\mathrm{eV} \qquad W^+/H^+ = \mathbf{12}$$

$$n_e = \mathbf{60\,cm^{-3}} \qquad T_e = 3\,\mathrm{eV} \qquad W^+/H^+ = \mathbf{12}$$

$$n_e = \mathbf{60\,cm^{-3}} \qquad T_e = \mathbf{2\,eV} \qquad W^+/H^+ = 6$$

$$n_e = \mathbf{60\,cm^{-3}} \qquad T_e = \mathbf{2\,eV} \qquad W^+/H^+ = 30,$$

where numbers in bold indicate the values assumed thus far. In each case, only one of the three constraints is different from the original set ($n_e = 60$ cm^{-3}, $T_e = 2$ eV, $W^+/H^+ = 12$). This modest sampling illustrates the dependence of plasma composition to each constraint.

Figure 2.8 shows the best fit for each case. Parameters yielding the best agreement with each set of constraints are shown in the left panels. In each chart, the original baseline case has been normalized to one, and the other two cases are given relative

to this value (see Table 2.1 to determine the actual value for each parameter). We have also generated sensitivity contours similar to those presented in Figure 2.4 and Figure 2.6 for each of these new constraint combinations (not shown), and from the $f_{\text{diff}} = 0.05$ contours have derived the ranges over-plotted on the parameters in Figure 2.8. No such ranges exist in the cases of $T_{\text{e}} = 1$ eV and $T_{\text{e}} = 3$ eV because the best fits have a total fractional difference of 0.43 and 0.19, respectively.

Water-group ion composition ratios are plotted in the right panel of each bar plot. Densities and temperatures have not been shown because we are primarily interested in the effect on composition. The top bar chart shows that neutral source rate, hot electron temperature, and hot electron fraction respond monotonically to n_{e}. In the middle chart, the neutral source and the hot electron temperature decrease, while the hot electron fraction and transport time increase with T_{e}.

Electron density is the least sensitive driver of composition, while the W^+/H^+ ratio is the strongest. In particular, H_3O^+ is the most abundant water-group ion only when $W^+/H^+ = 30$. This is an important result because obtaining the W^+/H^+ ratio from the CAPS data is more straightforward than obtaining the separate, individual abundances of each water-group species (*Wilson et al.*, 2008). Increasing the W^+/H^+ ratio requires a lower hot electron temperature. One reason for this is that the impact ionization rate of H depends less on the hot electron temperature than do the water-group ionization rates (Figure 2.5). Therefore, as the hot electron temperature lowers, the W^+/H^+ ratio increases. H_3O^+ on the other hand, is the only water-group ion that does not require hot electron impact ionization to exist (H_3O is not known to exist near Enceladus). Also, H_3O^+ is favorably produced whenever OH^+ and H_2O^+ charge exchange with

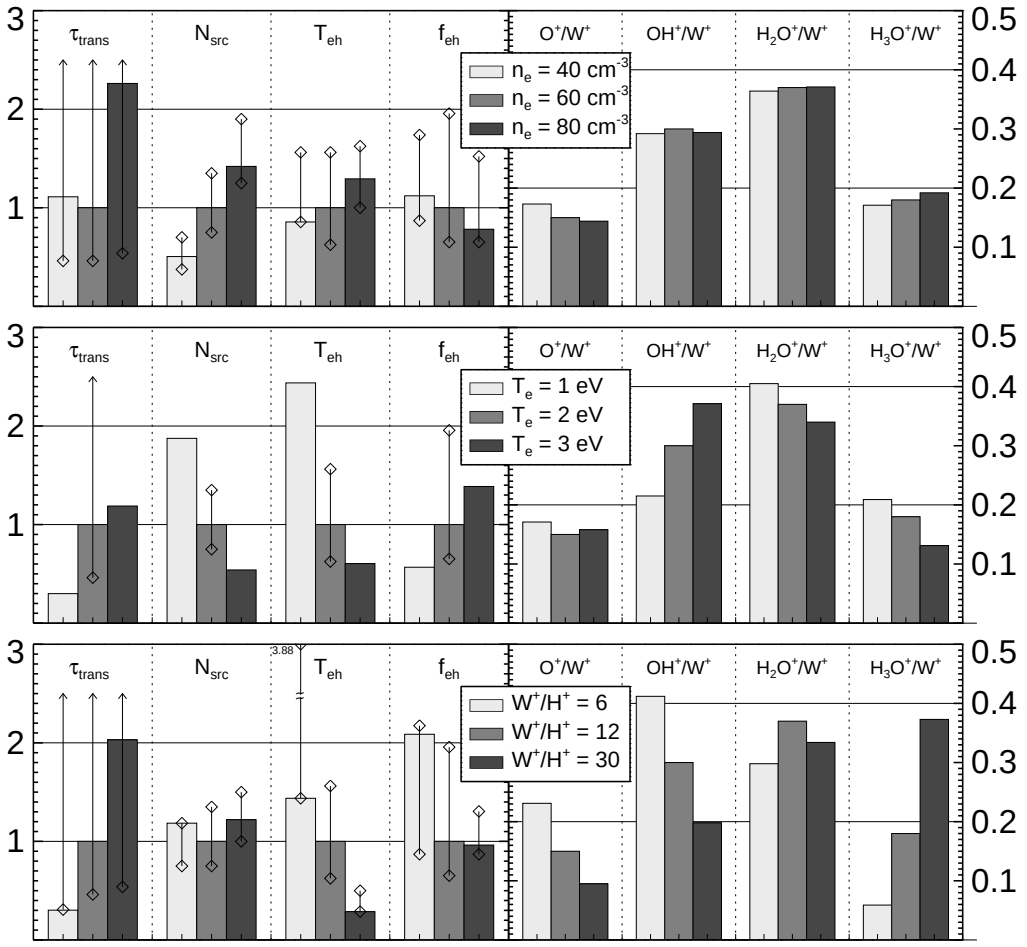


Figure 2.8 Solutions for primary constraint values representing a wide range of observations found from the grid search in Section 2.5.1. In each case, $n_{\rm e} = 60$ cm^{-3}, $T_{\rm e} = 2$ eV, and $\rm W^+/H^+ = 12$ unless otherwise specified. The parameter fits given in the left panel of each bar chart are normalized to the fit given in Table 2.1. The over-plotted ranges on the parameters are derived from the corresponding $f_{\rm diff} = 0.05$ sensitivity contours. No such ranges exist for the $T_{\rm e} = 1$ eV and $T_{\rm e} = 3$ eV solutions because the best fits have a fractional difference of 0.43 and 0.19, respectively. The corresponding model output for water-group composition is presented on the right. The choice of electron density ($n_{\rm e}$) has a weak effect, while the ratio $\rm W^+/H^+$ ratio alters composition markedly.

neutral H_2O (see Chapter 3, Chapter 4, Chapter 5). Thus, as required by the fit in Figure 2.8, the hot electron temperature decreases to raise the W^+/H^+ ratio, and in the process increases the H_3O^+/W^+ ratio.

2.6 Hot electron ($f_{\rm eh}$) modulation

Steffl et al. (2008) found that the interaction of two hot electron populations orbiting Jupiter with System III and System IV periods are required to recover Cassini UVIS observations of the Io torus composition, both in terms of amplitude and rotational period. *Delamere and Bagenal* (2008) proposed that the observed azimuthal electron density modulation at Saturn (*Gurnett et al.*, 2007) is also caused by an azimuthally-varying hot electron abundance. Motivated by their suggestion, we present compositional sensitivity to a (magnetic) longitude-dependent hot electron fraction. Figure 2.9 shows the response of the torus to a prescribed sinusoidal hot electron fraction:

$$f_{\rm eh}(\lambda_{\rm mag}) = f_{\rm eh}^{\rm baseline} + 0.0016\sin(\lambda_{\rm mag}), \tag{2.10}$$

where $f_{\rm eh}^{\rm baseline} = 0.0046$ and $\lambda_{\rm mag}$ is magnetic longitude with arbitrary phase. The modulation amplitude is chosen so that $n_{\rm e}$ modulates by roughly a factor of two ($\approx$40–80 cm^{-3}) consistent with the analysis of radio emission of *Gurnett et al.* (2007) (see their Figure 2). All other parameters are fixed at the baseline values listed in Table 2.1.

The top panel of Figure 2.9 indicates that $T_{\rm e}$ and $n_{\rm e}$ are in phase with $f_{\rm eh}$, while impact dissociation and ionization by hot electrons (Table 2.3) drive the W^+/H^+ ratio

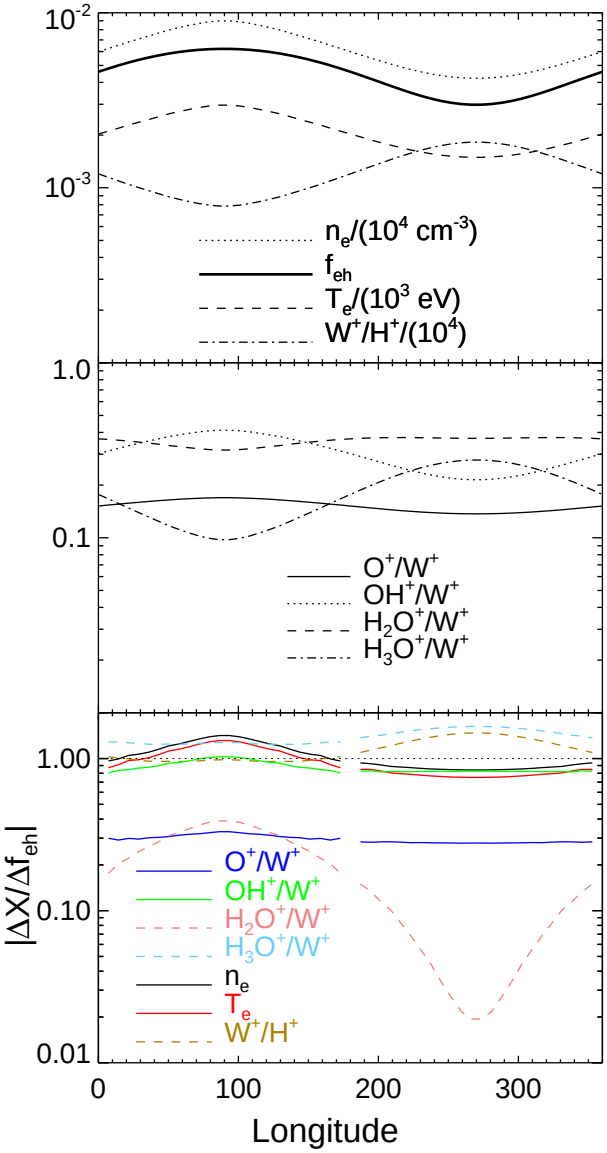


Figure 2.9 Composition variability due to hot electron modulation. The hot electron fraction, $f_{\rm eh}$, alone drives the variation since all other parameters are held at their baseline values. The quantities O^+/W^+, OH^+/W^+, n_e, and T_e are in phase while W^+/H^+, H_2O^+/W^+, and H_3O^+/W^+ are out of phase with $f_{\rm eh}$. The bottom panel shows how strongly and how linearly each quantity responds to perturbations in $f_{\rm eh}$; the solid lines represent quantities in phase with $f_{\rm eh}$, and the dashed lines represent quantities out of phase with $f_{\rm eh}$.

out of phase with $f_{\rm eh}$. All quantities are plotted on a logarithmic scale.

The middle panel shows the response of composition to $f_{\rm eh}$ (plotted on the same logarithmic scale as the top panel). The baseline abundance ratios at $\lambda_{\rm mag} = 0°$ (and 360°) are given in Table 2.1. The two hemispheres 0°–180° and 180°–360° are defined by a higher- and lower-than-baseline $f_{\rm eh}$, respectively. As $f_{\rm eh}$ increases in the 0°–180° hemisphere, the hierarchy becomes $OH^+ > H_2O^+ > O^+ > H_3O^+$. As $f_{\rm eh}$ decreases in the 180°–360° hemisphere, H_2O^+ begins to dominate and O^+ becomes the minor species ($H_2O^+ > H_3O^+ > OH^+ > O^+$).

The bottom panel shows how strongly composition and thermal electron parameters respond to $f_{\rm eh}$. Shown are the normalized changes in each parameter with respect to variation in $f_{\rm eh}$. Points are missing at the middle and endpoints because the plotted function diverges there as $\Delta f_{\rm eh} \equiv f_{\rm eh} - f_{\rm eh}^{\rm baseline} \to 0$. The solid and dashed lines respectively differentiate quantities in phase and out of phase with $f_{\rm eh}$. Quantities in phase with $f_{\rm eh}$ ($n_{\rm e}$, $T_{\rm e}$, O^+/W^+, and OH^+/W^+) have essentially flat curves, indicating nearly linear dependence on $f_{\rm eh}$, where O^+/W^+ responds to perturbations 3–4 times less strongly than the rest. Out-of-phase quantities (W^+/H^+, H_2O^+/W^+, and H_3O^+/W^+) also behave linearly with the exception of H_2O^+/W^+, which always reacts weakly and practically not at all when $f_{\rm eh}$ is small. H_3O^+/W^+ and W^+/H^+ are always driven by $f_{\rm eh}$ stronger than one-to-one.

Correlations and anti-correlations between electron density and composition such as those presented in Figure 2.9 have already been observed at Jupiter by *Steffl et al.* (2006). In particular, they find that S^+ and S^{3+} are in phase out-of-phase, respectively, with equatorial electron density modulations in the Io torus.

2.7 Conclusions

We have compared output from our model to the constraints on thermal electron density ($n_{\rm e}$), thermal electron temperature ($T_{\rm e}$), and the abundance ratio of water-group ions to protons (W^+/H^+) by exploring the parameter space spanned by the following four parameters: neutral source rate ($N_{\rm src}$), hot electron temperature ($T_{\rm eh}$), hot electron density ($n_{\rm eh} \equiv f_{\rm eh} n_{\rm e}$), and radial transport timescale ($\tau_{\rm trans}$). Important results are given below.

1. For the constraint choices of $n_{\rm e} = 60$ cm^{-3}, $T_{\rm e} = 2$ eV, and W^+/H^+=12, limits on the parameters are found to be:

   $1.5 \lesssim N_{\rm src}/(10^{-4}\ {\rm cm}^{-3}\ {\rm s}^{-1}) \lesssim 2.7$

   12 days $\lesssim \tau_{\rm trans}$

   $0.3 \lesssim f_{\rm eh}(\%) \lesssim 0.9$

   $100 \lesssim T_{\rm eh}/{\rm eV} \lesssim 250.$

   For a volume of $2\pi(4R_{\rm S})(2R_{\rm S})^2$, the source rate can be scaled to give a mass source rate of $100 \lesssim N_{\rm src}/({\rm kg\ s}^{-1}) \lesssim 180$. The solution space can be compared with independent estimates of the parameters ($N_{\rm src}$, $f_{\rm eh}$, $T_{\rm eh}$, $\tau_{\rm trans}$) and ion abundances from CAPS. Upper limits on UV power emanating from the Enceladus torus from neutral oxygen at 1304, 1356, and 6300 Å would also be a useful constraint.

2. With the full water-based chemistry, photo- plus impact ionization is nearly as important as charge exchange at providing energy by way of fresh pickup ions

(Figure 2.2).

3. The water-based chemistry (particularly dissociative recombination) increases the neutral-to-ion ratio from 12 (the *Delamere et al.* (2007) oxygen-based model) to ≈ 40. Further, the Enceladus torus remains neutral-dominated even when the thermal electron temperature equals that of electrons in Jupiter's ion-dominated Io torus (6 eV).

4. The H_3O^+/W^+ ratio is directly correlated with the W^+/H^+ ratio (Figure 2.8), implying that H_3O^+ is strongly anti-correlated with H^+ (Section 2.5.1).[a] This result is important because obtaining the W^+/H^+ ratio is more straightforward than obtaining individual water-group abundances from the CAPS data. However, *Sittler et al.* (2008) have shown, based on CAPS SOI data, that H_3O^+ dominates the water-group near the orbit of Enceladus (their Figure 15). The dominance of H_3O^+ seen in the CAPS data has not been obtained by our model with the given constraints. We show in Chapter 3, however, that the interaction of the corotating plasma with the Enceladus plumes does increase H_3O^+ abundance, at least locally (*Cravens et al.*, 2009).

5. Hot electrons in the Enceladus can explain observed ion abundances, but do not comprise more than 1% of the total electron population.

6. Substantial variation in composition can be driven by a small perturbation in the hot electron population (Figure 2.9). The sensitivity study presented here will be useful in a future interpretation of longitudinal and temporal observations

[a] The radial chemistry model in Chapter 5 bears this statement out.

(e.g., *Gurnett et al.* (2007)) of the Enceladus torus, especially in the context of a modulating hot electron density.

Acknowledgments

This study was supported by NASA award number NNX08AB17G under the Cassini Data Analysis Program. CHIANTI is a collaborative project involving the NRL (USA), RAL (UK), MSSL (UK), the Universities of Florence (Italy) and Cambridge (UK), and George Mason University (USA). Generous allocations of computing time provided by the OU Supercomputing Center for Education and Research (OSCER) at the University of Oklahoma permitted the high-resolution grid calculation.

Chapter 3

Modeling the plume–plasma interaction

Abstract

We investigate the chemical interaction between Saturn's corotating plasma and Enceladus's volcanic plumes. Using a physical chemistry model from Chapter 2, a parcel of ambient plasma is evolved as it passes through a prescribed H_2O plume. The flow field is assumed to be that of a plasma around an electrically-conducting obstacle centered on Enceladus and aligned with Saturn's magnetic field, consistent with Cassini magnetometer data. We explore the effects on the physical chemistry due to: (1) a small population of hot electrons; (2) a plasma flow decelerated in response to the pickup of fresh ions; (3) the source rate of neutral H_2O. The model confirms that charge exchange dominates the local chemistry and that H_3O^+ dominates the water-group composition downstream of the Enceladus plumes. We find that the amount of fresh pickup ionization depends heavily on the neutral source strength as well as the presence of a persistent population of hot electrons.

3.1 Introduction

Early Cassini encounters with Enceladus revealed surprising evidence of a significant source of water (with trace percentages of other neutrals, including CO_2) from geysers located at the moon's southern pole (*Hansen et al.*, 2006; *Porco et al.*, 2006; *Spencer et al.*, 2006; *Waite et al.*, 2006). The H_2O cloud reacts with Saturn's corotating plasma

torus, loading Saturn's magnetosphere with fresh ions. In this context, the pickup rate $\dot{M}$ quantifies the amount of fresh ions added to the magnetosphere from charge exchange and impact/photoionization. Respective contributions to pickup from charge exchange and impact/photoionization are fundamentally different in that charge exchange does not contribute to ion production because one ion replaces another. Both processes, however, introduce slow-moving ions which must subsequently be accelerated by Saturn's magnetosphere.

Early identification of the interaction between the local water source and Saturn's corotating plasma was made by *Dougherty et al.* (2006b). Based on the Cassini Plasma Spectrometer (CAPS, *Young et al.* (2004)) analysis by *Tokar et al.* (2006), *Pontius and Hill* (2006) modeled the interaction and derived a pickup rate of $\dot{M} \approx 100$ kg s^{-1}. *Khurana et al.* (2007) and *Saur et al.* (2008) (hereafter K07 and S08) discovered a range in $\dot{M}$ (0.2–3 kg s^{-1}) from Cassini magnetometer data in the three earliest Cassini Enceladus flybys (E0, 17 February 2005; E1, 09 March, 2005; E2, 14 July 2005). Constrained by Ion Neutral Mass Spectrometer (INMS, *Waite et al.* (2006)) and Ultraviolet Imaging Spectrograph (UVIS, *Hansen et al.* (2006)) observations, *Burger et al.* (2007) estimated a pickup rate of $\dot{M} \approx 2$–3 kg s^{-1} with a neutral cloud model. The large discrepancy between the pickup rates derived from CAPS and magnetometer data is due not only to the fact that the region considered by *Pontius and Hill* (2006) is much larger than that considered by K07 and S08, but also because the *Pontius and Hill* (2006) result depends on the poorly-constrained value of Saturn's Pederson conductivity.

In this chapter, we use a physical chemistry model to investigate the chemical

interaction between the corotating plasma and the Enceladus plumes. Charge exchange dominates the local chemistry and leads to an H_3O^+-dominated plasma downstream of Enceladus. We find that pickup increases when hot electrons are present—more so with a high neutral source rate.

3.2 Model

We use the physical chemistry model from Chapter 2 (*Delamere and Bagenal*, 2003; *Delamere et al.*, 2007; *Fleshman et al.*, 2010b) to investigate the composition of plasma traveling along prescribed flow lines. The model evaluates mass and energy rate equations for water-group ions ($W^+ \equiv O^+ + OH^+ + H_2O^+ + H_3O^+$), protons, and thermal electrons in a parcel of plasma transiting the simulation. Neutrals are assumed to be cold, and in this study neutral abundances are fixed. The full set of reactions includes charge exchange, photoionization, ionization by electron impact, radiative excitation, recombination, and molecular dissociation following both electron impact and recombination. All species have isotropic Maxwellian speed distributions, and energy is transferred between species via Coulomb collisions. The simulation spans a rectangular domain extending $5\,R_E$ from Enceladus in all directions except south, where the simulation extends to $15\,R_E$ ($R_E = 252$ km is the radius of Enceladus).

A second population of suprathermal (hot) electrons is imposed with a fixed density ($0.3\ cm^{-3}$) and temperature (160 eV). Hot electrons near Enceladus have been reported by *Tokar et al.* (2009) and have been observed throughout the torus by CAPS and the Radio and Plasma Wave Science Instrument (*Moncuquet et al.*, 2005; *Young et al.*, 2005). We showed in Chapter 2 that a small amount of hot electrons is necessary to

obtain the ambient ionization; here we investigate the importance of hot electrons near Enceladus itself.

Neutral source Following S08, the plume is prescribed by

$$n_{\mathrm{H_2O}}(r,\theta) = n_0 \left(\frac{\mathrm{R_E}}{r}\right)^2 \exp\left[-\left(\frac{\theta}{H_\theta}\right)^2 - \left(\frac{r-\mathrm{R_E}}{H_d}\right)\right], \tag{3.1}$$

where $H_\theta = 12^\circ$ and $H_d = 948$ km (4 $\times$ the Hill radius). S08 offset the plume from Enceladus's southern pole by 8° and considered more than one source with the form of Equation 3.1. We consider a single source whose origin coincides with Enceladus's south pole. In the nominal case, n_0 is set to 2.5×10^9 cm^{-3}, corresponding to a neutral source rate of ≈ 200 kg s^{-1} (S08). S08 found a much stronger source for E0, so we also investigate the implications of a source with $n_0 = 2.2 \times 10^{10}$ cm^{-3}, corresponding to a neutral source rate of ≈ 1600 kg s^{-1}.

Plasma flow field Because of the low Alfvén Mach number at Enceladus ($M_\mathrm{A} \approx 0.1$, *Sittler et al.* (2008)), perturbations travel rapidly along the magnetic field so that the source region presents a cylindrical obstacle to the corotating plasma. We adopt the flow field used by *Dols et al.* (2008) to study the plasma interaction with Jupiter's moon Io:

$$\frac{\mathbf{u}}{v_\mathrm{amb}} = \left[1 - \frac{\cos(2\phi)}{(\rho/\mathrm{R_E})^2}\right]\hat{\mathbf{x}} - \frac{\sin(2\phi)}{(\rho/\mathrm{R_E})^2}\hat{\mathbf{y}}, \tag{3.2}$$

where $v_\mathrm{amb} \approx 0.8 \times v_\mathrm{cor}$ ($v_\mathrm{cor} \approx 26$ km s^{-1}) is the ambient plasma speed far from Enceladus (*Wilson et al.*, 2009). The magnetic field defines the z-axis and ϕ is measured from the flow direction.

Along each flow line, parcels of plasma were started $5\,R_E$ upstream of Enceladus with the steady-state composition given in Table 2.1 from Chapter 2. The plasma was moved in the direction of the plasma flow to $5\,R_E$ downstream, and the chemistry was updated after each time step. The pickup energy—determined by the relative speed between neutrals and plasma flow (Equation A.6)—was also updated. Ions far from Enceladus are picked up at v_{amb}, while those near Enceladus are picked up more slowly upstream and downstream, and more rapidly on the flanks.

To investigate the effect of ion pickup, we also slowed the flow near the obstacle. We followed *Dols et al.* (2008) by decreasing the component of the plasma velocity in the flow direction: u_x was replaced by $\gamma(\rho)u_x$, where $\gamma(1\,R_E) = 0.5$, increasing linearly to $\gamma(2\,R_E) = 1$. We find, however, that a stronger slowing factor ($\gamma(1\,R_E) = 0.1$) does not qualitatively change our results. In Section 3.3, we compare the pickup rates both for when the plasma has been slowed (nominal case), and for when it has not.

Two effects are due directly to the slowing of the flow. First, the pickup energy is reduced, affecting the plasma temperature because fresh ions are picked up at the local plasma speed. Second, impact ionization from hot electrons increases which contributes directly to the pickup process, as well as indirectly, by seeding multiple charge exchanges.

We neglect gyromotion on the basis of scale. For example, an H_3O^+ ion picked up at v_{amb} has a gyroradius of only $0.1\,R_E$. Also, we ignore the velocity dependence of charge exchange, despite the fact that ions oscillate between zero and twice their pickup speed in the reference from of Enceladus. The effects of both gyromotion and enery-dependent charge exchange are addressed in Chapter 4.

Hot electrons We estimate that hot electrons cool rapidly near the dense plume via impact ionization, and thus impose a discontinuity at $\rho = 3\,\mathrm{R_E}$:

$$n_{\mathrm{eh}}/(\mathrm{cm}^{-3}) = \begin{cases} 0 & 1 < \rho/\mathrm{R_E} < 3 \\ 0.3 & 3 < \rho/\mathrm{R_E}. \end{cases} \tag{3.3}$$

However, *Dols et al.* (2008) showed that field-aligned electron beams (perhaps associated with the Io auroral footprint) are necessary for modeling the high plasma density in Io's wake. At Enceladus, hot electrons may also be related to weak UV auroral spots recently observed by UVIS (W. Pryor, personal comm.). To investigate the implication of hot electrons at Enceladus, we consider the additional case where n_{eh} is held at 0.3 cm^{-3} throughout the simulation domain. The pickup rates for each case are compared in Section 3.3.

Pickup rate calculation Fresh ions are added to the magnetosphere by both charge exchange ($\dot{\rho}_{\mathrm{exch}}$) and impact/photoionization ($\dot{\rho}_{\mathrm{ioz}}$):

$$\dot{\rho}_{\mathrm{ioz}} = \sum_j n_{\mathrm{e}} n_j m_j \kappa_j^{\mathrm{imp}} + \sum_k n_k m_k \kappa_k^{\mathrm{phot}} \tag{3.4}$$

$$\dot{\rho}_{\mathrm{exch}} = \sum_j n_j^{(1)} n_j^{(2)} m_j \kappa_j^{\mathrm{exch}}. \tag{3.5}$$

The reaction rates (Appendix A) are represented by κ^{imp}, κ^{exch} [cm ^{3} s^{-1}], and κ^{phot} [s^{-1}]; the ion masses by m; and $n^{(1)}$, $n^{(2)}$ are the charge-exchanging neutral and ion densities. Summations are carried out over processes involving the creation of fresh ions.

We calculated the time-averages of Equation 3.4 and Equation 3.5 to find the average pickup rates for plasma parcels migrating along each flow line and multiplied by the flow line volume to find the pickup rate for each flow line. The total pickup rate for each process was then determined by summing the contribution from all flow lines throughout the simulation.

3.3 Results

We consider the x–y plane 7.5 R_E south of the center of Enceladus. For this, the nominal case, hot electrons exist throughout the domain, the neutral source rate is ≈ 200 kg s^{-1}, and the plasma is slowed in the flow direction (Section 3.2). The pickup energy, heavy-to-light ion abundance ratio (W^+/H^+), H_3O^+/W^+, and H_3O^+ temperature ($T_{H_3O^+}$) in this plane are shown in Figure 3.1. The obstacle is plotted in black and 18 flow lines are over-plotted and labeled accordingly. Composition and temperatures along the overplotted dashed line are shown in Figure 3.2, where the corresponding flow lines are indicated. The H_3O^+ ion is the most abundant ion in the wake because charge exchanges lead to H_3O^+ in the presence of an abundant water source. All charge exchanges with H_2O in our model ultimately lead to either H_3O^+ or H_2O^+ by $H_2O^+ + H_2O \rightarrow H_2O + H_2O^+$ and $H_2O^+ + H_2O \rightarrow OH + H_3O^+$. The former reaction supports H_2O^+ density to a degree, but the H_2O^+ products also feed into the latter, ultimately producing H_3O^+. The W^+/H^+ ratio increases rapidly because protons are removed by $H^+ + H_2O \rightarrow H + H_2O^+$. The anti-correlation between protons and H_3O^+ ions was discussed in Chapter 2 and will be addressed once again in Chapter 5. The increase in electron density is due mainly to impact ionization of the plume by hot

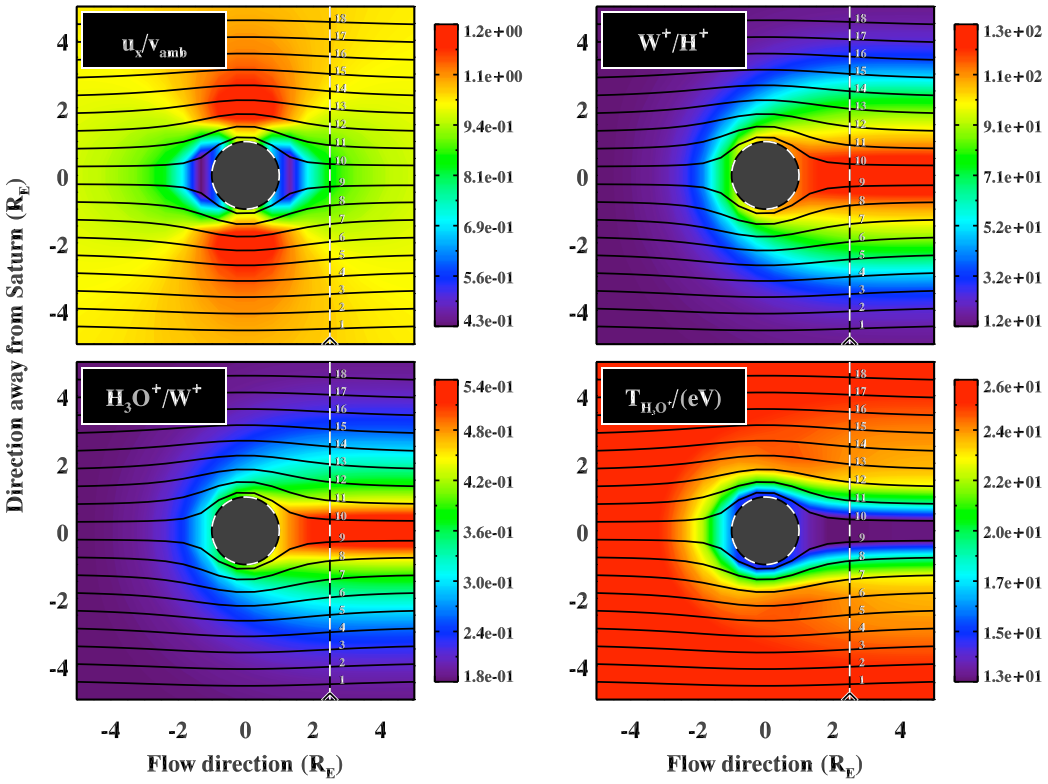


Figure 3.1 *Upper-left*: the x component of the assumed local plasma flow speed (Section 3.2) normalized to the ambient flow speed (80% of rigid corotation). *Upper-right*: water-group to proton abundance ratio. *Lower-left*: H_3O^+/W^+ abundance ratio. *Lower-right*: H_3O^+ temperature. The plane represented here is 7.5 R_E south of Enceladus. Model output along the dashed line is given in Figure 3.2.

electrons.

In Figure 3.2, the electron temperature has been normalized to the ambient electron temperature (2 eV), and the ion temperatures have been normalized to their respective ambient pickup energies (1.5 and 29 eV). Protons and H_3O^+ bear the signature of the cooler pickup temperature from where they were created by charge exchange. A similar decrease in ion temperature through Enceladus's wake has recently been observed by *Tokar et al.* (2009). The electron temperature has also been cooled by a factor of 2.

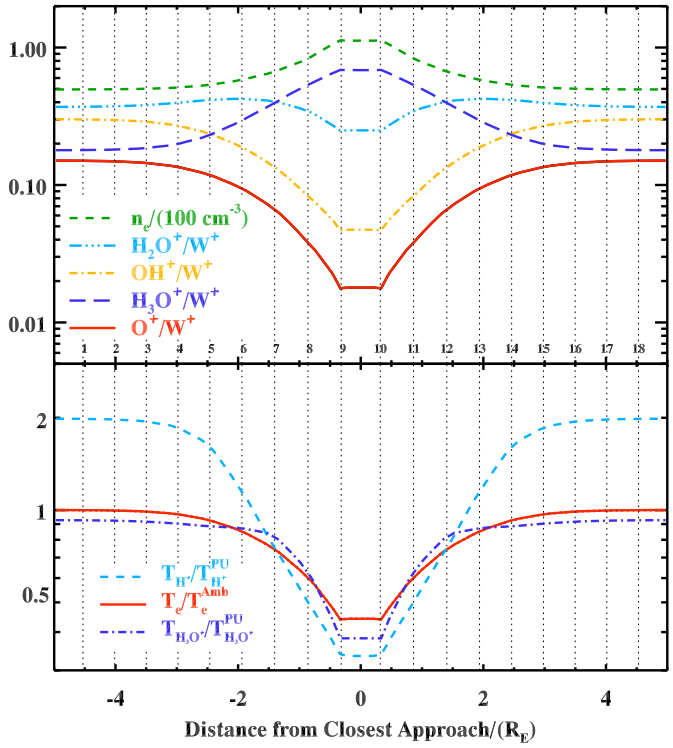


Figure 3.2 *Top*: Abundances and electron density from the simulation along the dashed line in Figure 3.1. *Bottom*: Electron, proton and H_3O^+ temperatures along the same cut. The electron temperature is normalized to its ambient temperature (2 eV), and the ion temperatures are normalized to their ambient pickup energies—1.5 and 29 eV for H^+ and H_3O^+ respectively.

Pickup rate We calculated individually (Section 3.2) the mass of fresh ions picked up via charge exchange, $\dot{M}_{\rm exch}$, and $\dot{M}_{\rm ioz}$—the ratio of which illustrates the importance of charge exchange over impact ionization. Models were run for the eight cases shown in Table 3.1. The flow-field, hot-electron, and source-rate treatments are described in Section 3.2. We discuss the cases corresponding to a 'weak' 200 kg s^{-1} source (Cases 1a–4a) and a 'strong' 1600 kg s^{-1} source (Cases 1b–4b) separately.

Weak source (Cases 1a–4a): When hot electrons exist locally (1a,2a), the total mass pickup rate is roughly 0.3 kg s^{-1} with a 40% increase when the plasma is slowed. Because of the longer occupation time associated with the slowed flow, hot electrons

Case		$\dot{M}_{\rm exch}$ kg s^{-1}	$\dot{M}_{\rm exch}$ (10^{25} H_2O s^{-1})	$\dot{M}_{\rm ioz}$ kg s^{-1}	$\dot{M}_{\rm ioz}$ (10^{25} H_2O s^{-1})	$\dot{M}_{\rm exch}/\dot{M}_{\rm ioz}$
(1a)	**Hot electrons + slowed flow**	**0.25**	**(0.84)**	**0.038**	**(0.13)**	**6.7**
(2a)	Hot electrons + un-slowed flow	0.22	(0.74)	0.034	(0.11)	6.6
(3a)	No hot electrons + slowed flow	0.18	(0.61)	0.0091	(0.030)	20
(4a)	No hot electrons + un-slowed flow	0.17	(0.58)	0.0087	(0.029)	20
(1b)	Hot electrons + slowed flow	2.2	(7.3)	0.33	(1.1)	7.0
(2b)	Hot electrons + un-slowed flow	1.9	(6.5)	0.30	(0.99)	6.6
(3b)	No hot electrons + slowed flow	0.77	(2.6)	0.079	(0.26)	9.8
(4b)	No hot electrons + un-slowed flow	0.77	(2.6)	0.076	(0.25)	10

Table 3.1 Pickup rates from charge exchange ($\dot{M}_{\rm exch}$) and impact/photoionization ($\dot{M}_{\rm ioz}$) for the eight cases discussed in the text. Only $\dot{M}_{\rm ioz}$ increases the plasma density ($n_{\rm e}$). The cases labeled with 'a' correspond to a neutral source rate of 200 kg s^{-1}; those labeled with 'b' correspond to a neutral source rate of 1600 kg s^{-1}. Case (1a), in bold, is the nominal case from which Figure 3.1 and Figure 3.2 have been generated.

increase seed ionization ($\dot{M}_{\rm ioz}$), which in turn increase charge exchange ($\dot{M}_{\rm exch}$). When hot electrons are removed (3a,4a), $\dot{M}_{\rm ioz}$ decreases by a factor of 4, but $\dot{M}_{\rm exch}$ drops by $\approx 30\%$, implying that much of the pickup is occurring outside the cut-off point at $3\,\mathrm{R_E}$. Slowing the plasma has less effect in 3a than in 1a because longer occupation does not boost seed ionization without hot electrons.

Strong source (Cases 1b–4b): The effect of the hot electrons becomes apparent with the strong source because a denser portion of the plume is intersected by the flow lines. The effect of slowing the plasma is similar to that in the weak-source case. The total mass pickup rate, however, is increased by a factor of 3 when comparing the cases with hot electrons (1b,2b) to cases without (3b,4b). The almost linear response of the total pickup to $\dot{M}_{\rm ioz}$ (compare 1b,2b to 3b,4b) suggests that, unlike in the weak source case, most of the pickup is occurring inside the hot electron cutoff at $3\,\mathrm{R_E}$.

K07 and S08 were in rough agreement on the total pickup rate. For E1 and E2, they found $\approx$ 0.2–0.6 kg $\mathrm{s^{-1}}$, and for E0 they found $\approx$ 3 kg $\mathrm{s^{-1}}$. Because our model relies on a physical chemistry calculation alone, it is remarkable to have obtained the same pickup rates using neutral plume distributions consistent with those used in S08 (E0: strong source, E1 and E2: weak source).

Charge exchange dominates the chemistry by at least a factor of 6 in all cases. Because of this, the water-group ion abundance ratios (shown only for the nominal case) are qualitatively unaffected. In particular, $\mathrm{H_3O^+/W^+}$ always increases while $\mathrm{O^+/W^+}$, $\mathrm{OH^+/W^+}$, and $\mathrm{H_2O^+/W^+}$ always decrease in Enceladus's wake. The dominance of $\mathrm{H_3O^+}$ has been observed elsewhere by CAPS during Cassini's orbital insertion period (*Tokar et al.*, 2006; *Sittler et al.*, 2008). Though few *new* ions are produced at Ence-

ladus, the process that produces H_3O^+ may have an important effect on the large-scale torus composition. The effects of dense H_2O on Saturn's corotating plasma demonstrated here shed light on the "missing H_3O^+" problem discussed in Chapter 2, a topic picked up once again in Chapter 5.

3.4 Discussion and conclusions

To investigate the impact of hot electrons on ion chemistry, we have chosen the simplest flow field possible with minimal perturbation by Enceladus. This flow is roughly consistent with the compact source derived from magnetometer data (K07) but is much less perturbed than the flow reported by *Tokar et al.* (2006). Similarly, we have started with a single symmetric plume oriented due-south. In future studies, one could explore multiple jets (S08), displaced sources (K07), and a minor spherically-symmetric global component (*Burger et al.*, 2007).

Our findings are summarized below:

1. Charge exchange dominates the plume–plasma chemistry, confirming previous work by *Burger et al.* (2007) and consistent with estimates by *Johnson et al.* (2006).

2. Charge exchange leads largely to an H_3O^+-dominated wake, consistent with INMS (*Cravens et al.*, 2009). Reactions leading to H_3O^+ are alse well known in the comet community (*Aikin*, 1974; *Haberli et al.*, 1997).

3. Comparing our mass pickup rates to those derived from the Cassini magnetometer (K07 and S08), INMS, and UVIS (*Burger et al.*, 2007), we find that a persistent

source of hot electrons are likely to exist near Enceladus. If present, beams of hot electrons at Enceladus may be related to the weak UV auroral spots recently observed by Wayne Pryor (personal communication).

Acknowledgements

This work was supported under NESSF grant Planet09F–0036 and CDAP grant 06-CASS06-0062.

Chapter 4

The roles of charge exchange and dissociation in spreading Saturn's neutral clouds

Abstract

Neutrals sourced directly from Enceladus's plumes are initially confined to a dense neutral torus in Enceladus's orbit around Saturn. This neutral torus is redistributed by charge exchange, impact/photodissociation, and neutral–neutral collisions to produce Saturn's neutral clouds. Here we consider the former processes in greater detail than in previous studies. In the case of dissociation, models have assumed that OH is produced with a single speed of 1 km s^{-1}, whereas laboratory measurements suggest a range of speeds between 1 and 1.6 km s^{-1}. We show that the high-speed case increases dissociation's range of influence from 9 to 15 R_S. For charge exchange, we present a new modeling approach, where the ions are followed within a neutral background, whereas neutral cloud models are conventionally constructed from the neutrals' point of view. This approach allows us to comment on the significance of the ions' gyrophase at the moment charge exchange occurs. Accounting for gyrophase: (1) has no consequence on the H_2O cloud; (2) doubles the local density of OH at the orbit of Enceladus; and (3) decreases the oxygen densities at Enceladus's orbit by less than 10%. Finally, we consider velocity-dependent and species-dependent cross sections and find that the oxygen cloud produced from charge exchange is spread out more than H_2O, whereas the OH cloud is the most confined.

4.1 Introduction

The Enceladus plumes directly produce a dense H_2O torus centered on Enceladus's orbit, within which charge exchange and dissociation subsequently produce neutrals that either feed Saturn's extended neutral clouds, collide (absorb) with Saturn and its rings, or leave the system altogether on escape orbits. This chapter is a report on the results of a sensitivity study of low-velocity charge exchange and dissociation within the neutral torus.

Several decades before Cassini arrived at Saturn and the Enceladus water plumes were discovered (*Hansen et al.*, 2006), neutral hydrogen was observed in Saturn's magnetosphere, both from Earth (*Weiser et al.*, 1977) and from Voyagers 1 and 2 (*Shemansky and Hall*, 1992). Hydroxyl was later discovered by *Shemansky et al.* (1993a) with HST, and more recently, *Esposito et al.* (2005) detected atomic oxygen. These observations collectively hinted at the presence of a source of water, and models predicted its location to be somewhere near the orbit of Enceladus (c.f., *Jurac et al.* (2002)).

After identifying the Enceladus plumes as the dominant source of the water-group neutrals (O, OH, H_2O)—and indeed the co-rotating plasma itself via electron impact and photoionization (*Young et al.*, 2005; *Sittler et al.*, 2005, 2008)—researchers have been attempting to understand how neutrals are transported from Enceladus to 20 Saturn radii ($R_S = 6 \times 10^9$ cm) and beyond, as observed by *Shemansky et al.* (1993a), *Esposito et al.* (2005), and most recently by *Melin et al.* (2009). Early on, *Jurac et al.* (2002) discussed the importance of charge exchange in this inflation process. *Johnson et al.* (2006) later showed that if magnetospheric plasma is slowed sufficiently with

respect to neutrals in the Enceladus torus, then charge exchange produces a sufficient number of particles with velocities capable of spreading the dense H_2O Enceladus torus into neutral the cloud observed by *Shemansky et al.* (1993a).

Farmer (2009) pointed out the importance of dipole–dipole interactions in collisions involving H_2O molecules. She showed that collisions inside the dense Enceladus torus (parameterized by a macroscopic viscosity) are alone sufficient for the creation of the extended component of Saturn's neutral cloud. *Cassidy and Johnson* (2010) later argued that Farmer's fluid treatment is inappropriate for neutral–neutral collisions in the Enceladus torus, where the mean free path is on the order of the torus size itself. Instead, *Cassidy and Johnson* (2010) approached the problem with a direct simulation Monte Carlo (DSMC) model. Their model self-consistently included losses due to charge exchange, dissociation, and ionization, whereas *Farmer* (2009) accounted for losses to charge exchange and ionization by evolving the neutral cloud for the time scales (months to a few years) found in *Sittler et al.* (2008). Both studies agree, however, that neutral–neutral collisions are necessary for the inflation of Saturn's neutral cloud.

Collisions between neutrals occur at a rate proportional to the square of the neutral density. Thus, where neutral densities peak near the orbit of Enceladus, neutral–neutral collisions occur more often than either charge exchange or dissociation, whereas near 6 R_S, neutral densities drop and all three processes become comparable (see Figure 3, *Cassidy and Johnson* (2010)). Models involving neutral collisions have recently been validated with Herschel observations by *Hartogh et al.* (2011), who attribute a warm and broadened Enceladus torus to heating via neutral–neutral collisions; the effect of these interactions should therefore be included in any attempt to fully model Saturn's

neutral clouds. Nevertheless, several first-order conclusions can be drawn by revisiting charge exchange and dissociation.

Previous neutral cloud models approach charge exchange from the neutrals' point of view, whereas we follow the ion along its trajectory, thus allowing us to identify the gyrophase at which an ion undergoes charge exchange. We find that including the phase dependence doubles OH densities at the orbit of Enceladus, decreases oxygen density by $\lesssim 10\%$, and has no effect on H_2O (Section 4.3.1). Also, the velocity-dependence of charge exchange varies by species. Previous studies (*e.g.*, *Johnson et al.* (2006); *Cassidy and Johnson* (2010)) have considered velocity-dependence, but have used a single cross section to represent all charge exchanges. We show in Section 4.3.1 that symmetric reactions such as $H_2O + H_2O^+ \rightarrow H_2O^+ + H_2O^*$ (the asterisk identifies a neutral released with the speed of the reacting ion) tend to distribute neutrals closer to Saturn, while asymmetric exchanges such as $H_2O + O^+ \rightarrow H_2O^+ + O^*$ populate a more extended cloud, with less absorption on Saturn.

With regard to dissociation, OH produced by impact/photodissociation of H_2O has previously been modeled with an initial speed of 1 km s^{-1} (*Jurac and Richardson*, 2005; *Cassidy and Johnson*, 2010), whereas recent laboratory measurements span 1 to 1.6 km s^{-1}, depending on the molecule's internal energy (*Wu and Chen*, 1993; *Makarov et al.*, 2004). We model this parameter space and find that, relative to charge exchange, most OH found inside 9 R_S is produced by dissociation when OH is dissociated from H_2O at 1 km s^{-1}, with that location extended to 15 R_S when OH is dissociated from H_2O at 1.6 km s^{-1} instead.

This chapter is organized as follows. The model for the production of neutrals via

dissociation and three illustrative charge exchanges is explained in Section 4.2. Our results are found in Section 4.3, followed by a discussion in Section 4.4. The important points are summarized in Section 4.5.

4.2 Model

We begin with a few words on nomenclature. The neutral torus in this chapter pertains to the primary neutral torus (not plasma torus) supplied directly by Enceladus's plumes. The neutral clouds refer to the secondary neutrals produced from charge exchange and dissociation in the neutral torus.

The production of Saturn's neutral cloud is modeled in two steps. We first construct a dense H_2O torus from a plume positioned at Enceladus's south pole with specifications based on several Cassini Enceladus flybys (*Smith et al.* (2010); see also *Smith et al.* (2004), *Smith* (2006), and *Smith et al.* (2007)). Secondary neutrals are then produced from the primary neutral torus by charge exchange and dissociation, some of which remain gravitationally bound to Saturn and form the neutral clouds. On the basis that they spend most of the time outside the neutral torus and plasma sheet, we assume their lifetimes to be determined solely by photo-processes, though in Section 4.3.3, we also consider the effects of charge exchange and electron impact.

4.2.1 Neutral torus model

The neutral torus and Enceladus plume models are described in the following subsections.

Enceladus H_2O torus

Our aim is to study the effects of several important reactions occurring in Enceladus's orbit. The primary neutral torus, fed directly by Enceladus, is produced in the model by evolving water molecules released from Enceladus into a dense neutral torus centered on Enceladus's orbit ($3.95\,\mathrm{R_S}$). The assumption is that all H_2O is initially produced by a single plume at Enceladus's south pole. In reality, more than one plume has been observed (*Porco et al.*, 2006), and researchers such as *Saur et al.* (2008) and *Smith et al.* (2010) have studied their signature on flyby observations. For our purposes, the detailed influence of multiple plumes can be neglected. The plume particles' radial speed distribution is prescribed as a one-dimensional Maxwellian with temperature $T = 180\,\mathrm{K}$ (*Spencer et al.*, 2006; *Hansen et al.*, 2006):

$$f(v) = \left(\frac{m_{\mathrm{H_2O}}}{2\pi kT}\right)^{1/2} \exp\left[-\frac{m_{\mathrm{H_2O}}}{2kT}(v - v_{\mathrm{bulk}})^2\right], \tag{4.1}$$

where v_{bulk} is the bulk speed, equal to $720\,\mathrm{m\,s^{-1}}$, $1.8\times$ the thermal speed estimated by *Smith et al.* (2010) ($v_{\mathrm{therm}} = \sqrt{2kT/m_{\mathrm{H_2O}}} = 400\,\mathrm{m\ s^{-1}}$). Additionally, a raised cosine distribution is used to determine from where the molecules are released:

$$g(\theta) = \begin{cases} \frac{1}{\theta_0}\left[1 + \cos\left(\frac{\theta}{\theta_0}\pi\right)\right] & \text{if } \theta < \theta_0 = 30^\circ \\ 0 & \text{otherwise.} \end{cases} \tag{4.2}$$

Co-latitude theta is measured from Enceladus's south pole, and $\theta_0 = 30^\circ$ is the plume half-width, based on INMS in situ observations (*Smith et al.*, 2010). We assume no azimuthal dependence.

Enceladus's gravity is ignored since the escape velocity, $v_{\rm esc} = 240$ m s^{-1}, is greatly exceeded for most molecules (99%), where $v_{\rm bulk} > v_{\rm therm} > v_{\rm esc}$; indeed, our results differ by less than one percent whether Enceladus's gravity is considered or not. Particles released from Enceladus are thus assumed to revolve around Saturn on Keplerian orbits. Each water molecule is allowed to orbit inside the torus for a period determined by the collective effects of photodissociation, electron-impact dissociation, and charge exchange. To be clear, the molecules forming the neutral torus are subject to all of the losses stated, while the neutral cloud is subject to photo-processes only (Section 4.2.2). Further reaction details are important for modeling plasma characteristics but only the timescales given below are required to model the neutral torus.

Photodissociation The photodissociation lifetime for H_2O, $\tau_{\rm phot} = 9.1 \times 10^6$ s, comes directly from *Huebner and Carpenter* (1979b), scaled to Saturn's distance from the Sun, noting that at peak solar activity, neutral abundances attributed to dissociation double (*Jackman and Arridge*, 2011).

Impact dissociation In the case of impact dissociation, suprathermal (hot) electrons dominate (Chapter 2). Assuming the conditions near Enceladus's orbit apply throughout the neutral torus, we estimate the hot electron density and temperature to be 160 eV and 0.3 cm^{-3} from Chapter 2, which fall within a range of observations (cf., *Young et al.* (2005), *Sittler et al.* (2008)). The rate coefficient for impact dissocation of water is found by convolving $\sigma(v)v$ with a 160 eV Maxwellian distribution to find $\kappa_{\rm imp} = 1.5 \times 10^{-6}$ cm^3 s^{-1} (Table A.9). Above 100 eV, $\kappa_{\rm imp}$ is insensitive to temperature, making this estimate valid for a range of observations. Assuming the hot electron

density, $n_{\rm eh}$, is constant over the neutral torus, the lifetime against impact dissociation is $\tau_{\rm imp} \approx [\kappa_{\rm imp} n_{\rm eh}]^{-1} = 2.2 \times 10^6$ s. Dissociation via thermal electrons—whose temperature and density are 2 eV and 60 cm^{-3}—is also expected, but such collisions occur 5× less often, and are thus ignored here (Table A.9).

Charge exchange The following three reactions are included in this study:

$$H_2O + H_2O^+ \rightarrow H_2O^+ + H_2O^* \tag{4.3a}$$

$$H_2O + H_2O^+ \rightarrow H_3O^+ + OH^* \tag{4.3b}$$

$$H_2O + O^+ \rightarrow H_2O^+ + O^*. \tag{4.3c}$$

Other charge exchanges are important in the neutral torus, some of which involve ions reacting with secondary neutrals such as H, O, and OH. To model their effect properly, one would calculate these neutral densities as in a conventional time-dependent neutral cloud model. We estimate that including all such reactions would increase our estimates on neutral cloud densities by approximately a factor of two. The primary purpose of choosing this combination of reactions is to study three classes of charge exchanges, for which the collision frequency decreases with, increases with, or is independent of the relative speed of the reacting pair (Reaction 4.3b, Reaction 4.3c, and Reaction 4.3a, respectively). We return to this point in Section 4.2.2.

An estimate of the charge exchange lifetime can be made by adding the rate coefficients for Reaction 4.3a, Reaction 4.3b, and Reaction 4.3c. Multiplying by the observed H_2O^+ and O^+ densities near the orbit of Enceladus (6 and 12 cm^{-3}, *Sittler et al.*

(2008)), we find $\tau_{\rm chex} = [\kappa_{\rm exch}^{\rm H_2O^+} n_{\rm H_2O^+} + \kappa_{\rm exch}^{\rm O^+} n_{\rm O^+}]^{-1} = [6.0 + 2.8]^{-1} \times 10^8$ s $= 1.1 \times 10^7$ s. The reaction rates are from *Lishawa et al.* (1990) and *Albritton* (1978) for $\kappa_{\rm exch}^{\rm H_2O^+}$ and $\kappa_{\rm exch}^{\rm O^+}$, respectively. The lifetime of H_2O against the sum of these processes is then

$$\tau_{\rm torus} = \left[\frac{1}{\tau_{\rm phot}} + \frac{1}{\tau_{\rm imp}} + \frac{1}{\tau_{\rm chex}}\right]^{-1} = (1.1 + 4.5 + 0.91)^{-1} \times 10^7 \text{ s}$$
$$= 1.6 \times 10^6 \text{ s} \approx 20 \text{ days.} \quad (4.4)$$

These estimates can be compared to Figure 3 of *Cassidy and Johnson* (2010). For example, our lifetime against dissociation is 1.7 $\times 10^6$ s, while they use 7×10^6 s near 4 R_S. The discrepancy comes mostly from the impact dissociation timescale. Cassidy's dissociation rate was calculated using *Schippers et al.* (2008), wherein CAPS-ELS hot electron densities were fitted and extapolated down from 5.5 R_S, while our own estimate hinges on a hot electron density derived from our chemistry model in Chapter 2. For charge exchange, we have a lifetime of 1.1 $\times 10^7$ s, and *Cassidy and Johnson* (2010) have a comparable 8×10^6 s.

Particles were created and tracked in each of our model runs, and the results were scaled to the number of water molecules in the real neutral torus. The total number is estimated from an assumed neutral source rate from Enceladus of $\dot{M} = 200$ kg s^{-1} (*Jurac and Richardson*, 2005; *Hansen et al.*, 2006, 2011) and lifetime, $\tau_{\rm torus}$ (Equation 4.4):

$$N_{\rm torus} = \dot{M} \tau_{\rm torus} / m_{\rm H_2O} \approx 1.1 \times 10^{34} \text{ } H_2O \text{ molecules.} \quad (4.5)$$

We bin and azimuthally average the results to find a 2-D density function, $n_{\rm torus}(r, \theta)$

(radius and latitude), through which to introduce ions for charge exchange. This function also determines from where dissociated neutrals are produced.

Plume model

Before describing dissociation and charge exchange within the torus, we address a calculation with the purpose of comparing the neutral production near Enceladus with that from the entire torus. In doing so, we prescribe a plume whose density is consistent with Equation 4.1 and Equation 4.2. In this case, the ambient neutral density can be ignored compared to the neutrals leaving the surface of Enceladus directly.

The densities are determined everywhere by imposing integrated flux ($\int n(r,\theta)v(r,\theta)dA$) and energy ($mv^2/2 - mM_{\rm E}G/r$) conservation at a given distance r. The picture can be simplified, however, since most neutrals have at least twice the escape velocity from Enceladus. The speeds are thus independent of r in the immediate vicinity of Enceladus. By equating the integrated flux at the surface of Enceladus to the same integral at another distance $r > {\rm R_E}$, we find a familiar $1/r^2$ dependence:[a]

$$n_{\rm plume}(r,\theta) = n(\theta)\left(\frac{\rm R_E}{r}\right)^2 \exp\left[-\left(\frac{r-{\rm R_E}}{H_r}\right)\right]. \tag{4.6}$$

The trailing exponential factor is imposed ad hoc to keep the total plume content finite, and reflects Saturn's influence as the molecules leave Enceladus. Consistent with *Saur et al.* (2008), H_r is set at 4 times the Hill radius of 948 km. The angular dependence is

[a]See also Equation 3.1 where we used a similar function to model mass-loading at Enceladus.

consistent with our velocity distribution in the previous section (Equation 4.1),

$$n(\theta) = \begin{cases} \frac{n_0}{2}\left[1 + \cos\left(\frac{\theta}{\theta_0}\pi\right)\right] & \text{if } \theta < \theta_0 = 30^\circ \\ 0 & \text{otherwise,} \end{cases} \tag{4.7}$$

which is normalized such that $n(0) = n_0$, where the plume strength n_0 is found to be 5.9×10^8 cm^{-3} by integrating $n(\theta)v_{\text{bulk}}$ over the area spanning the south pole of Enceladus from $\theta = 0^\circ$ to $\theta = \theta_0 = 30^\circ$, and setting that result equal to the plume production rate of $\dot{M}/m_{\text{H}_2\text{O}} = (200 \text{ kg s}^{-1})/m_{\text{H}_2\text{O}} = 6.7 \times 10^{27}$ molecules per second.

In Section 4.3, we compare the results of charge exchange with the plume (n_{plume}) to that with the entire torus (n_{torus}).

4.2.2 Neutral cloud model

Production of Saturn's neutral clouds entails following the neutrals produced by dissociation and charge exchange occurring within the neutral torus. The treatment of each of these processes are described below.

Dissociation

The hydroxyl radical, OH, produced largely by dissociated H_2O, has previously been modeled with a single speed of 1 km s^{-1} (*i.e.*, *Jurac and Richardson* (2005), *Cassidy and Johnson* (2010)). Dissociated OH has been measured in the lab, however, with speeds between 1 and 1.6 km s^{-1} (*Wu and Chen*, 1993; *Makarov et al.*, 2004). Here we bound this range by modeling the OH neutral clouds produced from an azimuthally-symmetric source (with respect to Saturn) with velocities drawn from Maxwellian distributions

with temperatures $T = \frac{1}{2} m_{\rm OH} v_{\rm mp}^2$, where the most probable speed, $v_{\rm mp}$, is set to 1 and 1.6 km s^{-1}, representing the low- and high-speed limits.

The initial locations of the ejected OH are determined by the spatial distribution of neutrals in the Enceladus torus ($n_{\rm torus}(r, \theta)$, Section 4.2.1), and the directions of their release are chosen randomly and isotropically. The molecules orbit Saturn until they are photodissociated and removed from the system.

By assuming a volume over which dissociations occur, the number of modeled OH molecules can be scaled to a realistic value. We take the volume to be a torus centered on Enceladus (3.95 R_S), with a minor radius of 1 R_S:

$$V \approx 2\pi (4\,R_S)(2\,R_S)^2 = 2 \times 10^{31}\,{\rm cm}^3. \tag{4.8}$$

For impact dissociation, we then expect a contribution of

$$N_{\rm cloud}^{\rm imp} = k_{\rm imp} \tau_{\rm phot}^{\rm OH} V = 2.8 \times 10^{34}\ {\rm OH\ molecules}, \tag{4.9}$$

where $k_{\rm imp} = 7.9 \times 10^{-5}$ cm^{-3} s^{-1} is the rate (per volume) of impact dissociations occurring between suprathermal electrons and H_2O molecules in the torus (*Fleshman et al.*, 2010b) and $\tau_{\rm phot}^{\rm OH} = 1.8 \times 10^7$ s is the photodissociation lifetime of OH at Saturn (*Huebner and Carpenter*, 1979b). The number of OH molecules produced by photodissociation in the torus is similarly given by

$$N_{\rm cloud}^{\rm phot} = k_{\rm phot} \tau_{\rm phot}^{\rm OH} V = 7.6 \times 10^{33}\ {\rm OH\ molecules}, \tag{4.10}$$

where $k_{\text{phot}} = 2.1 \times 10^{-5}$ cm^{-3} s^{-1} is the rate (per volume) of H_2O photodissociations occurring in the Enceladus torus (*Fleshman et al.* (2010b), Table S9). The total abundance attributed to dissociation is then given by the sum of Equation 4.9 and Equation 4.10. *Cassidy and Johnson* (2010) constrained their study with HST observations (*Melin et al.*, 2009) and found a similar OH content (see comparison in Figure 4.10c). That neutral production by photo- and impact dissociation are comparable in magnitude is itself noteworthy. This condition is not shared by systems with hotter and denser plasma. For example, electron impact dissociation and ionization dominate over photon-driven processes in Jupiter's Io torus, where the plasma is warmer due to pickup energies that are four times higher than at Enceladus (see Chapter 2 and *Delamere et al.* (2007)). We also note that unlike with Io, long neutral lifetimes in the Enceladus neutral torus inhibit the response of Saturn's neutral clouds to short-term plume variability, though variability on the order of months has been studied by *Smith et al.* (2010).

Charge exchange

We now describe the model for producing and following neutrals from charge exchange. *Cassidy and Johnson* (2010) and *Jurac and Richardson* (2005) also considered velocity-dependent charge exchange, but unlike these previous studies, we capture the gyrophase at which the reactions occur by following ions along their trajectories (Section 4.3.1). We also prescribe cross sections specific to each reaction, being particularly interested in the effects of low-velocity charge exchange.

At very high speeds, the cross sections go to zero for all charge exchanges (*Johnson*,

1990). At low relative velocities, however (few km s^{-1}), the details of the collision are determined by the nature of the reacting species. If the reactants and products are identical, apart from an electron (*i.e.*, $H_2O + H_2O^+ \rightarrow H_2O^+ + H_2O^*$), the reaction is termed resonant, or symmetric, and the cross sections grow as the inverse of the relative speed. If the reactants differ, as with $H_2O + O^+ \rightarrow H_2O^+ + O^*$, the cross sections are likely to vanish at low speeds (*Rapp and Francis*, 1962)—the difference being that the energy of the electron configurations is unchanged for symmetric-type charge exchanges (*Johnson*, 1990). Neutrals produced from resonant charge exchange therefore tend to have lower velocities than do neutrals produced from non-resonant (asymmetric) charge exchange. This is a key point central to much of our discussion in Section 4.3.

Individual ions are followed as they traverse the neutral torus (Section 4.2.1). This approach allows their gyrophase to be determined the instant that charge exchanges occur (see Figure 4.1). The implicit assumption is that the collision is elastic, and that the neutral product has an initial velocity given by the ion velocity just before the exchange takes place.

The ions are introduced into the model from two Maxwellian speed distributions,

$$f_\perp(v_\perp) = \frac{m_{\rm ion}}{kT_\perp} v_\perp \exp\left[-\frac{m_{\rm ion} v_\perp^2}{2kT_\perp}\right] \text{ (speeds perpendicular to } B) \tag{4.11}$$

$$f_\parallel(v_\parallel) = \sqrt{\frac{m_{\rm ion}}{2\pi kT_\parallel}} \exp\left[-\frac{m_{\rm ion} v_\parallel^2}{2kT_\parallel}\right] \text{ (speeds parallel to } B) \tag{4.12}$$

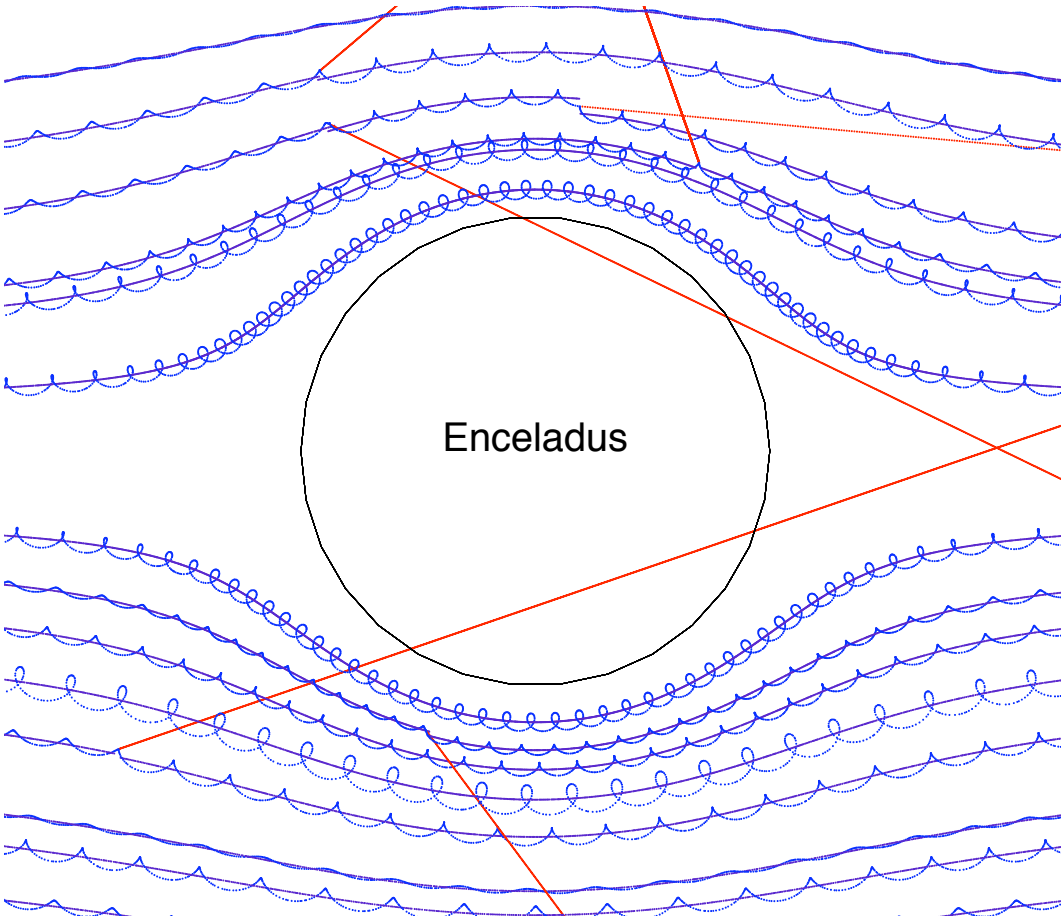


Figure 4.1 Sketch of gyrating ions in the neutral frame with guiding centers moving along a prescribed flow field, shown here near Enceladus for scale. Warm ions ($v_\perp > v_{\text{flow}}$) move on trajectories that coil around themselves and do not reach zero relative velocity with respect to the neutrals at any point. Cool ions ($v_\perp < v_{\text{flow}}$) essentially trace their guiding centers with 'snake-like' trajectories, and also do not obtain zero relative velocity. Fresh pickup ions ($v_\perp \approx v_{\text{flow}}$) do, however, obtain near zero relative velocity at the cusps of their cycloidal trajectories. Neutrals produced by charge exchange (whose trajectories are indicated by the red lines) tend to be created with velocities at which the respective reaction rates peak (Figure 4.2).

with a temperature anisotropy of

$$\frac{kT_\perp}{kT_\parallel} = \frac{27\,\mathrm{eV}}{5.4\,\mathrm{eV}} = 5 \tag{4.13}$$

for both O^+ and H_2O^+ (*Sittler et al.*, 2008). The perpendicular temperature is derived from the pickup ion velocity at the orbit of Enceladus, determined from CAPS data by *Wilson et al.* (2009) [$kT_\perp = \frac{1}{2} m_{W^+}(v_\phi - v_{\mathrm{Kep}})^2$]. The ions also rotate around a guiding center (field line) moving at $v_\phi = 18$ km s^{-1} in a frame rotating with the neutrals.

For the component of our study aimed at estimating local neutral production (Section 4.2.1), ions passing near Enceladus are diverted (treating Enceladus as a rigid cylinder) and are slowed to 10% of the ambient flow speed to account for the effects of mass-loading (see Chapter 3).

Time steps are taken at less than 1% of an ion's gyroperiod:

$$\Delta t = R \times T_{\mathrm{gyro}} = R \times \frac{2\pi m}{qB}, \tag{4.14}$$

where R is a random number between 0 and 0.01, T_{gyro} is the ion's gyroperiod (3.6 s for H_2O^+), $B = 325$ nT, and q and m are the charge and mass, respectively, of the reacting ion. Such resolution is necessary in order to capture the significance of the energy dependence at low relative speeds. After each time step, the collision frequency ν is calculated from

$$\nu(r, \theta, v_{\mathrm{rel}}) = n(r, \theta)\sigma(v_{\mathrm{rel}})v_{\mathrm{rel}}, \tag{4.15}$$

where $n(r, \theta)$ is the local H_2O density (Section 4.2.1), v_{rel} is the relative velocity between

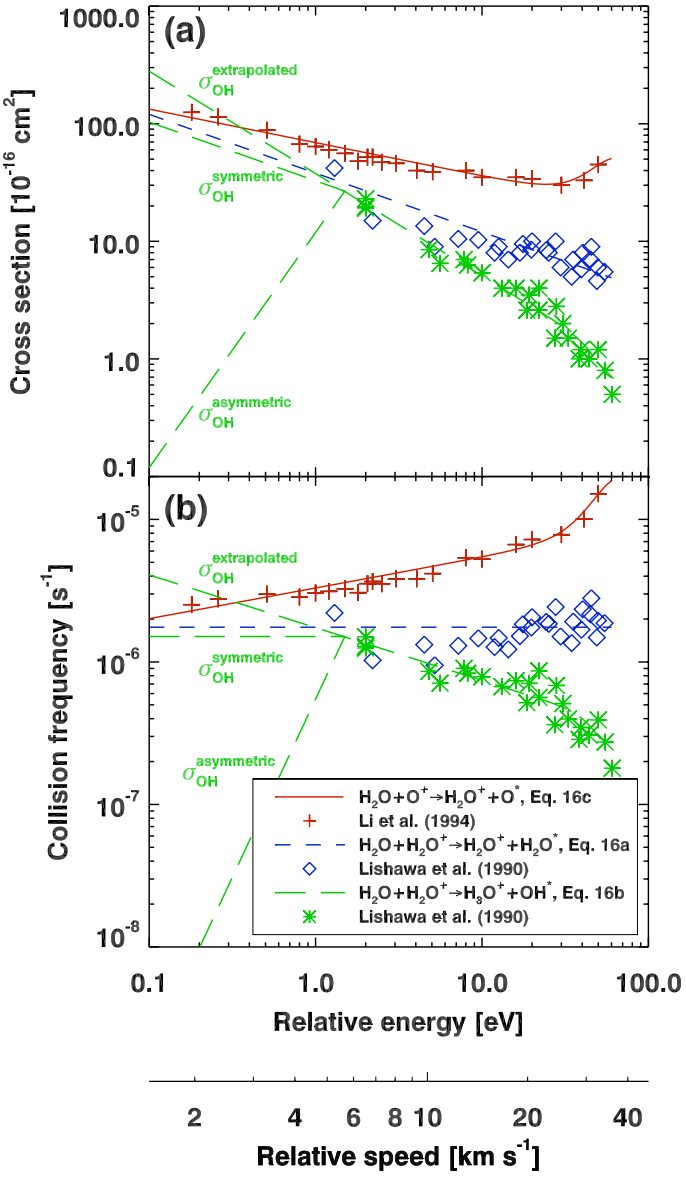


Figure 4.2 (a.) Cross sections for the reactions listed in the legend. Data for Reaction 4.3a and Reaction 4.3b are from *Lishawa et al.* (1990), and data for reaction Reaction 4.3c is from *Li et al.* (1995). $\sigma_{\mathrm{OH}}^{\mathrm{extrapolated}}$, $\sigma_{\mathrm{OH}}^{\mathrm{symmetric}}$, and $\sigma_{\mathrm{OH}}^{\mathrm{asymmetric}}$ are hypothetical fits applying to the OH*-producing reaction, and are explored in Figure 4.4. Ions oscillate between ≈ 0 and 36 km s^{-1}in the Enceladus torus. (b.) Collision frequency, $n\sigma(v)v$, for a given density of $n_{\mathrm{H_2O}} = 10^3$ cm^{-3} plotted over the same energy range. The collision frequency increases with energy in the oxygen-forming reaction, while the water-forming reaction is independent of energy and the OH-forming reaction declines with energy.

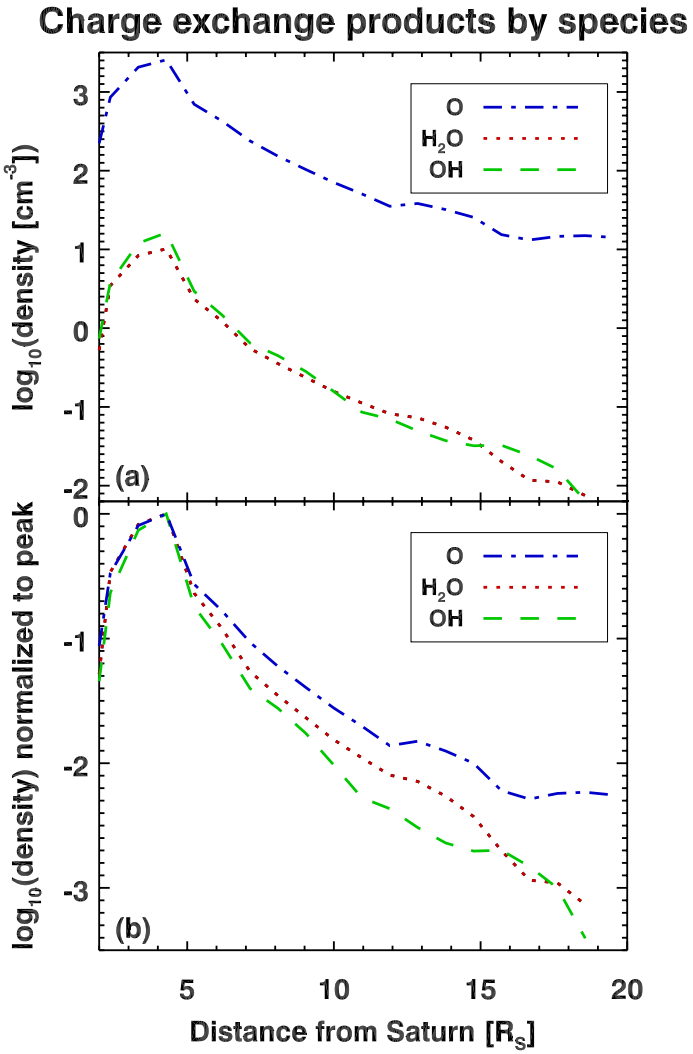


Figure 4.3 Neutral clouds produced by the reactions shown in Figure 4.2. (a.) Oxygen is the most abundant because the cross section is 10× higher than than with O and OH. The lifetime of oxygen against photoionization is also much longer than the lifetime for either OH or H_2O against photodissociation. (b.) Same as above, but normalized to peak. Oxygen shows the most spreading because reactants are produced with higher velocities (Figure 4.2b), which expands the cloud. The same trend holds with H_2O and OH, where OH tends to be created with the lowest velocities (Figure 4.2, $\sigma_{\rm OH}^{\rm extrapolated}$).

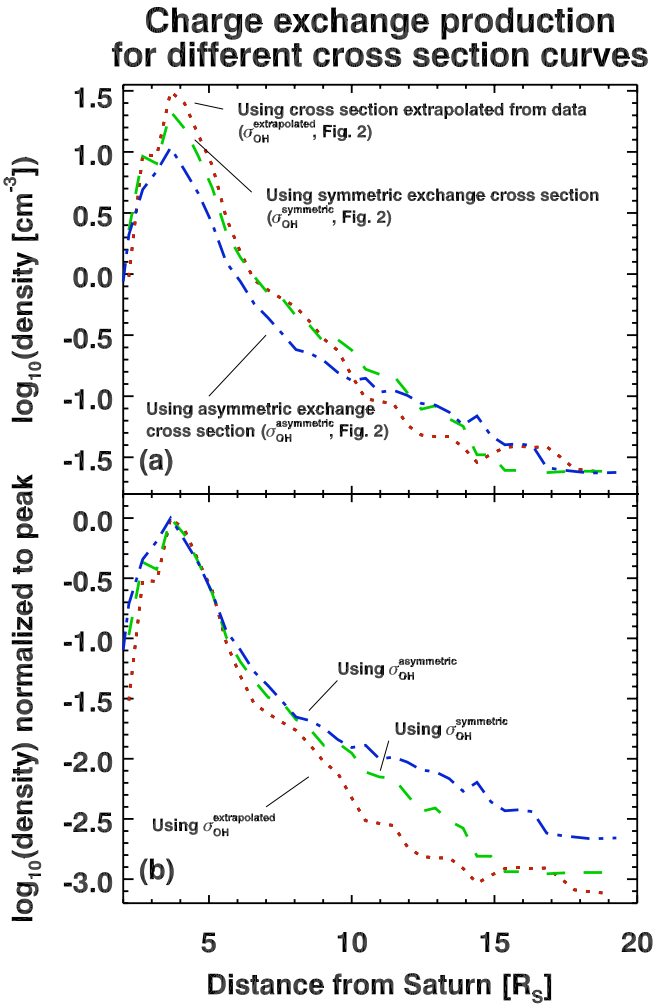


Figure 4.4 Neutral OH clouds produced from three hypothetical charge exchange cross sections: $\sigma_{\mathrm{OH}}^{\mathrm{extrapolated}}$, $\sigma_{\mathrm{OH}}^{\mathrm{symmetric}}$, and $\sigma_{\mathrm{OH}}^{\mathrm{asymmetric}}$ (Figure 4.2). (a.) $\sigma_{\mathrm{OH}}^{\mathrm{extrapolated}}$ produces the highest density ($\sigma_{\mathrm{OH}}^{\mathrm{asymmetric}}$, the lowest) at Enceladus because of the creation of additional low-velocity particles. (b.) Same as above, but normalized to peak. The differences in density in the tail is not an indication of spreading, but rather further illustrates the deficiency in the peak density, going from $\sigma_{\mathrm{OH}}^{\mathrm{extrapolated}}$ to $\sigma_{\mathrm{OH}}^{\mathrm{asymmetric}}$.

the reacting ion and neutral, and $\sigma(v_{\rm rel})$ is the velocity-dependent cross section. Poisson statistics are used to test the likelihood of one or more reactions having occurred within Δt. If $\exp(-\nu\Delta t)$ is less than a second random number between 0 and 1, then a reaction occurs. The possibility of multiple reactions occurring over Δt is taken into account, but usually neglectable (Appendix B).

As with OH produced by dissociation, neutrals produced by charge exchange are followed under the influence of Saturn's gravity until they are photodissociated or photoionized. Their initial location and velocity are taken to be that of the reacting ion, pre-transfer.

The model runs are centered on the orbit of Enceladus spanning 10 $\rm R_E$ in the direction of corotation ($\rm R_E$ = 250 km = radius of Enceladus) and $\pm$ 120 $\rm R_E$ (0.5 $\rm R_S$) in both the radial and z directions to adequately sample the H_2O torus (Section 4.2.1). Ions are introduced into the model on the upstream boundary, and their guiding centers flow downstream at a speed $v_{\rm plasma}$ = 18 km $\rm s^{-1}$ relative to the neutrals. Their starting location in (r, z) is chosen randomly.

Scaling The neutral clouds formed via charge exchange are done so in our model by following a relatively small number of ions, and must thus be scaled to facilitate comparison with observations and other models. The number of neutrals in our modeled clouds have been scaled by accounting for the following. First, the number of representative ions used to produce the neutral clouds via charge exchange falls short of, and must be scaled to, the number of ions present in the actual plasma torus, $n_{\rm ion}V$. The volume of the plasma torus, V, is given in Equation 4.8, and n = 12 and 6

cm^{-3} for O^+ and H_2O^+, respectively (*Sittler et al.*, 2008). Second, we have argued that photo-processes are more likely to occur than either charge exchange or electron-impact processes throughout the neutral clouds with the exception of very near the neutral torus. In keeping with this assumption, the plasma torus thus feeds the extended neutral clouds *via* charge exchange for a photodissociation (photoionization in the case of oxygen) time scale before equilibrium of the neutral cloud is achieved: $\tau_{\rm phot} = 14$, 0.6, 0.3 years for O, OH, and H_2O, respectively (Table A.7). Our model runs followed 10^5 ions for 100 seconds, and the resulting neutral clouds were scaled as described.

4.3 Results

In the following sections, we present and discuss the neutral clouds resulting from dissociation and charge exchange in our model.

4.3.1 Charge exchange

In the neutrals' reference frame, ions oscillate between ≈ 0 km s^{-1} and twice the local pickup speed ($v_\phi \approx 18$ km s^{-1}) due to gyro-motion. A cartoon of this can be seen in Figure 4.1, where $v_{\rm rel} \approx 0$ at the cusp of the ion trajectory and reaches a maximum of $v_{\rm rel} \approx 2v_\phi$ along the flow direction. Shown are several trajectories for which $v_\perp$ is either less than, greater than, or approximately equal to the bulk flow velocity. The neutrals formed via charge exchange follow the trajectories indicated in red.

The velocity dependence of Reaction 4.3a, Reaction 4.3b, and Reaction 4.3c are determined by the details of the reacting species (*Johnson*, 1990). Essentially, symmetric charge exchanges have cross sections that increase monotonically with decreasing ve-

locity, whereas cross sections for asymmetric exchange peak and then vanish at low relative speeds. The implication is that symmetric exchanges produce lower velocity neutrals and a more compact neutral cloud than do asymmetric charge exchanges.

With symmetric charge exchange, the cross sections go as ${v_{\rm rel}}^{-1}$, so that the collision frequency ($n\sigma v$) is independent of v, as with Reaction 4.3a, whereas asymmetric exchanges are defined by cross sections (and collision frequencies) which tend rapidly toward zero at low relative velocities ($\sim {v_{\rm rel}}^4$, *Rapp and Francis* (1962)).

The cross sections (10^{-16} cm^2) used in this chapter to study reactions Reaction 4.3a, Reaction 4.3b, and Reaction 4.3c plotted in Figure 4.2a are given by

$$\text{Reaction 4.3a} : \mathrm{H_2O} + \mathrm{H_2O^+} \rightarrow \mathrm{H_2O^+} + \mathrm{H_2O^*}$$

$$\sigma_{\mathrm{H_2O}} = 38 E_{\rm rel}^{-0.5} \tag{4.16a}$$

$$\text{Reaction 4.3b} : \mathrm{H_2O} + \mathrm{H_2O^+} \rightarrow \mathrm{H_3O^+} + \mathrm{OH^*}$$

$$\sigma_{\mathrm{OH}} = 38 E_{\rm rel}^{-0.88} - 0.39 \exp\left[-\frac{1}{2}\left(\frac{E_{\rm rel} - 57}{12}\right)^2\right] \tag{4.16b}$$

$$\text{Reaction 4.3c} : \mathrm{H_2O} + \mathrm{O^+} \rightarrow \mathrm{H_2O^+} + \mathrm{O^*}$$

$$\sigma_{\mathrm{O}} = 69 E_{\rm rel}^{-0.29} + 30 \exp\left[-\frac{1}{2}\left(\frac{E_{\rm rel} - 65}{18}\right)^2\right]. \tag{4.16c}$$

The Gaussian terms in Equation 4.16b and Equation 4.16c account for downward and upward trends in the associated data sets near 30 km s^{-1}, but have little consequence on the neutral cloud, given that most bound particles are produced at lower velocities.

Symmetric exchanges occur between like species by definition, although unlike species also exhibit symmetric behavior on occasion. Therefore, we explore several

hypothetical behaviors for the OH*-producing Reaction 4.3b at low energies. This test is separate from, but related to, the comparison between reactions Reaction 4.3a, Reaction 4.3b, and Reaction 4.3c themselves, and it motivates the point that both high and low energy behaviors have an important effect on the neutral cloud. With $\sigma_{\mathrm{OH}}^{\mathrm{extrapolated}}$, we have extropolated the best-fit curve (Equation 4.16b) to the lowest energies. Symmetric and asymmetric behaviors are explored with $\sigma_{\mathrm{OH}}^{\mathrm{symmetric}}$ and $\sigma_{\mathrm{OH}}^{\mathrm{asymmetric}}$ (*Rapp and Francis*, 1962; *Johnson*, 1990). $\sigma_{\mathrm{OH}}^{\mathrm{symmetric}}$ is the same as $\sigma_{\mathrm{OH}}^{\mathrm{extrapolated}}$ except that below 1.5 eV, $\sigma_{\mathrm{OH}}^{\mathrm{symmetric}} = 30E_{\mathrm{rel}}^{-0.5} \times 10^{-16}$ cm^2. Notice that a similar energy dependence also applies to Equation 4.16a, consistent with the behavior expected for symmetric charge exchange. $\sigma_{\mathrm{OH}}^{\mathrm{asymmetric}}$ is the same as $\sigma_{\mathrm{OH}}^{\mathrm{extrapolated}}$ except that below 1.5 eV, $\sigma_{\mathrm{OH}}^{\mathrm{asymmetric}} = 11E_{\mathrm{rel}}^{2} \times 10^{-16}$ cm^2. Although it could be argued that $\sigma_{\mathrm{OH}}^{\mathrm{symmetric}}$ better fits the data if the two measurements at 2 eV are ignored, our results for Reaction 4.3b were obtained with $\sigma_{\mathrm{OH}}^{\mathrm{extrapolated}}$ unless noted otherwise. We will discuss the implications of choosing $\sigma_{\mathrm{OH}}^{\mathrm{extrapolated}}$ over $\sigma_{\mathrm{OH}}^{\mathrm{symmetric}}$ and $\sigma_{\mathrm{OH}}^{\mathrm{asymmetric}}$ shortly.

The collision frequencies ($n\sigma v$) are plotted in Figure 4.2b for a given neutral density—in this case for $n_{\mathrm{H_2O}} = 10^3$ cm^{-3}. The collision frequency for oxygen increases with relative speed, while it is constant for water, and peaks at low velocities for OH. The significance is that the oxygen cloud tends to be more extended than either the OH or H_2O clouds. The average collision frequency is also much higher for oxygen ($\times 10$) than for either OH or H_2O, resulting in greater oxygen abundance.

The equatorial neutral cloud densities resulting from reactions Reaction 4.3a, Reaction 4.3b, and Reaction 4.3c are plotted in Figure 4.3. Only neutrals produced from charge exchange are shown; neither the Enceladus neutral torus, nor the neutrals pro-

duced via dissociation have been included. Oxygen is two orders of magnitude more abundant than either OH or H_2O because of the higher rate of production, but also because oxygen has a longer lifetime against photoionization than either OH or H_2O have against photodissociation. Unlike *Cassidy and Johnson* (2010), dissociated neutrals from the latter processes are not tracked in our model. Beyond the scope of the present study, this additional heating source would serve to further inflate the oxygen and OH clouds. Figure 4.3b is the same as Figure 4.3a, except that the profiles are normalized to the peak density at the orbit of Enceladus. The oxygen cloud is seen to be the most extended, followed by water, and finally by OH, with an order of magnitude separating the three species at $20\,R_S$.

The effects of low-velocity charge exchange can be seen in Figure 4.4. In Figure 4.4a, we see that the peak density (as well as the total neutral cloud content) is the highest with $\sigma_{OH}^{extrapolated}$ because more low-velocity neutrals are produced than with either $\sigma_{OH}^{symmetric}$ or $\sigma_{OH}^{asymmetric}$. Conversely, fewer low-velocity neutrals are available to populate the region near Enceladus's orbit with $\sigma_{OH}^{asymmetric}$ when compared to either $\sigma_{OH}^{extrapolated}$ or $\sigma_{OH}^{symmetric}$. Stated another way, $\sigma_{OH}^{extrapolated}$ yields a neutral cloud profile with the steepest slope, and $\sigma_{OH}^{asymmetric}$, the shallowest. Figure 4.4b is identical to Figure 4.4a, apart from normalization. In this case, the slope of the density profile should not be confused with the effect of inflating (spreading) the OH cloud. It should be viewed, rather, as the enhancement or depletion of low velocity neutrals to fill the region inside of $\approx 10\ R_S$. In other words, neutrals beyond $10\ R_S$ are mostly formed in charge exchanges at high velocities, for which all σ_{OH} converge to the same curve (Figure 4.2).

We have assumed to this point that the plasma is sub-corotating in Enceladus's orbit (18 km s^{-1}, *Wilson et al.* (2009)). One might expect, however, that the neutral clould would be affected in a measurable way if instead, the plasma corotates at 26 km s^{-1}. The H_2O cloud would be least affected, given that the collision frequency of Reaction 4.3a is independent of speed (Figure 4.2b), but what about reactions such as Reaction 4.3b and Reaction 4.3c, whose collision frequencies are velocity-dependent? Increasing the plasma speed amounts to shifting the spread of ion velocities in Figure 4.2 to the right, which would on average increase the speed of the neutral products. This is indeed the case, and in such a test where we increased the plasma speed from 18 to 26 km s^{-1}, the oxygen cloud increased in abundance and became even more extended. The OH cloud also expanded somewhat, but decreased in total abundance. Unfortunately, the differences were less than 10% in both the slope of the distribution and in total oxygen abundance, suggesting that neutral cloud observations are in this way unlikely to predict plasma speeds in the torus.

Neutral cloud sources: plume vs. neutral torus

We described in section Section 4.2.1 the production in our model of the neutral H_2O torus from the Enceladus plumes. The plumes themselves have also been prescribed as a separate background density (n_{plume}, Section 4.2.1) so that we can compare charge exchange occurring throughout the neutral torus to that occurring only within the Enceladus plumes.

The results are shown in Figure 4.5, where we have plotted the oxygen clouds produced from charge exchange within both the Enceladus plumes (local) and the

entire neutral torus (global). The results are for Reaction 4.3c, but the same test with Reaction 4.3a and Reaction 4.3b produces similar results. Immediately noticable is that the local production is $\approx 0.1\%$ of the overall neutral production. The torus's dominance of neutral production can be explained as follows. First, the volume of the torus where reactions are occurring can be estimated as $2\pi(4\mathrm{R_S})(0.2\mathrm{R_S})^2$, where $0.1\mathrm{R_S}$ is roughly the torus's scale height. The volume of the plume can be estimated from Equation 4.6, where the dimensions are on the order of a cylinder with width $2\mathrm{R_E}$ and height $H_r \approx 16\mathrm{R_E}$. Dividing these volumes gives roughly $250(\mathrm{R_E}/\mathrm{R_S})^3 \approx 10^{-5}$. Further, the collision frequencies are proportional to the neutral density, which in the plume are on the order of 10^7 cm^{-3}, whereas typical torus densities are 10^5 cm^{-3}, making collisions in the plume $100\times$ more frequent per volume than in the torus. All told, the ratio of the volumes (10^{-5}) combined with the ratio of densities (10^2) explain the local-to-global neutral production ratio of 10^{-3} shown in Figure 4.5a. A similar pattern has been shown to exist at Jupiter by *Bagenal* (1997) and *Dols et al.* (2008), where the majority of plasma is produced throughout the neutral torus, rather than near the interaction at Io itself.

The slopes of the neutral cloud profiles from the plume and torus are most easily compared in Figure 4.5b, in which the density profiles have been normalized at 4 $\mathrm{R_S}$. The local source produces a more confined neutral cloud because the ions from which they originate have been slowed near the plume to account for the effect of mass-loading (see Chapter 3). Nevertheless, such a signature would be difficult to untangle in the data since global exceeds local production so overwhelmingly.

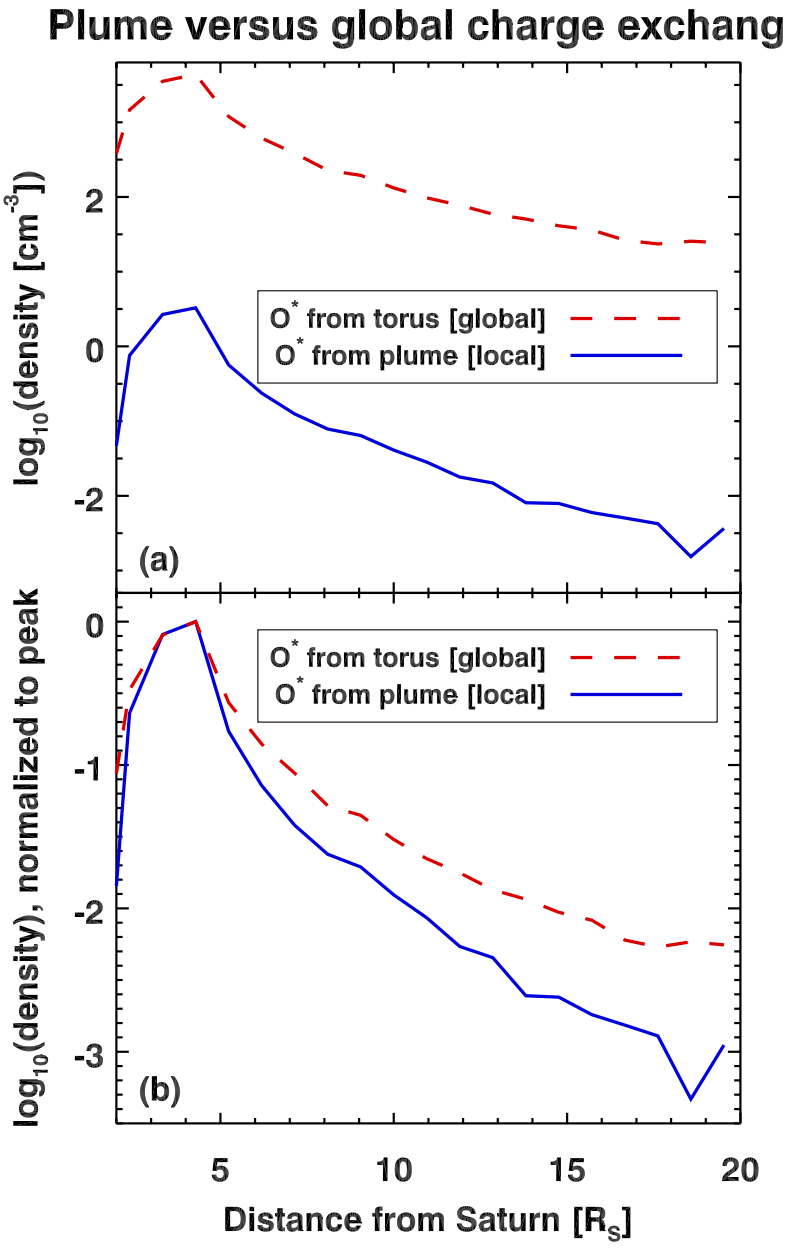


Figure 4.5 (a) Comparison between charge exchanged neutrals produced near the Enceladus plume and those produced from the neutral torus as a whole—in this case for oxygen. (b.) Though shown here for oxygen, all charge exchange reactions near the plume result in a cloud with less spreading than their global counterpart due to the imposed slowing of the plasma (and hence, the release of slower neutral products) near the plume in response to mass-loading (Chapter 3).

4.3.2 Dissociation

A major component of the OH cloud is produced by dissociation within the neutral torus, whereby the initial velocities of the OH products range from 1 to 1.6 km s^{-1} (*Wu and Chen*, 1993; *Makarov et al.*, 2004). In Figure 4.6, the clouds resulting from the high- and low-speed cases are plotted along with the result from velocity-dependent charge exchange in Section 4.3.1. First note that dissociation contributes 100× more OH than does charge exchange at the orbit of Enceladus (4 R_S); the total cloud mass is almost 100× greater as well. Second, dissociation dominates over charge exchange from the Enceladus torus out to 9 and 15 R_S in the low- and high-speed cases, respectively. The OH cloud content will only be marginally affected by variable solar activity (*Jackman and Arridge*, 2011), given that impact dissociation contributes 4× more neutrals than does photodissociation, by virtue of the respective reaction rates (Section 4.2.2). In both cases, few neutrals are absorbed by the rings, and even less by Saturn itself. The same is not true of charge exchange, where ≈ 50% of the neutrals are absorbed by Saturn (Section 4.3.3).

Figure 4.7c is a two-dimensional version of Figure 4.6, where the dissociation results have been averaged and added to the results from charge exchange. Saturn is at the left, and Enceladus's orbit is located on the equator at 4 R_S. In addition to being confined radially, the dissociated neutrals are also bound tightly to the equator, while neutrals from charge exchange tenuously fill the magnetosphere.

Figure 4.7a shows the hydrogen cloud that accompanies the dissociated OH clouds ($H_2O + e, \gamma \rightarrow OH^* + H^*$). To conserve momentum, the hydrogen atoms have 17× the speed of the dissociated OH molecules, and thus range between 17 and 27 km s^{-1},

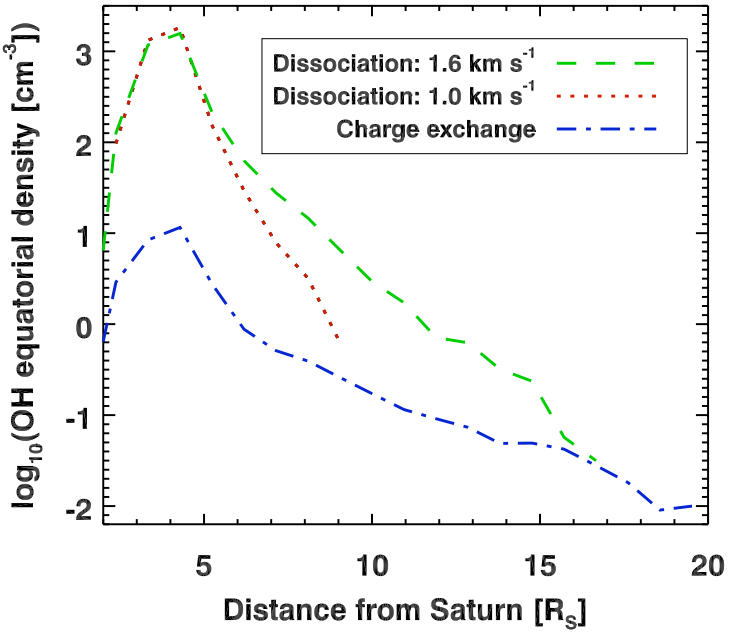


Figure 4.6 OH clouds produced from charge exchange and high- and low-speed dissociation. Dissociation dominates neutral cloud production inside 9–15 R_S, at which point charge exchange becomes the dominant contributor.

with a relatively large, diffuse neutral cloud. Shown is the result for the low-speed case, which produces more bound particles and thus a more substantial neutral cloud. Charge exchange from reactions such as $H_2O + H^+ \rightarrow H_2O^+ + H^*$ are also responsible for H-cloud production, and deserve attention in future studies.

4.3.3 Fates of neutral atoms and molecules

In our model, neutrals created by dissociation and charge exchange are eventually either absorbed by Saturn, escape the system, or orbit until they are destroyed (ionized) by photons. In Figure 4.8a the fates for each species are given by percentage. In the case of hydrogen, the results are from the dissociation model, described above in Section 4.3.2.

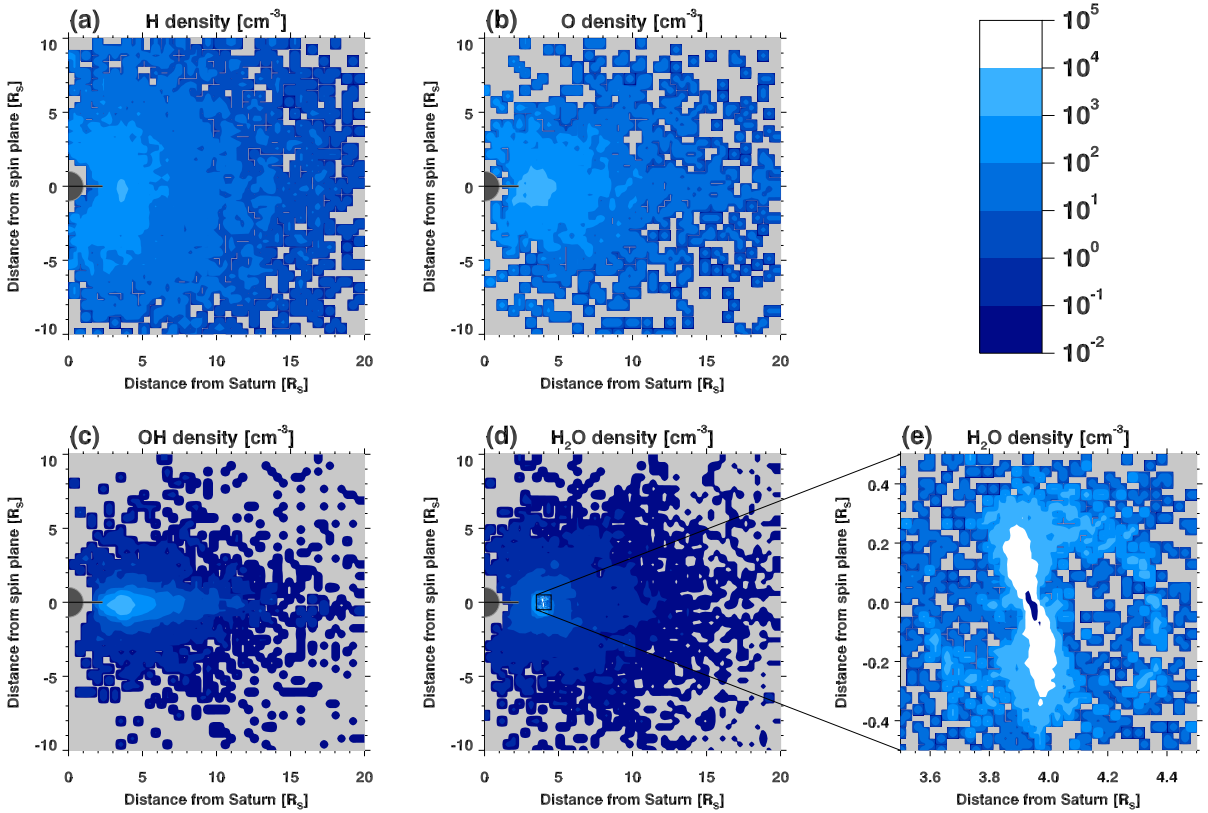


Figure 4.7 Neutral cloud densities in the r–z plane. (a.) Hydrogen produced purely from H_2O dissociation. (b.) Oxygen produced purely from charge exchange (Reaction 4.3c). (c.) Hydroxyl produced from the combination of charge exchange and dissociation. Dissociation dominates inward of 9–15 R_S along the equator, while charge exchange (Reaction 4.3b) tenuously fills the magnetosphere elsewhere. (d.) Water produced entirely by charge exchange (Reaction 4.3a). (e.) Dense torus fed directly by the Enceladus plumes (Section 4.2.1).

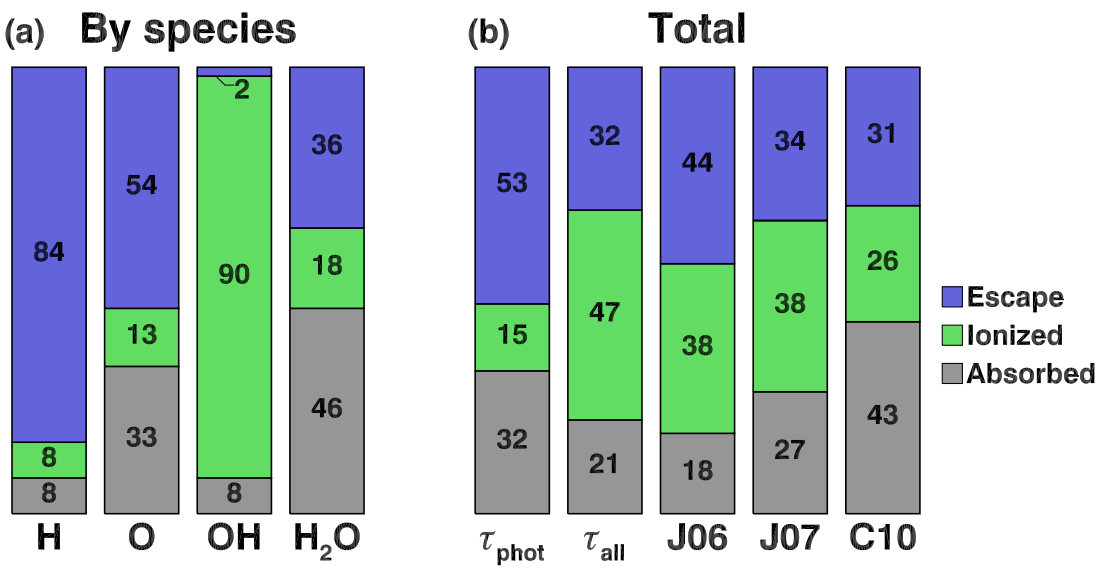


Figure 4.8 The fates of neutrals in the model along with the results from other models. (a.) Dissociation produces low-velocity neutrals and OH is thus not likely to escape or to be absorbed. Conversely, dissociation also produces hydrogen which largely leaves the system. (b.) The results of J06 (*Johnson et al.*, 2006), J07 (*Jurac and Richardson*, 2007), and C10 (*Cassidy and Johnson*, 2010), along with our own weighted totals (excluding hydrogen; see Section 4.3.3). In the case of $\tau_{\rm phot}$, the lifetime of the cloud is determined by photoionization/dissociation only, whereas with $\tau_{\rm all}$, we limit the lifetimes by also including electron impact and charge exchange. These limiting cases bound the previous studies, except that C10 has more absorption attributed to neutral–neutral collisions.

The enormous amount of escape (84%) is due to the high velocities (≈ 17 km s^{-1}) with which hydrogen is created following H_2O dissociation, and the 8% absorption is largely comprised of hydrogen which would otherwise escape the system.

Oxygen is produced purely from charge exchange in the model (Reaction 4.3c). About one-half escapes, one-third is absorbed, and the remaining 13% contributes to the neutral cloud before being photoionized. Water is also produced purely by charge exchange (Reaction 4.3a) with 18% contributing to the neutral cloud. Percentage-wise, more water is absorbed than oxygen because oxygen is produced with higher speeds

and generally larger orbits (Section 4.3.1).

The fate of OH is dominated by dissociation: 96% feed the neutral cloud (ultimately ionized), 4% are absorbed, and virtually none escape. The reason for the large percentage of bound and unabsorbed neutrals is that dissociated OH has a velocity spread of 1 to 1.6 km s^{-1} in the neutral frame, compared to the escape speed of ≈ 5 km s^{-1} in the same frame. Looking only at OH produced by charge exchange (minor compared to dissociation), 57% are absorbed, 23% supply the neutral cloud, and 20% escape. Compared to H_2O, an even greater percentage of charge-exchanged OH is absorbed because the cross sections favor production of low-velocity OH molecules (Figure 4.2b).

The production of oxygen via dissociation of H_2O has been ignored in this chapter on the grounds that, unlike OH, oxygen is largely produced by charge exchange. The cross section for oxygen-producing charge exchange is an order of magnitude higher than that for the OH-producing reaction near the plasma flow speed of $v_{\rm plasma} = 18$ km s^{-1} (Figure 4.2a), while the photodissociation rates are an order of magnitude smaller (*Huebner and Carpenter*, 1979b). We estimate that including oxygen produced from dissociation would increase the total oxygen cloud content by less than 20%.

Charge exchange and dissociation play a large role in creating Saturn's neutral clouds from the plume-fed neutral torus. The reactions we have included have been chosen to demonstrate the effects of low velocity charge exchange and dissociation, but they are also among the most important. The neutral cloud densities presented in this chapter are expected to undershoot the results from models which include the additional reactions found in Table 2.3 by no more than a factor of two. With this

caveat in mind, we now compare the present results with several other recent models.

Comparison with other models

Figure 4.8b: J06 is the work of *Johnson et al.* (2006), where they also investigated the neutral clouds created from low-velocity charge exchange in the stagnated flows in Enceladus's orbit. Figure 4.8b: J07 is from *Jurac and Richardson* (2007), where the authors were primarily interested in the interaction between the neutral cloud and Saturn's rings. The most recent model comes from *Cassidy and Johnson* (2010) (C10), where they investigated the spreading of the neutral cloud from neutral–neutral collisions.

To compare with these studies, we first had to weight our H, O, OH, and H_2O clouds. We did this for two limiting cases. In the first case ($\tau_{\rm phot}$, Figure 4.8b), we assume, as we have thus far, that the neutral clouds evolve until destroyed by either photoionization or photodissociation: H, O, OH, H_2O = 40, 14, 0.6, 0.3 years, respectively. These lifetimes yield an upper limit since charge exchange and electron impact are not included as losses. In the second case ($\tau_{\rm all}$) , we derived a lower limit to the lifetimes from Table 2.2 by summing the additional losses due to charge exchange and electron impact, finding: H, O, OH, H_2O = 0.4, 0.4, 0.2, 0.03 years, respectively. Notice in particular the drastically different times scales for H and O, where including the additional sinks reduce the size of the H cloud by a factor of $40/0.4 = 100$, and the oxygen cloud by $14/0.4 = 35$. This case represents an extreme limit, given that the neutrals spend almost all of their time orbiting outside of the Enceladus torus, where compared to photo-processes, the chances of charge exchange and electron impact are

relatively unlikely.

The individual clouds (excluding hydrogen) were weighted by the stated time scales and totaled in Figure 4.8b. When only losses to photodissociation/ionization are considered ($\tau_{\rm phot}$), the neutral cloud is dominated by oxygen, whose fate thus determines that of the neutral cloud. When charge exchange and electron impact are also included ($\tau_{\rm all}$), dissociated OH contributes significantly, driving the neutral cloud (ionized) percentage up, and the escape percentage down. We note that the neutral fates presented in *Bagenal and Delamere* (2011) (escape = 44%, ionized = 17%, absorbed = 39%) were based on an earlier version of the model which only included H_2O.

The particles that are neither absorbed nor lost by escape make up the neutral clouds. In the case where the cloud evolves for $\tau_{\rm phot}$, oxygen and hydrogen dominate since they are far less likely to be photoionized than are OH and H_2O to be photodissociated. With charge exchange and electron impact included ($\tau_{\rm all}$), however, more oxygen and hydrogen are removed from the system, which then tends to favor a molecular OH–H_2O cloud. In terms of total mass the same applies, although hydrogen accounts for only a few percent at most. We find the total mass of the neutral clouds to be bounded between ≈ 1 and 10 Mtons, for $\tau_{\rm all}$ and $\tau_{\rm phot}$, respectively.

It is worth pausing to re-emphasize that the system is in reality better represented by the $\tau_{\rm phot}$ case, from which all neutral clouds in this chapter have been derived. The $\tau_{\rm all}$ case is strictly valid only for neutrals within the Enceladus torus, though reactions with electrons and protons may also prove important.[a] What is illustrated,

[a]The work of *Rymer et al.* (2007, 2008) has shown that circulation patterns inside of 12 R_S at Saturn gives rise to "butterfly" hot electron pitch angle distributions, related to low temperature anisotropy ($T_\perp/T_\parallel$), on which proton field-aligned distributions depend (*Sittler et al.*, 2008).

however, is that Saturn's magnetosphere is less oxygen-dominated than is suggested when considering losses from photo-processes alone. These results suggest that our oxygen abundances are somewhat overestimated, likely by less than a factor of two.

Neutral absorption

The particles absorbed by Saturn and its rings are plotted by species and latitude in Figure 4.9. In Figure 4.9b, we see that most absorption comes from oxygen (74%), followed by H_2O (11%), OH (9%), and finally by hydrogen (6%). Absorption is equally divided between Saturn and its rings except in the case of OH, where twice as much falls on Saturn's rings. This is because OH is largely produced by impact dissociation, which creates slower neutrals than does charge exchange, whereby in the model, H_2O and oxygen are entirely formed.

In Figure 4.9b, absorption is plotted against Saturn's latitude. Because the model is symmetric about the equator, the results apply to either hemisphere. Oxygen, water, and OH follow the same trends because they all originate from charge exchange (dissociated OH is slow and does not reach Saturn), and have been created from ions with similar velocity distributions. Any second-order differences due to the velocity-dependence of the respective cross sections are not immediately apparent. Hydrogen, on the other hand, is produced entirely by dissociation in the model and exhibits a more uniform flux across Saturn. The explanation is that the velocity distribution from which hydrogen is produced is isotropic, whereas that which produces charge-exchanged neutrals is bi-Maxwellian (Section 4.2.2). The fluxes shown in Figure 4.9b are consistent with *Hartogh et al.* (2011), who modeled Herschel observations of Saturn's water torus

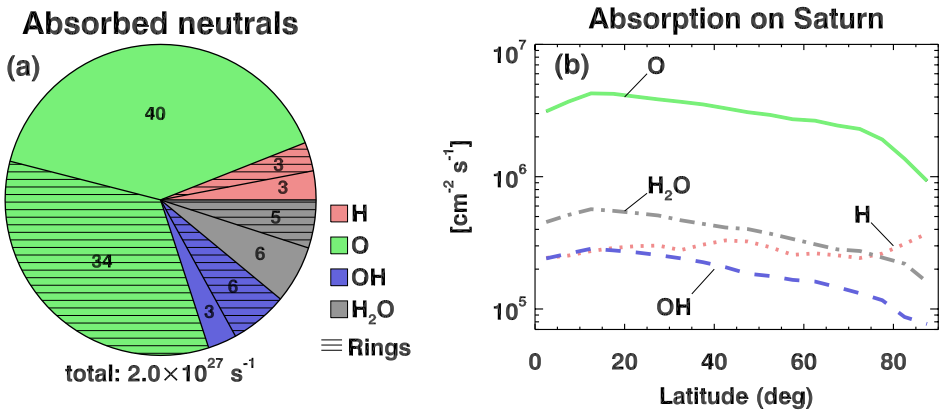


Figure 4.9 (a.) Neutrals absorbed by Saturn, plotted by species. Partitions with horizontal lines indicate percentages absorbed by Saturn's rings. (b.) Neutral flux on Saturn as a function of latitude. Neutrals produced by charge exchange (H_2O, OH, and O) peak in flux at low latitudes due to the nature of the ion distributions from which they orginate, which have initial velocity vectors predominantly in the ring plane. Conversely, hydrogen flux is constant across Saturn because it originates from dissociation, whose velocity distribution is prescribed as isotropic. Note that OH produced by dissociation is not energetic enough to reach Saturn.

and found an average flux of 6×10^5 cm^{-2} s^{-1} for H_2O + OH impinging on Saturn.

4.4 Discussion

Some useful conclusions can be drawn by further contrasting our results with *Cassidy and Johnson* (2010) (C10). It is important that we first mention a profound difference between our models. The model of C10 effectively carries out resonant charge exchange only, which does not chemically alter the neutral population; neutrals in their model are produced either directly from Enceladus or from subsequent dissociations. Neutrals in our model, on the other hand, originate from Enceladus (H_2O). OH is then created via dissociation (as with C10), but secondary O, OH, and H_2O populations are *created*

from H_2O via charge exchange with the dense plume-fed Enceladus torus. The C10 model redistributes neutrals around Saturn, while we redistribute and chemically reassign neutral abundances by allowing for asymmetric charge exchanges. Thus, it may well be a coincidence that our models are similar in total abundance. While it may be difficult to compare our total abundances, the slope of our radial density profiles can be contrasted directly because our redistribution mechanisms (charge exchange and dissociation) are similar. Differences are due largely to C10's inclusion of neutral collisions and our prescribing unique velocity-dependent charge exchange for each of the O-, OH-, and H_2O-producing reactions (Reaction 4.3a, Reaction 4.3b, and Reaction 4.3c).

Our neutral clouds are compared with C10 in Figure 4.10. All of our clouds include contributions from charge exchange, but the H_2O cloud is mostly comprised of water sourced directly from Enceladus ($3.95\,R_S$), and OH includes the additional source from dissociation. In the C10 model, the water molecules were spread due to neutral–neutral collisions, which explains our higher H_2O densities near Enceladus's orbit (Figure 4.10a). The slope of the oxygen profile agrees best with C10 because their charge exchange cross section most resembles our own (Equation 4.16c). Our H_2O profiles agree less, and our OH slopes, the least, due mainly to the strong effect that neutral collisions have on polar molecules. In particular, C10 used a much larger cross section for neutral collisions involving H_2O and OH (*Teske et al.*, 2005) than for atomic oxygen (*Bondi*, 1964). This helps to further explain our agreement with their oxygen profile since we exclude neutral–neutral collisions from our model altogether. We conclude that neutral–neutral collisions appear to play a less significant role with

atomic species, such as oxygen and hydrogen.

The column densities (Figure 4.10b) are similar to C10, who constrained their O and OH clouds with the most recent Cassini UVIS results of *Melin et al.* (2009). Our oxygen density—as well as our total oxygen content (Figure 4.10c)—is higher for two reasons. First, we use a larger cross section than does C10 for Reaction 4.3c, and second, the clouds presented here have been limited only by photoionization. Charge exchange and electron impact are second order losses beyond 6 R_S, but including them would favorably reduce the oxygen content more than OH and H_2O (Section 4.3.3), bringing our models into better agreement.

Our total H_2O content is 4× less than C10 found (Figure 4.10c). This is partly because we have subjected H_2O molecules in the primary (plume-fed) neutral torus to the shortest lifetimes possible (Section 4.2.1), whereas C10 tracks molecules that get kicked out of the densest plasma via neutral collisions, and thus survive longer, being less susceptible to both charge exchange and electron impact. That their total H_2O content is higher than ours (Figure 4.10c), does not contradict the fact that their H_2O column density is lower; neutral–neutral collisions would spread out the torus, lowering the column density, while allowing neutrals to survive longer, increasing the total abundance.

Our model would benefit by including the redistribution attributed to neutral collisions by allowing particles to interact in a direct simulation Monte Carlo (DSMC) model such as in C10. Likewise, DSMC models would benefit by including charge exchange cross sections specific to each reaction. Such models should also take into account asymmetric charge exchanges, which affects neutral cloud composition.

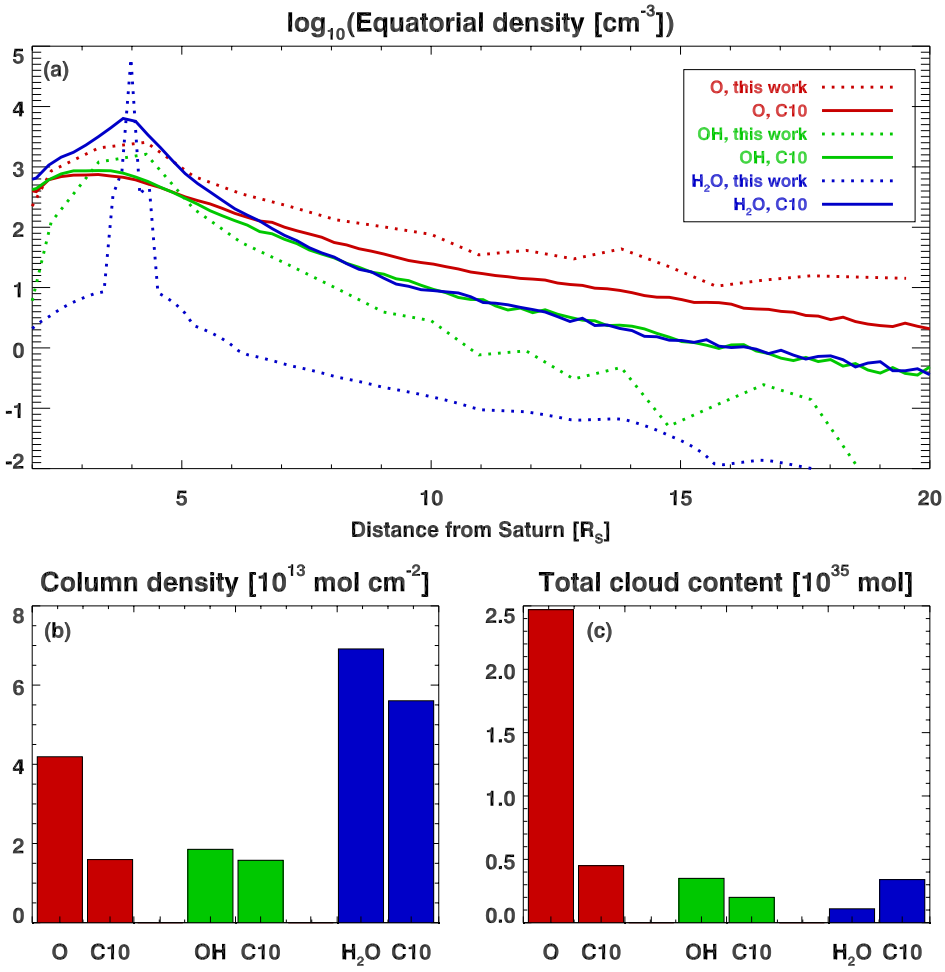


Figure 4.10 (a.) Total neutral clouds from our model, compared with *Cassidy and Johnson* (2010) (C10). All clouds include contributions from charge exchange (Reaction 4.3a, Reaction 4.3b, and Reaction 4.3c), while H_2O is largely comprised of water sourced directly from Enceladus, and OH includes contributions from dissociation. The cloud densities are limited by photodissociation for OH and H_2O and by photoionization for O. Including charge exchange as a loss for cloud neutrals would reduce the lifetime for O more than for either the OH or H_2O, and would lower the relative oxygen abundance accordingly. (b.) Equatorial column densities found by integrating the plotted equatorial densities. The H_2O column density is similar to C10, despite their having a very different radial distributions. (c.) Total neutral cloud content. Our total H_2O content is less than C10 found, while our H_2O column density is higher because our H_2O cloud is not subjected to neutral collisions and is thus more confined.

The reactions modeled in this study were chosen in order to measure the effect of symmetric and asymmetric charge exchange at low velocities. Building upon our findings, future studies should include additional neutral-producing charge exchanges, such as $OH^+ + H_2O \rightarrow OH^* + H_2O^+$, $H^+ + H_2O \rightarrow H^* + H_2O^+$, and $OH^+ + H_2O \rightarrow O^* + H_3O^+$, as well as dissociative recombination of H_2O^+.

4.5 Conclusions

We have modeled low-velocity charge exchange from the point of view of the ions, allowing us to study the effects of velocity as well as gyrophase. With Reaction 4.3a, Reaction 4.3b, and Reaction 4.3c, we have been able to offer an estimate on the size and shape of the neutral clouds at Saturn, while simultaneously exploring the sensitivity of the neutral clouds to a variety of velocity-dependent reactions.

We have also re-visited the production of OH following H_2O dissociation in the primary neutral torus. Previous models have used 1 km s^{-1} as the initial velocity for OH, while measurements suggest a range of speeds from 1 to 1.6 km s^{-1}. In our model, the higher speed increases the range within which dissociation dominates neutral production from 9 to 15 R_S.

Additional findings are:

(1.) Charge exchange cross sections that increase steeply at low speeds tend to produce neutral clouds more confined to the orbit of Enceladus, implying the most spreading for oxygen, moderate spreading for H_2O, and the least for OH (Figure 4.3). Accounting for gyrophase doubles the local OH density within Encelacus's orbit, has $\approx$ no effect on H_2O, and decreases oxygen density by less than 10%.

(2.) Enceladus is solely responsible for the creation of the neutral H_2O torus via thermal ejection from its plumes. However, Saturn's neutral clouds are overwhelmingly produced by charge exchange and dissociation occurring throughout the torus (99%), and not near Enceladus itself (Figure 4.5).

(3.) We estimate that roughly half of all neutrals escape the system, with the remaining equally divided between absorption by the rings/planet and the neutral clouds (Figure 4.8). Less than 50 kg s^{-1} is thus ionized and transported out of the system as plasma. This number is expected to represent an upper limit, given we have assumed that all particles forming the neutral clouds are ultimately ionized; a more accurate result would require modeling the detailed effects of charge exchange and neutral–neutral collisions within the neutral clouds (see Chapter 5). This estimate can be compared to *Sittler et al.* (2008), whose Figures 14 and 17 give roughly $([NL^2]_{W^+}/L^2) \times m_{W^+}/\tau_{\text{transport}} \approx 3 \times 10^{31} \times m_{W^+}/10^5$ s ≈ 10 kg s^{-1} at $L = 10$.

(4.) Saturn's neutral cloud has a total mass of at least 1 Mton, but likely much closer to 10 Mtons. The primary plume-fed neutral torus (0.3 Mtons) is comprised entirely of water in our model, while the secondary neutral clouds are broken down into H ($\lesssim 5\%$), O ($\lesssim 82\%$), OH ($\gtrsim 13\%$), and H_2O ($\approx 1\%$). Atomic oxygen dominates the composition both because of a high production rate from charge exchange as well as a long lifetime against photoionization. Charge exchange and reactions with electrons favorably remove hydrogen and oxygen, but are secondary loss mechanisms throughout the majority of the magnetosphere.

(5.) Our model predicts fluxes on Saturn from charge exchange of $\approx 6 \times 10^5$ cm^{-2} s^{-1} for both OH and H_2O (consistent with Herschel observations by *Hartogh et al.*

(2011)), and oxygen is about 5× higher. Absorption is divided equally between Saturn and its rings (Figure 4.9a).

(6.) Our total neutral abundances are similar to *Cassidy and Johnson* (2010) (C10) for both OH and H_2O, and 4× higher for oxygen (Figure 4.10). Differences in the slopes of our equatorial density profiles are in part due to our not including neutral–neutral collisions, while this fact appears to have no effect on the oxygen profile. On the other hand, C10 did not include the effects on neutral chemistry following asymmetric charge exchanges, nor did they use velocity-dependent cross sections specific to each reaction. Herschel observations by *Hartogh et al.* (2011) confirm the importance of neutral–neutral collisions for H_2O, but if oxygen is the dominant neutral species in Saturn's magnetosphere, as our model predicts, neutral–neutral collisions may play a smaller role in Saturn's neutral cloud than previously expected.

Given the effect on both the size and shape of the neutral clouds, we suggest that future neutral cloud models include charge exchange cross sections unique to each reaction. Asymmetric charge exchange also has an important effect on neutral chemistry that should be implemented. Regarding the ions' gyrophase, Monte Carlo models can account for its effect by using phase-dependent probability distributions. Finally, the range of OH velocities studied here should be considered when modeling dissociation.

In Chapter 5, we use our chemistry model, along C10's neutrals to build a radial model of ion temperatures and densities in Saturn's inner magnetosphere (< 20 R_S). An improved understanding of two issues is planned: (1) Where does plasma transport become important? (2) What is the role of hot electrons with regard to ion–neutral chemistry inside 20 R_S?

Acknowledgements

This work was supported under the NESSF program, fellowship 11-Planet11R-0005.

B. F. thanks two reviewers for their feedback and many useful suggestions.

Chapter 5

Characterizing ion conditions between 4 and 10 R_S

Abstract

Ion densities and temperatures in Saturn's inner magnetosphere are largely determined by the combined effects of hot (suprathermal) electrons, ion radial transport, and neutral cloud distributions. We have combined a 2-dimensional (radius and latitude) plasma chemistry model with a neutral cloud model to investigate the consequence of these aspects on ion properties between 4 and 10 Saturn radii. Relative ion abundances provided can be used for future Cassini CAPS analyses, while model sensitivity to transport timescales and hot electron density will be useful for relating these phenomena to observations. Selected results are: (1) Electron impact ionization and charge exchange conspire to produce H_3O^+ in the Enceladus neutral torus, wherein transport is found to be ignorable. (2) Hot electrons comprise at least 0.5% (but not more than 1%) of the total electron density at Enceladus. (3) The range over which Saturn's neutral clouds extend determines the relative abundances of water-group ions as well as their respective temperatures. (4) Total mass production rates agree well with independent estimates of the momentum lost by the solar wind at Saturn.

5.1 Introduction

In this chapter,[a] we combine the chemistry model from Chapter 2 with the latest neutral cloud models of *Cassidy and Johnson* (2010) to study variation of ion density and temperature between 4 and 10 R_S. We are interested in the system's sensitivity to the density of hot electrons and the radial transport of ions.

Sittler et al. (2006) showed that transport becomes important near 6 R_S with CAssini Plasma Spectrometer (CAPS) data from Cassini's first orbit of Saturn. They show that recombination is important for removing ions inside 6 R_S, but ignore the effects of charge exchange. Charge exchange is relevant, however, for its impact on radial variations in plasma density and temperature as well as water-group relative ion abundances—O^+/W^+, OH^+/W^+, H_2O^+/W^+, and H_3O^+/W^+, where $W^+ \equiv O^+ + OH^+ + H_2O^+ + H_3O^+$.

Hot electrons are necessary for the creation of ions, especially in Enceladus's orbit (4 R_S), where neutral densities are highest. Charge exchange is also important in the same region, generally occurring less rapidly than impact ionization/dissociation for neutral molecules, but more rapidly for atomic species (Chapter 2). Charge exchange and impact ionization both contribute to the pickup process, whereby fresh ions are produced and must be accelerated up to the speed of the magnetosphere.[b] Unlike charge exchange, however, impact ionization increases plasma density. Where transport is slow, hot electrons thus create ions which are later replaced by new ones via charge

[a]The work in this chapter is on-going at the time of writing this dissertation. The results should be considered as preliminary.

[b]The speed of the magnetosphere is often termed corotational if the angular velocity is equal to that of the planet.

exchange. For example, it was shown in Chapter 3 that H_3O^+ is created as a natural consequence of elevated H_2O densities through charge exchange (see also *Ip* (2000); *Cravens et al.* (2009)), but only after the formation of ions from electron impact.

In this chapter, we study several radial models of hot electron density and radial transport, by comparing the results to observed ion and electron temperatures and densities. fitting densities and temperatures simultaneously are also noted. Researchers such as *Richardson et al.* (1998) and *Jurac and Richardson* (2005) have done similar work with Saturn based on Voyager data from 1981, but before Enceladus's plumes were discovered by Cassini in 2005 (*Dougherty et al.*, 2006a; *Hansen et al.*, 2006).

We have developed both a 1-D model, in which latitudinal effects are ignored, and a 2-D model,[a] with the purpose of exploring the effects of the unique field-aligned distributions of protons and water-group ions, the latter being largely confined to the equator. Hot electron temperatures are fixed in the model because the relevant cross sections level off beyond ≈ 100 eV, allowing us to focus on hot electon density. Neutral densities are fixed with the latest results from *Cassidy and Johnson* (2010). The essential reason for fixing neutral densities is that neutrals are best treated with Monte Carlo models, given their eccentric orbits, wherein the loss rates vary with distance. Computation is also made more efficient by limiting the mass and energy rate equations to ions and electrons.

This chapter begins with a description of the 1-D and 2-D models in Section 5.2, with emphasis on the treatment of transport, followed by the results in Section 5.3 where we compare the models to data and present an extensive sensitivity study involving

[a]Where radial and latitudinal variations are considered, but conditions are assumed to be uniform azimuthally.

hot electrons and radial transport. A short discussion follows in Section 5.4, with concluding remarks in Section 5.5.

5.2 Model

5.2.1 Prescribed quantities

Neutral background densities

Unlike in Chapter 2, we do not calculate neutral densities self-consistently with the chemistry model. This is partly for computational advantage, but also because neutrals and neutral lifetimes are best handled with Direct Simuation Monte Carlo Models (DSMC) such as *Jurac and Richardson* (2005), *Johnson et al.* (2006), and *Cassidy and Johnson* (2010). One reason for this is that neutrals orbit Saturn on eccentric trajectories, sampling a variety of ambient ion conditions. Another reason is that neutrals collide with one another, expanding the cloud substantially from Enceladus out to beyond 10 R_S, an effect studied extensively by *Cassidy and Johnson* (2010). In order to model ion densities and temperatures as a function of distance from Saturn, we have chosen to use the neutral clouds from *Cassidy and Johnson* (2010) as the neutral source for the chemistry model, where those authors included the effects of charge exchange, dissociation, as well as neutral–neutral collisions (Chapter 4). The neutrals from *Cassidy and Johnson* (2010) are shown in Figure 5.1, where their equatorial densities have been extrapolated to higher latitudes using the following scale height:

$$n_W(\rho, z) = n_W(\rho, 0) \exp[-(z/\mathcal{H}_W)^2], \tag{5.1}$$

where W stands for one of either O, OH, or H_2O,[a] and $\mathcal{H}_W$ is the water-group neutral scale height (0.4 R_S; T. Cassidy, personal communication). For hydrogen densities,

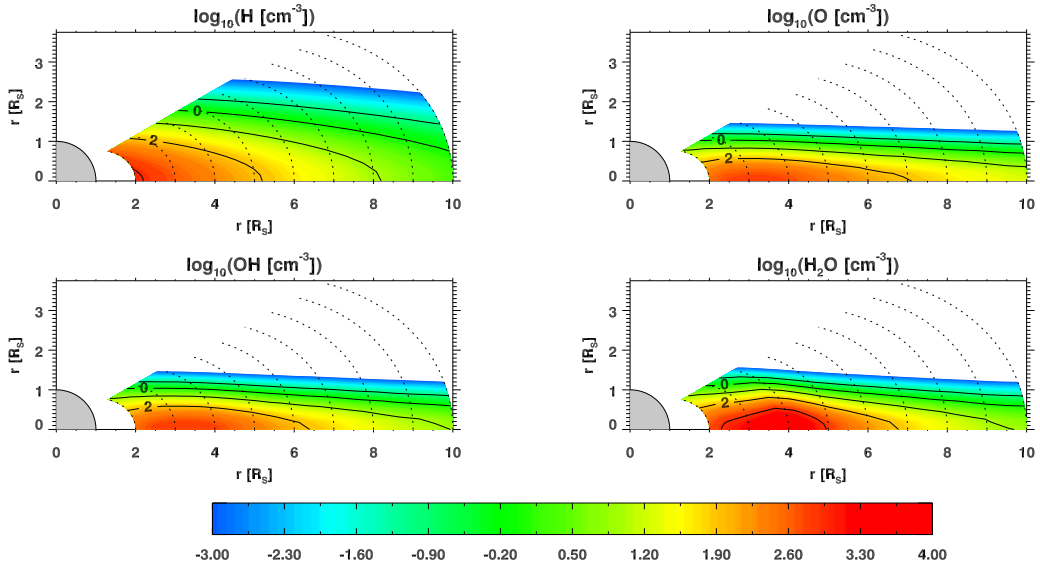


Figure 5.1 Neutral densities from *Cassidy and Johnson* (2010), extrapolated to higher latitudes using Equation 5.1 and Equation 5.2. H_2O peaks strongly at Enceladus's orbit (4 R_S), while the hydrogen cloud is the least confined to the equator. The oxygen and OH clouds represent intermediate cases, having been formed by the combination of dissociation and charge exchange.

Shemansky and Hall (1992) observed an average density of 100 cm^{-3} within, and more recent observations suggest that the longitudinal average of hydrogen near Enceladus is near 500 cm^{-3} (*Melin et al.* (2009); D. Shemansky, private communication). We choose an intermediate value, such that $n_H = 250$ cm^{-3} at Enceladus, and prescribe a function similar to Equation 5.1 that decreases exponentially according to

$$n_H(\rho, z) = n_H(\rho, 0) \exp[-(z/\mathcal{H}_H)^2]. \tag{5.2}$$

[a]There is no H_3O included in the model, nor is there any observational motivation to do so at present.

The scale height used for protons is twice that of the water group ($\mathcal{H}_{\rm H} = 0.8$ $\rm R_S$), and is based on our own neutral cloud study in Chapter 4. The equatorial profile is also based on the neutral hydrogen cloud model from Chapter 4 (see Figure 4.7):

$$n_{\rm H}(\rho, 0) = 10^{(13-\rho/\rm R_S)/3}/4. \tag{5.3}$$

The boundary conditions are $n_{\rm H}(\rho = 4\rm R_S, 0) = 250$ $\rm cm^{-3}$ and $n_{\rm H}(\rho = 10\rm R_S, 0) = 2.5$ $\rm cm^{-3}$. This is a very crude picture of the distribution of hydrogen, especially away from the equator, but does encompass the fact that the hydrogen cloud is less confined to the equator than are the heavy water-group neutrals. In addition, ions are also confined to the equator due do the centrifugal force, implying that most chemistry occurs near the equator anyhow. For these reasons, we expect the results presented here to be accurate to first-order.

Hot electron temperature

The hot electron temperature in the model is based on CAPS-ELS data from *Schippers et al.* (2008):

$$T_{\rm eh}^{\rm data}\ [\rm eV] = \begin{cases} 0.2L^{4.3} & (4 < L < 9.3) \\ 1.2 \times 10^6 L^{-2.7} & (9.3 < L < 10), \end{cases} \tag{5.4}$$

where L is a convenient (unitless) coordinate relating the usual polar coordinates to the surfaces defined by a magnetic dipole:

$$r = L\rm R_S \cos^2\theta. \tag{5.5}$$

Beyond 80 eV, the model is independent of $T_{\rm eh}$ up to several keV (Chapter 2). For this reason, we fix the hot electron temperature with Equation 5.4 and focus only on sensitivity to hot electron density.

5.2.2 Parameters

Two parameters are varied in the model to test their influence over ion properties—(1) the transport timescale and (2) the hot electron density. Each vary as a power low with distance, giving a total of four parameters with which to adjust the models to fit the data.

Transport rate

The transport rate between $L = 4$ and $L = 10$ is given as a function of L shell by

$$\tau = \tau_0 (L/L_0)^{\alpha}, \tag{5.6}$$

which is normalized to the orbit of Enceladus ($L_0 = 4$), so that $\tau(L_0) = \tau_0$.[a]

τ is integrated from L_j to L_{j+1} to find the rate at which plasma is transported from the jth radial bin into the $j+1$ radial bin. The total time required to transport ions from from Enceladus to $L > L_0$ is thus found with:

$$\begin{aligned} \mathcal{T}(L) &\equiv \int_{L_0}^{L} dL' \tau(L') \\ &= \frac{\tau_0}{L_0^{\alpha}} \frac{L^{\alpha+1} - L_0^{\alpha+1}}{\alpha+1}, \end{aligned} \tag{5.7}$$

[a] τ is actually defined as the transport time *per unit* L; total transport time is thus found by integrating $\tau(L)$. Because L is unitless, τ and $\int \tau(L) dL$ both have units of time. The important point is that τ and its integral are approximately equal when $\Delta L = 1$.

which is plotted in Figure 5.2 and Figure 5.3 for several values of α and τ_0. The best-fitting (nominal) model is the dashed line; the other functions are used for a sensitivity study in Section 5.3.2.

Hot electron fraction

The total electron distribution is often represented by a non-thermalized κ distribution (*Vasyliunas* (1968)), which has the characteristic of behaving as a Maxwellian distribution at low energies, but at high energies decreases gradually as a power law. These essential properties are captured by prescribing separate thermal- and suprathermal (hot) electron Maxwellian distributions. In doing so, we miss out on energies between $\approx$ 10–40 eV because the thermalized component decreases before the peak in the hot component. These intermediate-energy electrons are not expected to affect our results qualitatively, given we are interested primarily in ionization.

Hot electron densities are parameterized by a hot electron fraction, $f_{\rm eh} = n_{\rm eh}/\sum Z_i n_i^{\rm ion}$, where the mathematical limits are 0 and 1, though $f_{\rm eh}$ is generally constrained by observations to below 1 percent.[a] As with radial transport, $f_{\rm eh}$ varies with L as a power law, with normalization $f_{\rm eh0}$, and slope β:

$$f_{\rm eh} = f_{\rm eh0}(L/L_0)^{\beta}. \tag{5.8}$$

The best-fitting nominal values for τ_0, $f_{\rm eh0}$, α, and β are found in Table 5.1. Additional values are used to produce the plots in Figure 5.2 and Figure 5.3.

[a]Electron density cannot exceed ion density due to quasineutrality. However, negative dust grains have recently been observed near Enceladus, in which case, one might define $f_{\rm eh}$ as $n_{\rm eh}/(\sum Z_i n_i^{\rm ion} - \sum Z_j n_j^{\rm dust})$.

Model	τ_0 (days)		α		f_{eh0} ($\times 10^{-3}$)		β	
1–D	23	[1, 50]	−1.2	[−4, 0]	3.9	[1, 5]	1.4	[0, 2]
2–D	15	[1, 20]	−0.5	[−4, 0]	4.6	[1, 4.8]	0.8	[−1, 1.2]

Table 5.1 Parameters describing the radial profiles for radial transport and hot electron density (Equation 5.6 and Equation 5.8). Nominal values are given in each case. In square brackets are the ranges for which each parameter has been set in producing Figure 5.2 and Figure 5.3.

5.2.3 Constraints

The nominal models for τ and f_{eh} were determined by comparing model output to W^+ and H^+ densities and temperatures from CAPS data. Thermal-electron temperatures from CAPS-ELS were also used, bringing the total number of constraints to five.

The ion temperatures are from *Sittler et al.* (2006, 2007), where CAPS data have been fit to a power law:

$$T_{H^+}^{data} = 2.2(L/4)^{2.5} \text{ eV} \tag{5.9}$$

$$T_{W^+}^{data} = 35(L/4)^{2} \text{ eV}. \tag{5.10}$$

The thermal electron temperature is from CAPS-ELS data analyzed by *Schippers et al.* (2008). Because her data extended only down to $L = 5.5$, we have adopted an average temperature of 1.5 eV for $L < 5.5$, based on earlier observations by *Sittler et al.* (2006). Several other researchers have reported between 1 and 2 eV, not only with CAPS-ELS, but also by measuring plasma frequencies with the Radio and Plasma

Wave Science instrument (RPWS, *Moncuquet et al.* (2005)):

$$T_{\mathrm{e}}^{\mathrm{data}}\ [\mathrm{eV}] = \begin{cases} 1.5 & (4 < L < 5.5) \\ 6.8 \times 10^{-5} L^{5.9} & (5.5 < L < 10). \end{cases} \tag{5.11}$$

The ion density fits are from *Wilson et al.* (2008), and are based on several equatorial CAPS data sets:

$$n_{\mathrm{H^+}}^{\mathrm{data}}\ [\mathrm{cm}^{-3}] = 161.5 \exp(-0.042 L^2) \tag{5.12}$$

$$n_{\mathrm{W^+}}^{\mathrm{data}}\ [\mathrm{cm}^{-3}] = 8.3 \exp(-0.031 L^2) \tag{5.13}$$

How well the models reproduce the data is defined as the area bounded by the model output and the data on a log scale for each constraint:

$$f \equiv \sum_i \left| \log \frac{\mathrm{model}_i}{\mathrm{data}_i} \right|, \tag{5.14}$$

where the sum is over all radial bins, and f is one of either $f_{\mathrm{n_{H^+}}}$, $f_{\mathrm{n_{W^+}}}$, $f_{\mathrm{T_{H^+}}}$, $f_{\mathrm{T_{W^+}}}$, or $f_{\mathrm{T_e}}$. The sum over all constraints, f_{tot}, is the statistic used to determine the nominal values in Table 5.1, as well as the sensitivity study in Section 5.3.2.

5.2.4 Method

The purpose of this chapter is to study radial variation of ion temperature, density, and composition for a variety of hot electron and radial-transport profiles. This is done with a 1-D radial model as well as a 2-D model, wherein the effects of latitudinal distributions are included. Both models cool ions adiabatically as they are transported

into Saturn's outer magnetosphere.

The 2-D model was developed to study the effects of equatorial confinement for the various neutral and ion species (i.e., to study the effect of latitude-dependent collision rates between the various species), whereby the heavy water-group species are more confined than hydrogen and H^+.

1-D Model

The 1-D model does not include latitudinal averaging but does transport ions adiabatically to determine energy and mass transport rates from one radial bin to the next. The effect of field-aligned distributions is discussed below with the 2-D model. The algorithm for finding temperatures and densities in the 1-D model is as follows:

1. Provide initial guess for ion temperatures and (equatorial) densities.[a]
2. Advance $n(L)$ and $n(L)T(L) \equiv \varepsilon(L)$[b] by Δt with chemical rate equations (see Chapter 2).
3. Solve for $T(L) = \varepsilon(L)/n(L)$.
4. Update transported mass and energy source rate, $\dot{n}_{\text{diff}}(L)$ and $\dot{\varepsilon}_{\text{diff}}(L)$—described below.
5. Go to Step 2 until convergence.

1-D Mass transport Mass transport in the 1-D model is handled as follows. The volume associated with each radial bin is approximated as a washer shape centered on

[a] Temperatures are independent of latitude throughout this study.
[b] ε has units of pressure, or for our purposes, energy density (eV cm^{-3}).

the jth bin, with a height scale determined by the temperature of the ions. The jth volume is then given by $\pi(L_{j+1/2}^2 - L_{j-1/2}^2)H_j = (2\pi H_j L_j \Delta)\mathrm{R_S^3}$, where L_j is measured at bin center, Δ is the bin spacing (units of $\mathrm{R_S}$), and the scale height H_j is given by $\sqrt{2T_j(1 + ZT_{e,j}/T_j)/3m\Omega^2}$ (*Bagenal and Sullivan*, 1981; *Delamere et al.*, 2005). T_j is a particular species's temperature[a], Z is the charge state, m is the mass, and $2\pi/\Omega =$ 10 hrs 14 min is Saturn's rotation period.

The mass loss rate associated with transport is given in each cell by $\dot{n}_j = n_j/\tau_j$. The mass is then conserved when transported from one bin to the next so that $V_{j+1}\dot{n}_{j+1} = V_j n_j/\tau_j$, giving the following source rate for each bin:

$$\dot{n}_{j+1} = \frac{n_j}{\tau_j}\frac{H_j L_j}{H_{j+1}L_{j+1}}, \tag{5.15}$$

where $n = 0$ for all ions as the inner boundary condition. The transport of energy is similar for both models, and will be discussed shortly.

2-D Model

Calculating the transport of mass and energy in the 2-D model is complicated by the fact that one has to first update the chemistry in each latitudinal bin, then redistribute the ions after every timestep to maintain force balance and charge neutrality along the field (*Bagenal and Sullivan*, 1981). The steps for calculating densities and temperatures in the 2-D model are as follows:

1. Provide initial guess on ion temperatures and equatorial densities.

[a] All temperatures are in energy units unless stated otherwise.

2. Calculate ion densities along the field lines, where one iteratively solves for the electrostatic potential, Φ, at each latitude so that the electrostatic force balances the centrifugal and magnetic mirror forces exactly.

   The scheme is described in *Bagenal and Sullivan* (1981), where a Newton-Raphson solving algorithm is used to find the value for the electrostatic potential for which both force balance (electrostatic, magnetic mirror force, and centrifugal) and charge neutrality are achieved. The result can be written as:

$$n(L,\theta) = n(L,0)\exp\left[\overbrace{(1-A)\log\left(\frac{\sqrt{1+3\sin^2\theta}}{\cos^6\theta}\right)}^{\text{Mirror force}} + \left(\frac{2A+1}{3T(L)}\right)\left(\underbrace{\frac{1}{2}m(\Omega R_S L)^2(\cos^6\theta-1)}_{\text{Centrifugal force}} + \underbrace{Zq\Phi(L,\theta)}_{\text{Electrostatic force}}\right)\right] \quad (5.16)$$

   The anisotropies ($A \equiv T_\perp/T_\parallel$) for protons and water-group ions are set to 2 and 5, respectively, for all values of L (*Sittler et al.*, 2006).[a] The centrifugal and electrostatic terms become important when either the rotational speed ($\propto L\Omega$) or the electrostatic potential (Φ) become large compared to the thermal energy, T, whereas the mirror force is a function of latitude alone for a given anisotropy.[b]

3. Advance $n(L,\theta)$ and $nT(L,\theta) \equiv \varepsilon(L,\theta)$ by Δt with chemical rate equations (Chapter 2).

[a] To use Equation 5.16, we relate the (effective) temperatures from the chemistry to a bi-Maxwellian distribution for which $T_\perp$ is the ion temperature in the plane perpendicular to the magnetic field, and $T_\parallel$ is the temperature in the direction of the field. The relation between the three temperatures is given by $T \equiv (2T_\perp + T_\parallel)/3$.

[b] Equation 5.16 must be solved for each ion species, making their distributions coupled to one another. This fact is especially important for protons, whose degree of equatorial confinement depends on the anisotropy of all species involved.

4. Solving for $T(L)$ in 2-D is a bit more involved than in the 1-D model. In this case, we first calculate the temperature for each radial bin, first by finding the total energy by integrating ε in latitude. Because most ions are confined to the equator, we ignore latitudes above 30 deg throughout this chapter, giving:

$$N(L)T(L) \equiv \mathcal{E}(L) \propto \int_{-30^\circ}^{+30^\circ} \varepsilon(L,\theta)\cos^7\theta d\theta, \tag{5.17}$$

where the constant of proportionality is $4\pi {R_S}^3 \int_{L_j-\Delta/2}^{L_j+\Delta/2} L^2 dL = 4\pi {R_S}^3 L^2 \Delta(1 + \Delta^2/12) \approx 4\pi {R_S}^3 L^2 \Delta$, which reduces to $4\pi {R_S}^3 L^2$ when the bin sizes are for $\Delta = 1$ (*Siscoe* (1978), see their Equation A.11). The total number of ions in each bin are calculated similarly:

$$N(L) \propto \int_{-30^\circ}^{+30^\circ} n(L,\theta)\cos^7\theta d\theta. \tag{5.18}$$

Finally solve for $T(L) = \mathcal{E}(L)/N(L)$. Here we see why the constant of proportionality (which depends only on L) has been ignored, as it would divide out when calculating $T(L)$.

5. Calculate new field-aligned distributions from the updated total content and temperatures. This requires a sub-iteration to ensure that the balanced distributions yield the actual total content when integrated over all latitudes.

   The calculation is carried out first by guessing the equatorial ion densities and extrapolating to higher latitudes as in Step 2. A second Newton-Raphson routine is then used to update the equatorial densities, ensuring that the total integrated

ion content matches the actual amount. The two solvers converge rapidly in five iterations or fewer.

6. From the updated densities and temperatures, the updated mass and energy transport terms are calculated—described below.

7. Go to Step 3 until convergence. This procedure of advancing in time and updating chemical and transported sources repeats until a steady-state is reached, a period of time which depends on how well the initial densities and temperatures are chosen.[a]

2-D Mass transport In the 2-D model, the total flux tube volume per L shell is $\propto L^2 \int \cos^7\theta d\theta$ (*Siscoe*, 1978). For adjacent cells spanning the same latititude, the volumes are then $\propto [(L_j+\Delta/2)^3-(L_j-\Delta/2)^3] = L^2\Delta(1+\Delta^2/12) \approx L^2\Delta$. As with the 1-D model, the mass loss rate is given by $\dot{n}(L_i,\theta_j) = n(L_i,\theta_j)/\tau(L_i)$. Mass is conserved when transported from bin to bin, so that $V(L_{i+1})\dot{n}(L_{i+1},\theta_j) = V(L_i)n(L_i,\theta_j)/\tau(L_i)$, which yields the following source rate for each bin:

$$\dot{n}(L_{i+1},\theta_j) = \frac{n(L_i,\theta_j)}{\tau(L_i)}\left(\frac{L_i}{L_{i+1}}\right)^2, \tag{5.19}$$

which states simply that the cell volumes grow as L^2 at each latitude.

Energy transport (1-D and 2-D) The transport of energy is calculated identically for both models, since temperature is constant in latitude and varies only with L-shell.

[a]The initial guesses are often so poor that the model becomes unstable numerically, which in part has limited the range of parameters for which we have results at present.

We assume that the plasma expands adiabatically, so that temperature drops with L to account for the increasing volume according to $T(L_{i+1})V(L_{i+1})^{3/2} = T(L_i)V(L_i)^{3/2}$.

In both models, we used the ion scale height (defined above) to estimate the total volume of the jth radial bin occupied by ions, which are centrifugally confined to the equator: $V_\gamma(L_i) \propto H_\gamma(L_i)L_i$, where γ stands for either H^+, O^+, OH^+, H_2O^+, or H_3O^+. The transported ions in both models then are introduced into the next adjacent cell with a temperature given by $T(L_{i+1}) = T(L_i)(L_iH(L_i)/(L_{i+1}H(L_{i+1}))^{3/2}$. With the source rates, $\dot{n}$, from the respective models, one can show the energy source rate for each cell to be:

$$\begin{aligned}\dot{n}_{i+1}T_{i+1} &\equiv \dot{\varepsilon}_{i+1} \\ &= \frac{n_iT_i}{\tau_i}\left(\frac{L_iH_i}{L_{i+1}H_{i+1}}\right)^{5/2} \qquad \text{[1-D Model]}, \quad (5.20)\end{aligned}$$

$$\begin{aligned}\dot{n}(L_{i+1},\theta_j)T_{i+1} &\equiv \dot{\varepsilon}(L_{i+1},\theta_j) \\ &= \frac{n(L_i,\theta_j)T_i}{\tau_i}\left(\frac{L_i}{L_{i+1}}\right)^2\left(\frac{L_iH_i}{L_{i+1}H_{i+1}}\right)^{3/2} \qquad \text{[2-D Model]}. \quad (5.21)\end{aligned}$$

Notice that H implicitly depends on T, but is assumed to be constant whenever T is updated. This is a common issue with trancendental equations, but makes little difference after a few iterations, especially since our results are based on steady-state solutions.

The preceding procedure was repeated for several radial profiles for $\tau(L)$ and $f_{\text{eh0}}(L)$. The nominal values for α, β, τ_0, and f_{eh0} (Table 5.1) in each model were found by using a downhill simplex routine, which adjusts each parameter to find the combination for which the output best agrees with T_{H+}^{data} (Equation 5.9), T_{W+}^{data} (Equa-

tion 5.10), T_e^{data} (Equation 5.11), n_{H+}^{data} (Equation 5.12), and n_{W+}^{data} (Equation 5.13).

5.3 Results

5.3.1 Nominal case

The nominal transport and hot electron profiles are plotted for the 1-D and 2-D models in Figure 5.2 and Figure 5.3, respectively, along with several additional values discussed in the sensitivity study in Section 5.3.2.

Transport rate and $\dot{M}$

The timescale for transport at Enceladus (τ_0, Equation 5.6) is found to be 23 and 15.2 days for the 1-D and 2-D models, respectively. We attribute differences in the models to be associated with latitudial effects in the 2-D model, though both models can accommodate the transport rate of the other fairly well. For instance, solutions can be found for which transport times are longer, and the hot electron fraction is higher, in which case ion densities would increase over a shorter period of time due impact ionization. Such (anti-)correlations are discussed in Section 5.3.2.

Chemistry dominates the region close to Enceledus ($L = 4$), but eventually becomes less important than radial transport at some distance. The location of this critical point depends on the slope of the transport profile, α. For the nominal cases, we find $\alpha = -1.24$ and -0.49 for the 1-D and 2-D models, respectively. The steeper slope in the 1-D case is associated with a larger τ_0 than in the 2-D model, so that the rate of transport ($1/\tau(L)$) is equal in both models at $L = 7$.

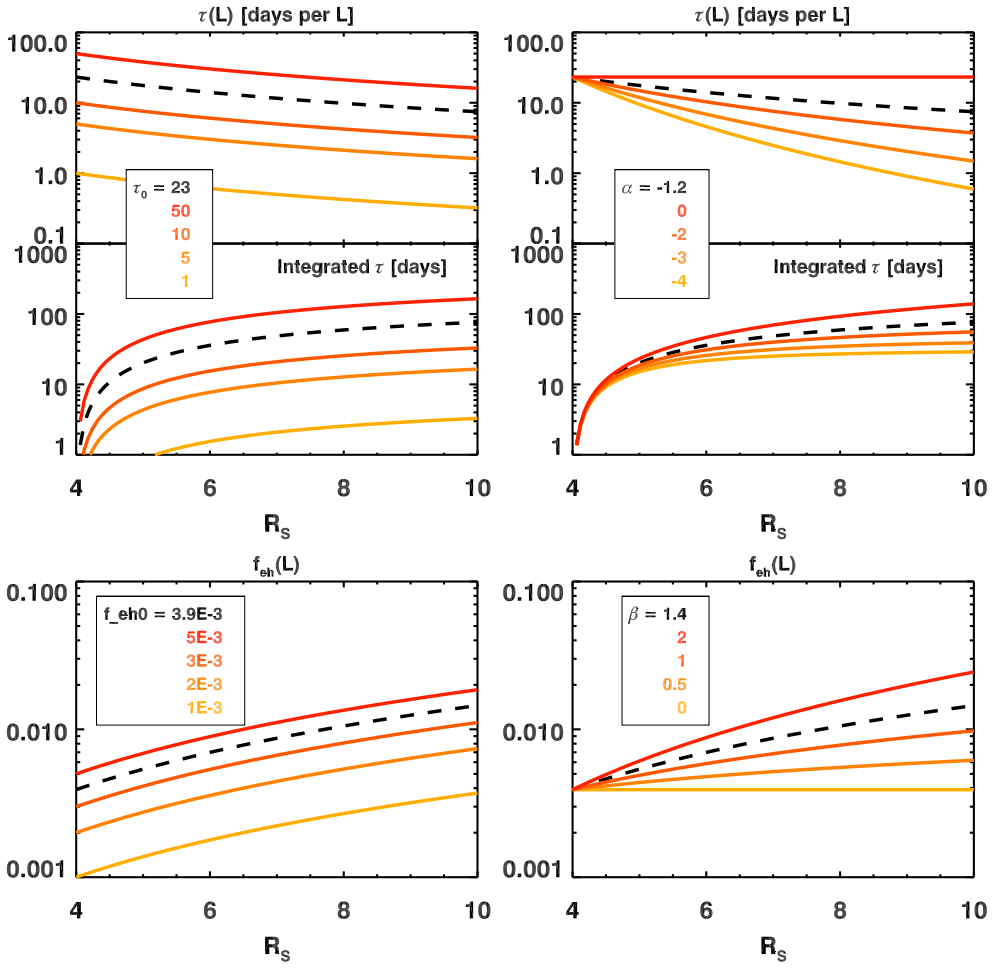


Figure 5.2 Selected hot electron and transport profiles, here for the 1-D model. Plots on the left are for varying normalization (τ_0 and f_{eh0}). On the right are plots for varying slopes (α and β). The middle panels are the integral of $\tau(L)$ from $L = 4$. Dashed lines are the nominal profiles.

Along with chemical reactions that create and remove ions, the transport rate directly determines the mass source rate, given by

$$\dot{M}(r) = v_r(L)\frac{dM(L)}{dL} = \frac{1}{\tau(L)}\frac{dM(L)}{dL}, \tag{5.22}$$

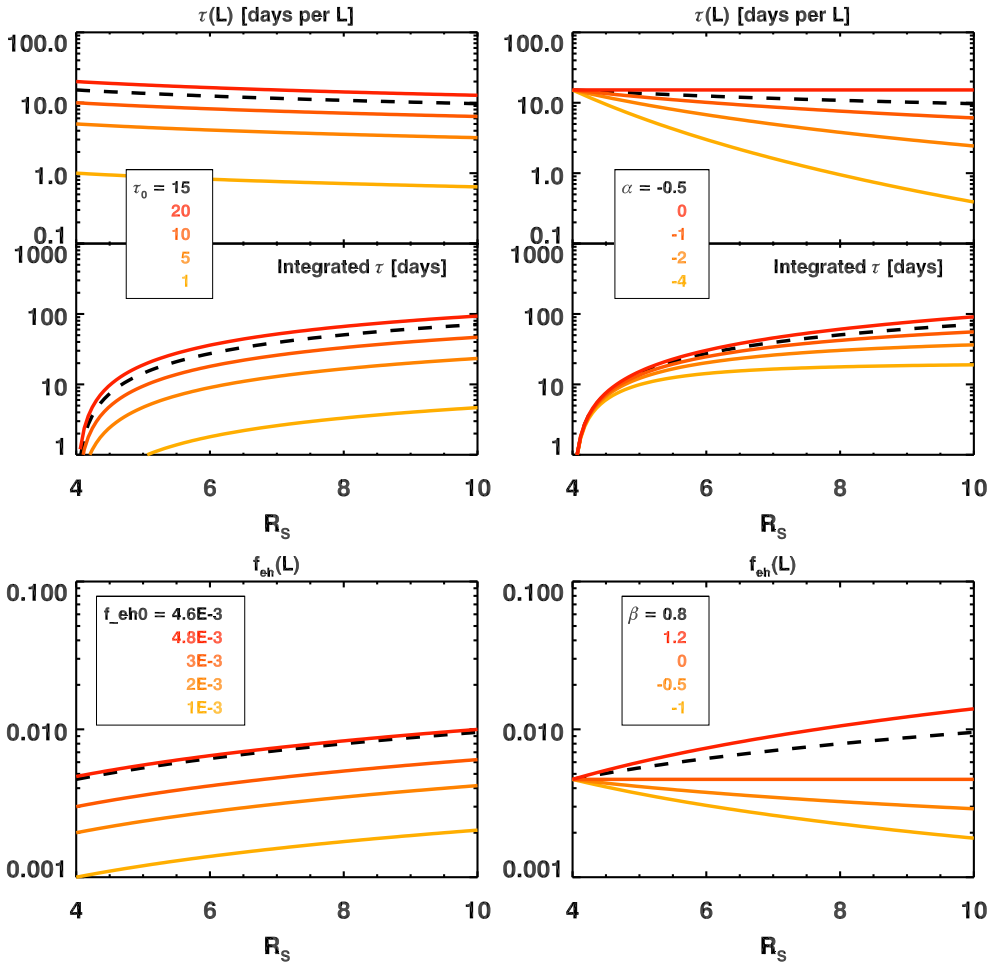


Figure 5.3 Selected hot electron and transport profiles, here for the 2-D model. Plots on the left are for varying normalization (τ_0 and f_{eh0}). On the right are plots for varying slopes (α and β). The middle panels are the integral of $\tau(L)$ from $L = 4$. Dashed lines are the nominal profiles.

where the radial speed, $v_r(L)$, is defined as the inverse of $\tau(L)$. The total content per unit L, $dM(L)/dL$, is found in the 1-D case with

$$\frac{dM(L)}{dL} = 2\pi^{3/2} mn(L) LH(L), \tag{5.23}$$

where m is the ion's mass, and the scale heights are given as before (*Bagenal and Delamere*, 2011) with:

$$H(L) = \sqrt{\frac{2}{3T(L)m\Omega^2}}. \tag{5.24}$$

For the 2-D case we use the latitudinal distributions to calculate $dM(L)/dL$ directly with

$$\frac{dM(L)}{dL} = 4\pi {R_S}^3 m L^2 \int_{0^\circ}^{30^\circ} n(L,\theta)\cos^7\theta d\theta. \tag{5.25}$$

The total mass source rate for each species is plotted in Figure 5.4 and Figure 5.5. For oxygen ions, $\dot{M}$ increases with distance in both models because recombination for O^+ is slower than for the molecular species (Section 5.3.1). At the other extreme is H_3O^+, where $\dot{M}$ drops the most rapidly of all species because of recombination, but also because the neutral H_2O source region (from which H_3O^+ is largely created) is less extended than either the oxygen, hydrogen, or hydroxyl neutral clouds, thus favoring the production of O^+, H_2O^+, and H_2O^+ from charge exchange farther out.

Differences in the models will be studied further in the future, but we note here that the $\dot{M}$ at $L = 10$ in both models of 20–30 kg s^{-1} agrees well with an unpublished calculation by Peter Delamere relating the mass source rate to solar wind conditions at Saturn (*Delamere and Bagenal*, 2012).[a]

[a]Paper in preparation comparing at Io, Jupiter, and Saturn. The end result of that calculation is given very briefly here. It can be shown by integrating the Maxwell stress tensor over the volume spanned by Saturn (with a characteristic radius of ≈ 22 R_S) that the solar wind exerts a tailward force of $F_{sw} = 2\rho_{sw} v_A v \pi {R_S}^2$, where v_A is the Alfvèn velocity of the solar wind at Saturn, and v is the tailward velocity of the ions, which couple to the solar wind by the Alfvèn wing. In steady-state ($dv/dt = 0$), Newton's second law gives $d(Mv)/dt = v\dot{M} = F_{sw}$, from which $\dot{M} = 2\rho_{sw} v_A \pi {R_S}^2 \approx$ 20–50 kg s^{-1} (P.

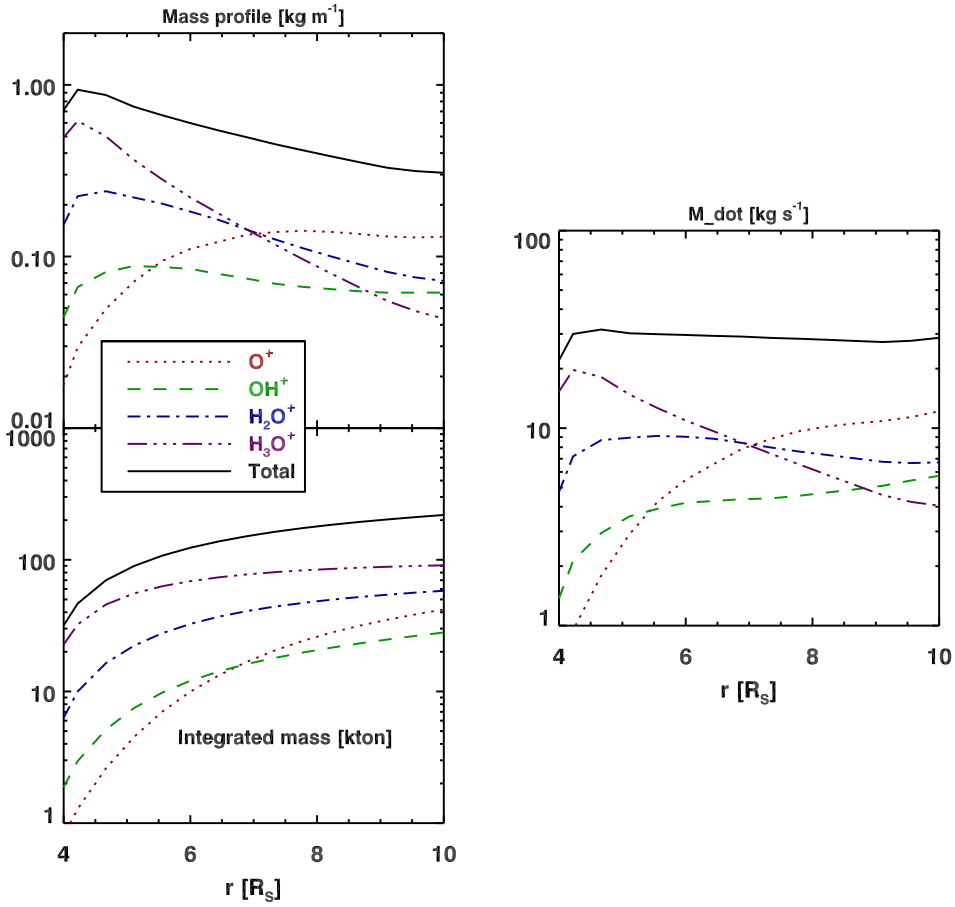


Figure 5.4 Total mass and total mass source rate for the 1-D model. The upper-left panel is the mass per L shell, the integral of which is plotted in lower-left. On the right is the mass source rate given by Equation 5.22.

Hot electron density

The hot electron fraction at Enceladus (f_{eh0}) is found to be 0.39% from the 1-D model and 0.46% from the 2-D model. This number can be compared to 0.46% found with our one-box study in Chapter 2, where we also used ion densities and electron temperature as model contraints. It is reassuring to find the same hot electron fraction, since the

Delamere, private communication).

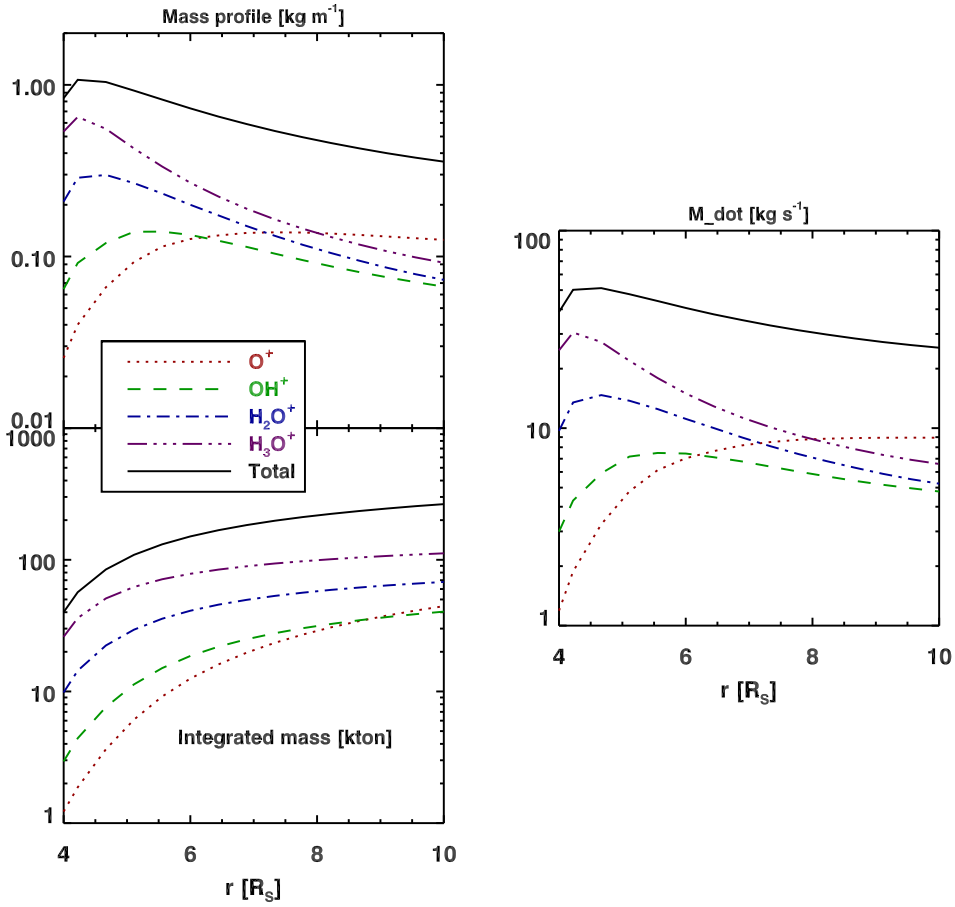


Figure 5.5 Total mass and total mass source rate for the 2-D model. The Upper-left panel is the mass per L shell, the integral of which is plotted in lower-left. On the right is the mass source rate given by Equation 5.22.

neutral densities have not been calculated self-consistently here in the radial model.

The slope, β, is found to be 1.43 and 0.8 with the 1-D and 2-D models, respectively. In this case, $f_{\rm eh}$ is equal in both models at $L = 5.2$. Most of the neutrals exist inside this location, especially the highly-abundant neutral H_2O (Figure 5.1), such that the relatively large number of hot electrons inside $L = 5$ largely determines the number of ions created and transported at the outset.

In both models, variation in ion temperatures is tied directly to the locations from which the respective species are created. H_3O^+ for example is created by charge exchange at $L \approx 4$, but not beyond this point by either charge exchange (because timescales are too long and H_2O densities fall off rapidly) or by impact ionization (because H_3O does not exist in the model, nor in observations). The result is that H_3O^+ temperatures are locked in with $L = 4$ pickup energies. OH^+ and H_2O^+ on the other hand are created continuously beyond $L = 4$ via impact ionization, serving to elevate their temperatures somewhat. Finally, O^+ temperatures increase not only because O^+ is created mostly beyond $L = 5$, but also because recombination removes O^+ much more slowly than molecular ions (Section 5.3.1).

Ion densities and temperatures

Equatorial ion and electron properties from the 1-D and 2-D models are plotted in Figure 5.6 and Figure 5.7, respectively. The pickup energy in the upper-right panels is derived from Equation A.6 with the v_ϕ profile from *Wilson et al.* (2008).

While the 1-D model does a better job at fitting the temperatures at large distances, the 2-D model does a better job fitting the densitites, though neither is able to reproduce thermal electron temperatures (T_e) reasonably. Temperature and density are difficult to reproduce simultaneously for the following reason: To increase ion temperatures, particularly beyond $L = 6$, fresh ion pickup must be increased where pickup energies are higher, which drives ion densities up by impact ionization to levels not supported by observations. Charge exchange could solve this conundrum, since it increases temperatures by increasing the number of fresh pickup ions, without affecting

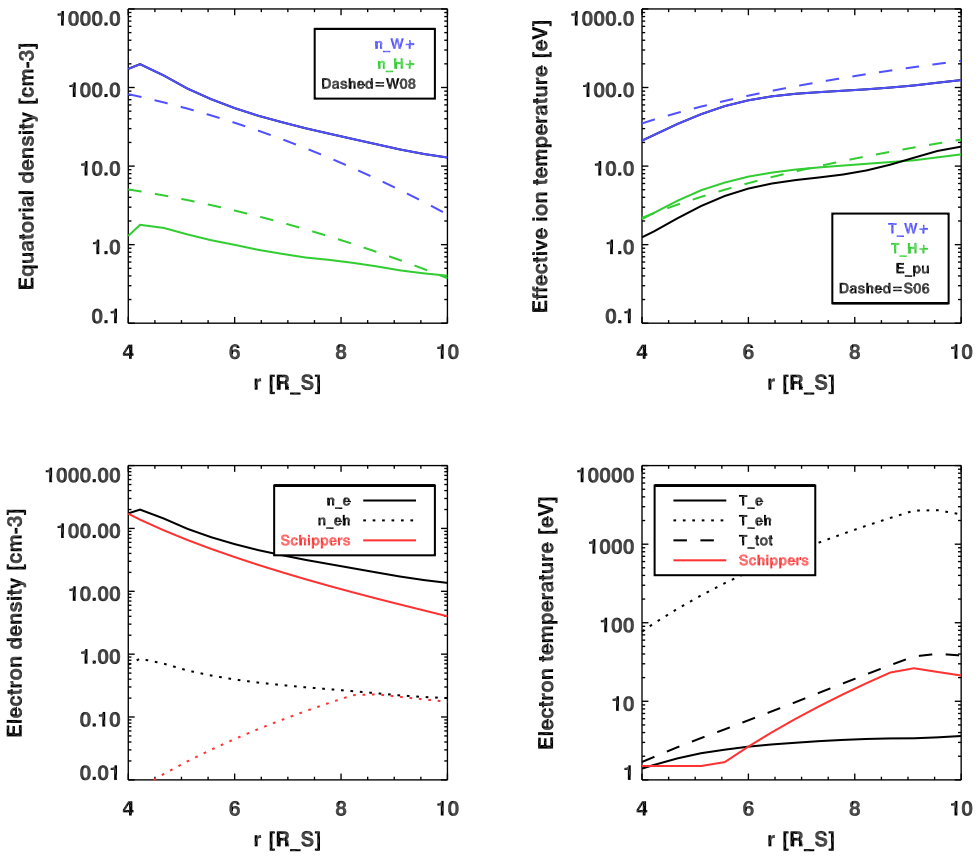


Figure 5.6 Equatorial ion and electron conditions for the 1-D nominal case. W08 are the fits from *Wilson et al.* (2008) given in Equation 5.12 and Equation 5.13. S06 are the fits from *Sittler et al.* (2006, 2007) given in Equation 5.9 and Equation 5.10. The electron densities and temperatures observations are from *Schippers et al.* (2008), where the temperatures given in Equation 5.11 and Equation 5.4. E_{pu} is the local pickup energy derived from the v_ϕ radial profile found in *Wilson et al.* (2008).

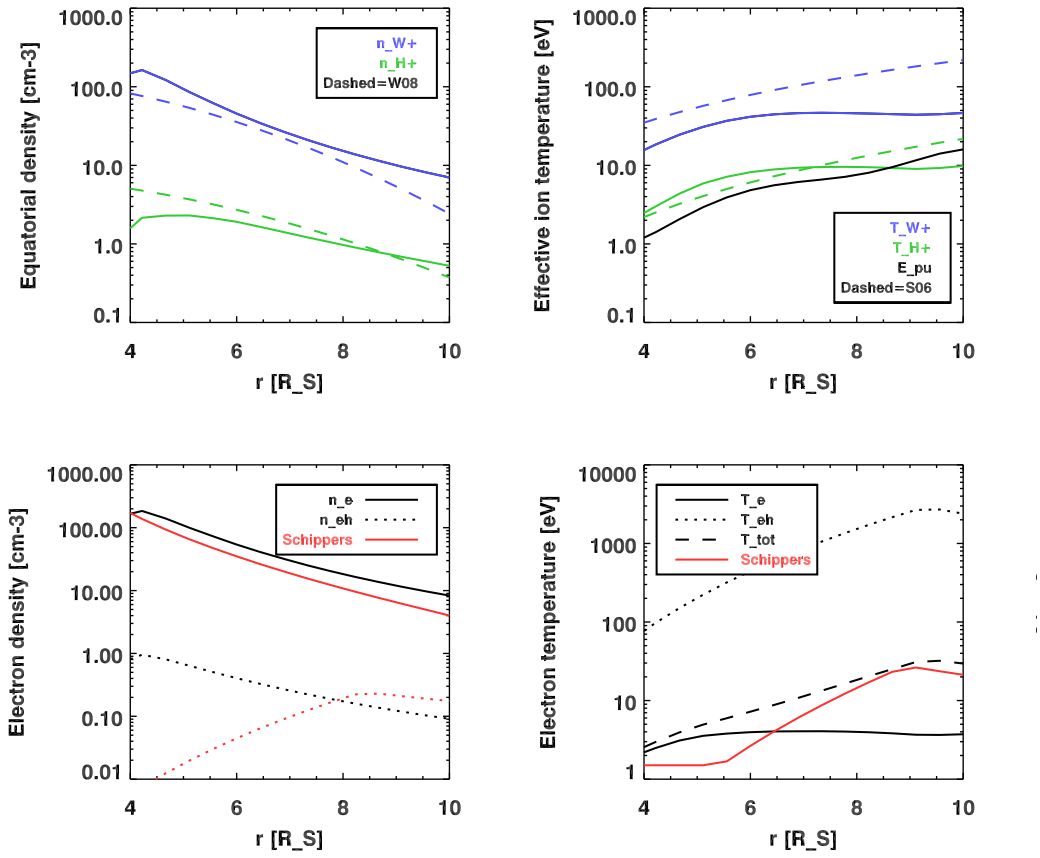


Figure 5.7 Equatorial ion and electron conditions for the 2-D nominal case. W08 are the fits from *Wilson et al.* (2008) given in Equation 5.12 and Equation 5.13. S06 are the fits from *Sittler et al.* (2006, 2007) given in Equation 5.9 and Equation 5.10. The electron densities and temperatures observations are from *Schippers et al.* (2008), where the temperatures given in Equation 5.11 and Equation 5.4. E_{pu} is the local pickup energy derived from the v_ϕ radial profile found in *Wilson et al.* (2008).

the overall plasma density, hinting at the need for additional neutral sources (or a more extended neutral cloud) beyond $L = 6$.

Low proton densities at Enceladus remain in the 2-D model, despite hopes that the proton latitudinal distribution would reduce proton losses from charge exchange. The most likely cause both for the low proton density and high water-group ion density at

Enceladus is charge exchange with the very high neutral H_2O density found there.

Ion densities are and temperatures are plotted for each species in Figure 5.8—Figure 5.11. The shaded region in the temperature plots (Figure 5.10 and Figure 5.11) is bounded from above by the local pickup energy for H_2O^+, and from below by the temperature of ions created at $L = 4$ and allowed to cool adiabatically when transported outward.

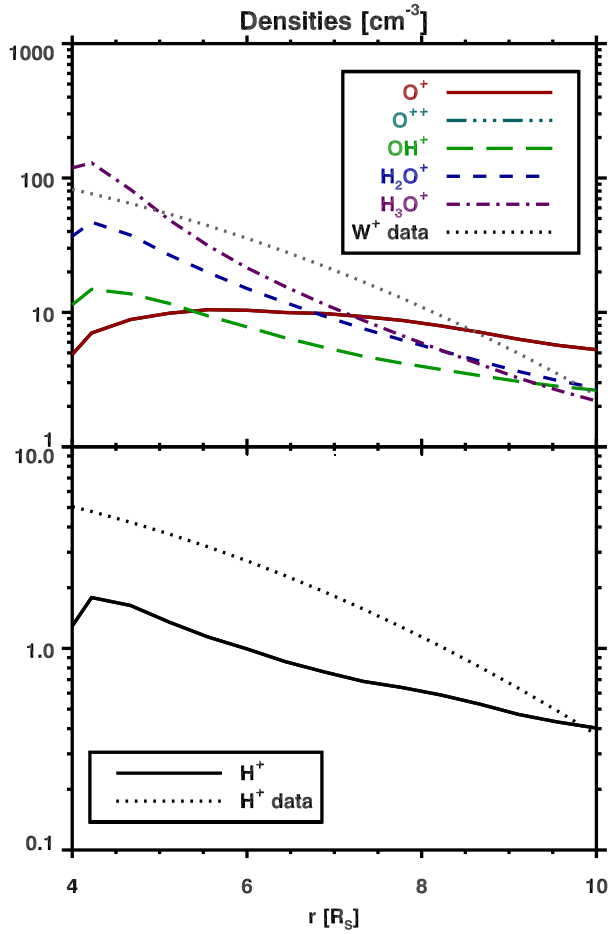


Figure 5.8 Nominal densities along the equator for the 1-D model. Proton and total water-group densities from observations are also plotted for reference (see Equation 5.12 and Equation 5.13).

The density of H_3O^+ peaks at $L = 4$ in both models (while O^+, OH^+, and H_2O^+ peak farther out between $L = 4$ and $L = 6$) because H_2O density is high and transport is slow at $L = 4$, allowing charge exchange and impact ionization to govern the ion properties. In Chapter 4, we discussed that such conditions necessarily drive high H_3O^+ densities because H_3O^+ is a stable ion, and unlike other water-group ions, is not removed by charge exchange. A consequence of H_3O^+ forming primarily at $L = 4$

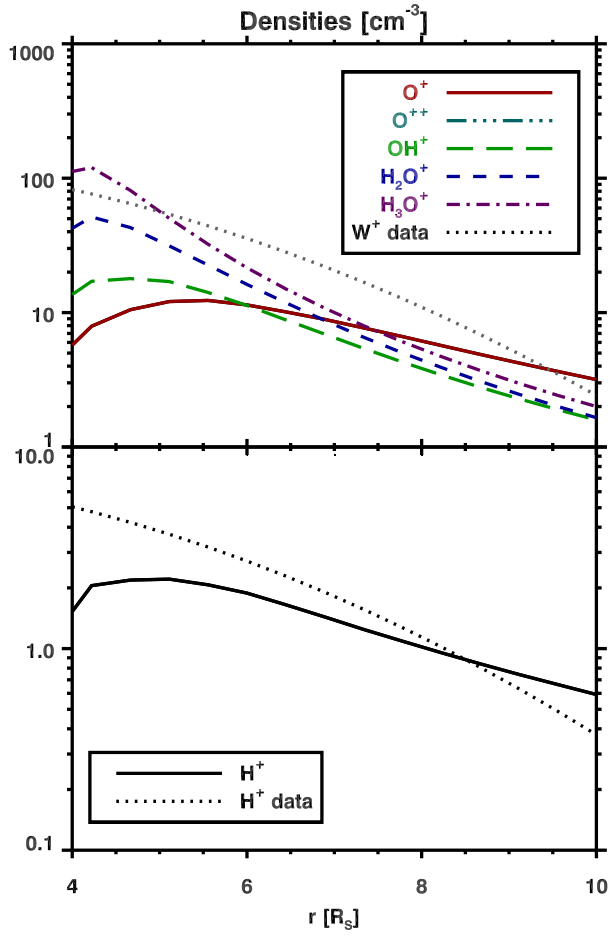


Figure 5.9 Nominal densities along the equator for the 2-D model. Proton and total water-group densities from observations are also plotted for reference (see Equation 5.12 and Equation 5.13).

is that the temperature remains nearly constant from $L = 4$ to $L = 10$. Any H_3O^+ added beyond $L = 4$ would serve to warm the population, although adiabatic cooling appears to balance this effect.

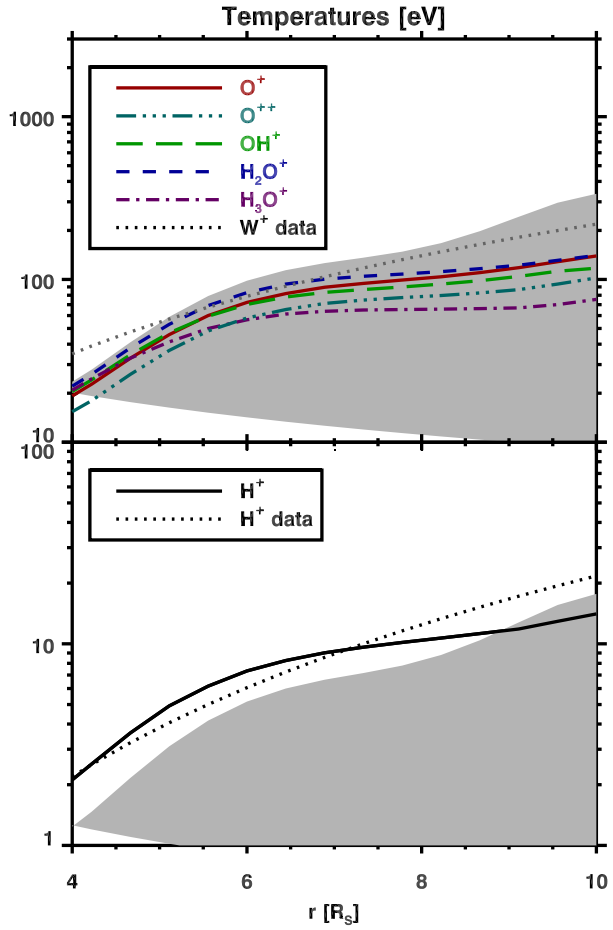


Figure 5.10 Nominal temperatures (independent of latitude) for the 1-D model. Proton and water-group ion data are given by Equation 5.9 and Equation 5.10, respectively (*Sittler et al.*, 2006, 2007). The shaded region is bounded from above by local pickup energies, and from below by the hypothetical temperature of fresh pickup ions transported adiabatically from at $L = 4$.

On the other hand, H_2O^+ is created by resonant charge exchange and warms more rapidly than H_3O^+, at least to $L = 5.5$. The effect of resonant charge exchange in

this case is to replace a cool H_2O^+ ion which has been transported from $L = 4$ with a member of the same species, except at a warmer pickup temperature. In this way, H_2O^+ temperature increases without affecting H_2O^+ density.

Proton temperatures are generally warmer that local pickup temperatures due to heating from the heavy ions via Coulomb collisions.

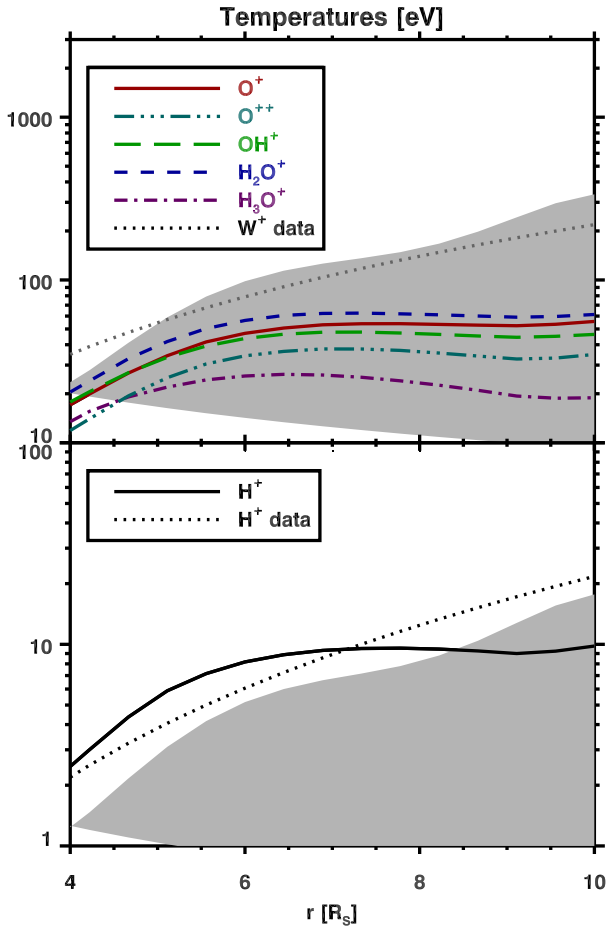


Figure 5.11 Nominal temperatures (independent of latitude) for the 2-D model. Proton and water-group ion data are given by Equation 5.9 and Equation 5.10, respectively (*Sittler et al.*, 2006, 2007). The shaded region is bounded from above by local pickup energies, and from below by the hypothetical temperature of fresh pickup ions transported adiabatically from at $L = 4$.

Note that densities drop beyond $L = 7$ for all species (including O^+) because transport begins to dominate, not because recombination becomes important. In the absence of sources and sinks, n must decrease as v increases in order for the mass flux ($\propto nv$) to remain constant,

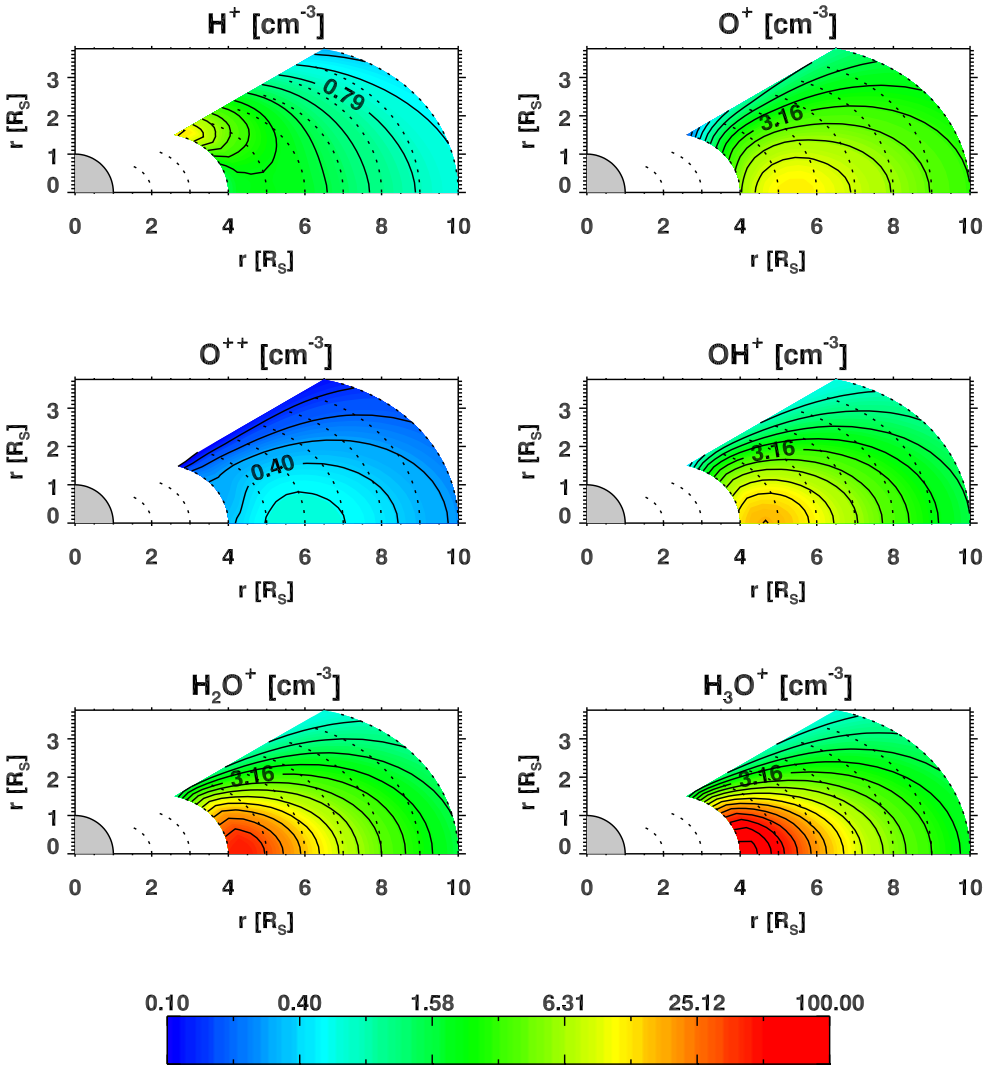


Figure 5.12 Nominal 2-D densities. Adjacent contours are separated by a factor of 0.41.

Relative water-group ion abundances

The relative abundance of water-group ions near Saturn's equator are plotted along with CAPS-IMS data from *Sittler et al.* (2008) in Figure 5.13 and Figure 5.14. The relative abundances in *Sittler et al.* (2008) are from Cassini's first orbit of Saturn (known as Saturn Orbital Insertion, or SOI). The model results have been interpolated to the spacecraft location to facilitate a direct comparison with observations.[a] The CAPS Ion Mass Spectrometer (IMS) provides the mass density of individual species first by identifying their energy-to-charge ratio. Along with knowledge of their velocity distributions, their mass-to-charge ratio is then used to determine individual masses by a time-of-flight apparatus (*Young et al.*, 2004). The 1-D and 2-D models are quite similar in this case. One small differences is that the 2-D case seems to plateau at $L = 9$, especially H_3O^+/W^+, while the 1-D case shows monotonic changes for all species out to $L = 10$. This is to be expected because τ decreases in the 2-D model more rapidly than in the 1-D model, resulting in a somewhat wider range over which chemistry (charge exchange and impact ionization) is important. We plan to eventually constrain the model with CAPS observations from many orbits, but it is reassuring that the present model at least produces the trends observed by *Sittler et al.* (2006).

Charge exchange near 4 R_S leads to large amounts of H_3O^+, while impact ionization and an extended neutral oxygen cloud lead to increased O^+ abundances beyond 7 R_S. The relative abundances of molecular species decrease away from 4 R_S due to dissociative recombination and the absence of a dense neutral source, which would otherwise replenish them by charge exchange.

[a] Cassini's latitude varied between 7° and 15° latitude on SOI.

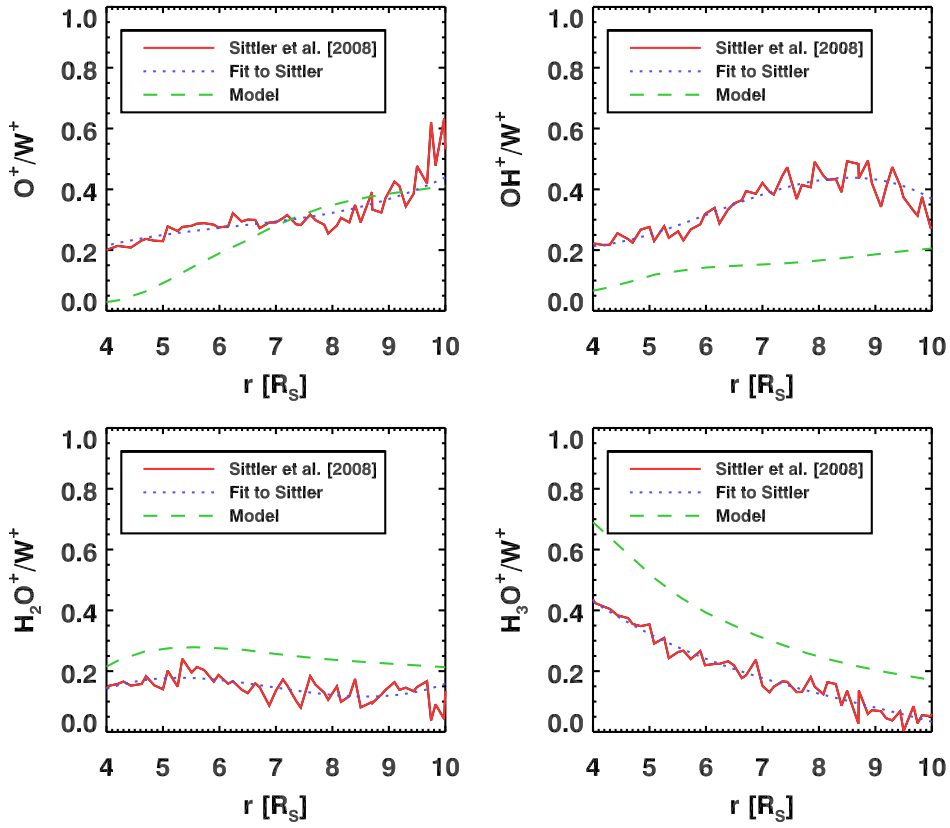


Figure 5.13 Nominal equatorial water-group composition from the 1-D model compared to data from *Sittler et al.* (2008). Although our results have not been constrained by these observations, the trends in the model bode well for a future comparison to CAPS data acquired throughout Cassini's Saturn campaign.

Loss rates and timescales

Loss rates along the equator are plotted for each species in Figure 5.15. Shown are the results for the 2-D case, but the 1-D case is very similar. Transport begins to dominate over chemistry at $L \approx 7$ for all species is near $L = 7$. This critical distance is a bit closer in for O^{++} , OH^+ and H_3O^+, and and a bit farther out for H^+. Charge exchange is the most important loss mechanism inside of this location for all but H_3O^+, which is stable

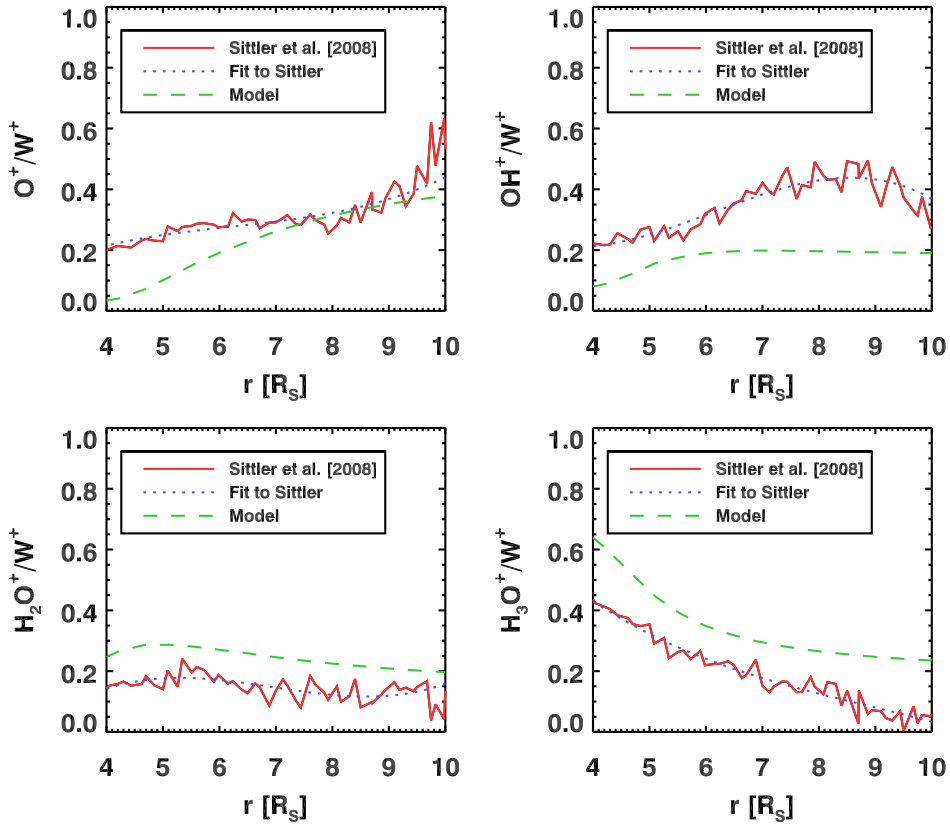


Figure 5.14 Nominal equatorial water-group composition from the 2-D model compared to data from *Sittler et al.* (2008). Although our results have not been constrained by these observations, the trends in the model bode well for a future comparison to CAPS data acquired throughout Cassini's Saturn campaign.

against electron transfer (Chapter 3). Recombination is not important anywhere for the atomic species, but does compete with both radial transport and charge exchange at $L \approx 7$ for the molecular species.

The important message is that the long lifetime of H^+ at $L = 4$ allows charge exchange with a dense neutral cloud to drive down proton densities in the model.[a] Conversely, a substantial number of H_3O^+ ions are formed by charge exchange at

[a]Which was in fact our primary motivation for developing the 2-D model.

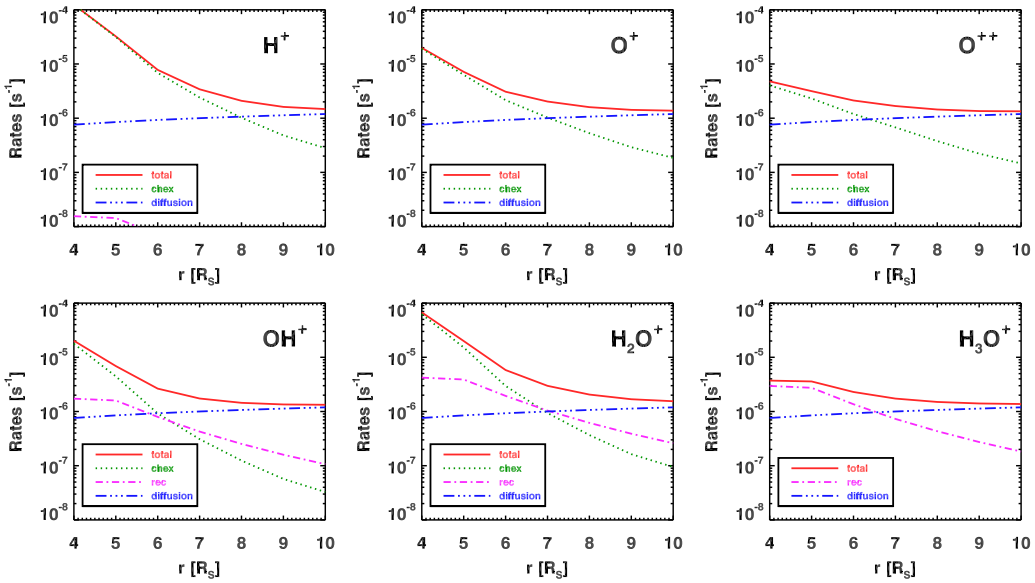


Figure 5.15 Loss rates for each species, derived from the 2-D model (similar in the 1-D model). Charge exchange dominates inside $L \approx 6$ for all species, beyond which transport dominates. Recombination plays an important role in removing H_3O^+ inside this critical point, but not for either OH^+ or H_2O^+. The short lifetimes for H^+ against charge exchange, make it difficult to match observed proton densities with the model (Figure 5.16–Figure 5.23).

$L = 4$, while only recombination and transport (which are both relatively slow there) remove it. The high relative abundance of H_3O^+ agrees at least qualitatively with *Sittler et al.* (2006, 2008) (Figure 5.16–Figure 5.23).

5.3.2 Sensitivity study

In addition to the nominal cases, we have run models with four additional values of each parameter (ranges given in Table 5.1) to test the sensitivity of the system, the results of which are given in Figure 5.16–Figure 5.23. The figures are ordered as 1-D, followed by 2-D, for each parameter, enabling efficient comparison between the two

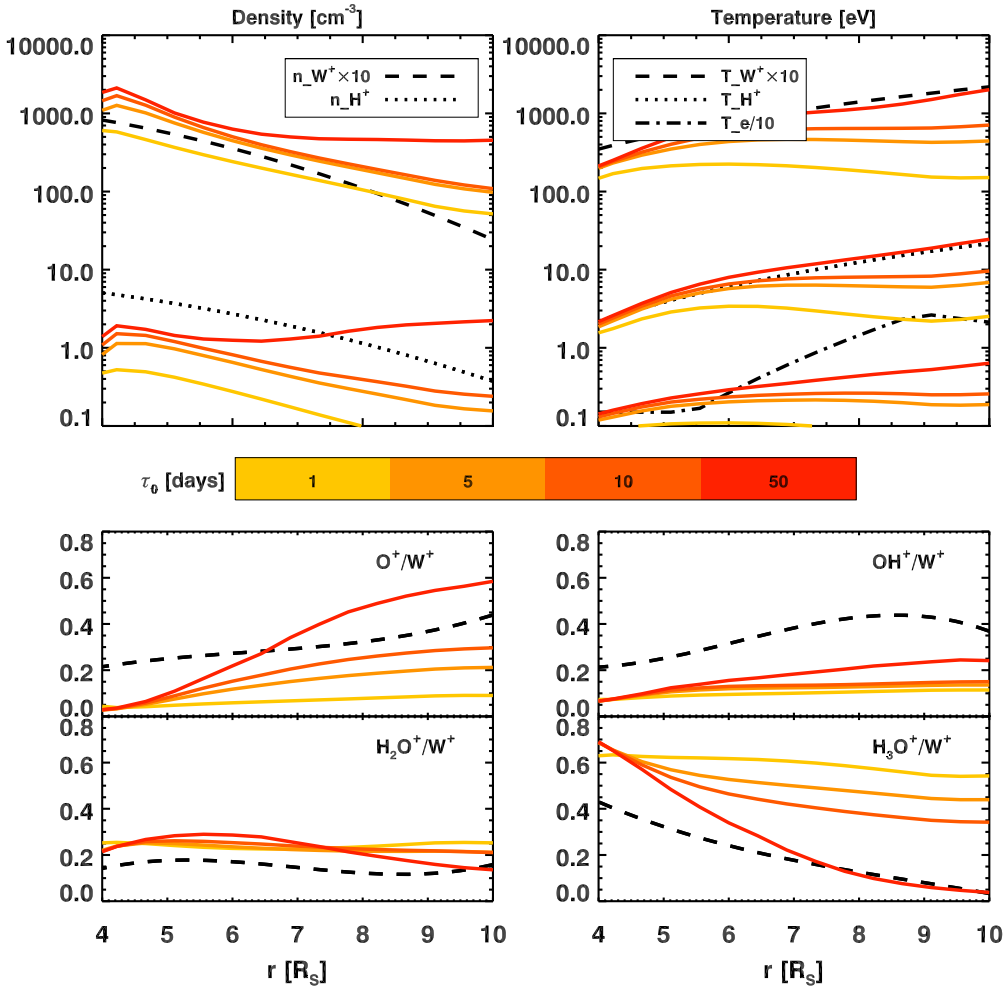


Figure 5.16 Results from the 1-D model for a range of τ_0. All other parameters are set to the values given in Table 5.1.

models. In each case, parameters not being varied are set to the nominal values in Table 5.1. Because the nominal values are not the same for each model, Figure 5.16–Figure 5.23 therefore do not strictly provide a direct quantitive comparison between the 1-D and 2-D models, but rather of qualitative behavior in the respective models with respect to increasing τ_0, α, f_{eh0}, and β.

We begin with some general points. At Enceladus ($L = 4$), no variation can be found

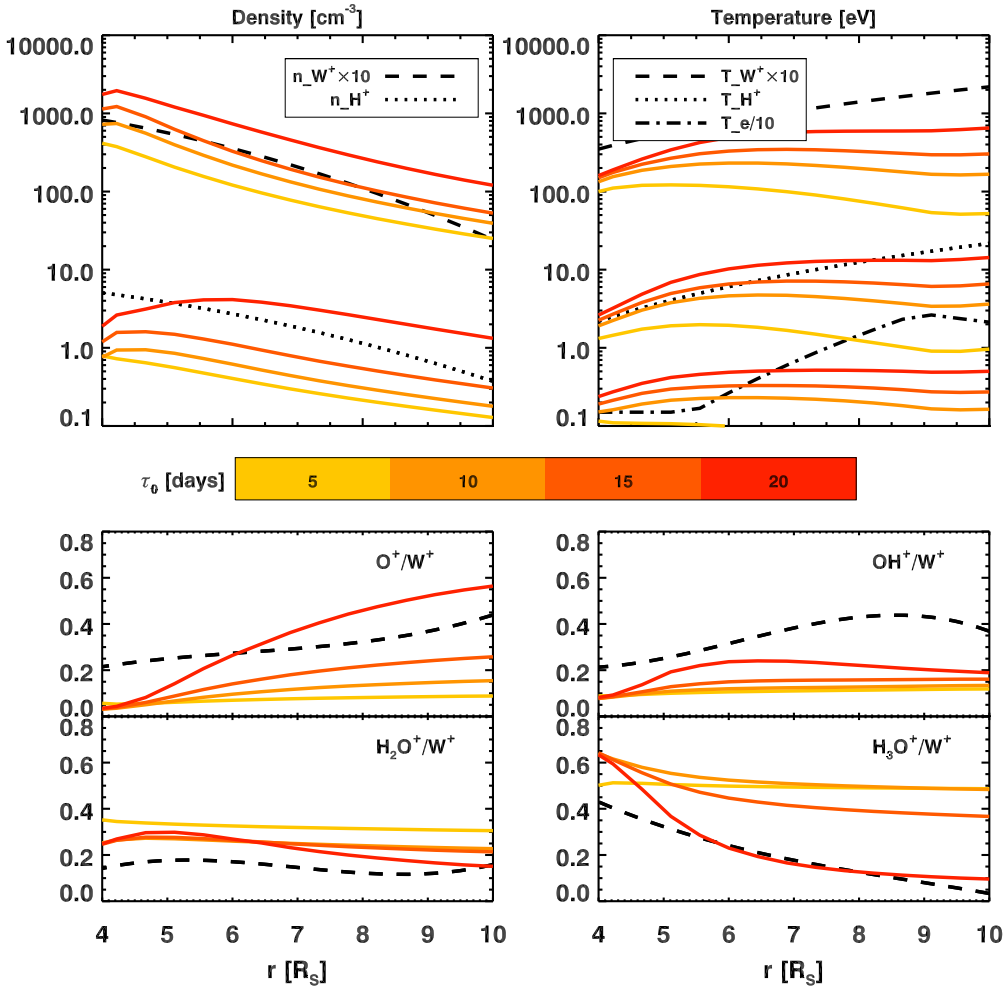


Figure 5.17 Results from the 2-D model for a range of τ_0. All other parameters are set to the nominal values in Table 5.1.

for varying α and β. This is due to the way in which $f_{\rm eh}(L)$ and $\tau(L)$ are prescribed in the model, wherein $f_{\rm eh}(L < 4) = f_{\rm eh0}^{\rm nominal} = \text{constant}$, and $\tau(L < 4) = \tau_0^{\rm nominal} = \text{constant}$. Increasing the slopes, α and β, does however increase the range over which $f_{\rm eh}$ and τ are important, and collectively determines where transport becomes rapid compared to chemical timescales.

Varying τ_0 and $f_{\rm eh0}$ also results in variation throughout, includeing at $L = 4$. While

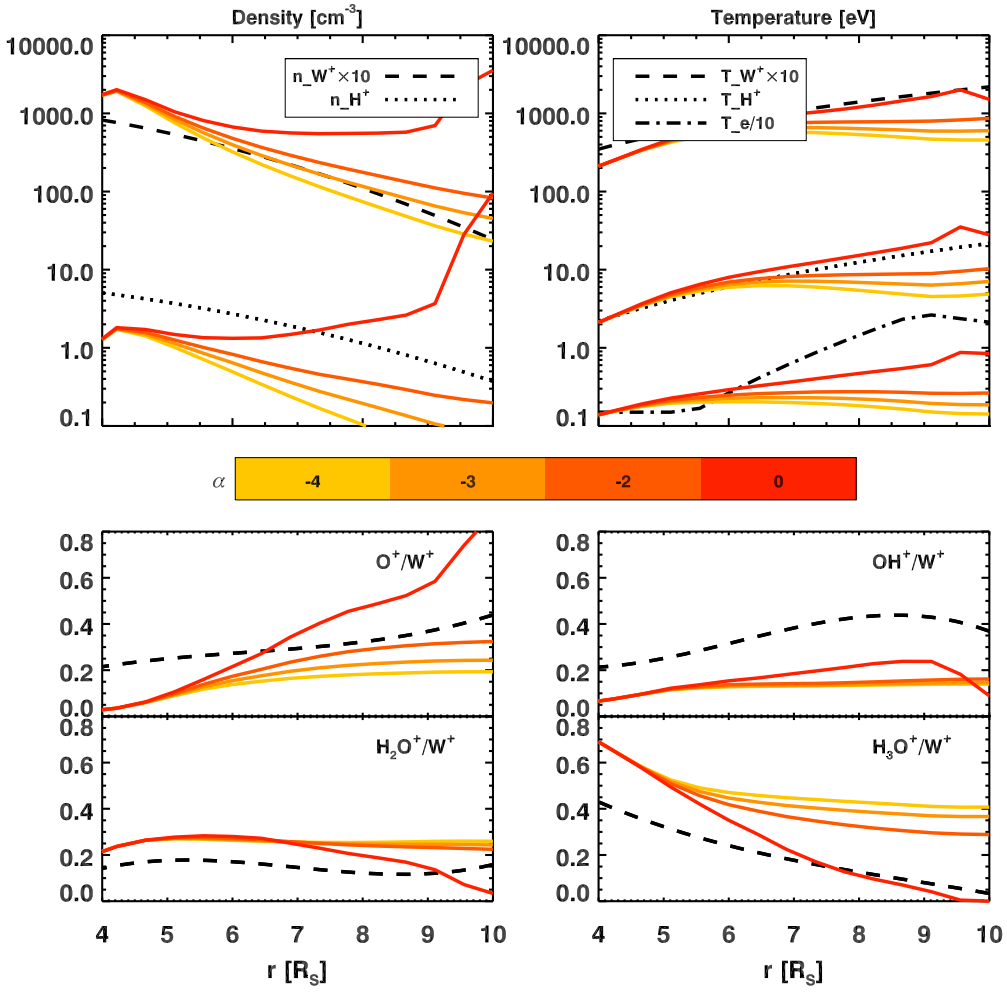


Figure 5.18 Results from the 1-D model for a range of α. All other parameters are set to the nominal values in Table 5.1.

differences at $L = 4$ are obviously caused by increasing τ_0 and f_{eh0}, ion properties outside $L = 4$ owe much of their variation to ions picked up and formed throughout $L = 4$–10.

Stated generally, the slopes (α and β) and the normalizations (τ_0 and f_{eh0}) conspire to drive variation within $L = 4$ to $L = 10$. Figure 5.16–Figure 5.23 single out their individual effects on temperatures and densities, as well as the relative abundances of

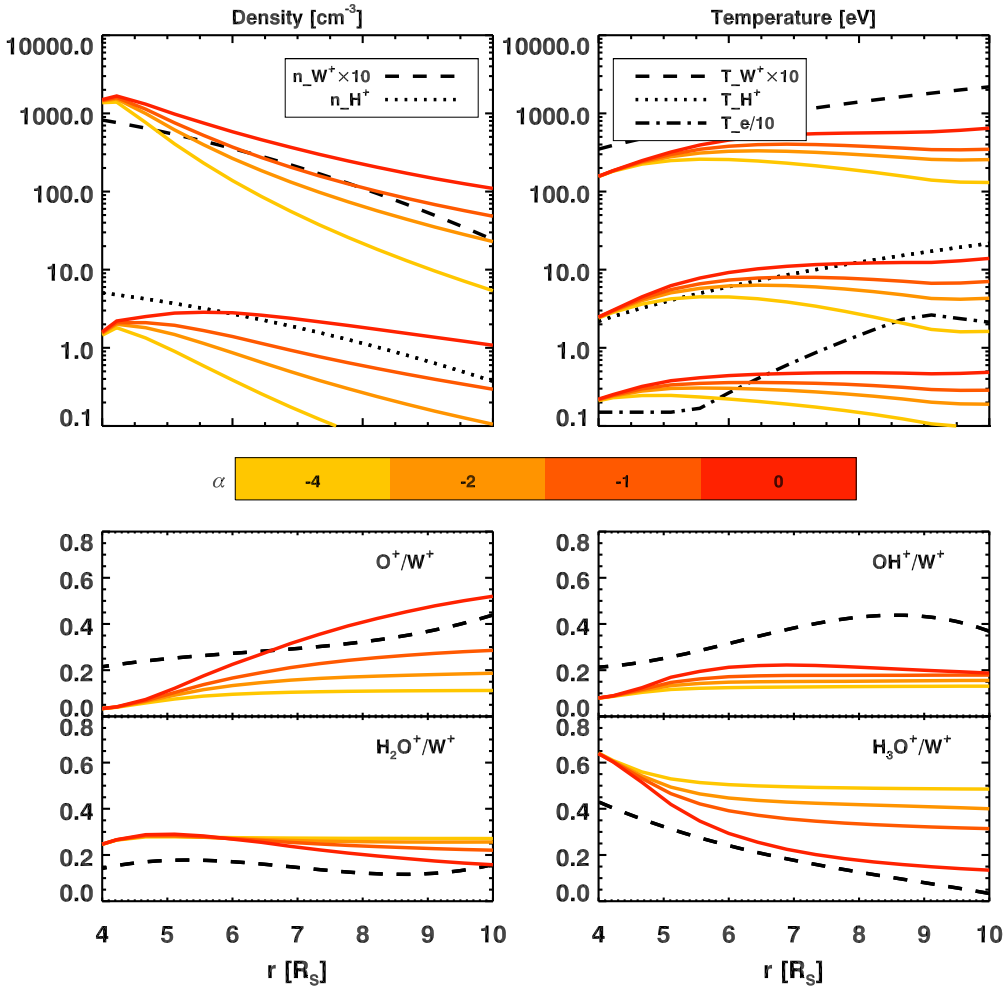


Figure 5.19 Results from the 2-D model for a range of α. All other parameters are set to the nominal values in Table 5.1.

the water-group species.

As for specifics, β appears to be the least sensitive parameter in both models (Figure 5.22 and Figure 5.23). What is most important in both models is that increasing β appears to improve the fit to the abundance ratios and temperatures while compromising the fit to densities. This can be explained as follows: The H_2O neutral cloud is more tightly confined than either the O or OH clouds (Figure 5.1). By increasing β,

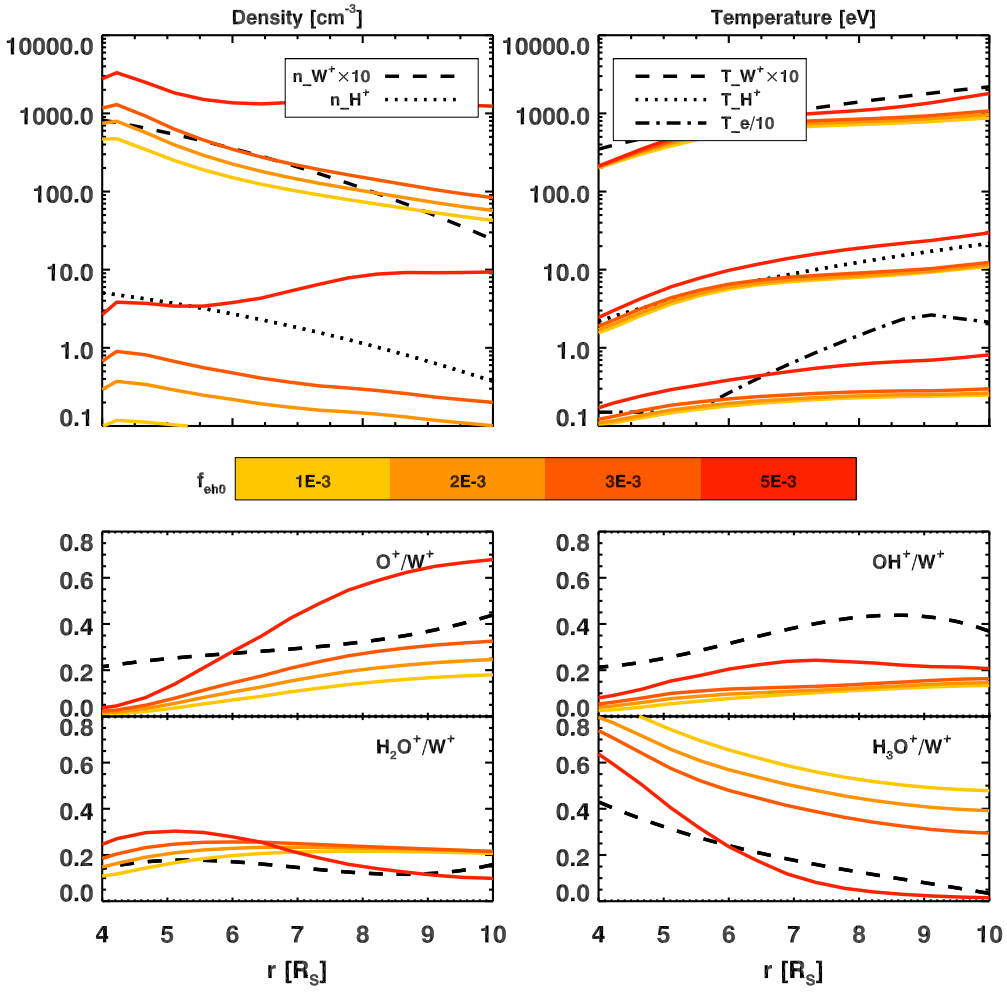


Figure 5.20 Results from the 1-D model for a range of f_{eh0}. All other parameters are set to the nominal values in Table 5.1.

and hence the region over with impact ionization occurs, O^+ and OH^+ are being added to the H_3O^+ ions being transported outward from $L = 4$. This increases the total ion abundance (τ is not long enough for recombination to occur; see Figure 5.15), and also brings composition into better agreement with data. Temperature increases in the higher-β cases because the ions picked up at $L > 4$ are warmer than those transported outward from $L = 4$.

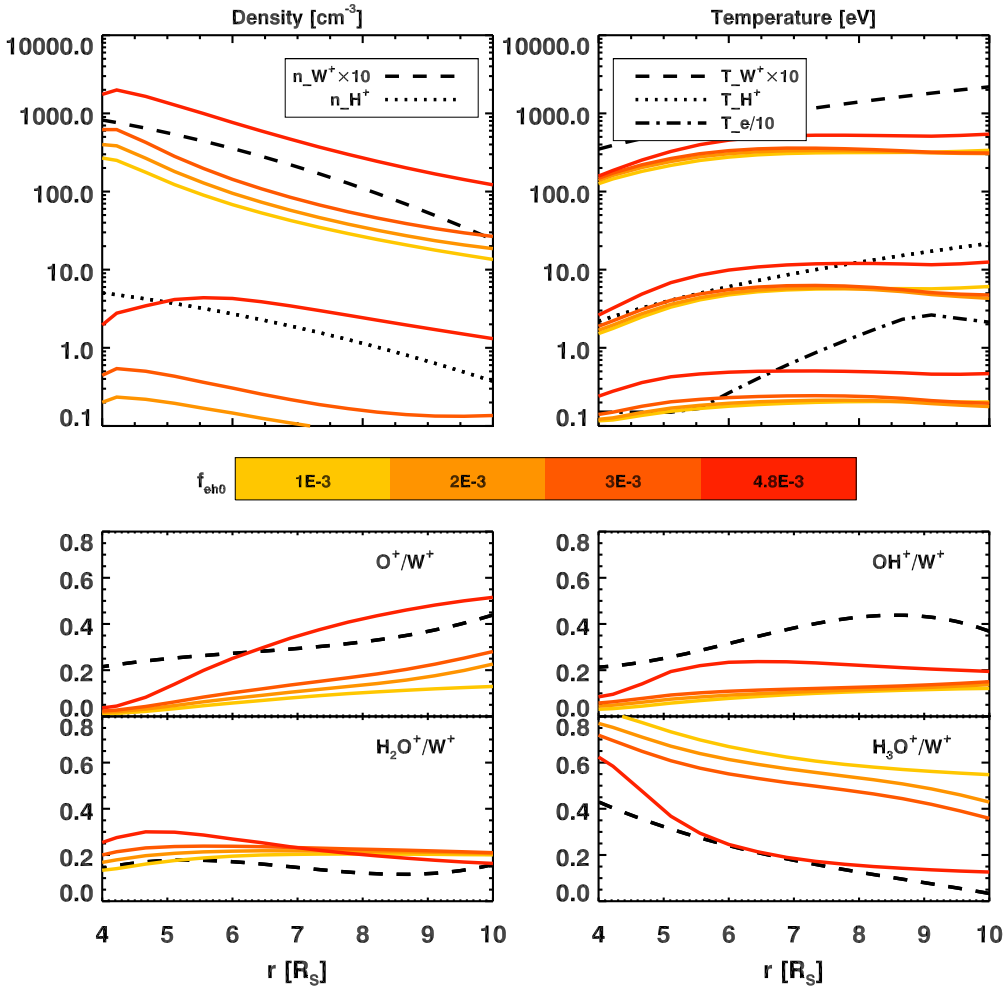


Figure 5.21 Results from the 2-D model for a range of f_{eh0}. All other parameters are set to the nominal values in Table 5.1.

This trend is not unique to β. Increasing τ_0, f_{eh0}, and α has a similar effect for the same reasons, only with greater sensitivity, particularly with respect to densities and temperatures. For example, increasing τ_0 increases the time allowing electron impact to occur not only at $L = 4$, but also for $L > 4$, which gives rise to the additional (and warmer) O^+ and OH^+ ions (Figure 5.16 and Figure 5.17). Interestingly, for $\tau_0 > 5$ days, the relative abundances at $L = 4$ are independent of τ_0, because charge

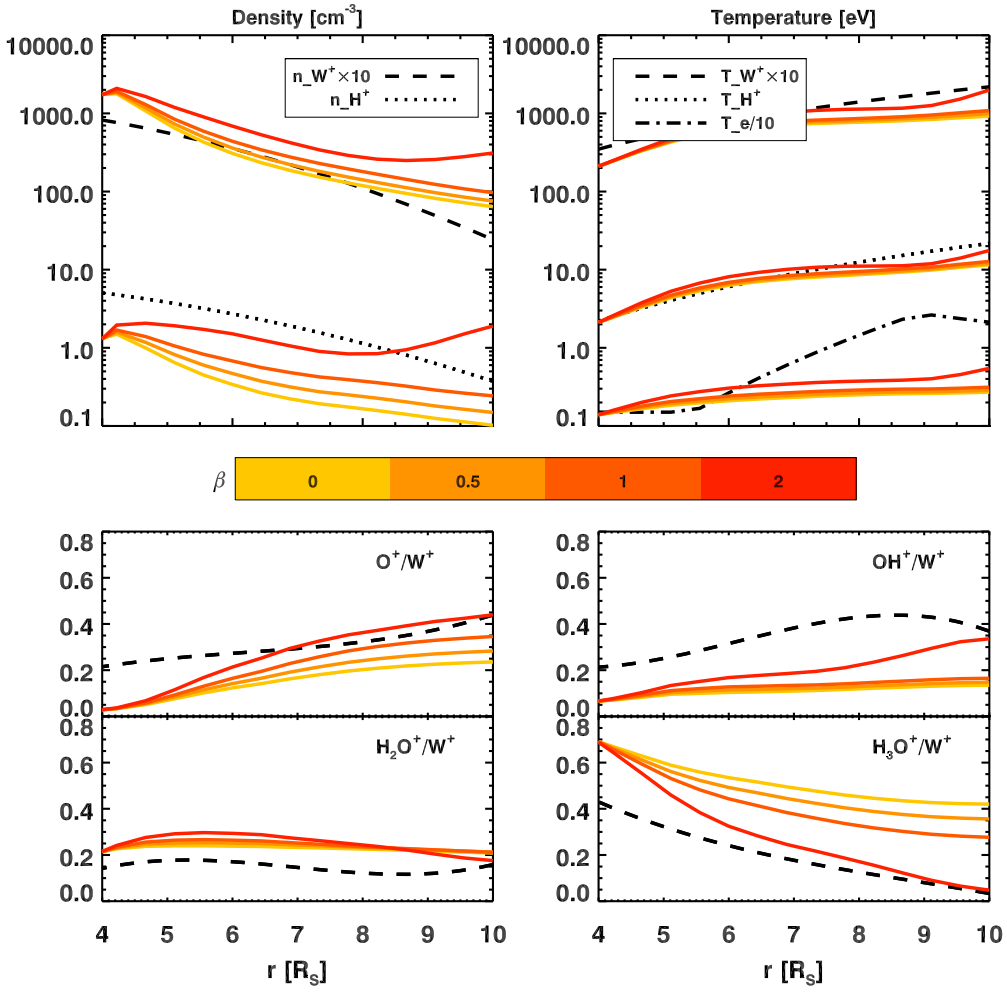


Figure 5.22 Results from the 1-D model for a range of β. All other parameters are set to the nominal values in Table 5.1.

exchange occurs rapidly enough to balance fresh ions formed by impact ionization (see Chapter 3 for discussion on production of H_3O^+ via charge exchange). Variation in relative abundances outward of $L = 4$ is due to variation of neutral cloud density, from which new ions are created, and also because O^+ is not as efficiently removed via recombination as are molecular ions.

An excellent fit for ion temperatures is found for $\tau_0 = 50$ days in the 1-D model

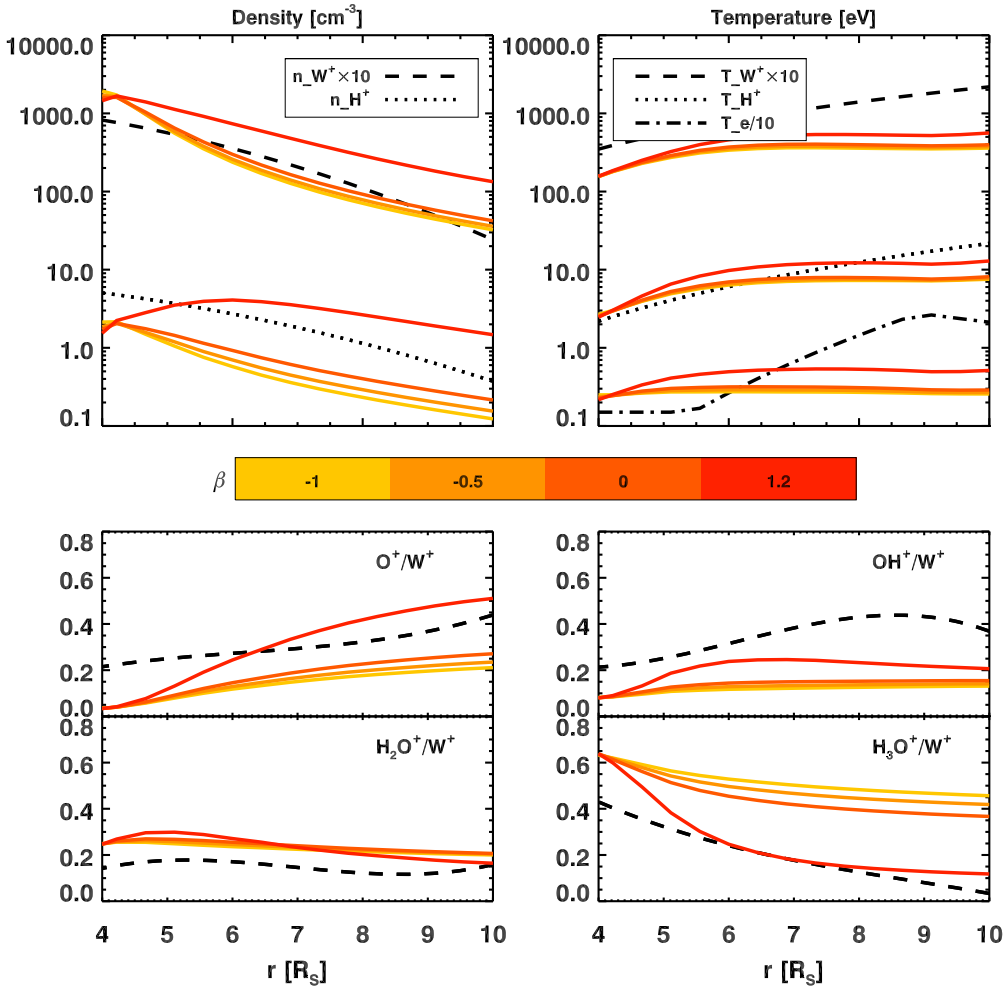


Figure 5.23 Results from the 2-D model for a range of β. All other parameters are set to the nominal values in Table 5.1.

(Figure 5.16), but at the expense of high ion densities. More study is needed to determine if temperatures can be made to agree with data in the 2-D model if τ_0 is allowed to increase to beyond 50 days (Figure 5.17). This is also true of the 2-D model, where densities depart from observations when τ_0 is increased to 20 days.

For $f_{\rm eh}$ = constant ($\beta = 0$), the 2-D model does a better job of fitting the data (Figure 5.22 and Figure 5.23). While the temperatures fit very well in 1-D for $\beta = 0$,

the densities diverge wildly by 2–3 orders of magnitude at $L = 10$. The trend is similar, but not as dramatic, for the 2-D case. In the 1-D model, virtually all ions are O^+ by $L = 10$ due to the fact that the oxygen neutral cloud is most extended (Figure 5.1), as well as the fact that electrons do not efficiently recombine with, and remove O^+ (Figure 5.15).

Without a doubt, f_{eh0} has the greatest control over ion densities at $L = 4$ in both models. It was shown in Chapter 2 that f_{eh} must be at least 0.46% and not more than 0.9% at $L = 4$, which agrees well with Figure 5.20 and Figure 5.21. Unlike in the one-box chemistry model of Chapter 2, we are currently using neutrals from *Cassidy and Johnson* (2010) as background, and not calculating those densities self-consistently. For that reason, H_2O densities are higher than we found in Chapter 2 by a factor of ≈ 4. This would explain the high W^+ densities presented in Figure 5.20 and Figure 5.21 if the water-group ion densities are correlated with the water-group neutral background. It also helps explain the low H^+ densities, which are readily removed by charge exchange (Figure 5.15).

The focus has intentionally not been on electron temperature (T_{e}) throughout this chapter. The main reason is that the model does not yet include additional heating terms due to warm secondary electrons formed from photoionization. This is a hot topic worthy of its own study (*Cravens et al.*, 2011). We note however that our modeled electron temperatures agree well with data at $L = 4$, which is important, given the volume of work suggesting between that T_{e} is between 1 and 2 eV there (*Moncuquet et al.*, 2005; *Young et al.*, 2005; *Sittler et al.*, 2006, 2007; *Lewis et al.*, 2008; *Schippers et al.*, 2008).

Extended sensitivity study

The fact that all parameters influence the model output in the same direction (i.e., densities and temperatures usually increase with increasing τ_0, f_{eh0}, α, β) makes it no surprise that the best fits parameters are related inversely. That is, moving from the nominal fits to lower τ_0 requires raising either f_{eh0}, α, or β—and so on—to offset otherwise decreased densities and temperatures.

In the spirit if making these trends explicit, we have plotted f, the statistic defined in Equation 5.14 for several parameter combinations in Figure 5.24–Figure 5.27. All other combinations can be found in the Appendix C. As defined, the value of f means nothing on its own, but it does serve as a statistic through which sensitivity of the model becomes apparent. It is sufficient to say that $0 < f$, where at no point in any plot does f exceed some arbitrary limit, normalized here to 2 (see color scale).

The hot electron density in Enceladus's orbit (f_{eh0}) is effectively a knob for controlling the amount of impact ionization occurring where neutral H_2O densities peak near $L = 4$. The slope of slope of the hot electron profile, β, drive only minor changes in the model for a given f_{eh0} (Figure 5.22 and Figure 5.23). On the other hand, τ_0 and α control the amount of charge exchange occurring throughout $L = 4$–10. In other words, charge exchange occurs more rapidly from $L = 5$ to $L = 10$ than impact ionization. Because of the models' insensitivity to β compared to the remaining three parameters (Figure 5.22 and Figure 5.23), we have therefore moved contours involving β to Appendix C, and discuss here only the relationships between τ_0, α, and f_{eh0}.

In each of Figure 5.24–Figure 5.27, f is plotted for each of the individual constraints: W^+ and H^+ ion densities; and W^+, H^+, and electron temperatures. The sum of f over

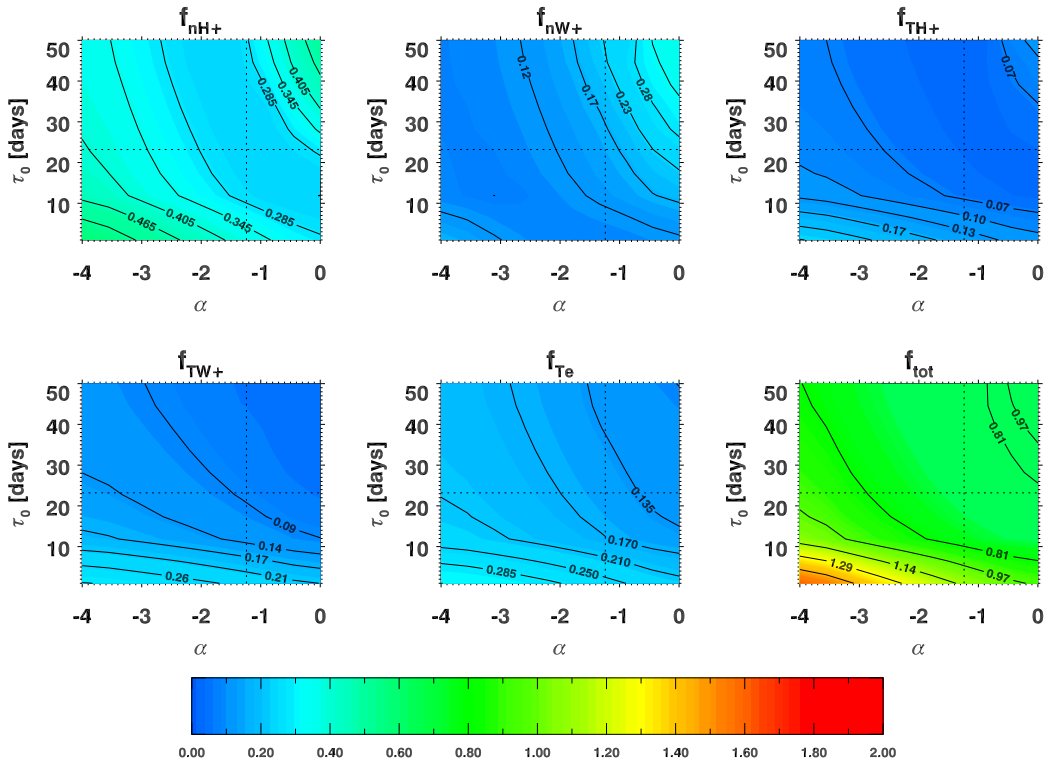


Figure 5.24 1-D model sensitivity: τ_0 versus α. The statistic f is defined by Equation 5.14.

all constraints, entitled $f_{\rm tot}$, is plotted in the lower-right panel of each figure.

In both the 1-D and 2-D models, τ_0 and α are anti-correlated, as discussed above (Figure 5.24 and Figure 5.25). Temperatures, however, are more sensitive to τ_0, while densities depend more on α. Combined, the separate statistics serve to form a pronounced valley for $f_{\rm tot}$, where the densities and temperatures are too large in the upper-right and too low in the lower-left. Unless α is quite large (> 2)—which would be unphysical on the grounds that transport is expected to increase (or remain constant) with increasing L—we see that it is unlikely that τ_0 is less than 10 days, a

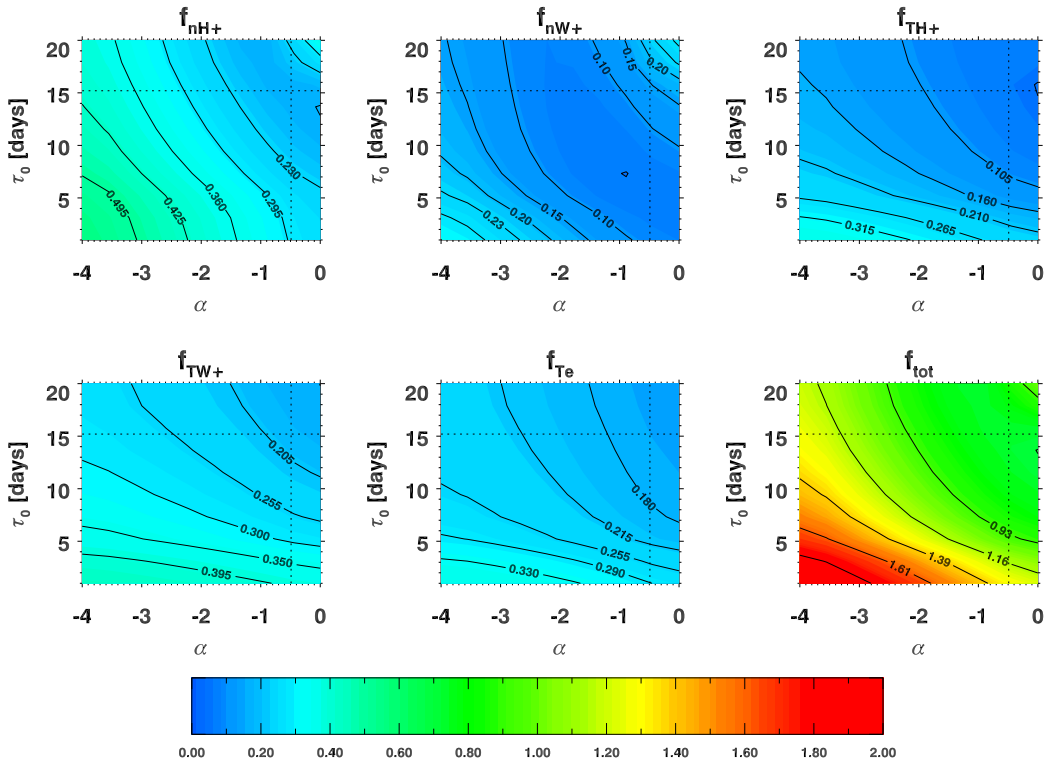


Figure 5.25 2-D model sensitivity: τ_0 versus α. The statistic f is defined by Equation 5.14.

conclusion we also arrived at in Chapter 2.[a]

The 2-D model has stricter requirements on the allowable range in τ_0 and α, which is made apparent by comparing $f_{\rm tot}$ for both models in Figure 5.24 and Figure 5.25 (note the different ranges of τ_0 plotted in each figure). Protons, however, impose the most stringent requirement on both models.

The orthogonality of the density and temperature sensitivity contours is quite pronounced between τ_0 and $f_{\rm eh0}$ in Figure 5.26 and especially so for the 2-D case in Figure

[a]This comment is not strictly true, however, since β and $f_{\rm eh0}$ have been fixed (there may well be a better combination of the latter, whereby $f_{\rm tot}$ would be reduced from values shown here). Future work could include such plots wherein $f_{\rm eh0}$ and β are also free to take on their best fit values as in Chapter 2.

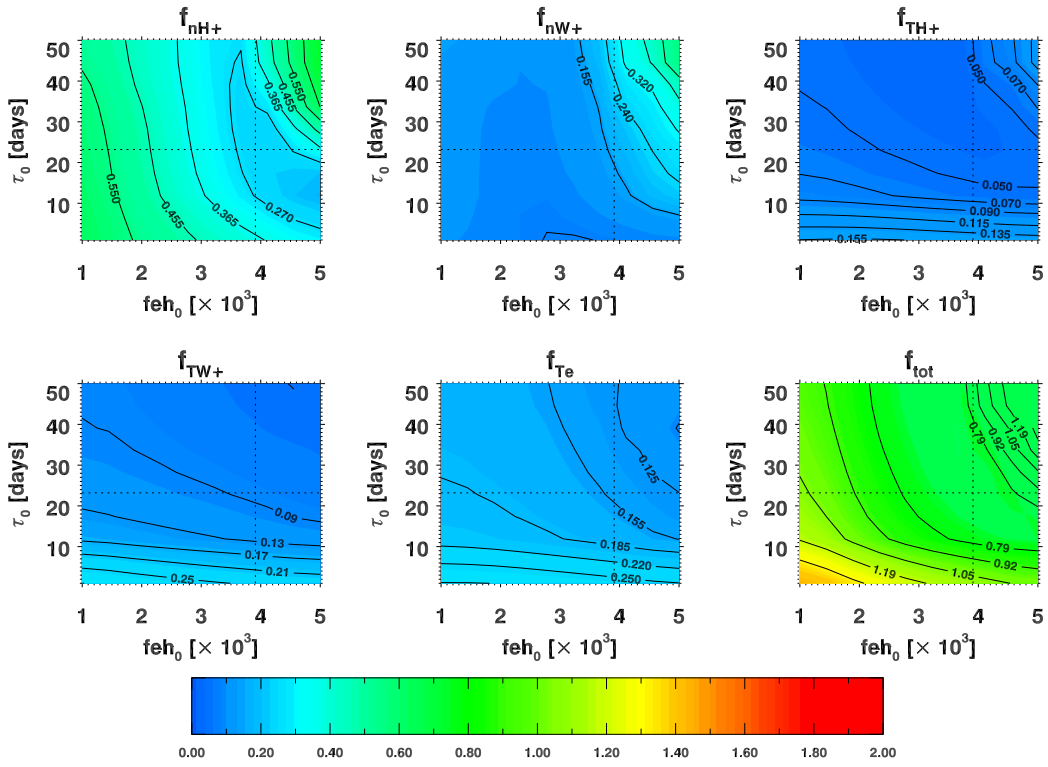


Figure 5.26 1-D model sensitivity: τ_0 versus f_{eh0}. The statistic f is defined by Equation 5.14.

5.27. We assume that the contours become less orthogonal for larger f_{eh0}, just to the right of the ranges plotted in Figure 5.27. It is most evident in these plots the utility of choosing ion density and temperature as constraints. Because of the inverse relationship of the respective parameters, however, Figure 5.24–Figure 5.27 provide only lower limits to each of τ_0, α, f_{eh0}, and β.

In all cases, large τ_0 results in a divergence of $f_{\mathrm{nH+}}$ and $f_{\mathrm{nW+}}$ when either f_{eh0} or β are also large, although agreement with temperatures is improved somewhat. Conversely, when τ_0 along with α or f_{eh0} are small, the temperatures and densities decrease, which creates a steep gradient for f_{tot} in all cases.

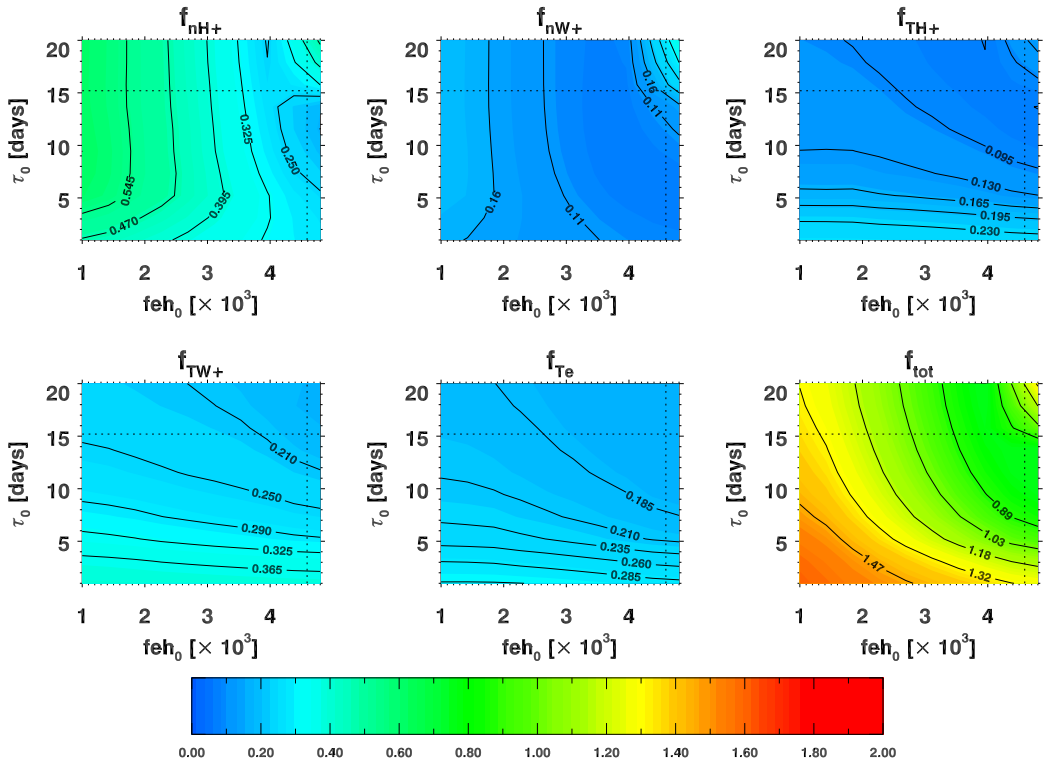


Figure 5.27 2-D model sensitivity: τ_0 versus f_{eh0}. The statistic f is defined by Equation 5.14.

5.4 Discussion

The models (especially the 2-D model) have difficulty simultaneously matching ion densities and electron temperatures beyond $L = 6$.[a] Possibilities are that adiabatic cooling is either not correct, or that the model does not yet include enough physics.

One reason for the disagreement with radial temperatures and densities is that the neutral cloud model used to derive them may need to be more spread out. For instance, reducing the H_2O density at 4 R_S would both lower the associated water-group ion densities (especially H_3O^+), and also increase proton densities, which are

[a] See however, Page 157, regarding electron temperatures.

removed rapidly by charge exchange at 4 R_S (Figure 5.15). In Chapter 2, we were able to model the observed heavy-to-light ion ratios of $W^+/H^+ = 10$, but only with a background neutral density weaker by a factor of ≈ 5.

As for ion relative abundances, there is not enough data published yet from multiple orbits. Also, the response functions used for analyzing CAPS time of flight data makes identifying individual water-group species difficult, particularly when the instrument is operated in the low-mass-resolution mode (*Young et al.*, 2004).

By comparing the 2-D model density and temperature plots (Figure 5.12 and Figure 5.11), one can correlate an ion's temperature with the peak in the neutrals' radial distributions. For example, H_3O^+ is formed largely near $L = 4$, and thus maintains a relatively low temperature as it is transported outward. Conversely, much of the H_2O^+ created near $L = 4$ is swapped for H_3O^+ via $H_2O + H_2O^+ \rightarrow OH + H_3O^+$, and is also recycled by resonant charge exchange, leaving its population formed mostly of that created at larger L, where pickup temperatures are higher.

To increase temperatures, one then might try to increase the range spatially over which fresh ions are produced. Increasing the region over which H_3O^+ is created—beyond $L = 4$—should thus raise water-group temperatures. In other words, by broadening the neutral distribution, one could increase pickup ion production farther out, where pickup energies are higher. Widely-spread neutral clouds have already been observed with HST (*Shemansky and Hall*, 1992), and recent observations with Cassini-UVIS suggest an even more extended neutral cloud (*Melin et al.*, 2009).

Resonant charge exchange between H and H^+ does not alter the proton density. From the point of view of energy, however, the field-aligned distribution of hydrogen

may yet play at least a small role in the input of energy via resonant pickup, since pickup energies at higher latitudes are larger than those at the equator. Future studies should include detailed hydrogen neutral clouds formed as by-products of charge exchange and dissociative recombination to address these issues in detail.

5.5 Conclusions and Future

We have presented our first attempt at a radial model of Saturn's inner magnetosphere ion chemistry. Relative abundances of water-group ions agree with observational trends for a variety of radial transport rates and hot electron densities. Work remains, however, before attempting to fit CAPS data quantitatively (i.e., *Sittler et al.* (2008)). In particular, the neutral cloud models need to be made self-consistent with models of ion chemistry such as the one presented here.

A major goal of this work is to provide CAPS teams with relative water-group abundances for use in their analyses, which with few exceptions (*Sittler et al.*, 2008) use mass=17 amu in their analysis due to uniqueness issues arising when separating out species with similar masses in CAPS time of flight data from.[a]

These results can also be used to improve neutral cloud models, which will in turn be used to improve our chemistry model. Neutral cloud models usually rely on observations extrapolated to all latitudes (*Cassidy and Johnson*, 2010) to calculate neutral loss rates, whereas the present model provides chemically self-consistent maps throughout. Additional conclusions and comments are enumerated below.

[a]For computational reasons, researchers using forward modeling techniques generally deem their identification less necessary than sorting out the more important issue of CAPS not observing the complete velocity distributions (R. Wilson, personal communication).

(1) Given the observed ion densities and temperatures, we find that hot electrons are expected to be at least 0.3% at Enceladus, and likely not more than 1%, consistent with our earlier one-box study (Chapter 2).

(2) Transport must occur on a time scale not less than 10 days per L at Enceladus in order for densities to be increased via impact ionization, but also to increase H_3O^+ abundances, which arise naturally from charge exchange in regions where H_2O densities are high and occupation periods are long (Chapter 3).

(3) Our estimate of the total ion mass of ($\approx$ 200 kton) agrees well with Figure 7 of *Bagenal and Delamere* (2011), while the mass source rate of 20–30 kg s^{-1} at $L = 10$ is consistent with a paper in preparation by Peter Delamere relating $\dot{M}$ to solar wind conditions at Saturn (*Delamere and Bagenal* (2012); Figure 5.4 and Figure 5.5).

The plan is to expand the current model to three dimensions to study both spatial and temporal effects in Saturn's inner magnetosphere associated with Enceladus's plume variabitity. One could also study seasonal effects associated with the relative importance of photo- and impact dissociation, which are responsible for many cloud-forming neutrals. A number of these processes may prove to drive observable responses in Saturn's magnetosphere on various timescales due to chemistry alone. It is expected that any process which alters the global distribution of neutrals—as well as their relative abundances—will have a dynamic effect on ion densities and temperatures throughout the inner magnetosphere.

Chapter 6

Future work

The work presented here summarizes the state of the models and interpretations thereof at present. The results within will be a useful resource for the analysis of CAPS data in the future, and for the improvement of neutral cloud models. Some suggestions for further study are listed below.

(1) The model of the local interaction (Chapter 3) serves as a first step in modeling the chemical evolution of ions as they pass through Enceladus's plumes. Future efforts should use loss rates based on the chemistry model to improve hybrid models, wherein electrons are treated as fluids and ions are collectively treated as a single kinetic species. The hybrid model would then self-consistently calculate the perturbed flows for use in the chemistry model, and so on.

(2) Neutral cloud models should be improved to include the effects of asymmetric charge exchange as well as species-dependent charge exchanges (Chapter 4). Both are expected to affect neutral cloud mass as well as morphology.

(3) The radial models presented in Chapter 5 provide insight into the parameter space within which hot electrons and radial transport compete to create and remove ions in Saturn's inner magnetosphere. Future work should take a more robust approach by including the diffusion equations for transport of mass and energy, though the present results are not expected to be affected qualitatively, given the short chemical timescales compared to transport, particularly inside of 7 R_S.

(4) Given the relatively high frequency of planets in our own solar system with

geologically-active moons protected by giant magnetospheres, one can expect that many such systems await discovery orbiting other stars. The results presented here, along with comparative studies involving Jupiter, provide a baseline for inderstanding neutral cloud morphology, ion composition, and the flow of mass and energy such systems, when discovered.

References[a]

Aikin, A. C. (1974), Cometary coma ions, ApJ, *193*, 263–+, doi:10.1086/153156. 70

Albritton, D. L. (1978), Ion-neutral reaction-rate constants measured in flow reactors through 1977, *Atomic Data and Nuclear Data Tables*, *22*(1), 1 – 89, doi:10.1016/0092-640X(78)90027-X. 80, 193

Bagenal, F. (1997), Ionization source near Io from Galileo wake data, Geophys. Res. Lett., *24*, 2111, doi:10.1029/97GL02052. 97

Bagenal, F., and P. A. Delamere (2011), Flow of mass and energy in the magnetospheres of Jupiter and Saturn, *Journal of Geophysical Research (Space Physics)*, *116*, A05,209, doi:10.1029/2010JA016294. 105, 134, 165

Bagenal, F., and J. D. Sullivan (1981), Direct plasma measurements in the Io torus and inner magnetosphere of Jupiter, J. Geophys. Res., *86*, 8447–8466, doi:10.1029/JA086iA10p08447. 126, 127

Bagenal, F., J. D. Sullivan, and G. L. Siscoe (1980), Spatial distribution of plasma in the Io torus, Geophys. Res. Lett., *7*, 41–44. 17

Bagenal, F., T. E. Dowling, and W. B. McKinnon (2004), *Jupiter : the planet, satellites and magnetosphere*. 5

Barbosa, D. D. (1994), Neutral cloud theory of the Jovian nebula: Anomalous ionization effect of superthermal electrons, ApJ, *430*, 376–386, doi:10.1086/174413. 25

Barbosa, D. D., F. V. Coroniti, and A. Eviatar (1983), Coulomb thermal properties and stability of the Io plasma torus, ApJ, *274*, 429–442, doi:10.1086/161459.

Bondi, A. (1964), van der waals volumes and radii, *Journal of Physical Chemistry*, *68*(3), 441–451. 108

Book, D. L. (1983), NRL (Naval Research Laboratory) plasma formulary, revised, *Tech. rep.* 182

Bridge, H. S., et al. (1981), Plasma observations near Saturn - Initial results from Voyager 1, *Science*, *212*, 217–224, doi:10.1126/science.212.4491.217. 16

Bridge, H. S., et al. (1982), Plasma observations near Saturn - Initial results from Voyager 2, *Science*, *215*, 563–570, doi:10.1126/science.215.4532.563. 16

Burger, M. H., E. C. Sittler, R. E. Johnson, H. T. Smith, O. J. Tucker, and V. I. Shematovich (2007), Understanding the escape of water from Enceladus, *Journal of Geophysical Research (Space Physics)*, *112*, 6219–+, doi:10.1029/2006JA012086. 19, 60, 70

[a]Numbers trailing the references are the pages on which they are cited.

Cassidy, T. A., and R. E. Johnson (2010), Collisional spreading of Enceladus's neutral cloud, *Icaraus* , *209*, 696–703, doi:10.1016/j.icarus.2010.04.010. xiii, xiv, 5, 9, 10, 74, 75, 80, 82, 84, 95, 102, 104, 107, 110, 113, 116, 117, 118, 119, 157, 164

Cravens, T. E., R. L. McNutt, J. H. Waite, I. P. Robertson, J. G. Luhmann, W. Kasprzak, and W.-H. Ip (2009), Plume ionosphere of Enceladus as seen by the Cassini ion and neutral mass spectrometer, Geophys. Res. Lett., *36*, 8106–+, doi: 10.1029/2009GL037811. 44, 57, 70, 117

Cravens, T. E., N. Ozak, M. S. Richard, M. E. Campbell, I. P. Robertson, M. Perry, and A. M. Rymer (2011), Electron energetics in the Enceladus torus, *Journal of Geophysical Research (Space Physics)*, *116*, A09205, doi:10.1029/2011JA016498. 157

Delamere, P. A., and F. Bagenal (2003), Modeling variability of plasma conditions in the Io torus, *Journal of Geophysical Research (Space Physics)*, *108*, 1276–+, doi: 10.1029/2002JA009706. 14, 24, 25, 61, 178

Delamere, P. A., and F. Bagenal (2008), Longitudinal plasma density variations at Saturn caused by hot electrons, Geophys. Res. Lett., *35*, 3107–+, doi:10.1029/ 2007GL031095. 53

Delamere, P. A., and F. Bagenal (2012), Estimating the size of the giant magnetospheres: Contraints on internal plasma transport rates, *(in preparation)*. 12, 134, 165

Delamere, P. A., F. Bagenal, and A. Steffl (2005), Radial variations in the Io plasma torus during the Cassini era, *Journal of Geophysical Research (Space Physics)*, *110*, A12223, doi:10.1029/2005JA011251. 7, 126

Delamere, P. A., F. Bagenal, V. Dols, and L. C. Ray (2007), Saturn's neutral torus versus Jupiter's plasma torus, Geophys. Res. Lett., *34*, 9105–+, doi:10.1029/ 2007GL029437. 14, 15, 25, 33, 34, 38, 40, 57, 61, 84

Dere, K. P., E. Landi, H. E. Mason, B. C. Monsignori Fossi, and P. R. Young (1997), CHIANTI - an atomic database for emission lines, A&AS, *125*, 149–173. 183

Dols, V., P. A. Delamere, and F. Bagenal (2008), A multispecies chemistry model of Io's local interaction with the Plasma Torus, *Journal of Geophysical Research (Space Physics)*, *113*, 9208–+, doi:10.1029/2007JA012805. 1, 16, 62, 63, 64, 97

Dougherty, M. K., K. K. Khurana, F. M. Neubauer, C. T. Russell, J. Saur, J. S. Leisner, and M. E. Burton (2006a), Discovery of a Dynamic Atmosphere at Enceladus from Cassini Magnetometer Observations, in *37th Annual Lunar and Planetary Science Conference*, *Lunar and Planetary Institute Conference Abstracts*, vol. 37, edited by S. Mackwell and E. Stansbery, pp. 1585–+. 117

Dougherty, M. K., K. K. Khurana, F. M. Neubauer, C. T. Russell, J. Saur, J. S. Leisner, and M. E. Burton (2006b), Discovery of a Dynamic Atmosphere at Enceladus from Cassini Magnetometer Observations, in *37th Annual Lunar and Planetary Science*

Conference, *Lunar and Planetary Institute Conference Abstracts*, vol. 37, edited by S. Mackwell and E. Stansbery, pp. 1585–+. x, 4, 35, 60

Esposito, L. W., et al. (2005), Ultraviolet Imaging Spectroscopy Shows an Active Saturnian System, *Science*, *307*, 1251–1255, doi:10.1126/science.1105606. 45, 73

Farmer, A. J. (2009), Saturn in hot water: Viscous evolution of the enceladus torus, *Icarus*, *In Press, Corrected Proof*, –, doi:DOI:10.1016/j.icarus.2009.02.031. 36, 37

Farmer, A. J. (2009), Saturn in hot water: Viscous evolution of the Enceladus torus, *Icaraus* , *202*, 280–286, doi:10.1016/j.icarus.2009.02.031. 9, 74

Fleshman, B. L., P. A. Delamere, and F. Bagenal (2010a), Modeling the Enceladus plume-plasma interaction, Geophys. Res. Lett., *37*, L03,202, doi:10.1029/2009GL041613. 12

Fleshman, B. L., P. A. Delamere, and F. Bagenal (2010b), A sensitivity study of the Enceladus torus, *Journal of Geophysical Research (Planets)*, *115*, 4007–+, doi:10.1029/2009JE003372. 12, 61, 83, 84

Fleshman, B. L., P. A. Delamere, F. Bagenal, and T. Cassidy (2012), The roles of charge exchange and dissociation in spreading Saturn's neutral clouds, *Journal of Geophysical Research (Planets)*, *117*, E05007, doi:10.1029/2011JE003996. 12

Frank, L. A., B. G. Burek, K. L. Ackerson, J. H. Wolfe, and J. D. Mihalov (1980), Plasmas in Saturn's magnetosphere, J. Geophys. Res., *85*, 5695–5708, doi:10.1029/JA085iA11p05695. 16

Giguere, P. T., and W. F. Huebner (1978), A model of comet comae. I - Gas-phase chemistry in one dimension, ApJ, *223*, 638–654, doi:10.1086/156298. 193

Gurnett, D. A., A. M. Persoon, W. S. Kurth, J. B. Groene, T. F. Averkamp, M. K. Dougherty, and D. J. Southwood (2007), The Variable Rotation Period of the Inner Region of Saturn's Plasma Disk, *Science*, *316*, 442–, doi:10.1126/science.1138562. 53, 58

Gurnett, D. A., et al. (2004), The Cassini Radio and Plasma Wave Investigation, *Space Science Reviews*, *114*, 395–463, doi:10.1007/s11214-004-1434-0. 23

Gurnett, D. A., et al. (2005), Radio and Plasma Wave Observations at Saturn from Cassini's Approach and First Orbit, *Science*, *307*, 1255–1259, doi:10.1126/science.1105356. 22

Haberli, R. M., M. R. Combi, T. I. Gombosi, D. L. de Zeeuw, and K. G. Powell (1997), Quantitative Analysis of H_2O^+ Coma Images Using a Multiscale MHD Model with Detailed Ion Chemistry, *Icarus*, *130*, 373–386, doi:10.1006/icar.1997.5835. 70

Hansen, C. J., L. Esposito, A. I. F. Stewart, J. Colwell, A. Hendrix, W. Pryor, D. Shemansky, and R. West (2006), Enceladus' Water Vapor Plume, *Science*, *311*, 1422–1425, doi:10.1126/science.1121254. x, 4, 14, 19, 59, 60, 73, 77, 80, 117

Hansen, C. J., et al. (2011), The composition and structure of the Enceladus plume, Geophys. Res. Lett., *381*, L11,202, doi:10.1029/2011GL047415. 80

Hartogh, P., et al. (2011), Direct detection of the Enceladus water torus with Herschel, A&A, *532*, L2+, doi:10.1051/0004-6361/201117377. 74, 106, 112, 113

Huebner, W. F., and C. W. Carpenter (1979a), Solar photo rate coefficients, *NASA STI/Recon Technical Report N*, *80*, 24,243–+. 192

Huebner, W. F., and C. W. Carpenter (1979b), Solar photo rate coefficients, *NASA STI/Recon Technical Report N*, *80*, 24,243–+. 78, 83, 103

Huntress, W. T., Jr. (1977), Laboratory studies of bimolecular reactions of positive ions in interstellar clouds, in comets, and in planetary atmospheres of reducing composition, ApJS, *33*, 495–514. 193

Ip, W.-H. (2000), Thermal plasma composition in Saturn's magnetosphere, Planet. Space Sci., *48*, 775–783, doi:10.1016/S0032-0633(00)00036-2. 117

Jackman, C. M., and C. S. Arridge (2011), Solar Cycle Effects on the Dynamics of Jupiter's and Saturn's Magnetospheres, Sol. Phys., pp. 77–+, doi:10.1007/s11207-011-9748-z. 78, 99

Johnson, R. E. (1990), *Energetic Charged-Particle Interactions with Atmospheres and Surfaces*. 84, 85, 92, 94

Johnson, R. E., H. T. Smith, O. J. Tucker, M. Liu, M. H. Burger, E. C. Sittler, and R. L. Tokar (2006), The Enceladus and OH Tori at Saturn, ApJ, *644*, L137–L139, doi:10.1086/505750. xiii, 9, 70, 73, 75, 102, 104, 118, 181

Jurac, S., and J. D. Richardson (2005), A self-consistent model of plasma and neutrals at Saturn: Neutral cloud morphology, *Journal of Geophysical Research (Space Physics)*, *110*, 9220–+, doi:10.1029/2004JA010635. 10, 14, 16, 19, 30, 75, 80, 82, 84, 117, 118

Jurac, S., and J. D. Richardson (2007), Neutral cloud interaction with Saturn's main rings, Geophys. Res. Lett., *34*, L08,102, doi:10.1029/2007GL029567. xiii, 102, 104

Jurac, S., M. A. McGrath, R. E. Johnson, J. D. Richardson, V. M. Vasyliunas, and A. Eviatar (2002), Saturn: Search for a missing water source, Geophys. Res. Lett., *29*(24), 2172, doi:10.1029/2002GL015855. 16, 19, 30, 73

Khurana, K. K., M. K. Dougherty, C. T. Russell, and J. S. Leisner (2007), Mass loading of Saturn's magnetosphere near Enceladus, *Journal of Geophysical Research (Space Physics)*, *112*, 8203–+, doi:10.1029/2006JA012110. 60

Landi, E., G. Del Zanna, P. R. Young, K. P. Dere, H. E. Mason, and M. Landini (2006), CHIANTI-An Atomic Database for Emission Lines. VII. New Data for X-Rays and Other Improvements, ApJS, *162*, 261–280, doi:10.1086/498148. 183

Lewis, G. R., N. André, C. S. Arridge, A. J. Coates, L. K. Gilbert, D. R. Linder, and A. M. Rymer (2008), Derivation of density and temperature from the Cassini–Huygens CAPS electron spectrometer, Planet. Space Sci., *56*, 901–912, doi:10.1016/j.pss.2007.12.017. 20, 21, 22, 23, 157

Li, X., Y.-L. Huang, G. D. Flesch, and C. Y. Ng (1995), Absolute total cross sections for the ion-molecule reaction $O^+(^4S^o)+H_2O$, J. Chem. Phys., *102*, 5100–5101, doi:10.1063/1.469561. xii, 88

Lichtenberg, G., N. Thomas, and T. Fouchet (2001), Detection of S(IV) 10.51 μm emission from the Io plasma torus, J. Geophys. Res., *106*, 29,899–29,910, doi:10.1029/2001JA900020. 25

Lishawa, C. R., R. A. Dressler, J. A. Gardner, R. H. Salter, and E. Murad (1990), Cross sections and product kinetic energy analysis of h2o+?h2o collisions at suprathermal energies, *93*(5), 3196–3206, doi:DOI:10.1063/1.458852. ix, xii, 80, 88, 193

Makarov, O. P., J. M. Ajello, P. Vattipalle, I. Kanik, M. C. Festou, and A. Bhardwaj (2004), Kinetic energy distributions and line profile measurements of dissociation products of water upon electron impact, *Journal of Geophysical Research (Space Physics)*, *109*, A09,303, doi:10.1029/2002JA009353. 75, 82, 99

Massey, H. S. W., E. H. S. Burhop, and H. B. Gilbody (1974), *Electronic and ionic impact phenomena*, The International Series of Monographs on Physics, Oxford: Clarendon Press, 1969-1974, 2nd ed. 193

McGrath, M. A., and R. E. Johnson (1989), Charge exchange cross sections for the Io plasma torus, J. Geophys. Res., *94*, 2677–2683. 193

Melin, H., D. E. Shemansky, and X. Liu (2009), The distribution of atomic hydrogen and oxygen in the magnetosphere of Saturn, Planet. Space Sci., *57*, 1743–1753, doi:10.1016/j.pss.2009.04.014. 73, 84, 109, 119, 163

Millar, T. J., A. Bennett, J. M. C. Rawlings, P. D. Brown, and S. B. Charnley (1991), Gas phase reactions and rate coefficients for use in astrochemistry - The UMIST ratefile, A&AS, *87*, 585–619. 193

Moncuquet, M., A. Lecacheux, N. Meyer-Vernet, B. Cecconi, and W. S. Kurth (2005), Quasi thermal noise spectroscopy in the inner magnetosphere of Saturn with Cassini/RPWS: Electron temperatures and density, Geophys. Res. Lett., *32*, 20–+, doi:10.1029/2005GL022508. 20, 21, 22, 23, 26, 31, 61, 124, 157

Mul, P. M., J. W. McGowan, P. Defrance, and J. B. A. Mitchell (1983), Merged electron-ion beam experiments. V - Dissociative recombination of OH(+), H2O(+), H3O(+) and D3O(+), *Journal of Physics B Atomic Molecular Physics*, *16*, 3099–3107. 191

Nahar, S. N. (1999), Electron-Ion Recombination Rate Coefficients, Photoionization Cross Sections, and Ionization Fractions for Astrophysically Abundant Elements. II. Oxygen Ions, ApJS, *120*, 131–145, doi:10.1086/313173. 190

Newman, J. H., J. D. Cogan, D. L. Ziegler, D. E. Nitz, R. D. Rundel, K. A. Smith, and R. F. Stebbings (1982), Charge transfer in H/+/-H and H/+/-D collisions within the energy range 0.1-150 eV, Phys. Rev. A, *25*, 2976–2984. 193

Orient, G. S., and S. K. Strivastava (1987), Electron impact ionization of H_2O, CO, CO_2 and CH_4, *Journal of Physics B: Atomic and Molecular Physics*, *20*, 3923–3936. 188, 189

Peart, B., and K. T. Dolder (1974), Collisions between electrons and H_2^+ ions. V. Measurements of cross sections for dissociative recombination, *Journal of Physics B: Atomic and Molecular Physics*, *7*, 236–243. 191

Persoon, A. M., D. A. Gurnett, W. S. Kurth, G. B. Hospodarsky, J. B. Groene, P. Canu, and M. K. Dougherty (2005), Equatorial electron density measurements in Saturn's inner magnetosphere, Geophys. Res. Lett., *32*, 23,105–+, doi: 10.1029/2005GL024294. 22

Persoon, A. M., et al. (2009), A diffusive equilibrium model for the plasma density in Saturn's magnetosphere, *Journal of Geophysical Research (Space Physics)*, *114*, 4211–+, doi:10.1029/2008JA013912. 17, 22, 24, 26, 27

Pontius, D. H., and T. W. Hill (2006), Enceladus: A significant plasma source for Saturn's magnetosphere, *Journal of Geophysical Research (Space Physics)*, *111*, 9214–+, doi:10.1029/2006JA011674. 60

Porco, C. C., et al. (2006), Cassini Observes the Active South Pole of Enceladus, *Science*, *311*, 1393–1401, doi:10.1126/science.1123013. 3, 59, 77

Pryor, W. R., et al. (2011), The auroral footprint of Enceladus on Saturn, Nature, *472*, 331–333, doi:10.1038/nature09928.

Rapp, D., and W. E. Francis (1962), Charge Exchange between Gaseous Ions and Atoms, J. Chem. Phys., *37*, 2631–2645, doi:10.1063/1.1733066. 85, 93, 94

Reif, F. (1965), *Fundamentals of statistical and thermal physics / [by] F. Reif*, international student ed. ed., x, 651 p. : pp., McGraw-Hill Kogakusha, Tokyo :. 201

Richardson, J. D., and E. C. Sittler, Jr. (1990), A plasma density model for Saturn based on Voyager observations, J. Geophys. Res., *95*, 12,019–12,031, doi:10.1029/JA095iA08p12019. 26, 31

Richardson, J. D., A. Eviatar, and G. L. Siscoe (1986), Satellite tori at Saturn, J. Geophys. Res., *91*, 8749–8755, doi:10.1029/JA091iA08p08749. 16

Richardson, J. D., A. Eviatar, M. A. McGrath, and V. M. Vasyliũnas (1998), OH in Saturn's magnetosphere: Observations and implications, J. Geophys. Res., *103*, 20,245–20,256, doi:10.1029/98JE01127. 16, 19, 20, 26, 117

Rymer, A. M., B. H. Mauk, T. W. Hill, C. Paranicas, D. G. Mitchell, A. J. Coates, and D. T. Young (2008), Electron circulation in Saturn's magnetosphere, *Journal of Geophysical Research (Space Physics)*, *113*, A01201, doi:10.1029/2007JA012589. 20, 105

Rymer, A. M., et al. (2007), Electron sources in Saturn's magnetosphere, *Journal of Geophysical Research (Space Physics)*, *112*, A02201, doi:10.1029/2006JA012017. 105

Saur, J., N. Schilling, F. M. Neubauer, D. F. Strobel, S. Simon, M. K. Dougherty, C. T. Russell, and R. T. Pappalardo (2008), Evidence for temporal variability of Enceladus' gas jets: Modeling of Cassini observations, Geophys. Res. Lett., *35*, 20,105–+, doi: 10.1029/2008GL035811. 6, 8, 60, 77, 81

Schippers, P., et al. (2008), Multi-instrument analysis of electron populations in Saturn's magnetosphere, *Journal of Geophysical Research (Space Physics)*, *113*, 7208–+, doi:10.1029/2008JA013098. xiv, xv, 21, 23, 80, 120, 123, 138, 139, 157

Schreier, R., A. Eviatar, and V. M. Vasyliūnas (1998), A two-dimensional model of plasma transport and chemistry in the Jovian magnetosphere, J. Geophys. Res., *103*, 19,901–19,914, doi:10.1029/98JE00697. 25

Shemansky, D. E. (1988), Energy branching in the Io plasma torus - The failure of neutral cloud theory, J. Geophys. Res., *93*, 1773–1784. 25

Shemansky, D. E., and D. T. Hall (1992), The distribution of atomic hydrogen in the magnetosphere of Saturn, J. Geophys. Res., *97*, 4143–4161, doi:10.1029/91JA02805. 73, 119, 163, 194

Shemansky, D. E., P. Matheson, D. T. Hall, H. Hu, and T. M. Tripp (1993a), Detection of the hydroxyl radical in the Saturn magnetosphere, Nature, *363*, 329–331, doi: 10.1038/363329a0. 73, 74

Shemansky, D. E., P. Matheson, D. T. Hall, H.-Y. Hu, and T. M. Tripp (1993b), Detection of the hydroxyl radical in the Saturn magnetosphere, Nature, *363*, 329–331, doi:10.1038/363329a0. 14, 181

Siscoe, G. L. (1978), Jovian plasmaspheres, J. Geophys. Res., *83*, 2118–2126, doi: 10.1029/JA083iA05p02118. 128, 129

Sittler, E. C., et al. (2005), Preliminary results on Saturn's inner plasmasphere as observed by Cassini: Comparison with Voyager, Geophys. Res. Lett., *32*, 14–+, doi: 10.1029/2005GL022653. 15, 73

Sittler, E. C., et al. (2006), Cassini observations of Saturn's inner plasmasphere: Saturn orbit insertion results, Planet. Space Sci., *54*, 1197–1210, doi:10.1016/j.pss.2006.05.038. xiv, xv, 20, 23, 24, 26, 30, 31, 36, 116, 123, 127, 138, 139, 142, 143, 145, 148, 157

Sittler, E. C., et al. (2007), Erratum to "Cassini observations of Saturn's inner plasmasphere: Saturn orbit insertion results". [Planetary and Space Science 54 (2006) 1197 1210], Planet. Space Sci., *55*, 2218–2220, doi:10.1016/j.pss.2006.11.022. xiv, xv, 23, 24, 26, 30, 31, 36, 123, 138, 139, 142, 143, 157

Sittler, E. C., et al. (2008), Ion and neutral sources and sinks within Saturn's inner magnetosphere: Cassini results, Planet. Space Sci., *56*, 3–18, doi:10.1016/j.pss.2007.06.006. xv, 17, 21, 24, 34, 35, 36, 44, 46, 57, 62, 69, 73, 74, 78, 79, 87, 92, 105, 112, 145, 146, 147, 148, 164

Sittler, E. C., Jr., K. W. Ogilvie, and J. D. Scudder (1983), Survey of low-energy plasma electrons in Saturn's magnetosphere - Voyagers 1 and 2, J. Geophys. Res., *88*, 8847–8870, doi:10.1029/JA088iA11p08847. 16, 21

Smith, H. T. (2006), The search for nitrogen in Saturn's magnetosphere, Ph.D. thesis, University of Virginia, Virginia, USA. 76

Smith, H. T., R. E. Johnson, and V. I. Shematovich (2004), Titan's atomic and molecular nitrogen tori, Geophys. Res. Lett., *311*, L16,804, doi:10.1029/2004GL020580. 76

Smith, H. T., R. E. Johnson, M. E. Perry, D. G. Mitchell, R. L. McNutt, and D. T. Young (2010), Enceladus plume variability and the neutral gas densities in Saturn's magnetosphere, *Journal of Geophysical Research (Space Physics)*, *115*, 10,252–+, doi:10.1029/2009JA015184. 76, 77, 84

Smith, H. T., et al. (2007), Enceladus: The likely dominant nitrogen source in Saturn's magnetosphere, *Icaraus* , *188*, 356–366, doi:10.1016/j.icarus.2006.12.007. 76

Spencer, J. R., et al. (2006), Cassini Encounters Enceladus: Background and the Discovery of a South Polar Hot Spot, *Science*, *311*, 1401–1405, doi:10.1126/science.1121661. 3, 59, 77

Stebbings, R. F., and J. A. Rutherford (1968), Low-Energy Collisions Between O^+ (4 S) and H (1s), J. Geophys. Res., *73*, 1035–1038. 193

Stebbings, R. F., A. C. H. Smith, and H. Ehrhardt (1964), Charge Transfer between Oxygen Atoms and O^+ and H^+ Ions, J. Geophys. Res., *69*, 2349–2355. 193

Steffl, A. J., F. Bagenal, and A. I. F. Stewart (2004a), Cassini UVIS observations of the Io plasma torus. II. Radial variations, *Icarus*, *172*, 91–103, doi:10.1016/j.icarus.2004.04.016. 14

Steffl, A. J., A. I. F. Stewart, and F. Bagenal (2004b), Cassini UVIS observations of the Io plasma torus. I. Initial results, *Icarus*, *172*, 78–90, doi:10.1016/j.icarus.2003.12.027. 14

Steffl, A. J., P. A. Delamere, and F. Bagenal (2006), Cassini UVIS observations of the Io plasma torus. III. Observations of temporal and azimuthal variability, *Icarus*, *180*, 124–140, doi:10.1016/j.icarus.2005.07.013. 14, 55

Steffl, A. J., P. A. Delamere, and F. Bagenal (2008), Cassini UVIS observations of the Io plasma torus. IV. Modeling temporal and azimuthal variability, *Icarus*, *194*, 153–165, doi:10.1016/j.icarus.2007.09.019. 14, 15, 53

Tarnovsky, V., H. Deutsch, and K. Becker (1998), Electron impact ionization of the hydroxyl radical, J. Chem. Phys., *109*, 932–936, doi:10.1063/1.476635. 188

Tawara, H. (1978), Cross sections for charge transfer of hydrogen beams in gases and vapors in the energy range 10 eV−10 keV , *Atomic Data and Nuclear Data Tables*, *22*, 491–525. 193

Teske, V., E. Vogel, and E. Bich (2005), Viscosity measurements on water vapor and their evaluation, *Journal of Chemical & Engineering Data*, *50*(6), 2082–2087, doi: 10.1021/je050288d. 108

Thomas, N., F. Bagenal, T. W. Hill, and J. K. Wilson (2004), *The Io neutral clouds and plasma torus*, pp. 561–591. 14

Tokar, R. L., R. E. Johnson, M. F. Thomsen, R. J. Wilson, D. T. Young, F. J. Crary, A. J. Coates, G. H. Jones, and C. S. Paty (2009), Cassini detection of Enceladus' cold water-group plume ionosphere, Geophys. Res. Lett., *36*, 13,203–+, doi:10.1029/ 2009GL038923. 61, 66

Tokar, R. L., et al. (2006), The Interaction of the Atmosphere of Enceladus with Saturn's Plasma, *Science*, *311*, 1409–1412, doi:10.1126/science.1121061. 19, 60, 69, 70

Tokar, R. L., et al. (2008), Cassini detection of water-group pick-up ions in the Enceladus torus, Geophys. Res. Lett., *35*, 14,202–+, doi:10.1029/2008GL034749. 26

Trainor, J. H., F. B. McDonald, and A. W. Schardt (1980), Observations of energetic ions and electrons in Saturn's magnetosphere, *Science*, *207*, 421–425, doi:10.1126/ science.207.4429.421. 16

Vasyliunas, V. M. (1968), Low-Energy Electrons in the Magnetosphere as Observed by OGO-1 and OGO-3, in *Physics of the Magnetosphere*, *Astrophysics and Space Science Library*, vol. 10, edited by R. D. L. Carovillano and J. F. McClay, p. 622. 122

Verner, D. A., and G. J. Ferland (1996), Atomic Data for Astrophysics. I. Radiative Recombination Rates for H-like, He-like, Li-like, and Na-like Ions over a Broad Range of Temperature, ApJS, *103*, 467–+, doi:10.1086/192284. 190

Voronov, G. S. (1997), A practical fit formula for ionization rate coefficients of atoms and ions by electron impact: Z=1–28, *Atomic Data and Nuclear Data Tables*, *65*, 1–35. 188

Waite, J. H., et al. (2006), Cassini Ion and Neutral Mass Spectrometer: Enceladus Plume Composition and Structure, *Science*, *311*, 1419–1422, doi:10.1126/science. 1121290. 59, 60

Weiser, H., R. C. Vitz, and H. W. Moos (1977), Detection of Lyman-alpha emission from the Saturnian disk and from the ring system, *Science*, *197*, 755–757, doi:10.1126/science.197.4305.755. 73

Williams, J. D., P. A. Delamere, F. Bagenal, D. Reisenfeld, and R. Fleshman (2008), Water Group Composition Near the Orbit of Enceladus, *AGU Fall Meeting Abstracts*, pp. B1384+. 44

Wilson, R. J., R. L. Tokar, M. G. Henderson, T. W. Hill, M. F. Thomsen, and D. H. Pontius (2008), Cassini plasma spectrometer thermal ion measurements in Saturn's inner magnetosphere, *Journal of Geophysical Research (Space Physics)*, *113*, 12,218–+, doi:10.1029/2008JA013486. xiv, xv, 24, 51, 124, 137, 138, 139

Wilson, R. J., R. L. Tokar, and M. G. Henderson (2009), Thermal ion flow in Saturn's inner magnetosphere measured by the Cassini plasma spectrometer: A signature of the Enceladus torus?, Geophys. Res. Lett., *36*, L23104, doi:10.1029/2009GL040225. 62, 87, 96

Wolfe, J. H., J. D. Mihalov, H. R. Collard, D. D. McKibbin, L. A. Frank, and D. S. Intriligator (1980), Preliminary results on the plasma environment of Saturn from the Pioneer 11 plasma analyzer experiment, *Science*, *207*, 403–407, doi:10.1126/science.207.4429.403. 16

Wu, C. Y. R., and F. Z. Chen (1993), Velocity distributions of hydrogen atoms and hydroxyl radicals produced through solar photodissociation of water, J. Geophys. Res., *98*, 7415–7435, doi:10.1029/92JE03016. 75, 82, 99

Young, D. T., et al. (2004), Cassini Plasma Spectrometer Investigation, Space Sci. Rev., *114*, 1–112, doi:10.1007/s11214-004-1406-4. 60, 145, 163

Young, D. T., et al. (2005), Composition and Dynamics of Plasma in Saturn's Magnetosphere, *Science*, *307*, 1262–1266, doi:10.1126/science.1106151. 20, 21, 23, 24, 34, 61, 73, 78, 157

Zwillinger, D., and C. R. Company (1996), *CRC standard mathematical tables and formulae*, no. v. 30 in CRC Standard Mathematical Tables & Formulae, CRC Press. 201

Appendix A

One-box model: calculations and tables

A.1 Equations

The basic equations (*Barbosa et al.*, 1983) for number density and energy density for species α are

$$\frac{\partial n_\alpha}{\partial t} = \mathcal{S}_{\mathrm{m},\alpha} - \mathcal{L}_{\mathrm{m},\alpha} \tag{A.1}$$

and

$$\frac{\partial(\frac{3}{2} n_\alpha T_\alpha)}{\partial t} = \mathcal{S}_{\mathrm{E},\alpha} - \mathcal{L}_{\mathrm{E},\alpha}. \tag{A.2}$$

The $\mathcal{S}_\alpha$'s and $\mathcal{L}_\alpha$'s represent source rates and loss rates, respectively, for species α. Following the convention of *Delamere and Bagenal* (2003), the pre-factor of 3/2 in Equation A.2 will be dropped henceforth, so that we are actually solving for temperature balance instead of energy balance. In cgs, photolytic reaction rates have units of s^{-1}. All other reaction rates have units of $\mathrm{cm}^3\,\mathrm{s}^{-1}$, giving the $\mathcal{S}_\mathrm{m}$'s and $\mathcal{L}_\mathrm{m}$'s units of $\mathrm{cm}^{-3}\,\mathrm{s}^{-1}$ and the $\mathcal{S}_\mathrm{E}$'s and $\mathcal{L}_\mathrm{E}$'s units of $\mathrm{eV}\,\mathrm{cm}^{-3}\,\mathrm{s}^{-1}$. A complete set of reactions and reaction rates found in Table A.3–Table A.9.

A.1.1 Ion Rate Equations

The mass source rate for ion species α is given by

$$\begin{aligned}\mathcal{S}^{\text{ion}}_{\text{m},\alpha} &= (I_{\alpha_-} n_{\text{e}} + I^{\text{h}}_{\alpha_-} n_{\text{eh}}) n_{\alpha_-} + \sum_{\beta,j} (I^{\text{diss}}_{\beta(j)} n_{\text{e}} + I^{\text{diss,h}}_{\beta(j)} n_{\text{eh}}) n_\beta \\ &+ (R_{\alpha_+} n_{\text{e}} + R^{\text{h}}_{\alpha_+} n_{\text{eh}}) n_{\alpha_+} + \sum_{\beta,j} (R^{\text{diss}}_{\beta(j)} n_{\text{e}} + R^{\text{diss,h}}_{\beta(j)} n_{\text{eh}}) n_\beta \\ &+ \kappa^{\text{ion}}_{\alpha_-} n_{\alpha_-} + \sum_{\beta,j} (\kappa^{\text{diss}}_{\beta(j)} + \kappa^{\text{diss,ion}}_{\beta(j)}) n_\beta + \sum_{\gamma,\beta,j} k_{\gamma\beta(j)} n_\gamma n_\beta. \end{aligned} \tag{A.3}$$

The I_{α_-}'s are the electron impact ionization rate coefficients for reactions which produce species α from one higher ionization state. For this study, only singly-ionizing events are relevant for any mechanism. The h's are attached to the second term to indicate impact ionization involving electrons from a separate hot-electron population, whose temperature and density (relative to thermal electrons) are two of the five parameters investigated in this study. Similarly, the I^{diss}'s are the rate coefficients for impact ionization events which also dissociate the affected molecule. All summations are carried out over those reactions which produce species α, including a summation over branching number j if multiple pathways create species α from any given set of reactants. For example, $\text{H}_2\text{O} + \text{e} \rightarrow \text{OH}^+ + 2\text{e} + \text{H}$ and $\text{H}_2\text{O} + \text{e} \rightarrow \text{O}^+ + 2\text{e} + 2\text{H}$ each produce H. The R_{α_+}'s are the rate coefficients for electronic-recombination reactions which produce species α from one lower ionization state. The recombination reactions involving hot electrons are included for completeness, though hot electrons are far more likely to participate in impact ionization. Dissociative recombination is represented symbolically (R^{diss}), despite the fact that no ion-producing dissociative re-

combinations are included in the model. The $\kappa^{\rm ion}$'s and $\kappa^{\rm diss}$'s are the photoionization and photodissociation rate coefficients, respectively, while the $\kappa^{\rm diss,ion}$'s are the rate coefficients for photolytic events which are both ionizing and dissociating. The $\kappa^{\rm diss}$'s are included, though no such reaction is a source of ions in the model. The $k_{\gamma\beta}$'s are the charge-exchange rate coefficients between species γ and species β. One of the two species is an ion, and the second one may either be neutral or ionized. If more than one outcome exists from a charge exchange, each branch involves a different reaction rate (e.g., see charge-exchange reactions involving O^{++} in Table A.8). The mass loss rate for ion species α is given by

$$\begin{aligned}\mathcal{L}^{\rm ion}_{{\rm m},\alpha} &= (I_\alpha n_{\rm e} + I^{\rm h}_\alpha n_{\rm eh})n_\alpha + \sum_j (I^{\rm diss}_{\alpha(j)} n_{\rm e} + I^{\rm diss,h}_{\alpha(j)} n_{\rm eh})n_\alpha \\ &+ (R_\alpha n_{\rm e} + R^{\rm h}_\alpha n_{\rm eh})n_\alpha + \sum_j (R^{\rm diss}_{\alpha(j)} n_{\rm e} + R^{\rm diss,h}_{\alpha(j)} n_{\rm eh})n_\alpha \\ &+ \kappa^{\rm ion}_\alpha n_\alpha + \sum_j (\kappa^{\rm diss}_{\alpha(j)} + \kappa^{\rm diss,ion}_{\alpha(j)})n_\alpha + \sum_{\beta,j} k_{\alpha\beta(j)} n_\alpha n_\beta \\ &+ \frac{n_\alpha}{\tau_{\rm trans}}. \end{aligned} \tag{A.4}$$

The impact-ionization reactions removing species α are given by the terms involving I's, and the terms involving the R's give the losses due to electronic recombination. The summation over charge-exchange reactions is taken over all exchanges involving ion species α. Resonant reactions can be included, but are unnecessary since an ion of species α is created to replace the one that is lost. The last term in Equation A.4 represents ion radial diffusion. $\tau_{\rm trans}$ parameterizes the diffusive transport timescale and is treated as a free parameter in this investigation. We assume there is no outward

radial transport inside $\sim 3R_{\rm S}$, so there is no such source term in Equation A.3. The energy density source rate for species α is given by

$$\begin{aligned}
\mathcal{S}^{\rm ion}_{{\rm E},\alpha} = \; & (I_{\alpha_-} n_{\rm e} + I^{\rm h}_{\alpha_-} n_{\rm eh}) n_{\alpha_-} T_{\alpha_-} + \sum_{\beta,j} (I^{\rm diss}_{\beta(j)} n_{\rm e} + I^{\rm diss,h}_{\beta(j)} n_{\rm eh}) n_\beta T_\beta \\
& + (R_{\alpha_+} n_{\rm e} + R^{\rm h}_{\alpha_+} n_{\rm eh}) n_{\alpha_+} T_{\alpha_+} + \sum_{\beta,j} (R^{\rm diss}_{\beta(j)} n_{\rm e} + R^{\rm diss,h}_{\beta(j)} n_{\rm eh}) n_\beta T_\beta \\
& + \kappa^{\rm ion}_{\alpha_-} n_{\alpha_-} T_{\alpha_-} + \sum_{\beta,j} (\kappa^{\rm diss}_{\beta(j)} + \kappa^{\rm diss,ion}_{\beta(j)}) n_\beta T_\beta \\
& + \sum_{\gamma,\beta,j} k_{\gamma\beta(j)} n_\gamma n_\beta T_\beta + \sum_{\beta={\rm i,e,eh}} \nu^{\alpha/\beta} n_\alpha (T_\beta - T_\alpha). \qquad \text{(A.5)}
\end{aligned}$$

Equation A.5 resembles Equation A.3 with the addition of the final term, which represents energy input from Coulomb interactions with all other ion and electron (Maxwellian) populations. This term may actually be negative, representing an energy loss, but we choose to include it in $\mathcal{S}^{\rm ion}_{{\rm E},\alpha}$. The temperature T_β in the charge-exchange reactions is that of the charge-exchanged ion which becomes species α. Any discrepancy between T_β before and after the exchange due to electron momentum transfer is considered negligible and is not accounted for. Neutrals produced in this process are not retained because the ions from which they are formed are super-Keplerian, corotating with the magnetosphere. *Johnson et al.* (2006) have not neglected these products. They showed that low-velocity charge exchange is capable of creating the extended OH cloud in Saturn's inner magnetosphere (*Shemansky et al.*, 1993b). Ions produced from a *neutral* via charge exchange pick up a relative velocity equal to the difference between Keplerian and magnetospheric velocity at $4R_{\rm S}$ (rigid inner-magnetospheric rotation is

assumed):

$$v_{\rm rel} = v_{\rm cor} = \Omega_{\rm S} r - \left(\frac{GM_{\rm S}}{r}\right)^{1/2}\Bigg|_{r=4R_{\rm S}} = 26 \text{ km s}^{-1}. \quad \text{(A.6)}$$

$\Omega_{\rm S}$ is the angular frequency of Saturn's magnetosphere (period = 10.8 hours). A small correction can be made to Equation A.6 if, in addition, the ion picks up a gyrospeed equal to $v_{\rm cor}$. In that case, the cycloidal path average $<v_{\rm rel}> = (v_{\rm cor}/2\pi)\int_0^{2\pi} d\theta\sqrt{2+2\cos\theta} = 4v_{\rm cor}/\pi$. The pick-up temperature for species α in terms of $v_{\rm rel}$ is defined as

$$\frac{3}{2}T_{{\rm pu},\alpha} \equiv \frac{1}{2}m_\alpha v_{\rm rel}^2 = E_{{\rm pu},\alpha} \rightarrow \frac{T_{\rm pu}}{\rm amu} = 2.4 \text{ eV}. \quad \text{(A.7)}$$

Here the pick-up temperature per atomic mass unit is evaluated (with Equation A.6) at $r = 4R_{\rm S}$. [NOTE: Because we consider isotropic Maxwellian temperature distributions, the effective temperatures given by our model should be compared to the average temperature from the data, $T^{\rm data} = (2T_\perp^{\rm data} + T_\parallel^{\rm data})/3$.] Ions picked up in a resonant exchange (e.g., $H_2O + H_2O^+ \rightarrow H_2O^+ + H_2O$) present an energy gain to the system because the freshly-acquired ion is hotter than the ejected neutral. $\nu^{\alpha/\beta}$ in Equation A.5 is the thermal equilibrium rate due to Coulomb interactions between ion or electron Maxwellian distributions (*Book*, 1983):

$$\nu^{\alpha/\beta} = 1.8\times10^{-19}\frac{(m_\alpha m_\beta)^{1/2} Z_\alpha^2 Z_\beta^2 n_\beta \lambda_{\alpha\beta}}{(m_\alpha T_\beta + m_\beta T_\alpha)^{3/2}} \text{ sec}^{-1}. \quad \text{(A.8)}$$

The m's and n's are in cgs units and the T's are in eV. $\lambda_{\alpha\beta}$ is the Coulomb logarithm ($10 \lesssim \lambda_{\alpha\beta} \lesssim 20$). The energy density loss rate for ion species α is directly derivable

from Equation A.4:

$$\mathcal{L}^{\rm ion}_{{\rm E},\alpha} = (I_\alpha n_{\rm e} + I^{\rm h}_\alpha n_{\rm eh}) n_\alpha T_\alpha + \sum_j (I^{\rm diss}_{\alpha(j)} n_{\rm e} + I^{\rm diss,h}_{\alpha(j)} n_{\rm eh}) n_\alpha T_\alpha$$
$$+ (R_\alpha n_{\rm e} + R^{\rm h}_\alpha n_{\rm eh}) n_\alpha T_\alpha + \sum_j (R^{\rm diss}_{\alpha(j)} n_{\rm e} + R^{\rm diss,h}_{\alpha(j)} n_{\rm eh}) n_\alpha T_\alpha$$
$$+ \kappa^{\rm ion}_\alpha n_\alpha T_\alpha + \sum_j (\kappa^{\rm diss}_{\alpha(j)} + \kappa^{\rm diss,ion}_{\alpha(j)}) n_\alpha T_\alpha$$
$$+ \sum_{\beta,j} k_{\alpha\beta(j)} n_\alpha n_\beta T_\alpha + \frac{n_\alpha T_\alpha}{\tau_{\rm trans}}. \tag{A.9}$$

A.1.2 Electron Rate Equation

Charge neutrality is imposed at each time step ($\sum_{j={\rm ions}} n_j Z_j = n_{\rm e}$), so Equation A.1 is not necessary for electrons. Equation A.2 for electrons is expressed as

$$\frac{\partial (n_{\rm e} T_{\rm e})}{\partial t} = \sum_{\beta={\rm i,eh}} \nu^{\beta/e} n_{\rm e} (T_\beta - T_{\rm e}) - \frac{2}{3} \sum_{\beta,\lambda} \rho_{\beta,\lambda} n_{\rm e} n_\beta - \frac{n_{\rm e} T_{\rm e}}{\tau_{\rm trans}}. \tag{A.10}$$

The summation over Coulomb interactions involves all ion species as well as the parameterized hot-electron population. The $\rho_{\beta,\lambda}$'s are radiative rate coefficients (eV cm^3 s^{-1}) for electron-impact excitation and depend on electron density and temperature. The factor of 2/3 appears because the emission rate coefficients are given for energy, whereas we have dropped the 3/2 in our notation and are instead calculating a temperature balance. The $\rho_{\beta,\lambda}$'s are calculated from the CHIANTI database for H, O^+, and O^{++} (*Dere et al.*, 1997; *Landi et al.*, 2006). The O^+ rate coefficients are used for OH^+, and cross sections for the 1356, 1304 and 6300 Å lines are taken from Darrell Strobel, personal communication, to calculate emission rates for O. Because radiation

represents only 4% of the energy output in the nominal case (Table A.2), we believe adding radiative lines from other species (i.e., H_2O) will cool the core electrons and affect the overall energy budget minimally. Future versions of the model will include radiative cooling effects of H_2O.

A.1.3 Neutral Rate Equations

The energy density equation (Equation A.2) applies only to ions. Unreacted neutrals are assumed to be cold, having only orbital bulk motion. The density rate equations for neutral species are the same as Equation A.3 and Equation A.4 with five exceptions: (1) the transport term and (2) the loss terms from recombination do not exist in Equation A.4; (3) the source terms from pure ionization do not exist in Equation A.3; (4) electron-impact dissociation reactions (represented by D_α) must be included in both Equation A.3 and Equation A.4; (5) a source is added to the r.h.s. of Equation A.3 for $\alpha = H_2O$. Thus, for neutrals

$$\begin{aligned}\mathcal{S}^{\text{neut}}_{\text{m},\alpha} &= N_{\text{src},\alpha}\delta^{\text{H}_2\text{O}}_{\alpha} + \sum_{\beta,j}(D_{\beta(j)}n_{\text{e}} + D^{\text{h}}_{\beta(j)}n_{\text{eh}})n_\beta \\ &+ \sum_{\beta,j}(I^{\text{diss}}_{\beta(j)}n_{\text{e}} + I^{\text{diss,h}}_{\beta(j)}n_{\text{eh}})n_\beta + \sum_{\beta,j}(R^{\text{diss}}_{\beta(j)}n_{\text{e}} + R^{\text{diss,h}}_{\beta(j)}n_{\text{eh}})n_\beta \\ &+ \sum_{\beta,j}(\kappa^{\text{diss}}_{\beta(j)}n_\beta + \kappa^{\text{diss,ion}}_{\beta(j)}n_\beta) \end{aligned} \tag{A.11}$$

and

$$\mathcal{L}^{\text{neut}}_{\text{m},\alpha} = (I_\alpha n_\text{e} + I^\text{h}_\alpha n_\text{eh})n_\alpha + \sum_j (I^\text{diss}_{\alpha(j)} n_\text{e} + I^{\text{diss,h}}_{\alpha(j)} n_\text{eh})n_\alpha$$
$$+ \kappa^\text{ion}_\alpha n_\alpha + \sum_j (\kappa^\text{diss}_{\alpha(j)} + \kappa^{\text{diss,ion}}_{\alpha(j)})n_\alpha + \sum_{\beta,j} k_{\alpha\beta(j)} n_\alpha n_\beta$$
$$+ \sum_j (D_{\alpha(j)} n_\text{e} + D^\text{h}_{\alpha(j)} n_\text{eh})n_\alpha, \tag{A.12}$$

where δ^m_n is the Kronecker delta function. In addition, notice that charge-exchange and pure-recombination terms are not included in Equation A.11; neutrals produced from corotating ions have sufficient velocity to exit the model before being further reacted upon. However, these fast-moving hot neutrals are tracked in the interest of calculating energy and mass flow (Table A.2). The source and loss equations for both neutrals and ions can be modified to accommodate the more general case where the reaction set involves multiply-ionizing and recombining reactions (e.g., $\kappa^\text{ion}_\alpha n_\alpha \rightarrow \sum_j \kappa^\text{ion}_{\alpha(j)} n_\alpha$). Here we deal with singly-ionizing and singly-recombining events only.

Species	Particle Flux (10^{-4} cm $^{-3}$ s^{-1})	Mass Flux (kg s^{-1})
	Fast Neutrals	
H	2.1 (50.6)	7.8 (6.1)
H_2	0.11 (2.6)	0.78 (0.6)
O	0.86 (20.3)	50 (38.9)
OH	0.55 (13.1)	34 (26.7)
H_2O	0.31 (7.2)	20 (15.6)
	4.0 (93.8)	**110 (87.9)**
	Radial Transport	
H^+	0.020 (0.5)	0.073 (0.1)
$H_2{}^+$	$\ll 1$	
O^+	0.037 (0.9)	2.1 (1.7)
O^{++}	$\ll 1$	
OH^+	0.073 (1.7)	4.5 (3.5)
H_2O^+	0.089 (2.1)	5.8 (4.5)
H_3O^+	0.043 (1.0)	3.0 (2.3)
	0.26 (6.2)	**15 (12.1)**

Table A.1 Particle flow for the baseline solution. Listed are fast neutrals and transported ions in both particle flux and mass flux for a torus volume of $2\pi(4R_S)(2R_S)^2$. The source is $N_{H_2O} = 2.0 \times 10^{-4}\,\mathrm{cm^{-3}\,s^{-1}} = 130\,\mathrm{kg\,s^{-1}}$. Percentages are given in parentheses, and the bold-facings are sub-totals.

Input			Output		
Species	Energy Flux (10^{-4} eV cm $^{-3}$ s^{-1})	Volumetric Power (GW)	Species	Energy Flux (10^{-4} eV cm $^{-3}$ s^{-1})	Volumetric Power (GW)
	Ionization Pick-up			*Transport*	
H^+	0.24 (0.2)	0.081	e	0.61 (0.7)	0.21
H_2^+	$\ll 1$		e_h	0.22 (0.2)	0.077
O^+	7.8 (8.4)	2.7	H^+	0.094 (0.1)	0.033
O^{++}	$\ll 1$		H_2^+	$\ll 1$	
OH^+	13 (14.2)	4.6	O^+	1.6 (1.7)	0.56
H_2O^+	15 (16.8)	5.5	O^{++}	$\ll 1$	
	37 (39.6)	**13**	OH^+	3.3 (3.5)	1.1
	Exchange Pick-up		H_2O^+	4.3 (4.6)	1.5
H^+	1.3 (1.4)	0.45	H_3O^+	2.0 (2.2)	0.72
H_2^+	$\ll 1$			**12 (13.0)**	**4.2**
O^+	18 (19.1)	6.2		*Fast Neutrals*	
O^{++}	0.12 (0.1)	0.040	H	3.8 (4.1)	1.3
OH^+	1.2 (1.3)	0.43	H_2	0.44 (0.5)	0.15
H_2O^+	29 (30.6)	10	O	38 (40.3)	13
H_3O^+	5.6 (6.0)	2.0	OH	21 (22.6)	7.3
	55 (58.6)	**19**	H_2O	15 (15.8)	5.2
	Hot-electron Coupling			**78 (83.2)**	**27**
e	**1.7 (1.8)**	**0.58**		*Radiation*	
			H	0.59 (0.6)	0.21
			O	2.8 (2.9)	0.96
Internal e–Ion Coupling			O^+	0.061 (0.1)	0.021
	1.9 (2.4)	**0.67**	O^{++}	$\ll 1$	
			OH^+	0.12 (0.1)	0.042
				3.5 (3.8)	**1.2**

Table A.2 Energy flow for the baseline solution. Charge-exchange and impact ionization as well as hot-electron coupling serve as energy input. (Internal electron–ion coupling is *not* part of the energy input.) Energy leaves the box via radial transport, hot neutrals, and radiation by electron impact excitation. Power is calculated for a torus volume of $2\pi(4R_S)(2R_S)^2$. Percentages are given in parentheses, and the bold-facings are sub-totals.

Reaction		I_α ($cm^3\ s^{-1}$)	$n_\alpha n_e I_\alpha$ ($cm^{-3}\ s^{-1}$)	Reference
$H + e$	$\rightarrow H^+ + 2e$	1.1×10^{-11}	4.7×10^{-7}	*Voronov* (1997)
$O + e$	$\rightarrow O^+ + 2e$	1.3×10^{-11}	5.3×10^{-7}	*Voronov* (1997)
$O^+ + e$	$\rightarrow O^{++} + 2e$	2.4×10^{-16}	1.2×10^{-13}	*Voronov* (1997)
$OH + e$	**$\rightarrow OH^+ + 2e$**	5.3×10^{-11}	2.5×10^{-6}	*Tarnovsky et al.* (1998)
$H_2O + e$	$\rightarrow H_2O^+ + 2e$	7.0×10^{-12}	7.9×10^{-8}	*Orient and Strivastava* (1987)
		I_α^h	$n_\alpha n_{eh} I_\alpha^h$	
$H + e_h$	**$\rightarrow H^+ + 2e$**	3.2×10^{-8}	6.4×10^{-6}	*Voronov* (1997)
$O + e_h$	**$\rightarrow O^+ + 2e$**	9.0×10^{-8}	1.8×10^{-5}	*Voronov* (1997)
$O^+ + e_h$	$\rightarrow O^{++} + 2e$	2.7×10^{-8}	6.3×10^{-8}	*Voronov* (1997)
$OH + e_h$	**$\rightarrow OH^+ + 2e$**	1.2×10^{-7}	2.5×10^{-5}	*Tarnovsky et al.* (1998)
$H_2O + e_h$	**$\rightarrow H_2O^+ + 2e$**	9.1×10^{-8}	4.8×10^{-6}	*Orient and Strivastava* (1987)

Table A.3 Electron impact ionization reactions. Values presented are for the baseline solution. The I's are the rate coefficients [$I_\alpha \equiv I_\alpha(T_e)$; $I_\alpha^h \equiv I_\alpha(T_{eh})$], and the third column gives the number of each reaction occurring per cubic centimeter per second. The bold facing guides the eye to the most important reactions.

Reaction		$I_\alpha^{\rm diss}$ ($\rm cm^3\ s^{-1}$)	$n_\alpha n_{\rm e} I_\alpha^{\rm diss}$ ($\rm cm^{-3}\ s^{-1}$)	Reference
H_2O + e	$\rightarrow H^+$ + OH + 2e	5.3×10^{-14}	6.1×10^{-10}	*Orient and Strivastava* (1987)
H_2O + e	$\rightarrow O^+$ + 2H + 2e	3.2×10^{-15}	3.6×10^{-11}	*Orient and Strivastava* (1987)
H_2O + e	$\rightarrow OH^+$ +H + 2e	1.1×10^{-12}	1.2×10^{-8}	*Orient and Strivastava* (1987)
		$I_\alpha^{\rm diss,h}$	$n_\alpha n_{\rm eh} I_\alpha^{\rm diss,h}$	
$\mathbf{H_2O + e_h}$	$\mathbf{\rightarrow H^+ + OH + 2e}$	4.1×10^{-8}	2.2×10^{-6}	*Orient and Strivastava* (1987)
H_2O + e_h	$\rightarrow O^+$ +2H + 2e	1.1×10^{-8}	5.9×10^{-7}	*Orient and Strivastava* (1987)
$\mathbf{H_2O + e_h}$	$\mathbf{\rightarrow OH^+ +H + 2e}$	4.5×10^{-8}	2.3×10^{-6}	*Orient and Strivastava* (1987)

Table A.4 Electron impact ionization–dissociation reactions. Values presented are for the baseline solution. The I's are the rate coefficients [$I_\alpha^{\rm diss} \equiv I_\alpha^{\rm diss}(T_{\rm e})$; $I_\alpha^{\rm diss,h} \equiv I_\alpha^{\rm diss}(T_{\rm eh})$], and the third column gives the number of each reaction occurring per cubic centimeter per second. The bold facing guides the eye to the most important reactions.

Reaction	R_α ($cm^3\ s^{-1}$)	$n_\alpha n_e R_\alpha$ ($cm^{-3}\ s^{-1}$)	Reference
$H^+ + e \rightarrow H$	8.5×10^{-11}	2.4×10^{-8}	*Verner and Ferland* (1996)
$O^+ + e \rightarrow O$	3.2×10^{-13}	1.6×10^{-10}	*Nahar* (1999)
$O^{++} + e \rightarrow O^+$	1.9×10^{-12}	8.9×10^{-12}	*Nahar* (1999)
	R^h_α	$n_\alpha n_{eh} R^h_\alpha$	
$H^+ + e_h \rightarrow H$	6.4×10^{-12}	8.2×10^{-12}	*Verner and Ferland* (1996)
$O^+ + e_h \rightarrow O$	3.0×10^{-13}	7.0×10^{-13}	*Nahar* (1999)
$O^{++} + e_h \rightarrow O^+$	1.5×10^{-12}	3.2×10^{-14}	*Nahar* (1999)

Table A.5 Electron recombination reactions. Values presented are for the baseline solution. The R's are the rate coefficients [$R_\alpha \equiv R_\alpha(T_e)$; $R^h_\alpha \equiv R_\alpha(T_{eh})$], and the third column gives the number of each reaction occurring per cubic centimeter per second. Notice that molecular recombinations (Table A.6) are far more likely than the atomic recombinations listed here.

Reaction	$R_\alpha^{\rm diss}$ ($\rm cm^3\ s^{-1}$)	$n_\alpha n_{\rm e} R_\alpha^{\rm diss}$ ($\rm cm^{-3}\ s^{-1}$)	Reference
$H_2^+ + e \rightarrow H + H$	2.0×10^{-8}	2.9×10^{-11}	*Peart and Dolder* (1974)
$\mathbf{OH^+ + e \rightarrow O + H}$	9.6×10^{-9}	9.7×10^{-6}	*Mul et al.* (1983)
$\mathbf{H_2O^+ + e \rightarrow OH + H}$	2.0×10^{-8}	2.4×10^{-5}	*Mul et al.* (1983)
$\mathbf{H_3O^+ + e \rightarrow OH + H_2}$	1.4×10^{-8}	8.0×10^{-6}	*Mul et al.* (1983)
	$R_\alpha^{\rm diss,h}$	$n_\alpha n_{\rm eh} R_\alpha^{\rm diss,h}$	
$H_2^+ + e_h \rightarrow H + H$	2.0×10^{-8}	1.3×10^{-13}	*Peart and Dolder* (1974)
$OH^+ + e_h \rightarrow O + H$	1.1×10^{-9}	5.0×10^{-9}	*Mul et al.* (1983)
$H_2O^+ + e_h \rightarrow OH + H$	8.9×10^{-11}	5.0×10^{-10}	*Mul et al.* (1983)
$H_3O^+ + e_h \rightarrow OH + H_2$	4.7×10^{-11}	1.3×10^{-10}	*Mul et al.* (1983)

Table A.6 Dissociative electronic recombination reactions. Values presented are for the baseline solution. The R's are the rate coefficients [$R_\alpha^{\rm diss} \equiv R_\alpha^{\rm diss}(T_{\rm e})$; $R_\alpha^{\rm diss,h} \equiv R_\alpha^{\rm diss}(T_{\rm eh})$], and the third column gives the number of each reaction occurring per cubic centimeter per second. The bold facing guides the eye to the most important reactions.

Reaction		$\kappa_\alpha^{\rm ion}$ (s^{-1})	$n_\alpha\kappa_\alpha^{\rm ion}$ ($cm^{-3}\ s^{-1}$)	Reference
$H + \gamma$	$\rightarrow H^+ + e$	8.0×10^{-10}	5.8×10^{-7}	*Huebner and Carpenter* (1979a)
$H_2 + \gamma$	$\rightarrow H_2^+ + e$	5.9×10^{-10}	8.8×10^{-12}	*Huebner and Carpenter* (1979a)
$\mathbf{O + \gamma}$	$\mathbf{\rightarrow O^+ + e}$	2.3×10^{-9}	1.6×10^{-6}	*Huebner and Carpenter* (1979a)
$\mathbf{OH + \gamma}$	$\mathbf{\rightarrow OH^+ + e}$	3.7×10^{-9}	2.9×10^{-6}	*Huebner and Carpenter* (1979a)
$H_2O + \gamma$	$\rightarrow H_2O^+ + e$	3.7×10^{-9}	7.0×10^{-7}	*Huebner and Carpenter* (1979a)
		$\kappa_\alpha^{\rm diss}$	$n_\alpha\kappa_\alpha^{\rm diss}$	
$H_2 + \gamma$	$\rightarrow H + H$	4.9×10^{-10}	7.3×10^{-12}	*Huebner and Carpenter* (1979a)
$\mathbf{OH + \gamma}$	$\mathbf{\rightarrow O + H}$	5.5×10^{-8}	4.2×10^{-5}	*Huebner and Carpenter* (1979a)
$\mathbf{H_2O + \gamma}$	$\mathbf{\rightarrow H + OH}$	1.1×10^{-7}	2.1×10^{-5}	*Huebner and Carpenter* (1979a)
$\mathbf{H_2O + \gamma}$	$\mathbf{\rightarrow H_2 + O}$	1.5×10^{-8}	2.9×10^{-6}	*Huebner and Carpenter* (1979a)
		$\kappa_\alpha^{\rm diss,ion}$	$n_\alpha\kappa_\alpha^{\rm diss,ion}$	
$H_2 + \gamma$	$\rightarrow H^+ + H + e$	1.0×10^{-10}	1.5×10^{-12}	*Huebner and Carpenter* (1979a)
$H_2O + \gamma$	$\rightarrow H^+ + OH + e$	1.4×10^{-10}	2.7×10^{-8}	*Huebner and Carpenter* (1979a)
$H_2O + \gamma$	$\rightarrow O^+ + H_2 + e$	6.4×10^{-11}	1.2×10^{-8}	*Huebner and Carpenter* (1979a)
$H_2O + \gamma$	$\rightarrow OH^+ + H + e$	6.1×10^{-10}	1.2×10^{-7}	*Huebner and Carpenter* (1979a)

Table A.7 Photolytic reactions. The κ's are the rate coefficients at 9.5 AU, and the third column gives the number of each reaction occurring per cubic centimeter per second for the baseline solution. The bold facing guides the eye to the most important reactions.

Reaction		$k_{\alpha\beta}$ ($cm^3\ s^{-1}$)	$n_\alpha n_\beta k_{\alpha\beta}$ ($cm^{-3}\ s^{-1}$)	Reference
$\mathbf{H^+ + H}$	$\rightarrow \mathbf{H + H^+}$	9.7×10^{-9}	3.2×10^{-5}	*Newman et al.* (1982)
$H^+ + H_2$	$\rightarrow H + H_2{}^+$	1.6×10^{-9}	1.1×10^{-10}	*Tawara* (1978)
$\mathbf{H^+ + O}$	$\rightarrow \mathbf{H + O^+}$	3.0×10^{-9}	9.7×10^{-6}	*Stebbings et al.* (1964)
$\mathbf{H^+ + OH}$	$\rightarrow \mathbf{H + OH^+}$	3.0×10^{-10}	1.1×10^{-6}	*Giguere and Huebner* (1978)
$\mathbf{H^+ + H_2O}$	$\rightarrow \mathbf{H + H_2O^+}$	2.0×10^{-8}	1.8×10^{-5}	*Tawara* (1978)
$H_2{}^+ + H_2$	$\rightarrow H_2 + H_2{}^+$	3.6×10^{-9}	1.3×10^{-15}	*Massey et al.* (1974)
$H_2{}^+ + O$	$\rightarrow H + OH^+$	1.0×10^{-9}	1.7×10^{-11}	*Giguere and Huebner* (1978)
$H_2{}^+ + OH$	$\rightarrow H + H_2O^+$	7.6×10^{-10}	1.4×10^{-11}	*Millar et al.* (1991)
$H_2{}^+ + OH$	$\rightarrow H_2 + OH^+$	7.6×10^{-10}	1.4×10^{-11}	*Millar et al.* (1991)
$H_2{}^+ + H_2O$	$\rightarrow H + H_3O^+$	3.4×10^{-9}	1.6×10^{-11}	*Huntress* (1977)
$H_2{}^+ + H_2O$	$\rightarrow H_2 + H_2O^+$	3.9×10^{-9}	1.8×10^{-11}	*Huntress* (1977)
$\mathbf{O^+ + H}$	$\rightarrow \mathbf{O + H^+}$	3.4×10^{-9}	2.1×10^{-5}	*Stebbings and Rutherford* (1968)
$O^+ + H_2$	$\rightarrow H + OH^+$	1.6×10^{-9}	2.0×10^{-10}	*Huntress* (1977)
$\mathbf{O^+ + O}$	$\rightarrow \mathbf{O + O^+}$	6.2×10^{-9}	3.7×10^{-5}	*Stebbings et al.* (1964)
$\mathbf{O^+ + OH}$	$\rightarrow \mathbf{O + OH^+}$	3.0×10^{-10}	1.9×10^{-6}	*Giguere and Huebner* (1978)
$\mathbf{O^+ + H_2O}$	$\rightarrow \mathbf{O + H_2O^+}$	2.3×10^{-9}	3.7×10^{-6}	*Albritton* (1978)
$O^{++} + O$	$\rightarrow O^+ + O^+$	5.2×10^{-10}	2.9×10^{-8}	*McGrath and Johnson* (1989)
$O^{++} + O$	$\rightarrow O + O^{++}$	5.4×10^{-9}	3.0×10^{-7}	*McGrath and Johnson* (1989)
$OH^+ + H_2$	$\rightarrow H + H_2O^+$	1.1×10^{-9}	2.8×10^{-10}	*Huntress* (1977)
$\mathbf{OH^+ + OH}$	$\rightarrow \mathbf{O + H_2O^+}$	7.0×10^{-10}	9.0×10^{-6}	*Millar et al.* (1991)
$\mathbf{OH^+ + H_2O}$	$\rightarrow \mathbf{O + H_3O^+}$	1.3×10^{-9}	4.1×10^{-6}	*Huntress* (1977)
$\mathbf{OH^+ + H_2O}$	$\rightarrow \mathbf{OH + H_2O^+}$	1.6×10^{-9}	5.1×10^{-6}	*Huntress* (1977)
$H_2O^+ + H_2$	$\rightarrow H + H_3O^+$	6.1×10^{-10}	1.9×10^{-10}	*Huntress* (1977)
$\mathbf{H_2O^+ + H_2O}$	$\rightarrow \mathbf{OH + H_3O^+}$	2.1×10^{-9}	8.1×10^{-6}	*Huntress* (1977)
$\mathbf{H_2O^+ + H_2O}$	$\rightarrow \mathbf{H_2O + H_2O^+}$	7.9×10^{-9}	3.1×10^{-5}	*Lishawa et al.* (1990)[a]

Table A.8 Charge exchange reactions. The k's are the reaction rates, and the third column gives the number of each reaction occurring per cubic centimeter per second for the baseline solution. The bold facing guides the eye to the most important reactions. [a]The resonant exchange reaction rate for H_2O is calculated as a function of ion temperature by convolution of the cross sections from *Lishawa et al.* (1990); the k presented here is for the baseline solution (all other k's are constants).

Reaction		D_α (cm^3 s^{-1})	$n_\alpha n_e D_\alpha$ (cm^{-3} s^{-1})	Reference
$H_2 + e$	$\rightarrow H + H + e$	1.9×10^{-9}	1.7×10^{-9}	*Shemansky and Hall* (1992)
OH + e	$\rightarrow$ **O + H + e**	6.7×10^{-11}	3.1×10^{-6}	*Shemansky and Hall* (1992)
H_2O + e	$\rightarrow$ **OH + H + e**	1.2×10^{-9}	1.4×10^{-5}	*Shemansky and Hall* (1992)
		D_α^h	$n_\alpha n_{eh} D_\alpha^h$	
$H_2 + e_h$	$\rightarrow H + H + e$	2.3×10^{-6}	9.7×10^{-9}	*Shemansky and Hall* (1992)
OH + e_h	$\rightarrow$ **O + H + e**	8.4×10^{-8}	1.8×10^{-5}	*Shemansky and Hall* (1992)
H_2O + e_h	$\rightarrow$ **OH + H + e**	1.5×10^{-6}	7.9×10^{-5}	*Shemansky and Hall* (1992)

Table A.9 Impact dissociation reactions. Values presented are for the baseline solution. The D's are the rate coefficients [$D_\alpha \equiv D_\alpha(T_e)$; $D_\alpha^h \equiv D_\alpha(T_{eh})$], and the third column gives the number of each reaction occurring per cubic centimeter per second. The bold facing guides the eye to the most important reactions.

Reaction		Rate (s^{-1})	τ (days)	Reaction		Rate (s^{-1})	τ (days)
H + H+	**→ H^+ + H**	4.5×10^{-8}	2.6×10^{2}	OH + e	→ OH^+ + 2e	3.2×10^{-9}	3.6×10^{3}
H + O^+	**→ H^+ + O**	2.9×10^{-8}	4.1×10^{2}	OH + O^+	→ OH^+ + O	2.5×10^{-9}	4.6×10^{3}
H + e_h	→ H^+ + 2e	8.9×10^{-9}	1.3×10^{3}	OH + H^+	→ OH^+ + H	1.4×10^{-9}	8.4×10^{3}
H + γ	→ H^+ + e	8.0×10^{-10}	1.5×10^{4}	OH + $H_2{}^+$	→ H_2O^+ + H	1.9×10^{-14}	6.3×10^{8}
H + e	→ H^+ + 2e	6.5×10^{-10}	1.8×10^{4}	OH + $H_2{}^+$	→ OH^+ + H_2	1.9×10^{-14}	6.3×10^{8}
H_2 + e_h	**→ H + H + e**	6.5×10^{-7}	1.8×10^{1}	**H_2O + e_h**	**→ H + OH + e**	4.2×10^{-7}	2.8×10^{1}
H_2 + e	**→ H + H + e**	1.1×10^{-7}	1.0×10^{2}	**H_2O + H_2O^+**	**→ H_2O^+ + H_2O**	1.6×10^{-7}	7.2×10^{1}
H_2 + OH^+	→ H + H_2O^+	1.8×10^{-8}	6.3×10^{2}	**H_2O + γ**	**→ H + OH**	1.1×10^{-7}	1.1×10^{2}
H_2 + O^+	→ H + OH^+	1.3×10^{-8}	8.6×10^{2}	**H_2O + H^+**	**→ H_2O^+ + H**	9.2×10^{-8}	1.3×10^{2}
H_2 + H_2O^+	→ H + H_2O^+	1.2×10^{-8}	9.3×10^{2}	**H_2O + e**	**→ H + OH + e**	7.3×10^{-8}	1.6×10^{2}
H_2 + H^+	→ H + $H_2{}^+$	7.4×10^{-9}	1.6×10^{3}	**H_2O + H_2O^+**	**→ H_3O^+ + OH**	4.3×10^{-8}	2.7×10^{2}
H_2 + γ	→ $H_2{}^+$ + e	5.9×10^{-10}	2.0×10^{4}	**H_2O + OH^+**	**→ H_2O^+ + OH**	2.7×10^{-8}	4.3×10^{2}
H_2 + γ	→ H + H	4.9×10^{-10}	2.4×10^{4}	**H_2O + e_h**	**→ H_2O^+ + 2e**	2.5×10^{-8}	4.6×10^{2}
H_2 + γ	→ H^+ + H + e	1.0×10^{-10}	1.2×10^{5}	H_2O + OH^+	→ H_3O^+ + O	2.2×10^{-8}	5.3×10^{2}
H_2 + $H_2{}^+$	→ $H_2{}^+$ + H_2	8.8×10^{-14}	1.3×10^{8}	H_2O + O^+	→ H_2O^+ + O	1.9×10^{-8}	6.0×10^{2}
O + O^+	**→ O^+ + O**	5.2×10^{-8}	2.2×10^{2}	H_2O + γ	→ H_2 + O	1.5×10^{-8}	7.7×10^{2}
O + e_h	**→ O^+ + 2e**	2.5×10^{-8}	4.7×10^{2}	H_2O + e_h	→ OH^+ + 2e +H	1.2×10^{-8}	9.4×10^{2}
O + H^+	→ O^+ + H	1.4×10^{-8}	8.4×10^{2}	H_2O + e_h	→ H^+ + OH + 2e	1.1×10^{-8}	1.0×10^{3}
O + γ	→ O^+ + e	2.3×10^{-9}	5.0×10^{3}	H_2O + γ	→ H_2O^+ + e	3.7×10^{-9}	3.1×10^{3}
O + e	→ O^+ + 2e	7.5×10^{-10}	1.5×10^{4}	H_2O + e_h	→ O^+ + 2e +2H	3.1×10^{-9}	3.7×10^{3}
O + O^{++}	→ O^{++} + O	4.3×10^{-10}	2.7×10^{4}	H_2O + γ	→ OH^+ + H + e	6.1×10^{-10}	1.9×10^{4}
O + O^{++}	→ O^+ + O^+	4.1×10^{-11}	2.8×10^{5}	H_2O + e	→ H_2O^+ + 2e	4.2×10^{-10}	2.8×10^{4}
O + H_2^+	→ OH^+ + H	2.4×10^{-14}	4.8×10^{8}	H_2O + γ	→ H^+ + OH + e	1.4×10^{-10}	8.3×10^{4}
OH + γ	**→ O + H**	5.5×10^{-8}	2.1×10^{2}	H_2O + γ	→ O^+ + H_2 + e	6.4×10^{-11}	1.8×10^{5}
OH + e_h	**→ OH^+ + 2e**	3.2×10^{-8}	3.7×10^{2}	H_2O + e	→ OH^+ + 2e +H	6.4×10^{-11}	1.8×10^{5}
OH + e_h	**→ O + H + e**	2.3×10^{-8}	5.0×10^{2}	H_2O + e	→ H^+ + OH + 2e	3.2×10^{-12}	3.6×10^{6}
OH + OH^+	→ H_2O^+ + O	1.2×10^{-8}	9.9×10^{2}	H_2O + e	→ O^+ + 2e +2H	1.9×10^{-13}	6.1×10^{7}
OH + e	→ O + H + e	4.0×10^{-9}	2.9×10^{3}	H_2O + $H_2{}^+$	→ H_2O^+ + H_2	9.5×10^{-14}	1.2×10^{8}
OH + γ	→ OH^+ + e	3.7×10^{-9}	3.1×10^{3}	H_2O + $H_2{}^+$	→ H_3O^+ + H	8.3×10^{-14}	1.4×10^{8}

Table A.10 Baseline lifetimes for neutral species by reaction in descending order of importance (Rate $= 1/\tau$). Dominant loss mechanisms are typeset in bold (the cut-off is arbitrarily chosen at 500 days).

Reaction		Rate (s^{-1})	τ (days)
$\mathbf{H^+ + H_2O}$	$\mathbf{\rightarrow H + H_2O^+}$	3.8×10^{-6}	3.1×10^{0}
$\mathbf{H^+ + O}$	$\mathbf{\rightarrow H + O^+}$	2.1×10^{-6}	5.5×10^{0}
$H^+ + OH$	$\rightarrow H + OH^+$	2.3×10^{-7}	5.0×10^{1}
$H^+ + e$	$\rightarrow H$	5.1×10^{-9}	2.3×10^{3}
$H^+ + H_2$	$\rightarrow H + H_2{}^+$	2.4×10^{-11}	4.8×10^{5}
$H^+ + e_h$	$\rightarrow H$	1.8×10^{-12}	6.5×10^{6}
$\mathbf{H_2^+ + e}$	$\mathbf{\rightarrow H + H}$	1.2×10^{-6}	9.6×10^{0}
$\mathbf{H_2^+ + H_2O}$	$\mathbf{\rightarrow H_2 + H_2O^+}$	7.4×10^{-7}	1.6×10^{1}
$\mathbf{H_2^+ + O}$	$\mathbf{\rightarrow H + OH^+}$	7.0×10^{-7}	1.7×10^{1}
$\mathbf{H_2^+ + OH}$	$\mathbf{\rightarrow H + H_2O^+}$	5.9×10^{-7}	2.0×10^{1}
$\mathbf{H_2^+ + OH}$	$\mathbf{\rightarrow H_2 + OH^+}$	5.9×10^{-7}	2.0×10^{1}
$H_2^+ + e_h$	$\rightarrow H + H$	5.5×10^{-9}	2.1×10^{3}
$\mathbf{OH^+ + e}$	$\mathbf{\rightarrow O + H}$	5.8×10^{-7}	2.0×10^{1}
$\mathbf{OH^+ + OH}$	$\mathbf{\rightarrow O + H_2O^+}$	5.4×10^{-7}	2.1×10^{1}
$OH^+ + H_2O$	$\rightarrow OH + H_2O^+$	3.0×10^{-7}	3.8×10^{1}
$OH^+ + H_2O$	$\rightarrow O + H_3O^+$	2.5×10^{-7}	6.1×10^{1}
$OH^+ + e_h$	$\rightarrow O + H$	3.0×10^{-10}	3.9×10^{4}
$OH^+ + H_2$	$\rightarrow H + H_2O^+$	1.7×10^{-11}	7.0×10^{5}

Reaction		Rate (s^{-1})	τ (days)
$\mathbf{O^+ + H}$	$\mathbf{\rightarrow O + H^+}$	2.5×10^{-6}	4.7×10^{0}
$O^+ + H_2O$	$\rightarrow O + H_2O^+$	4.4×10^{-7}	2.7×10^{1}
$O^+ + OH$	$\rightarrow O + OH^+$	2.3×10^{-7}	5.0×10^{1}
$O^+ + e_h$	$\rightarrow O^{++} + 2e$	7.5×10^{-9}	1.5×10^{3}
$O^+ + H_2$	$\rightarrow H + OH^+$	2.4×10^{-11}	4.8×10^{5}
$O^+ + e$	$\rightarrow O$	1.9×10^{-11}	6.1×10^{5}
$O^+ + e_h$	$\rightarrow O$	8.4×10^{-14}	1.4×10^{8}
$O^+ + e$	$\rightarrow O^{++} + 2e$	1.4×10^{-14}	8.1×10^{8}
$\mathbf{O^{++} + O}$	$\mathbf{\rightarrow O^+ + O^+}$	3.7×10^{-7}	3.2×10^{1}
$O^{++} + e$	$\rightarrow O^+$	1.1×10^{-10}	1.0×10^{5}
$O^{++} + e_h$	$\rightarrow O^+$	4.1×10^{-13}	2.8×10^{7}
$\mathbf{H_2O^+ + e}$	$\mathbf{\rightarrow OH + H}$	1.2×10^{-6}	9.9×10^{0}
$H_2O^+ + H_2O$	$\rightarrow OH + H_3O^+$	4.0×10^{-7}	2.9×10^{1}
$H_2O^+ + e_h$	$\rightarrow OH + H$	2.5×10^{-11}	4.7×10^{5}
$H_2O^+ + H_2$	$\rightarrow H + H_3O^+$	9.1×10^{-12}	1.3×10^{6}
$\mathbf{H_3O^+ + e}$	$\mathbf{\rightarrow OH + H_2}$	8.1×10^{-7}	1.4×10^{1}
$H_3O^+ + e_h$	$\rightarrow OH + H_2$	1.3×10^{-11}	9.0×10^{5}

Table A.11 Baseline lifetimes for charged species by reaction in descending order of importance (Rate $= 1/\tau$). The bolding indicates the cut-off for those reactions occuring within the radial transport timescale ($\tau_{\rm trans}^{\rm baseline} = 26$ days).

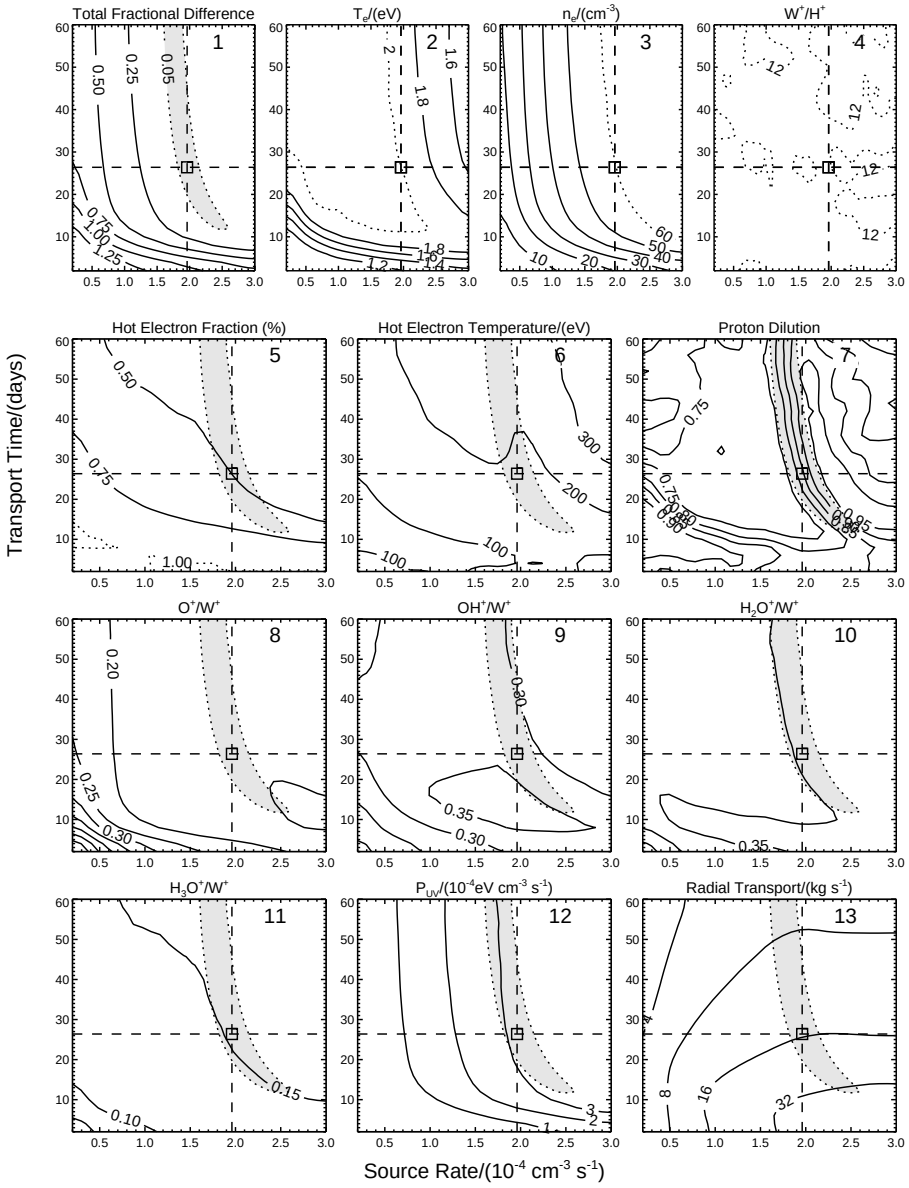


Figure A.1 Sensitivity plot of transport time versus neutral source rate. The intersection of dashed lines indicates the baseline solution. Panel 1 gives the total fractional difference ($f_{\rm diff}$) between model output and $n_{\rm e}$ = 60 cm^{-3}, $T_{\rm e}$ = 1 eV, and W^+/H^+ = 12. Panels 5−7 give the values of the 3 free parameters, and Panels 8−13 give the values for water-group composition, UV power, and mass-loading due to radially-diffused ions. Volumetric quantities (Panels 12 and 13) are calculated using a volume = $2\pi(4R_{\rm S})(2R_{\rm S})^2$. The over-plotted gray region on Panels 5−13 delineates $f_{\rm diff} = 0.05$ (Panel 1).

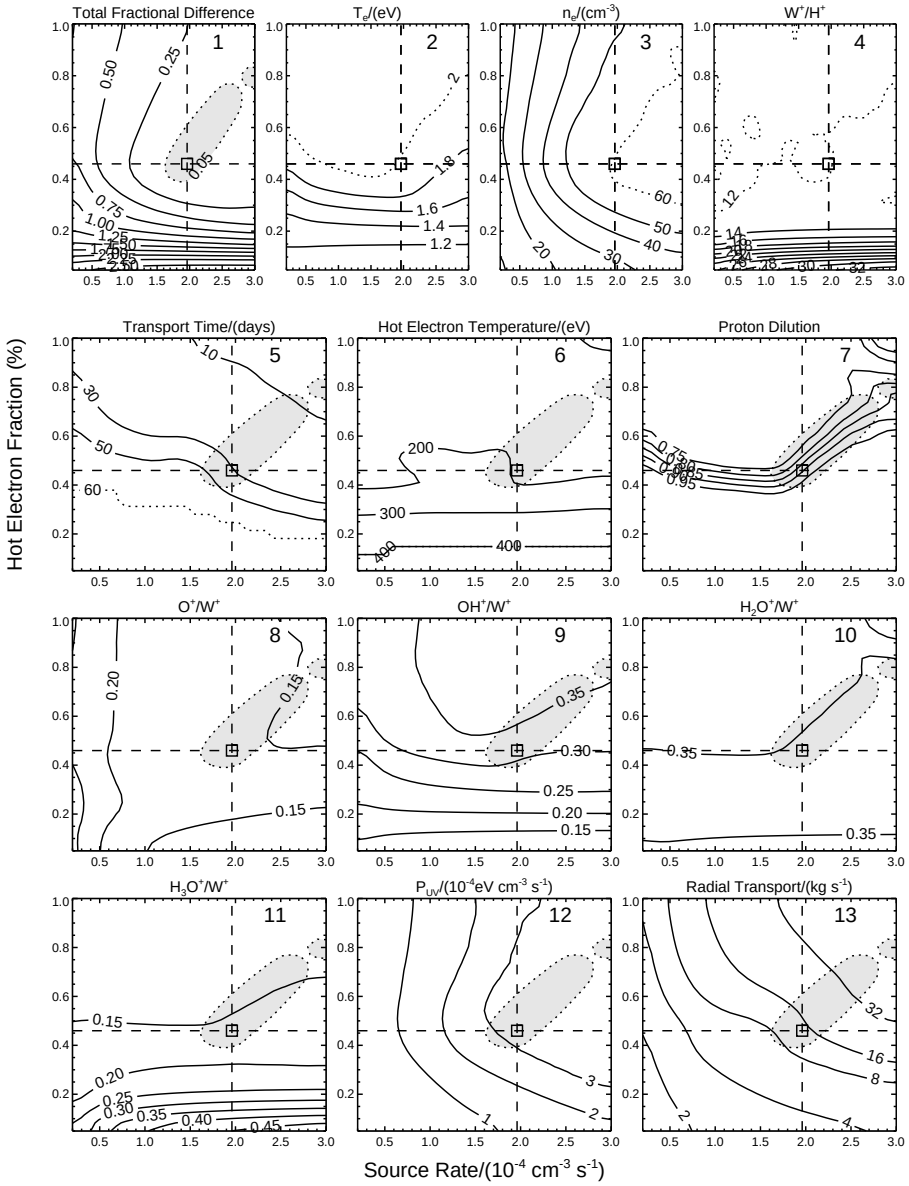


Figure A.2 Sensitivity plot of hot-electron fraction versus neutral source rate. See also caption, Figure A.1.

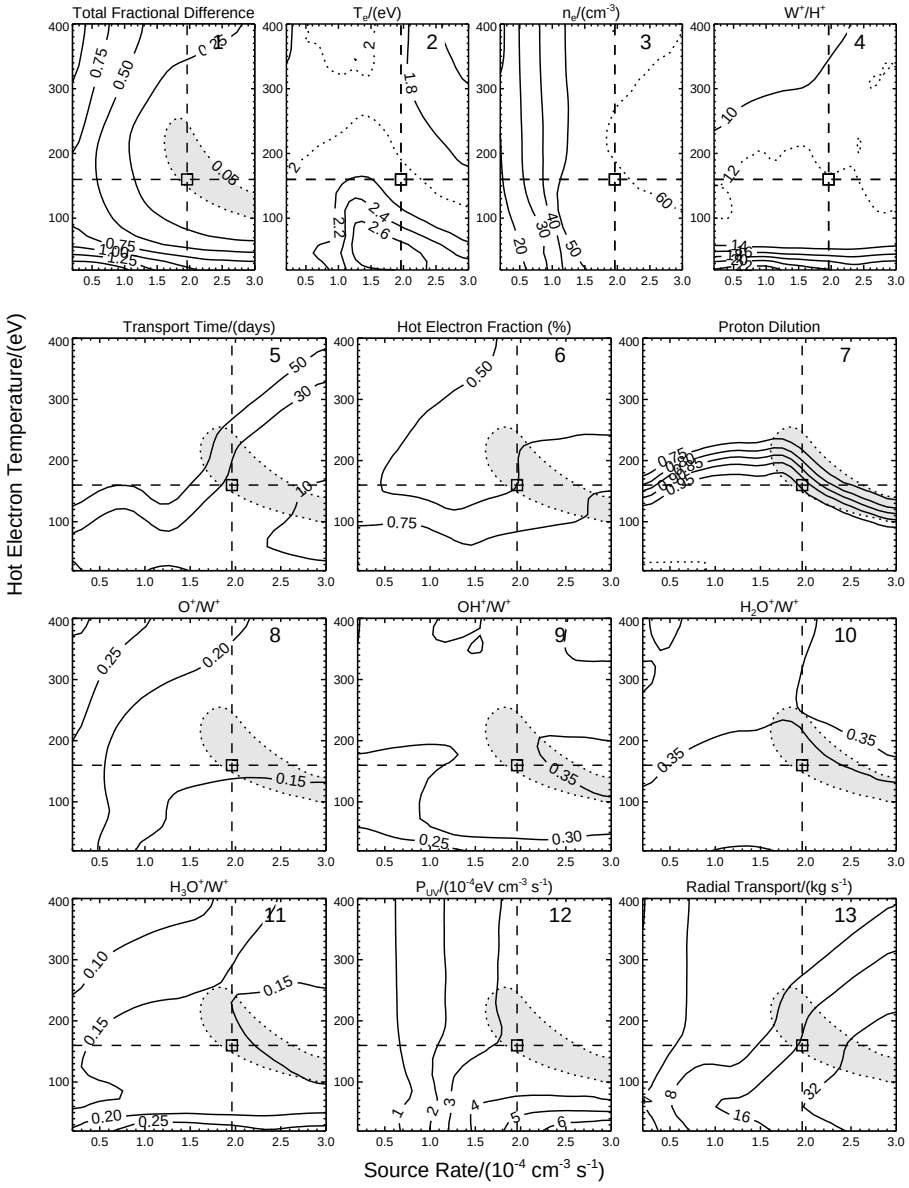


Figure A.3 Sensitivity plot of hot-electron temperature versus neutral source rate. See also caption, Figure A.1.

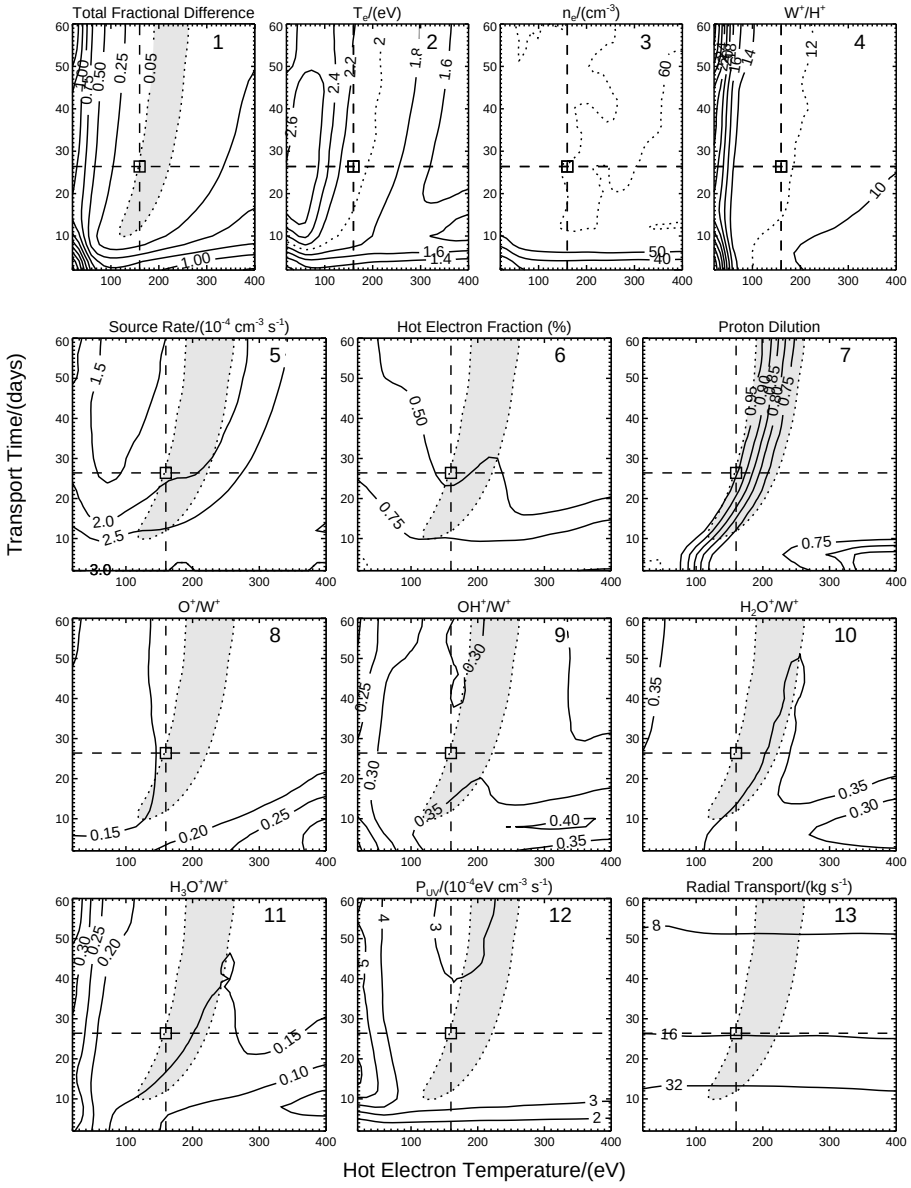


Figure A.4 Sensitivity plot of radial transport timescale versus hot-electron temperature. See also caption, Figure A.1.

Appendix B

Charge exchange collision probability

The average number of collisions occurring during a time interval Δt is given by $\lambda \equiv \nu \Delta t$, where $\nu = n_{\text{neutrals}} \sigma(v_{\text{rel}}) v_{\text{rel}}$ is the local collision frequency, assumed to be constant during Δt. Statistics are applied to determine if and how many reactions occur during Δt. The Poisson distribution (*Zwillinger and Company*, 1996; *Reif*, 1965) gives the probability of suffering exactly n collisions for a given λ:

$$f(n;\lambda) = \frac{e^{-\lambda}\lambda^n}{n!}. \tag{B.1}$$

Notice that Equation B.1 peaks at $n = \lambda$ if one treats n as a continuous variable. Summing Equation B.1 discretely from $n = k$ to $n = \infty$ gives the probability of suffering *at least* k collisions during Δt,

$$P_k(\lambda) = e^{-\lambda} \sum_{n=k}^{\infty} \frac{\lambda^n}{n!}. \tag{B.2}$$

Because Equation B.1 is normalized ($e^{-\lambda} \sum_{n=0}^{\infty} \lambda^n/n! = e^{-\lambda}e^{\lambda} = 1$), Equation B.2 can be conveniently rewritten as

$$P_k(\lambda) = 1 - e^{-\lambda} \sum_{n=0}^{k-1} \frac{\lambda^n}{n!}. \tag{B.3}$$

A random number ($0 < N < 1$) is compared to each P_k at each timestep. The largest k for which $P_k > N$ determines how many fast neutrals (collisions), k, are produced

during Δt.

In practice, it is only necessary to compare to the first few P_k when $\lambda \ll 1$, made evident by the leading terms in Equation B.2 for $k+1$ and k:

$$\frac{P_{k+1}}{P_k} \approx \frac{f(k+1;\lambda)}{f(k;\lambda)} = \frac{\lambda^{k+1}/(k+1)!}{\lambda^k/k!} = \frac{\lambda}{k+1} \xrightarrow[\lambda \to 0]{} 0. \tag{B.4}$$

Multiple collisions are thus increasingly unlikely when $\lambda \ll 1$. In such cases, comparison with $P_1 = 1 - e^{-\lambda} \approx \lambda = \nu \Delta t$ is sufficient.

Appendix C

Radial model sensitivity plots

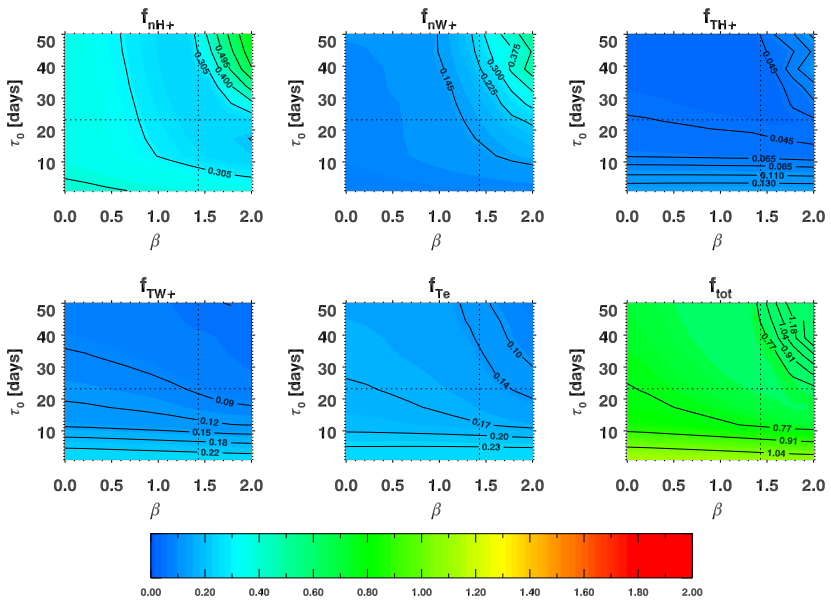


Figure C.1 1-D model sensitivity: τ_0 versus β. The statistic f is defined by Equation 5.14 on Page 124.

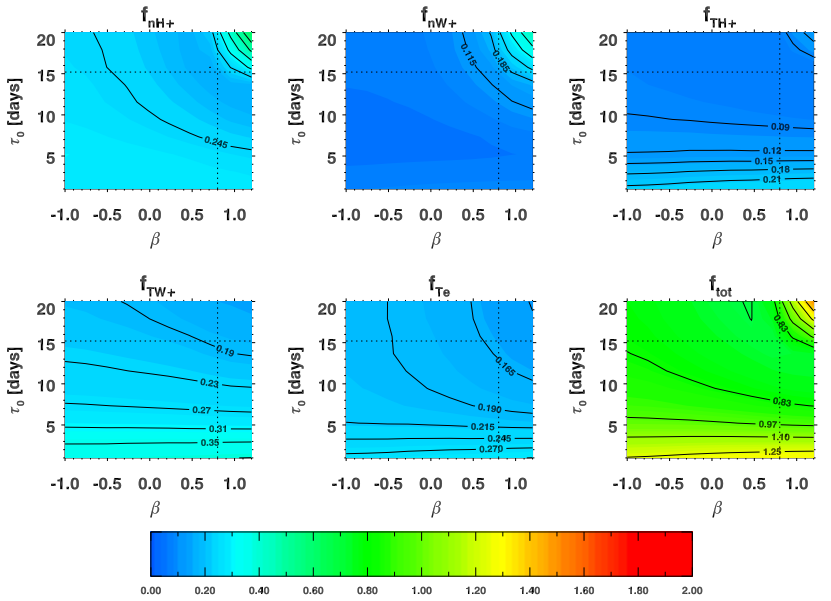


Figure C.2 2-D model sensitivity: τ_0 versus β. The statistic f is defined by Equation 5.14 on Page 124.

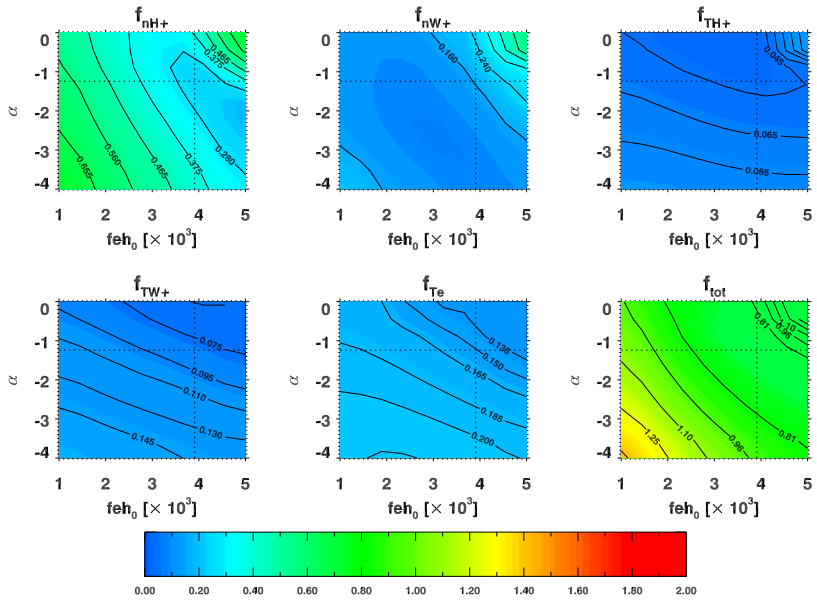


Figure C.3 1-D model sensitivity: α versus f_{eh0}. The statistic f is defined by Equation 5.14 on Page 124.

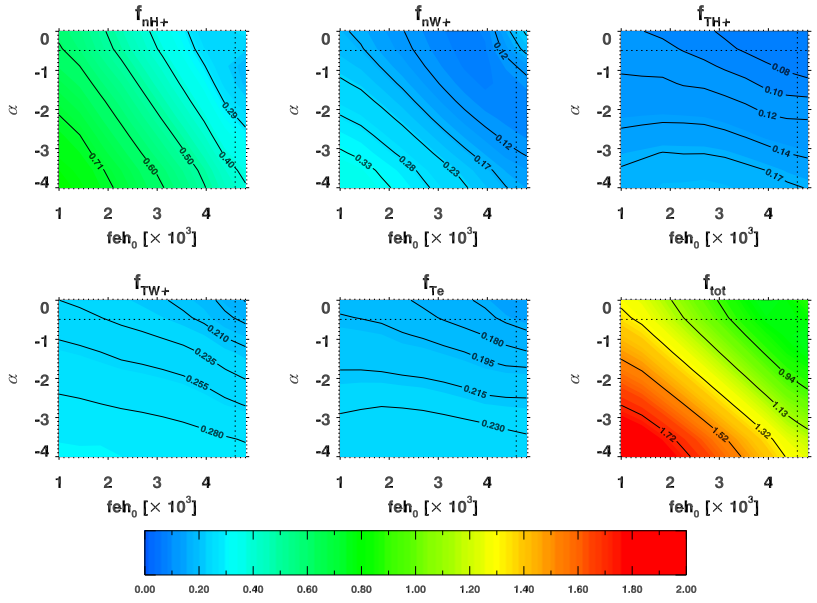


Figure C.4 2-D model sensitivity: α versus f_{eh0}. The statistic f is defined by Equation 5.14 on Page 124.

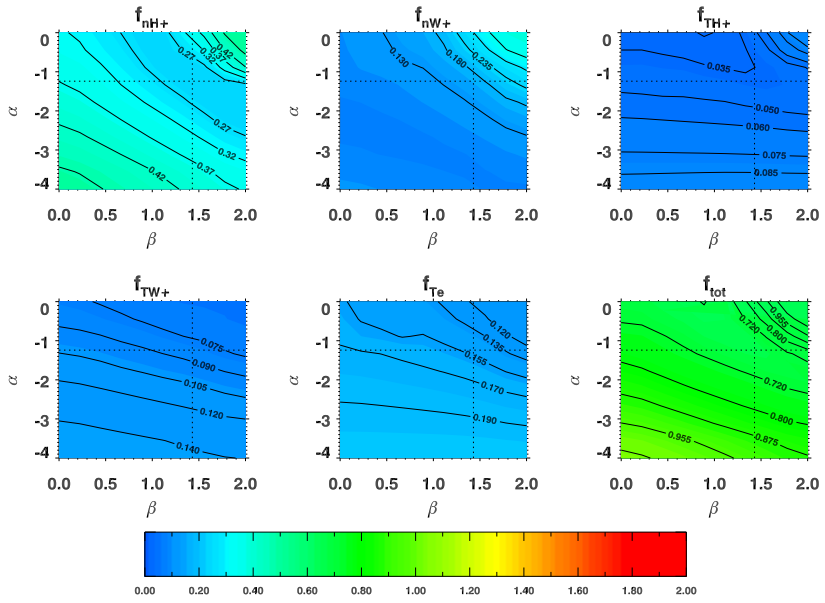


Figure C.5 1-D model sensitivity: α versus β. The statistic f is defined by Equation 5.14 on Page 124.

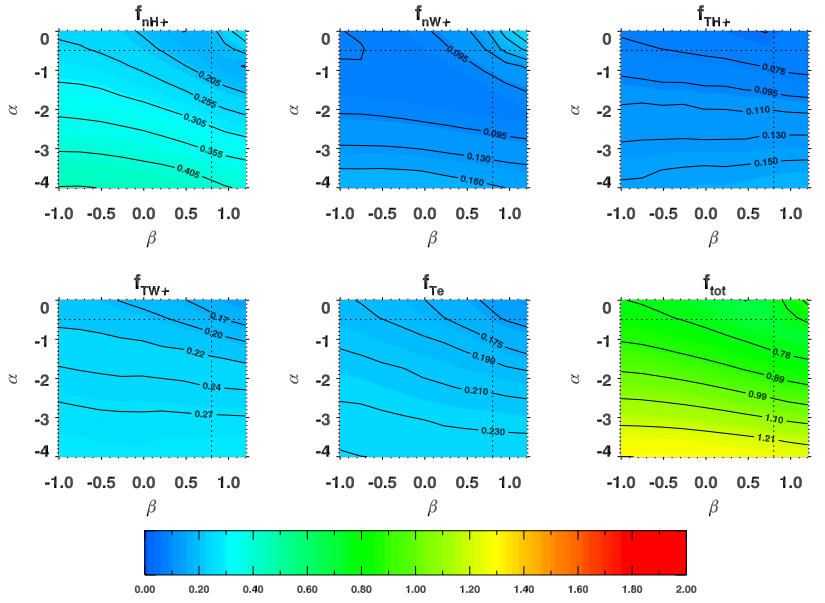


Figure C.6 2-D model sensitivity: α versus β. The statistic f is defined by Equation 5.14 on Page 124.

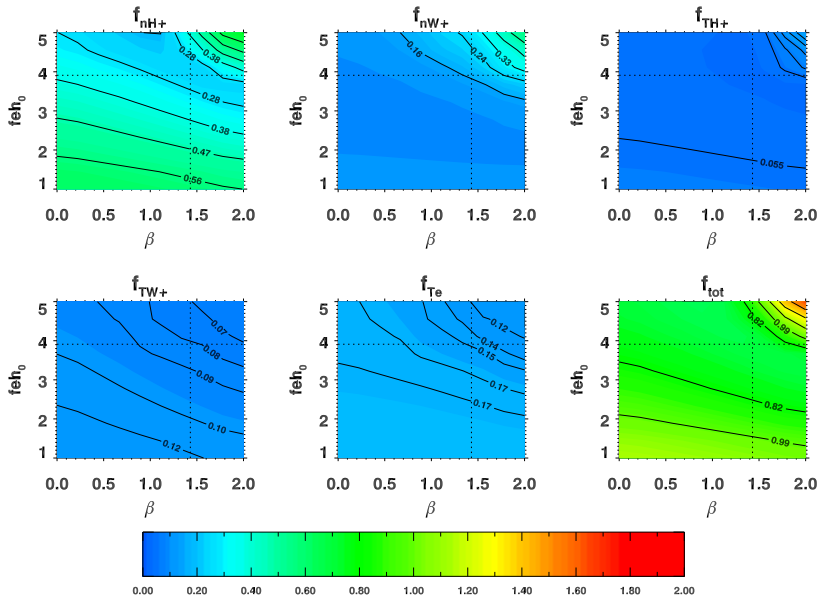


Figure C.7 1-D model sensitivity: f_{eh0} versus β. The statistic f is defined by Equation 5.14 on Page 124.

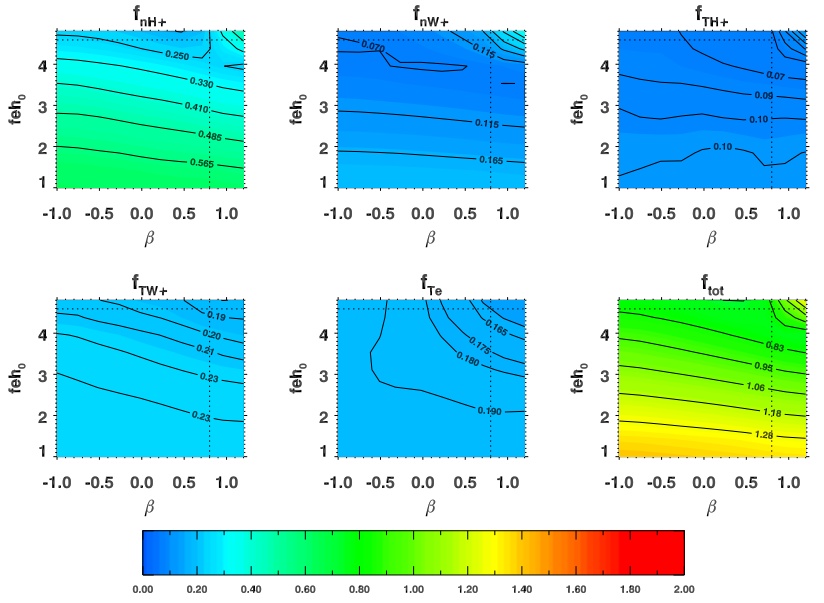


Figure C.8 2-D model sensitivity: f_{eh0} versus β. The statistic f is defined by Equation 5.14 on Page 124.